## FACULTY
## OF MATHEMATICS
## AND PHYSICS
### Charles University

# DOCTORAL THESIS

## Vojtěch Vozda

# Interaction of short-wavelength laser pulses with matter on various time scales

Institute of Physics of Charles University

| | |
|---|---|
| Supervisor of the doctoral thesis: | RNDr. Jan Kunc, PhD. |
| Advisor of the doctoral thesis: | Mgr. Jaromír Chalupský, PhD. |
| Study programme: | Physics |
| Study branch: | Optics and Optoelectronics |

Prague 2020

## Acknowledgement

Title: Interaction of short-wavelength laser pulses with matter on various time scales

Author: Vojtěch Vozda

Institute: Institute of Physics of Charles University

Supervisor: RNDr. Jan Kunc, PhD., Institute of Physics of Charles University

Advisor: Mgr. Jaromír Chalupský, PhD., Institute of Physics of the Czech Academy of Sciences

Abstract: An advent of powerful sources producing intense and ultrashort laser pulses containing high-energy photons opened up a wide range of possibilities to conduct experiments formerly achievable only through theoretical calculations and models. This thesis provides a complex overview of processes which occur right after arrival of the first photons, through lattice heating, up to resolidification and formation of irreversible changes. Irradiated spots and craters formed in various materials are examined employing a wide range of microscopic and spectroscopic methods which provide a deep insight into laser-induced modifications such as detachment of a graphene layer from SiC substrate or thermally-induced diffusion of tellurium inclusions through CdTe lattice. An increased emphasis is placed on beam characterization utilizing ablation and desorption imprints in suitable solids. A proper knowledge of the beam fluence profile may serve for evaluation of diverse damage thresholds as well as for modelling of the pulse propagation or consequent retrieval of otherwise unmeasurable opacity of warm dense aluminium plasma heated to temperatures exceeding tens of thousands of Kelvins. Moreover, the method of desorption imprints is extended to accurate characterization of pulses delivered at MHz repetition rate. This work aims to contribute to general understanding of interaction between short-wavelength laser pulses and matter at different time scales.

Keywords: interaction, laser, time scale, warm dense matter, graphene, CdTe

# Contents

# 1. Introduction

Generation of intense and coherent pulses employing stimulated emission at various photon energies became very popular since 1960 when T. H. Maiman lit up the first laser operating in visible regime employing radiative transition in ruby [1]. Great progress in achieving much higher intensities was attained in 1980's by D. Strickland and G. Mourou who developed a technique called chirped pulse amplification [2]. Using this technique, it is possible to amplify laser pulses up to petawatt intensities without damaging an active medium. Increase of the pulse energy in terms of number of photons is therefore known for quite a long time. Generation of intense pulses consisting of high-energy photons ranging from extreme ultraviolet (XUV) to soft X-rays (SXR), i.e. 10 eV–10 keV, is however not possible using conventional approaches as the interaction of such photons with matter can be entirely different. A notable milestone in generation of short-wavelength radiation was set by an advent of free-electron lasers (FELs) capable to deliver ultrashort (1–100 fs) and extremely bright pulses covering otherwise unreachable short-wavelength part of the photon spectrum [3–12].

Two decades ago, R. W. Lee *et al.* [13,14] proposed that construction of X-ray laser sources based on X-ray FEL (XFEL) can move our understanding of processes in dense plasmas beyond the current knowledge. Modern FELs providing femtosecond pulses with energies reaching multi-millijoules are focusable down to sub-micron spots giving thus intensities from $10^{17}$ W/cm$^2$ [15] up to immense $10^{20}$ W/cm$^2$ [16].

In correspondence to experiment described later in this work, let us consider an ultrashort pulse consisting of $10^{12}$ 40-eV photons which are focused down to a $2 \times 2$ $\mu$m large spot on an aluminium target. Attenuation length of the 40-eV radiation is 430 nm and irradiated volume is thus approximately 0.4 $\mu$m$^3$. Photons of such energy interact predominantly with free electrons via the inverse bremsstrahlung process. Each of $10^{11}$ irradiated Al atoms provides 3 M-shell electrons into the conduction band and every of them hence absorbs around 3 photons. This corresponds to thermal energy exceeding 100 eV, i.e. million Kelvins! It is important to note, that after transfer of the pulse energy into electrons there are still relatively cold ions which had no time to move so far and such heating can be thus considered as isochoric. This exotic state is called warm dense matter (WDM) and is a part of the high energy density physics (HEDP) encompassing states of matter with energy densities exceeding the threshold of $10^{11}$ J/m$^{3(1)}$. WDM is naturally not present on Earth and in laboratory conditions it lasts only for a very limited time. It can be however found in astrophysical objects such as cores of large planets and stars (Saturn or Jupiter) [18–20], white dwarfs and neutron stars [21]. Proper understanding and description of WDM is also important for inertial confinement fusion (ICF) – a potential almost infinite source of energy for future generations [22,23].

Complex processes connected with high energy density usually play a negligible role in ideal dilute plasmas. They may however significantly affect properties and time-evolution of WDM and other kinds of dense plasmas. Experimental investigation of such states of matter thus forms an excellent testbed for current

---

[1]This threshold was defined by authors of HEDP journal [17].

theoretical models and computer simulations. Nevertheless, reliability of experimental data is due to high complexity of such experiments often questionable and great attention must be paid on valid data interpretation.

Besides using strong EM field intensities and laser-produced plasma, HEDP including the WDM regime can be achieved also by intense ion beams [24] or shock compression experiments. In the latter case laser-driven shock wave compresses volume of metals to half and more of the original one which induces pressures reaching units of Mbars[(2)] [26–29] while heating the material to modest temperatures around 1 eV [30]. These conditions provide an insight into structure and dynamics of terrestrial and extra terrestrial planets, asteroid and meteorite impact, planet formation by collision processes and new compounds [31]. M. Ross in his paper titled *"The ice layer in Uranus and Neptune – diamonds in the sky?"* [32] suggested that Mbar pressures and temperatures of ∼5000 K, which can be found inside the cores of large gaseous planets, lead to disintegration of methane and other hydrocarbons. And, that carbon exposed to these extreme conditions can be then found in a metallic or possibly diamond form. Latest shock-wave experiments showed, that diamond formation at these conditions is indeed feasible [33]. Recent experiments employing diamond anvil cells [34] confirm more than 80-years-old theoretical prediction that hydrogen can be found in metallic form under megabar pressures and explain thus origin of Jupiter's magnetosphere [35]. Although researchers originally thought that use of diamond anvil cells is limited to Mbar pressures because of finite strength of diamond, a special technique shown that even higher pressures, up to terapascals, can be reached [36]. Pressures exceeding 1 Mbar can be also used to increase critical temperature of superconductors up to 250 K [37].

As outlined in the previous paragraphs, FELs facilities and other powerful light sources open up unprecedented opportunities to explore new kinds of interaction such as isochoric heating and generation of extreme pressures. Great brightness of XFEL pulses further pushes resolution of X-ray microscopy [38] and coherent diffractive imaging (CDI) [39] beyond the current limits. Availability of these pulses at megahertz repetition rates makes it feasible to record thousands up to millions of diffraction patterns and reconstruct fine structures of mimivirus particles and nanocrystals [40–42].

Furthermore, complex diagnostic methods provide us opportunity to determine time scales of various processes with delicious temporal resolution. We are nowadays able to describe and observe processes which start right after arrival of the first energetic photons such as direct core-electron ionization followed by Auger decay or inverse bremsstrahlung dependent on electron temperature. Light energy is, by these and other absorption processes, transferred into electron ionization and formation of high-energy electron distribution. Removal of binding electrons from their positions may lead to ultrafast nonthermal phase transitions, melting and consequential lattice disruption [43–48]. Equilibration of electron and ion temperatures via electron–phonon coupling and/or electron–ion collisions leads to thermal melting of the irradiated material which can be then

---

[(2)]Mbar pressure could be experienced, for example, while swimming in depth of 10 thousand kilometres below the sea level. This cannot be unfortunately experienced on Earth and better comparison was proposed by Gérard Mourou in his Nobel Lecture [25] where he suggested that similar pressures could be reached by balancing one Eiffel tower on a fingertip.

potentially removed in ablation or desorption process [44, 49]. The time scale which we are interested in spans from arrival of the first photons, i.e. from the first femtosecond, until the end of the interaction when the material cools down and resolidificates which usually happens within several microseconds.

At the first glance, formation of ablation and desorption craters might seem uninteresting and rather harmful. These can be however utilized for characterization of the incident laser beam. Shapes of created imprints are directly related to spatial distribution of the beam fluence profile impacting the target. By recording many ablation or desorption imprints at various attenuation levels and different positions along the beam propagation axis, it is possible to obtain full spatial description of the beam [50]. Advanced methods provide also opportunity to retrieve phase as well as coherence degree of the beam [51].

Knowledge of the beam profile or at least its effective area is indispensable to evaluation of damage threshold in various materials which is important for minimization of damage to optical elements used in beamlines [52,53]. Ablative imprints and other irreversible surface modifications also provide a lot of information about processes which took place during the interaction. Comparing a map of a particular process, e.g. an intensity map of a selected vibration mode measured by micro-Raman spectroscopy, to the fluence profile, it is possible to determine the threshold fluence above which the given process may occur [54,55].

## 1.1 Structure of the thesis

The aim of this work is to provide a complex and detailed description of short-wavelength interaction with matter supplemented by experimental studies. The first part of this thesis is focused on a review of latest experiments which significantly contribute to description of elementary processes taking place during the interaction and assign them a corresponding time scale. The stress is put on latest experiments and consequent results rather than on complex theoretical models and calculations. The second part presents several experiments conducted by the author. This work is separated into eight chapters organised in the following way:

Chapter 1 introduces phenomena connected with the short-wavelength interaction with mater and, among others, describes the structure of the thesis. Chapter 2 provides a brief introduction to formation of laser plasma and processes accompanying its dynamics. The stress is put on effects taking part in strongly coupled plasmas and generation and diagnosis of WDM accessible with FELs.

Chapter 3 is focused on a detailed review of current state of knowledge of interaction between intense short-wavelength pulses and matter. This chapter is divided into several sections according to the time scale of various processes occurring since the arrival of the first photons up to cooling and resolidification of molten material.

Chapter 4 describes main sources of coherent short-wavelength radiation with an emphasis put on operation and characterization of FELs. These sources belong to one of the most convenient ways used for generation of exotic WDM otherwise unavailable in laboratory conditions nor in common natural environment. List and description of other lasers used for irradiation experiments and other laser facilities with extreme parameters is also provided in this chapter.

Chapter 5 introduces microscopic and spectroscopic methods used for characterization of created imprints. Good understanding of these methods helps for correct interpretation of measured data presented in next chapters.

Chapter 6 gives an overview of various methods used for characterization of focused short-wavelength pulses. This chapter is focused mainly on methods of ablative and desorption imprints frequently employed in our experiments. The second part of this chapter deals with a novel method developed for nonlinear response function recovery. Using this method it is possible to accurately reconstruct the beam profile from the imprint's shape without an *a priori* knowledge of the material response. Experimental data shows this approach is applicable also to characterization of beam delivered at megahertz repetition rate.

Chapter 7 summarizes three main experiments conducted at large laser facilities. These experiments are sorted consistently with the interaction timeline: Free-free opacity measurements in Chap. 7.1 are focused on effects occurring in dense aluminium plasma within the first hundreds of femtoseconds up to several picoseconds. XUV laser-induced detachment of a graphene layer from SiC substrate emerging from both thermal and nonthermal processes and taking place within several tens of picoseconds is described in Chap. 7.2 . The last experiment in Chap. 7.3 describes thermal diffusion of tellurium inclusions through a cadmium telluride lattice. Thermal effects may start at several tens of picoseconds and last up to a millisecond. The three different materials used in these three experiments provide a great insight into numerous effects which can take place during the exposure and thus nicely supplement the interaction timeline described in Chapter 3. All these works have been also published in peer-reviewed journals.

Finally, Chapter 8 concludes with main contribution of presented experiments and discusses possible ways of further research.

## 1.2 Author contributions

Complex experiments conducted at large-scale facilities usually require involvement of many people specialized in various fields of physics and engineering. Each researcher contributes to a specific part of a given experiment and ensures smooth running and correctness of the corresponding procedure. For this reason, author lists of publications reporting on experimental results emerging from these experiments typically count tens of authors from various institutions.

The author of this thesis participated in several various experimental campaigns conducted at free-electron laser and other laser facilities and is a (co)author of published Refs. [52–60] and submitted Ref. [61]. All of these experiments required precise characterization of the focal spot and spatial intensity distribution. The characterization was usually conducted by J. Chalupský and his colleagues from the Department of Physics, Czech Academy of Sciences. The author contributed to automation of a target holder, beam characterization and data processing.

Characterization of laser beams delivered at megahertz repetition rate (Chapter 6.3) was done in 2014 at Free-electron laser in Hamburg (FLASH), Germany. The author participated in the irradiation experiment, analysed data and together with J. Chalupský developed the NoReFry (**No**nlinear **Re**sponse **F**unction Recove**ry**) algorithm and wrote the manuscript submitted to Optics Express [61].

The experiment focused on free-free opacity measurements (Chapter 7.1) was conducted in 2015 also at FLASH. The author participated in the campaign and significantly contributed to data analysis during his three-month-long stay at the Department of Physics, University of Oxford. Forward model used for retrieval of a functional form of an absorption coefficient and writing of the manuscript published in Physical Review Letters [60] was done by S. M. Vinko and other co-authors. Samples of epitaxial graphene on SiC substrate used for irradiation experiment at Prague Asterix Laser System (PALS) (Chapter 7.2) were delivered by J. Kunc who used a noncommercial experimental furnace for the growing procedure. The author participated in the irradiation experiment, did *ex situ* post-exposure analysis involving atomic force microscopy (together with V. Hájková), white light interferometry, micro-Raman spectroscopy and XPS spectroscopy (together with J. Čechal) and wrote the manuscript published in [55]. Theoretical predictions calculated using XTANT code were done by N. Medvedev. Irradiation of cadmium telluride (Chapter 7.3) was done at PALS and capillary discharge laser (CDL) with a great contribution of T. Burian. The author did all *ex situ* post-exposure analyses and together with J. Franc interpreted the data and wrote the manuscript published in [54].

# 2. Laser plasma

High-energy photons carry enough energy to directly photoionize the most tightly bond electrons which subsequently collide with other atoms (ions) and electrons and transform absorbed laser energy into heat leading to plasma formation. Derivation of full classical plasma theory and proper description of light propagation and absorption in dense plasmas is beyond the scope of this text. These topics are well described in literature and a potential passionate reader is hence referred to following references which might serve as a great study material for deeper understanding of this topic [62–67]. In this section we will focus on description of laser plasma properties which are crucial for our purposes.

## 2.1 Plasma oscillations

A classical Drude model describes metals as a field of positively charged ions immersed into a sea of freely moving electrons. This approach is basically applicable also to plasma description. Interaction of free electrons with electromagnetic (EM) waves propagating through a collisional plasma can be described via induced dipole moments proportional to the dielectric function [63]:

$$\varepsilon = 1 - \frac{\omega_p^2}{\omega(\omega + i\nu)}, \quad \text{where} \quad \omega_p = \sqrt{\frac{n_e e^2}{\varepsilon_0 m_e}}. \tag{2.1}$$

Here $\nu$ is a mean electron collisional frequency including electron–ion as well as electron–electron collisions, $n_e$ is the electron density, $e$ elementary charge, $m_e$ electron mass, $\varepsilon_0$ vacuum permittivity, $\omega$ frequency of EM waves and $\omega_p$ is the plasma frequency which stands for collective oscillations of free electrons. Real and complex parts of refractive index $n = \sqrt{\varepsilon}$ result in absorption of EM waves propagating through the collisional plasma. The absorption is realized through inverse bremsstrahlung where an electron gains photon energy while colliding with an ion. This process is described in more detail in Chapter 3.1.1. In collisionless plasma, where $\nu = 0$, the Eq. (2.1) reduces to:

$$\varepsilon = 1 - \frac{\omega_p^2}{\omega^2}. \tag{2.2}$$

Refractive index for $\omega > \omega_p$ has no imaginary part and such light can thus freely propagate through the collisionless plasma. An interesting situation however occurs when $\omega < \omega_p$. In this case, the refractive index becomes purely imaginary and light is totally reflected from the plasma surface. Typical values of the plasma frequency for metals are of the order of electronvolts, i.e. in the ultraviolet spectral range. A particular value of solid-density aluminium with electron density $1.8 \times 10^{23}$ cm$^{-1}$ is $\omega_p \approx 15$ eV.

This behaviour of conductive matter is extremely important for experiments and proper choice of photon source and its wavelength. Irradiation of a metal sample with light of frequency less than $\omega_p$ means that photons do not penetrate into the volume but transfer their energy only to a thin surface layer. The heated metal surface quickly transforms into plasma which expands towards the laser

beam. Created plasma plume is called corona which might have a considerable degree of ionization and behaves according to plasma dynamics. Its formation starts at the time scale of ∼100 ps and is thus important mainly for nanosecond pulses. Electron density $n_e$ inside the corona decreases towards its outer parts and surface where $\omega_p(n_e) = \omega$ is called critical surface beyond which the light cannot propagate and further heating of the sample is thus significantly limited. A bit more about the corona formation and accompanying processes is described in Chapter 3.3.1.

In order to probe plasma we therefore necessarily need photons whose frequency is higher than $\omega_p$. The plasma waves then cannot follow rapid oscillations of the EM field and light can propagate into the material. From Eq. (2.2) it follows that the higher the electron density, the more energetic photons are required. Considering relatively long ($\sim 1\ \mu$m) attenuation length of short-wavelength radiation in metals we may attain volumetric heating of volume counting several cubic microns. Employing pulses with femtosecond duration, heating of this volume can be considered as isochoric leading to formation of the solid-density plasma.

## 2.2 Coupling parameter

All plasma states described here are typically highly ionized and quasi-neutral, i.e. charge-balanced. Prior to description of particular states of laser plasma, it is a great idea to differentiate ideal classical plasma (often referred to as "good" plasma) from other forms of heated and ionized matter which might be appropriately called "bad" plasma. For this reason, the plasma coupling parameter $\Gamma$ which compares electrons' potential Coulomb energy $E_C$ with their kinetic energy $k_B T_e$, where $k_B$ is the Boltzmann constant and $T_e$ is the electron temperature, is defined:

$$\Gamma = \frac{E_C}{k_B T_e}. \tag{2.3}$$

If we assume Coulomb energy in its typical form $E_C = q_e^2/(4\pi\varepsilon_0\langle r\rangle)$, where $q_e$ is the charge of the electron and the inter-particle distance $\langle r\rangle$ is approximated with the Wigner-Seitz radius $\langle r\rangle = (3/4\pi n_e)^{1/3}$, we can rewrite the coupling parameter as:

$$\Gamma = \frac{q_e^2}{4\pi\varepsilon_0 k_B T_e}\sqrt[3]{\frac{4\pi n_e}{3}} \propto \frac{\sqrt[3]{n_e}}{T_e}. \tag{2.4}$$

$\Gamma$ is hence proportional to ratio of electron density and electron temperature. Examples of various states of matter placed into a $\rho_e - T_e$ phase diagram of the electron density $\rho_e$ and temperature are shown in Figure 2.1. Equation (2.4) was used for calculation of the coloured background which helps to distinguish between the ideal and nonideal plasma states.

Here we also note that definition of $\Gamma$ according to Eq. (2.3) is accurate only until the thermal de Broglie wavelength is smaller than ion spacing and ion–ion system is classical. In case of very high electron densities the plasma becomes degenerate and quantum-mechanical effects start to play a significant role. Electrons in this case cannot get arbitrarily close and $\Gamma$ is thus defined as ratio of the potential energy to the Fermi energy. This region in Fig. 2.1 is to the right from

the line where the chemical potential is $\mu = 0$. The coupling parameter $\Gamma$ in this degenerate regime is inversely proportional to the electron density ($\Gamma \propto n_e^{-1/3}$) and used background calculated by Eq. (2.4) is thus not absolutely correct. More detailed information can be found in [14].
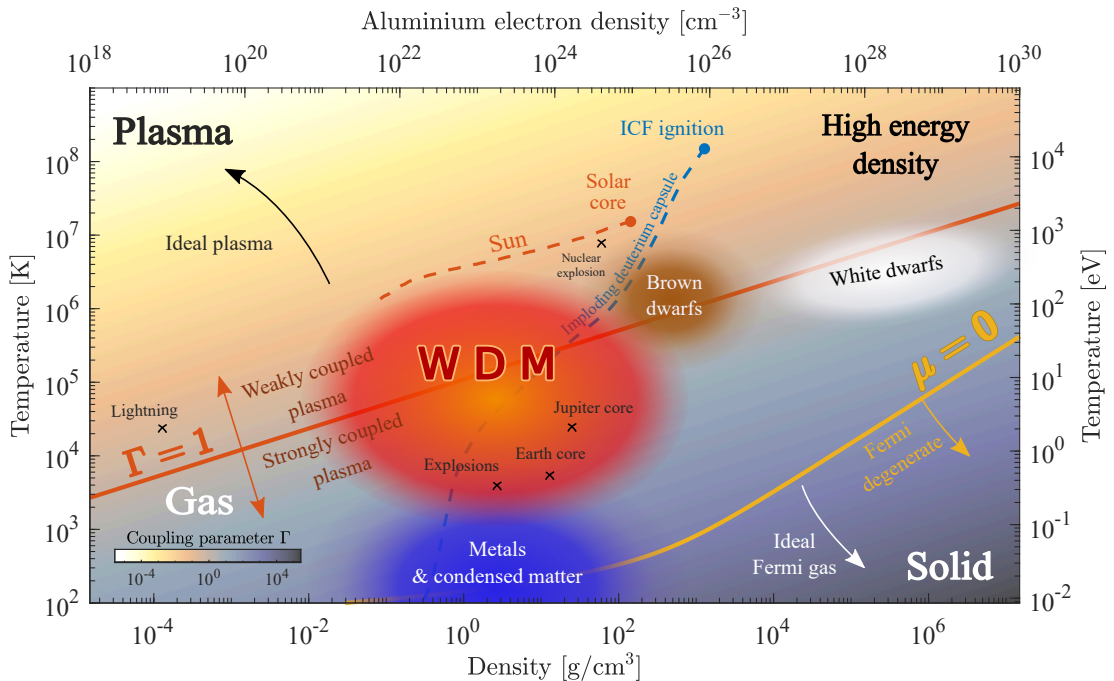


**Figure 2.1:** Density–temperature phase diagram surrounding warm dense matter regime. Figure is based on data from [14, 67–71]. Equation (2.4) was used to plot the background.

## 2.3 Weakly coupled plasma

If the thermal energy of charged particles exceeds their mean energy of the Coulomb interaction and $\Gamma \ll 1$, plasma is weakly coupled and its equation of state equals to that of an ideal gas. Weakly coupled plasma is usually very hot and dilute and because of a very weak interaction between individual electrons it is sometimes called collisionless. It is therefore clear that many-body effects[1] play a negligible role in ideal plasmas and collisions, although not occurring very often, are treated as binary. Hence behaviour of ideal plasma can be relatively well described by common kinematic models. All particles are assumed to interact only with a background electromagnetic field created by surrounding charged particles. Suppression of the Coulomb interaction makes it feasible to characterize this plasma in local thermodynamic equilibrium (LTE) by Saha-Langmuir equation, which determines its ionization degree from particle velocity, i.e. temperature [63]. Although description of the weakly coupled plasma looks like some strong mathematical approximation it is characteristic for solar wind, interstellar gas, ionospheric and space plasma physics.

Correct treatment of the ionization degree, scattering and collisional cross section is very important for estimation of collisional rates closely related to plasma

---

[1] Although 3 is usually not considered to be a number of some astronomical value, the word "many" in the term "many-body" means indeed "three and more".

transport properties and its evolution. High kinetic energy of colliding particles results only in a very small deflection angle and cumulative effect from many scattering events is hence calculated. Derivation of change of a perpendicular momentum of an electron passing through a field of other charged particles leads to the Coulomb logarithm $\ln \Lambda_c$ defined as [72, 73]:

$$\ln \Lambda_c = \int\limits_0^\infty \frac{\mathrm{d}b}{b} = [\ln b]_0^\infty = \ln \left( \frac{b(\infty)}{b(0)} \right), \qquad (2.5)$$

where parameter $b$ is known as the impact parameter, i.e. the closest approach of the electron to the scattering centre. The Coulomb logarithm obviously diverges for both small and large impact parameters; hence lower and upper estimate is needed. Minimal value $b_{\min} = b(0)$ is usually taken as the closest approach naturally limited by the de Broglie wavelength $\lambda_B$ and $b_{\max} = b(\infty)$ as the Debye length $\lambda_D$ which is a distance characteristic for given plasma where electrostatic potential significantly decreases due to screening by other charged particles. The form of the Coulomb logarithm then is:

$$\ln \Lambda_c = \ln \left( \frac{\lambda_D}{\lambda_B} \right) = \ln \left( \frac{m_e v}{h} \sqrt{\frac{\varepsilon_0 k_B T_e}{n_e e^2}} \right), \qquad (2.6)$$

where $v$ is the electron relative velocity and $h$ is the Planck constant. Ordinary values of $\ln \Lambda_c$ within the classical plasma theory range from 5 to 20.

## 2.4 Strongly coupled plasma

A counterpart of high-temperature and low-density plasma, being ideal for modelling and theoretical description, is the strongly coupled plasma with $\Gamma \geq 1$. Its typical representatives found in the Universe are noted in the phase diagram in Fig. 2.1. Matter in this regime is relatively cold but density of charged particles is very high, similar to that of condensed matter. Coulomb repulsive energy thus becomes comparable with the thermal energy and many effects, which could be neglected in the weakly coupled plasma, must be considered here.

The first obvious difference, which follows from high density, is the treatment of collisions and related collisional rates. Whereas all potential collisions in weakly coupled plasma were treated as binary, many-body effects start to play a significant role here and must be taken into account [74]. Although the classical form of the Coulomb logarithm as defined in Eq. (2.5) is used in many theoretical models dealing with strongly coupled plasmas, its application is not valid here [75]. It has been shown, that collisional rates in strongly coupled plasmas reach much higher values than initially anticipated [58, 76] and predicted evolution of the plasma state can thus significantly differ. Large number of collisions rapidly drives the system into local thermodynamic equilibrium (LTE) and contributes to a fast formation of a stable electronic distribution as well as relevant plasma emission intensities [76]. A proper estimation of collisional rates is also extremely important for free-free opacity studies involving absorption via the inverse bremsstrahlung process. Such measurements were done at the FLASH facility [60] and results are described in Chapter 7.1.

Many-body effects are, together with equally important degeneracy and thermal excitations [77], reasons why simple kinetic models cannot be used any longer in strongly coupled plasma modelling and some approximations must be used. Simply put, conventional theories are suitable for description of the classical state of matter and matter which is dilute, extremely hot and completely stripped of electrons. A problem occurs when we try to describe atoms which absorbed a large amount of energy within a very short period of time without loosing all their electrons. For this reason, new theoretical approaches, such as complex density functional theory (DFT) models [56, 58, 78], hybrid models combining molecular dynamics with thermal and nonthermal transitions [53, 79], two-temperature models [80] and others, are nowadays being developed.

High degree of ionization is responsible for a shift of atomic levels not only in strongly coupled plasmas. Removal of electrons from an atomic shell induces a decrease of overall negative charge surrounding the positive core and remaining electrons, originally also influenced by removed electrons which partially screened the positive charge, are bound more tightly. Such decrease of the screening connected with a shift of atomic levels can be observed via emission spectroscopy and will be discussed later. Another effect which acts in an opposite way is responsible for shifting of orbital energies towards the continuum. It results from a large number of free electrons whose negative field helps to screen the positive core. It is called ionization potential depression.

### 2.4.1 Ionization potential depression

Strongly coupled and highly ionized plasmas are characterized by high density of free electrons which form a locally charged environment perturbing atomic potentials. Screening of positive core of an atom results in a shift of its atomic levels and reduction of the ionization threshold. Some electrons, which are bound under normal conditions, might be promoted into the continuum. This effect, where ionization energy threshold is lowered because of the environment influence, is known as ionization potential depression (IPD) or continuum lowering [81, 82].

Ionization of bound electrons without any additional heat due to the effect of continuum lowering can be observed for high pressures and is referred to as pressure ionization [83]. As an illustrative example we can mention an isolated aluminium atom which has 13 bound electrons, three of them in the M-shell. After putting a bunch of aluminium atoms together into a bulk material, the three M-shell electrons are promoted into the conduction band as the core is screened by electrons from neighbouring atoms. The ground state of the bulk aluminium is thus $Al^{+3}$ which is usually denoted as Al IV. The conduction electrons play a crucial role in absorption of XUV light via the inverse bremsstrahlung process as described in Chapter 3.1.1.

The charged environment does not affect only utmost electronic levels, directly related to the ionization threshold, but also energies of inner shells. Experimental studies observing K-$\alpha$ fluorescence of solid-density aluminium [84] and other low-Z material plasmas [85] heated to ~100 eV revealed that IPD effect is much stronger than predicted by standard theoretical models. Disagreement between theoretical estimates and experimental results was confirmed also by spectrally resolved X-ray scattering [86].

A representative example of IPD shown in Figure 2.2 is taken from the work published by O. Ciricosta *et al.* [84] who created solid-density aluminium plasmas of temperatures reaching 180 eV. Using the soft X-ray photoemission spectroscopy the extent of IPD was evaluated. The figure shows energy needed to photoionize a K-shell electron to other states (L-shell, M-shell, continuum) calculated for the first five charge states. Atomic edges of continuum calculated for isolated atoms where all electrons remain bound, i.e. energy of continuum edge is greater than energy of M-shell, are shown by dashed black lines. Grey regions depict a continuum of the bulk Al and dark grey intervals experimentally measured K-edge energies. All M-shell electrons are therefore obviously located in continuum for all displayed charge states. Important are also red and blue lines showing continuum edges calculated by two different theoretical approaches: Stewart–Pyatt model (SP) [82] and Ecker–Kröll model (EK) [81]. It is clear that SP model, which was widely implemented into many codes focused on strongly coupled plasma dynamics, cannot reproduce experimentally observed values. EK approach which predicts much higher IPD and agrees with experimental data should be thus used.
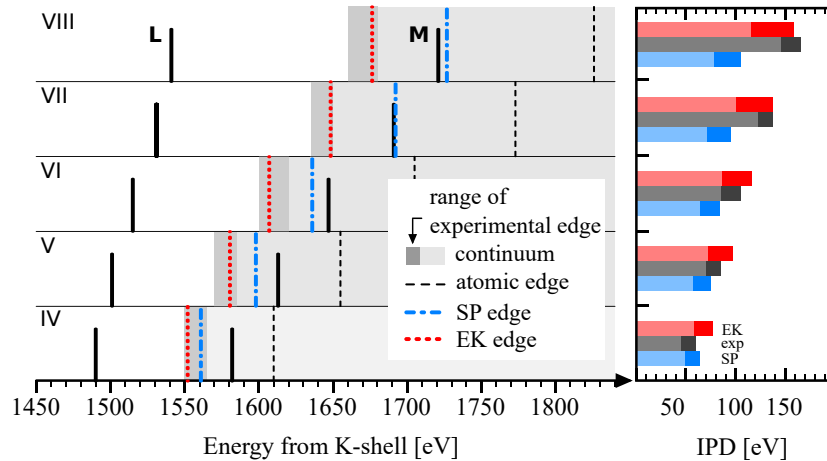


**Figure 2.2:** Effect of IPD for different charge states of aluminium. Left part shows energy difference between the K-edge and other various levels. Right part compares experimentally observed IPD to values predicted by two different theoretical models. Figure adapted from [84].

Estimation of IPD is crucial for dense plasma studies where ionization threshold specifies ionic binding energies essential for absorption cross section, temperature and emission spectra. The effect of IPD is the most important for plasmas of temperatures exceeding 100 eV but it plays a role also in colder systems [87].

## 2.4.2 Ionization bottleneck

Removal of electrons from an electron shell leads to a decrease of the core screening and consequently to increase of binding energy of remaining electrons. At a certain ionization degree there is a sudden large step in change of energy needed for ionization of one additional electron from an atom. Observation of this effect is typical for hot dense plasmas and is called ionization bottleneck [88].

As an representative example, let us again assume a single aluminium atom from which we try to remove electrons one by one starting from the utmost energy level. The energy needed to remove the first of the 13 electrons is quite low, only 6 eV. Singly ionized aluminium ion, termed as magnesium-like aluminium, has

now only 12 electrons which are, due to the absence of one electron, bound to the positive core more strongly. Energy needed to remove the second electron is thus larger – in this particular case 19 eV. To remove the third electron (now from the sodium-like Al ion) we need 28 eV because of the same reason. However, to remove the fourth electron we need incredible 120 eV. Origin of this large step resides in the fact that configuration with 10 atoms is very stable (closed shell) and the atom "hesitates" to give away any other electron. Element with 10 electrons is neon and it is not a coincidence that neon is absolutely inert. Aluminium with three missing electrons is thus called Ne-like aluminium and it is quite difficult to remove additional electron from it. Another bottleneck occurs when we try to remove one of the last two electrons. This configuration is typical of helium – other absolutely inert element. To transform Li-like Al into He-like Al we need 442 eV but to create H-like Al from He-like Al we need additional 2086 eV! The described effect is often employed in soft X-ray plasma lasers. A typical example can be the Ne-like zinc quasi-steady-state plasma-based laser emitting at 21.2 nm which is pumped with the Prague Asterix Laser System (PALS) providing kilojoule sub-nanosecond pulses in the NIR spectral range. More details about this laser are provided in Chap. 4.2.1.

### 2.4.3 Warm dense matter

As outlined in the introduction, irradiation of condensed matter with an intense sub-picosecond laser pulse in short-wavelength region leads to isochoric and volumetric heating to temperatures around 1–100 eV. Kinetic energy of particles is, due to high density, comparable to Coulomb energy but also to Fermi energy of typical metal and bond strength. This leads to ionization, strong coupling and electron degeneracy. Also other effects typical of strongly coupled plasma like IPD may play a significant role here. This state is called warm dense matter (WDM) and is typical of intense laser heating, ICF and astronomical objects. Material heated to higher temperatures about $\sim 1$ keV is then called hot dense matter (HDM). As pictured in the $\rho_e - T_e$ phase diagram (Fig. 2.1), WDM is approximately defined as a region where density and temperature may exceed typical values of solids by several orders of magnitude. It spans over the intersection of all condensed matter physics, plasma physics and high energy density physics.

The most straightforward way to access the WDM regime is definitely heating of metal samples to temperatures of hundreds of thousands of Kelvins by employing XFEL-produced radiation [60,85,89,90]. Nevertheless, it can be also reached by utilization of shock waves and compression of laser-produced plasma [26,87]. Cooling of HDM or diluting heated solids of extreme densities is probably superfluously complicated experimental work.

However easy and straightforward the generation of WDM with use of FEL pulses might seem, isolation and measurements of well-defined WDM conditions in laboratory is tremendously difficult. The first issue we have to consider is that WDM is usually just in a transient regime which is not in the thermodynamic equilibrium (TDE) and lasts therefore only for a very limited time. Hence the characterization must be done in sophisticated ways such as pump–probe experiments, Thomson scattering, X-ray diffraction or X-ray emission spectroscopy.

Furthermore, heated volume is very small and steep spatial gradients of temperature, ionization degree and other properties are thus very common especially at the borders of the irradiated area. Therefore, a special attention should be paid also to a proper characterization of the spatial profile of the generated plasma which is very valuable in post-processing calculations and data interpretation. How to correctly deal with all these complex problems is described in Chapter 7.1.

**Diagnostic methods**

An important effect to be investigated in dense plasmas is a dependence of electron transition energy on the charge state of a given ion. Increasing number of holes in electron shells induce decrease of the screening of the positive core charge and photons emitted during electron deexcitation thus have higher energies. Measured emission spectra then directly reflect ionization state of the examined plasma, charge-resolved fluorescence spectrum [84,85,91], K-shell opacity [56] and collisional dynamics [58].

A typical example of the emission spectra observed upon creation of solid-density aluminium plasma is shown in Figure 2.3. It consists of a large set of measured spectra obtained at various photon energies. Such an experiment is possible owing to a great wavelength tunability of X-ray free-electron lasers. The photoabsorption process is dominated by a direct ionization of K-shell electron. Created hole is filled either by nonradiative KLL Auger decay or by measurable radiative deexcitation from the L-shell. The main $K_\alpha$ line at $\approx$1486 eV corresponding to the charge state IV is followed by a number of weaker lines which emerge from higher charge states. These were created not directly by the X-ray pulse, but by electron impact ionization. As can be seen, number of various
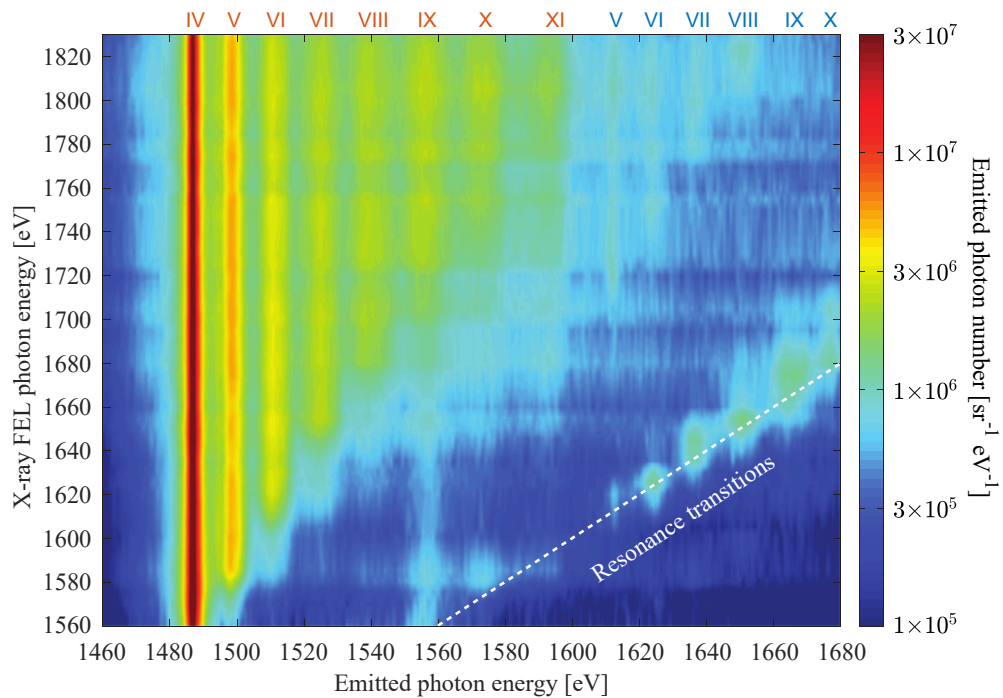


**Figure 2.3:** Emission spectra corresponding to radiative $K_\alpha$ transition measured for a wide range of different excitation photon energies. Figure adapted from [91].

charge states is strongly dependent on incident photon energy. At very high photon energies it is even possible to observe transitions corresponding to double K-shell hole. These states can be observed also below the dashed white line which corresponds to emission from resonantly-pumped K–L transitions. Such experiment cannot be conducted with use of visible light where ionization of electrons from outer shells predominates and formation of ions with a single K-shell hole is extremely rare.

Further properties of WDM like electron temperature and density can be obtained from spectrally-resolved X-ray scattering [86]. Atomic motion as well as electronic processes occurring within tens of femtoseconds can be observed via Bragg reflection [26,92,93]. One of the most used and versatile diagnostic methods of WDM utilizes measurement of Thomson scattering spectra. Detected signal can be used for estimation of plasma temperature, electron density, dielectric function as well as ionization stage [28, 94–97].

To investigate temporally-resolved processes occurring in the WDM regime, pump–probe experiments are very beneficial. The first pulse of high energy (pump) creates homogeneous WDM conditions and detection of a weaker delayed second pulse (probe), which penetrates through the heated matter, provides information about its properties. WDM state can be prepared by the pump consisting of photons in a wide range of energies. Frequency of photons in the probe must be, however, higher than the plasma frequency which is usually in the XUV regime. Chapter 7.1 describes transmission experiment of opacity measurements where XUV pulse was split and relative delay between these two pulse was set.

### Theory and calculations

Calculations of WDM properties and opacity are difficult as it cannot be treated as ideal plasma. The thermal energy of free electrons is comparable to repulsive Coulomb forces as well as to Fermi energy of a typical metal and usual approximations cannot be thus applied here. Because of high electron density, IPD starts to play a significant role and estimation of plasma properties becomes more and more difficult. Due to relatively cold ions, WDM also may still possess a band structure. Moreover, as temperature increases, there are warmer electrons which occupy higher bands which have to be taken into account and computational time then increases with square of the temperature [78]. Materials of interest thus contain mainly low-Z elements like Al, Mg, Si, $Al_2O_3$, etc. [85] which are relatively easy to heat and are accessible for theoretical calculations. Pushing of high-Z metals into WDM regime is also doable, large intensities about $10^{20}$ W/cm$^2$ are however needed [16].

# 3. Time scale of the interaction

When we irradiate a sample with an intense XFEL pulse and examine induced changes post-exposure, i.e. after the interaction, we may detect irreversible modifications of the sample surface like ablation or desorption imprints, phase transitions, changes in optical parameters and others. A proper investigation of these changes may provide a valuable information about beam characteristics as well as material parameters. Various methods of this characterization are discussed in Chapter 5. Here we focus on finding answers to other questions: Which mechanisms stand beyond these final changes? How does the timeline of the interaction process look like? What happens just after the arrival of first photons? Which processes lead to establishment of the thermodynamic equilibrium (TDE)? How does absorbed energy spread throughout the material and how does the material cool down?

The following text aims to summarize main processes which take place during and after the irradiation, assign them a characteristic time scale and compare them also with possible interaction of visible light. The vast majority of the following knowledge comes from experimental works conducted at FELs with a significant contribution of theoretical models which are currently waiting for experimental confirmation. A summary of all processes is provided at the end of this section. The overall stress is placed on processes connected with high-energy photons and formation of plasma. Bandgap typical for insulators and semiconductors collapses on the order of hundreds of femtoseconds after the pulse absorption and such material thus undergoes a rapid nonthermal phase transition into metal [44, 45, 98, 99]. Detailed information about optical properties of condensed matter, interband transitions and quasiparticles can be found in literature [100–102].

The interaction starts with arrival of 10–100-fs pulse containing around $10^{12}$ photons of energy between tens of eV up to tens of keV. This pulse is focused onto a tiny spot with an area of only several square microns and intensity reaching values up to $10^{20}$ W/cm$^2$.[1]

Very short pulse duration is often essential as it determines the overall time resolution of an experiment. Here we assume pulses of duration approximately 100 fs. It means that energy deposition can be considered as instant for processes occurring on nanoseconds or greater time scale.[2]

Despite very short pulse duration, there are processes like electron dynamics and cascades [53, 103], strong-field ionisation [104] or nanoplasma dynamics [105] which happen 100× or even 1000× faster than the pulse duration. In order to observe dynamics of these processes, sub-femtosecond pulses must be used. Creation of such pulse requires a very broad spectrum spanning up to the soft X-ray regime generated, for example, with use of high-order harmonic sources. This spectrum can be then used for synthetisation of attosecond pulses which

---

[1]Compare to ambitious ELI project described in Chapter 4.2.4 ($10^{25}$ W/cm$^2$), laboratory lasers ($10^{10}$–$10^{20}$ W/cm$^2$), laser pointers (0.5 W/cm$^2$) or a direct sunlight (0.1 W/cm$^2$).

[2]To visualize how short the 100 fs pulse is we may compare its length to the distance between the Earth and Moon. Light travels this distance approximately one second, whereas during 100 fs it can travel only about 30 $\mu$m. So one second versus 100 fs is the same ratio as the distance between Earth and the Moon versus the hair thickness!

can be employed in tracking motion of electrons on atomic scales. For further information about attosecond physics see [106] and references cited therein. Here we start with processes measurable with FEL pulses, i.e. at femtosecond time scale.

## 3.1 Femtoseconds

Range of femtoseconds is a characteristic time for many elementary processes and predominantly electronic processes, e.g. chemical reactions, nonthermal melting, Auger decay, impact ionization, bandgap collapse and others. Prior to describing the time scale of the interaction, an introduction to basic processes of the light–matter interaction is given in the following text.

### 3.1.1 Fundamental photon processes

A fundamental photo-absorption process in condensed matter, an isolated atom, or a molecule, depends primarily on the photon energy. All absorption processes result in a characteristic absorption spectrum unique for each material. An example for aluminium is shown in Figure 3.1.
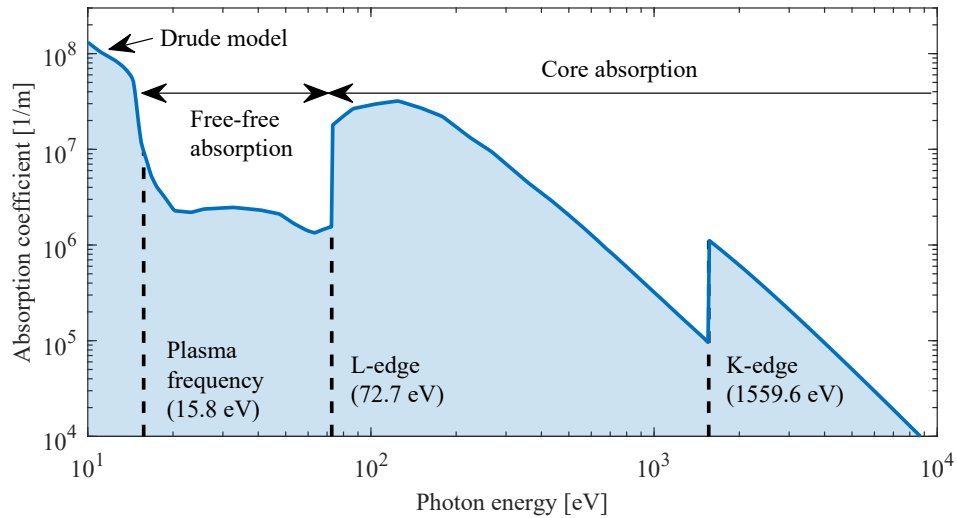


**Figure 3.1:** Absorption spectrum of aluminium. Data from [107].

**Free–free absorption**

Interaction of low-energy photons may be described by the Drude model. Photons of frequency lower than the material plasma frequency are reflected, whereas photons of higher energy can penetrate into the sample and be potentially absorbed via the inner photoelectric effect [108]. If the frequency is yet below the ionization potential, photons interact exclusively with free electrons, i.e. electrons in the conduction band. This relatively rare process is called free–free absorption

or inverse bremsstrahlung.[3] As shown in the Feynman diagram in Fig. 3.2b, this process must be accompanied by the third particle because of the momentum conservation law. For that reason, this process is also often called collisional absorption as electron–electron or electron–nucleus collisions are needed for the photon absorption.

Knowledge of free-electron density and collisional cross sections is essential for modelling of the absorption across a wide range of photon energies. Inverse bremsstrahlung is the leading absorption process on free electrons and can be found in conduction bands of metals, in coronal plasma, and also in the Sun: A typical proton–proton reaction in the Sun produces energy of 6.5 MeV per proton. Here, 2% of the released energy is taken away by neutrinos but rest 98% is transported towards exterior by means of photon diffusion where inverse bremsstrahlung plays a significant role [18].

Energetic photon (approximately 0.1–10 MeV) can loose energy on behalf of a free charged particle, typically electron. This inelastic process is called Compton scattering. Low-energy limit of the Compton scattering is Thomson scattering. In this case there is no interchange of energy between the photon and the charged particle. On the contrary, photons whose energy surpasses 1.022 MeV can result in formation of electron–positron pairs [110].

**Bound–free absorption**

Photons with energy above the ionization potential may promote electrons directly into the continuum. These bound–free transition is known as direct photoionization. Multiphoton processes, ordinarily observed in the visible region, become less probable for energetic photons as the lifetime of high-energy virtual levels, according to the Heisenberg's uncertainty principle, rapidly decreases with increasing photon energy and extremely high intensities are thus needed. Formation of highly charged ions is typically done via sequential single-photon ionization [111–113]. Instead of the multiphoton ionization, so-called above threshold ionization can be sometimes observed in the X-ray regime. In this process, an electron absorbs two or more photons spending energy of the first one on ionization and energy of others on an increase of its kinetic energy. It is worth noting that X-ray photons are characteristic for their selective ionization – they interact rather with tightly bound electrons in inner shells than with electrons in the valence band. This is dictated by photoionization cross sections of each particular shell or orbital. Highest value of each cross section is reached just above the respective edge [114]. Tuning of the photon energy thus enables to attain resonance absorption and photoionize only electrons from a particular atomic subshell.

Formation of single holes K-shell is thus relatively common. In case of high intensities, a strong field ionization can be reached in the visible regime. Nevertheless, field oscillations in the short-wavelength range are so fast that electron has just a very short time to escape and this effect is thus not so significant. It is therefore not a coincidence that this effect is sometimes called optical field ionization (OFI).

---

[3] Condensed matter physics uses term free carrier absorption. It is an intraband transition where an electron within a partially occupied band absorbs low-frequency radiation. Spectrum of such absorption spans from zero frequency up to interband energy [100, 109].

**Bound–bound absorption**

Finally, if the photon energy is below ionization threshold of given electron, the photon can be absorbed and photoexcite the electron to a higher energetic level. Inverse process to photoexcitation is deexcitation when an excited electron transits to a lower energetic level and emits a photon. Resonant transitions between two bound states can be observed in Fig. 2.3.

Overview of main photoabsorption processes is given in Table 3.1.

**Table 3.1:** Main photoabsorption processes.

| Transition | Absorption process |
|------------|--------------------|
| Free–free | inverse bremsstrahlung <br> Compton scattering |
| Bound–free | photoionization <br> optical field ionization <br> multiphoton ionization <br> above-threshold ionization |
| Bound–bound | photoexcitation |

### 3.1.2 Fundamental electron processes

An electron excited to a higher energetic level or into the continuum may, on the contrary, emit a photon or collide with other particle and loose its energy. Emitted photons can be detected and sorted according to their energy in an X-ray spectrometer. Recorded emission spectrum may then serve as a valuable source of information about the plasma already described in Chapter 2.4.3.

Among the most important electronic processes we should mention deceleration radiation known as bremsstrahlung described in Figure 3.2a. In this process the electron emits a photon while being decelerated by another charged particle. Next, radiative recombination is a process where the free electron is captured by an ion and the excess energy is emitted as a continuum radiation. Auger recombination (sometimes also termed as three-body recombination) is similar to the radiative recombination but instead of producing light the electron promotes another electron to a higher level, line emission, where a bound electron transits to lower energy level and emits a photon at a characteristic wavelength



(a) Bremsstrahlung          (b) Inverse bremsstrahlung
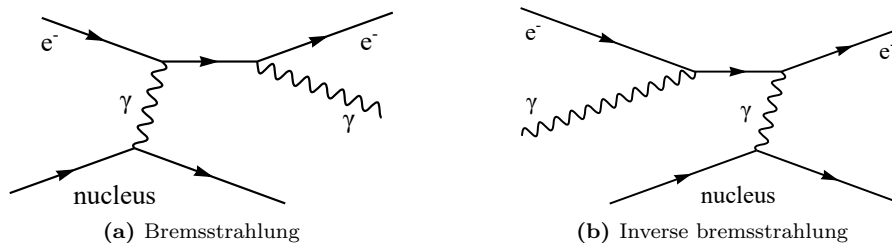
**Figure 3.2:** Feynman diagrams of bremsstrahlung (a) and inverse bremsstrahlung (b). Here $e^-$ denotes an electron and $\gamma$ a photon. Accompanying nucleus or other particle is required because of the law of momentum conservation. The interaction between the electron and the nucleus is, according to the Standard Model, mediated by a virtual photon which can transfer momentum and energy but cannot be detected.

and dielectronic recombination, where the free electron is captured by an ion and gives energy to a bound electron. This doubly excited ion can autoionize or emit so-called satellite line, which provides information about the degree of ionization. Nonradiative processes like electron impact ionization, Auger effect, elastic or inelastic scattering on ions and phonons play a significant role in evolution of electron density and energy redistribution. Overview of these processes is shown in Table 3.2.

**Table 3.2:** Main radiative and non-radiative electronic processes.

|  | **Process** | **Inverse process** |
|---|---|---|
| Radiative | bremsstrahlung<br>radiative recombination<br>deexcitation | inverse bremsstrahlung<br>photoionization<br>photoexcitation |
| Non-radiative | Auger recombination<br>dielectronic recombination<br>nonradiative deexcitation | impact ionization<br>autoionization<br>collisional excitation |

### 3.1.3  Direct core electron ionization

For now, we will focus on processes which follow after the ionization of a core electron. This process is one of the most investigated effects in the HEDP [56, 58, 84, 85, 91, 115–117].

As outlined in previous paragraphs, created core vacancy can be filled either via a radiative or nonradiative decay channel. The radiative decay is represented by fluorescence — a photon emission with a characteristic energy. The most probable nonradiative transition is the Auger effect shown in Figure 3.3, where an electron from a higher energy level fills the hole and the excess energy is spent on ionization of another (or more [118]) electron from the same atom. The Auger effect is much more probable in lightweight (low-Z) elements [119, 120] and does not usually play a significant role during irradiation by the visible light. Electrons in atoms exposed to low-energy photons are actually being stripped from the utmost shells towards higher inner shells. Creation of atoms with a single core hole, which is the main prerequisite for the Auger effect, is unique for



**(a)** Isolated aluminium atom          **(b)** Aluminium metal

**Figure 3.3:** KLL Auger decay in an isolated aluminium atom (a) and in aluminium metal (b), whose 3 M-shell electrons are pressure-ionized. The X-ray photon (1) photoionizes a K-shell electron (2). The K-hole is filled by the L-shell electron and excess energy is taken away by other L-shell electron (4).

short-wavelength radiation and is not so probable in the visible regime. This effect causes a difficulty in the X-ray em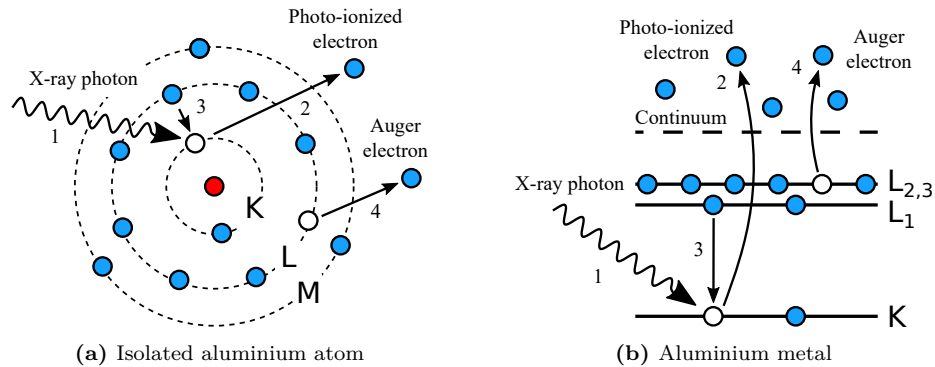ission spectroscopy since only a few percent of core holes are filled by the radiative decay [84, 91]. A lifetime of vacancy which is filled via the Auger effect is just about several femtoseconds and usually decreases with the energetic depth of the vacancy [121–124]. Duration of the FEL pulse is relatively long (10–100 fs) compared to the extremely fast Auger process and many electrons from a single atom can be thus photoionized during one individual pulse.

### 3.1.4 Impact of environment

Relaxation of the excited system may become slightly more complicated if it is embedded in an environment or if it is a part of a molecule. In the first case, the system can relax to a lower-energy state by simultaneous emission of a low-energy electron from a neighbouring atom or a molecule. This process is called interatomic/intermolecular Coulombic decay (ICD) [125] and lasts 1–100 fs [126, 127]. In the second case, so-called electron transfer mediated decay (ETMD) can take place. This process is very similar to ICD but the hole is filled by an electron from a neighbouring atom within one molecule and can take even several picoseconds [128]. The fact, that impact of the environment may lead to a qualitatively different response of excited system has been shown in an experiment [129], where up to 50 electrons were released from a single molecule during several tens of femtoseconds. This was possible as electrons provided by neighbouring molecules rapidly filled created holes and served thus as new targets for subsequent photons.

### 3.1.5 Saturable absorption

Although the recombination rate of processes filling the core holes is very high, it can be, in case of immense pulse intensity, surpassed by the photoionization rate. Subsequent photons within the same pulse will notice only depleted shells and may pass through the sample. This nonlinear phenomenon, well-known in the visible regime, called saturable absorption, was first observed in core-electron transitions by B. Nagler *et al.* [116] who exposed aluminium foils to a laser beam at photon energy of 92.5 eV (just above the aluminium L-edge) and intensities exceeding $10^{16}$ W/cm$^2$. High penetration depth at this photon energy together with the extreme intensity lead to rapid ionization of the L-shell electrons from many aluminium atoms. Removal of one single L-shell electron reduces the core screening and Al L-edge thus shifts to 93 eV which is now above the FEL photon energy. Therefore, aluminium with high number of single L-shell holes becomes highly transmissive for subsequent radiation. In the next years, various mechanisms of the saturable absorption at different materials were observed [16, 130–132]. An interesting effect was described by D. S. Rackstraw *et al.* [131] who irradiated aluminium by photons of energies just above the K-edge. Photons in a forehead of the pulse photoionized K-shell electrons and created K-holes were rapidly filled by L-shell electrons via the Auger effect. A sudden increase of the ionization degree blue-shifted K-edge and later-coming photon had therefore not enough energy for photoionization and could freely propagate through the sample.

### 3.1.6 Electronic cascades and electron energy distribution

Energy of photoionized and Auger electrons depends on material and photon wavelength and typically spans from a few eV up to several keV. The photoionization of core electrons thus leads to a formation of highly non-equilibrium electron distribution, where low-energy part is represented by intact electrons from the conduction band and electrons produced by ICD and ETMD processes. A delta-like function in the energy spectrum can be found at $E_{h\nu} - E_{\mathrm{core}}$, where $E_{h\nu}$ is the photon energy and $E_{\mathrm{core}}$ is ionization energy of the core electron. Hot tail at energy $E_{\mathrm{core}} - E_1 - E_2$ is formed by Auger electrons, where $E_1$ and $E_2$ are the energies of shells which participate in the Auger decay. For example, in the KLL Auger decay the Auger electron energy would be $E_{\mathrm{Auger}} = E_K - E_L - E_L$. Hot electrons loose their energy via photon emission, inelastic scattering and impact ionization. The last effect leads to an increase of the ionization degree and free-electron density in the conduction band. Both almost thermalized low-energy part of the electron distribution as well as its hot tail can be observed in X-ray emission spectra as parts corresponding to the radiative decay and bremsstrahlung. Analysis of emission spectra can thus result in two discrepant electron temperatures [91,115] which can be only explained by a proper description of the electron distribution [133].

Cascading effects are ongoing as long as energies of free electrons exceed the impact ionization threshold. Electron thermalization is usually fast [53,134] but in case of very high-energy electrons it may take up to several hundreds of femtoseconds prior to establishing the equilibrium Fermi-Dirac distribution [133,135]. At this stage, it is reasonable to apply the two temperature model which declares one temperature for electrons and the second for colder ions.[4]

Except of delay in formation of the equilibrium state, hot electrons of kiloelectronvolt energies may also travel long distances (micrometers) while creating secondary electrons and thus heating the material lattice [53,136–138].

Another effect which can influence damage threshold is a number of electrons emitted from the surface. This number is usually very small ($<10\%$ [53]) and vast amount of energy is deposited into the material. This situation can be however changed in case of grazing incident angles where large number of escaping electrons can take away a significant portion of the pulse energy and thus increase a material damage threshold [139].

### 3.1.7 Coulomb explosion

Electronic cascades, where one photon excites several electrons step by step into the vacuum on time scales $< 100$ fs, can be observed also in gas clusters [124,140]. A typical example can be irradiation of Ne–Kr clusters [140] where one photon ionizes an electron from a neon K-shell (1s). The second electron (2p) is emitted via the Auger effect (2p→1s transition), and the third is emitted from a krypton 4p state during the ETMD process. Coulomb repulsive forces between one $Ne^+$ and two $Kr^+$ atoms surpass bonding strength and the cluster undergoes the so-called Coulomb explosion. In this process, high potential Coulomb energy of

---

[4] As temperature can be well-defined only for systems in TDE, it is clear that usage of the two temperature model is quite limited.

positively charged ions is almost completely converted into their kinetic energy and the cluster may dissociate within 100 fs [141]. The Coulomb explosion is relatively common destructive way of ArXe [142], Ne–Kr [140], $C_{60}$ [141,143] and other clusters or molecules [126,127]. This process was also identified as a leading mechanism causing surprisingly low radiation resistance of fullerene crystals consisting of heavy $C_{60}$ molecules, bound by weak Van der Waals (VdW) bonds, to 92 eV radiation [144]. Photoionization of electrons from $C_{60}$ buckyballs induces accumulation of a positive charge and strong repulsive forces between molecules. Simulation shows, that although the charge imbalance is created within the 100-fs pulse duration, the VdW bonds are elongated to a critical distance where they break and intact $C_{60}$ cages are slowly separated from the crystal after around 2 ps because of large inertia. The Coulomb effect induced by spatial charge accumulation decreases with increasing size of the cluster where only ions from outer layers are ejected while keeping the ones in the core still neutral due to efficient recombination [145–147].

### 3.1.8 Nonthermal melting

In a bulk material, the charge accumulation accompanied by repulsive Coulomb forces may play a significant role only for the topmost atoms near the surface. This effect is nevertheless usually neglected as it is overshadowed by other processes. A rapid and substantial change of the overall electron density distribution may lead to modification of an interatomic potential followed by lattice instability. This process can be induced by core holes concentration as low as 0.1% [43]. It has been shown [44,45] that cascading effects of photo- and Auger electrons promote several percent of bound electrons into antibonding states in the conduction band potentially leading to a bandgap collapse and lattice disordering on the time scale of several hundreds of femtoseconds [46,47]. It is worth noting, this process is faster than electron–phonon coupling being responsible for lattice heating. Inasmuch as described phase transition is not triggered by an increase of the atomic (lattice) temperature, it is called nonthermal melting. An increasing disorder of the lattice can be easily observed via decreasing intensity of Bragg reflections which are highly dependent on fine lattice modifications [43,46,48].

### 3.1.9 Nonthermal phase transitions

In recent years, a great attention was attracted by diamond which structure might be transformed into graphite. Theoretical predictions and models [45,135,148] confirmed by experimental works [47,149,150] revealed that this anomalous solid-to-solid phase transition might be completed in times shorter than 200 fs. This is also shown in Fig. 3.4. Interestingly, diamond bandgap collapse is faster for irradiation with low-energy photons as electronic cascade, which promotes electrons into the conduction band, is faster for electrons of lower energies [135]. A natural question whether it is possible to transform graphite into diamond was indeed asked by many researchers. Theoretically it is possible, but it seems that except of heat an enormous pressure must be applied as well [33,151]. This is feasible with use of shock waves, discussed in the nanosecond time scale (Chapter 3.3).

Sub-picosecond nonthermal melting and phase transitions are not unique only

for short-wavelength irradiation but can be observed also in optical regime when employing intense femtosecond pulses [46, 152, 153].
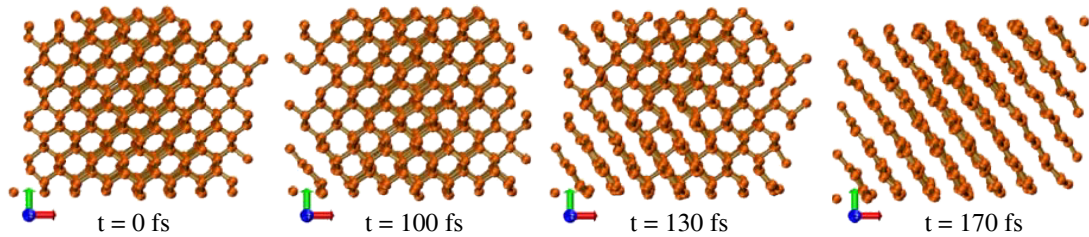


**Figure 3.4:** Snapshots of diamond graphitization after absorbing 0.85 eV/atom at 10 keV. Adapted from [45].

### 3.1.10  Isochoric heating

Processes like photoionization, Auger effect, impact ionization and electron–electron collisions described above lead to a high degree of ionization, rise of free-electron population and its thermalization into Fermi-Dirac-like distribution within tens or hundreds of femtoseconds. Although small atomic movements in a nanometre range can be observed as soon as after a few femtoseconds [93, 141, 154–156], electron–phonon coupling when electrons transfer their energy to the crystal lattice spans from a half up to several picoseconds [53, 157]. Nevertheless, even if this transfer was instant and, for example, a single aluminium atom gained as high energy as 100 eV, it would not move more than 3 nanometres during 100 fs. Any hydrodynamic motion of created plasma can be thus neglected and heating rightfully considered as isochoric keeping the material density at the initial level. The fact, that phonons do not propagate over long distances during the 100 fs pulse can be also derived from the speed of sound which is typically ≤10000 m/s in metals. Sound can therefore travel only several ångströms during the pulse duration and its propagation can be neglected.

### 3.1.11  Coherent diffractive imaging

The fact that atoms practically do not change their positions during the first several tens of femtoseconds makes it possible to utilize single-shot diffraction to record diffraction pattern corresponding to intact structure although the sample explodes relatively shortly after the pulse departure as pictured in Figures 3.5 and 3.6.
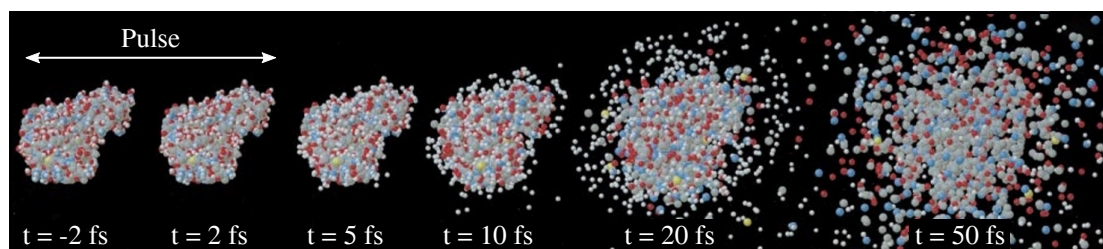


**Figure 3.5:** Explosion of a protein molecule (T4 lysozyme) after irradiation by an X-ray pulse at 12 keV with FWHM of 2 fs. Adapted from [158].
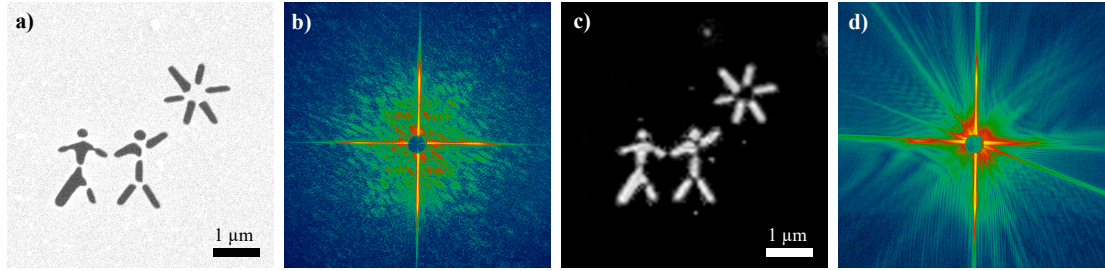
**Figure 3.6:** "Prove of concept" experiment on femtosecond diffractive imaging. (a) SEM image of original structure. (b) Diffraction pattern obtained by scattering intense 25 fs pulse at 32 nm. (c) Reconstructed image from the diffraction pattern. (d) Diffraction pattern of the structure damaged by the first pulse which formed (b). Adapted from [164].

Imaging of tiny structures using diffraction patterns is a well known technique already used for many decades. The first valuable results were presented already in 1953 by J. D. Watson and F. H. C. Crick who irradiated DNA and using X-ray diffraction patterns they discovered its double helix structure [159]. Another great discovery was achieved a few years later by M. Perutz *et al.* who described haemoglobin structure using the same method [160]. In the next decades, structure of many different proteins was obtained using synchrotron radiation and method called protein and molecular crystallography [161, 162]. This approach however requires a complex growth of protein crystals and accumulation of many not-so-bright synchrotron pulses for various sample orientations. In 1995 R. Henderson predicted that greatest potential for a single molecular imaging lies in electron microscopy [163]. The main problem of X-rays produced by simple sources resides in large radiation damage per number of useful elastic scattering events which puts limitations on scales of irradiated samples and enormous number of images ($\sim 1000$) required for proper reconstruction. An advent of XFELs, sources delivering pulses of astonishing brilliance at megahertz repetition rate, started a revolution in the field of diffractive imaging. The extreme brilliance is important for collection of enough scattered signal required for high-quality diffraction pattern and for successful reconstruction. Already in 2000 it was proposed by R. Neutze *et al.* [158] that duration of the 10-fs pulse is so short that diffraction pattern should not be influenced by the Coulomb explosion of a protein molecule occurring just after the pulse departure. Results of the simulation are shown in Fig. 3.5. Several years later in a proof-of-concept experiment [39, 164] shown in Fig. 3.6 experimentalists managed to determine structure of a mimivirus particle and nanocrystal using up to millions of single-shot snapshots of randomly oriented specimen [40, 41]. Single virus imaging is possible also at synchrotrons, however, with much lower resolution [165]. These experiments started a new era of coherent diffractive imaging (CDI) [42] which is being implemented at new instruments [166] and enhances knowledge required for advanced medical imaging applications [167].

Reconstruction of 3D images is similar to computational tomography where many images acquired from different angles of view are used for 3D reconstruction of tissues important for medical use. Problem with tiny samples and shorter photon wavelengths resides in high transparency of probed materials. Instead of calculating the 3D image from intensity variation, it must be obtained from the phase shift. This process is more difficult as CCDs do not record holograms

but solely 2D intensity images. Complex backpropagation algorithms must be therefore employed to obtain the phase shift and consequently the 3D image. Novel methods involve more sophisticated approaches where calculations involve also coherence and using correlation spectroscopy [168, 169] or intensity correlations [170] can reach very high resolution applicable, for example, also to 3D imaging of integrated circuits with resolution below 20 nm [171]. The world record in synchrotron 3D tomography was done by G. García-Moreno who managed to obtain 208 tomograms per second of a foaming metal employing 40 kHz frame rate. An interesting fact is, that main limitation of further increase of the rep. rate were centrifugal forces acting on the sample [172]. The 3D tomography should not be confused with X-ray microscopy which is nowadays, with use of XFELs, possible at MHz rep. rates [38].

## 3.2 Picoseconds

Matter by the end of the first picosecond is highly ionized and contains hot lightweight electrons speedily moving around heavy ions which still had no time to significantly move so the material density remains close to the original value. This warm/hot and dense exotic state of matter lasts until electrons transfer their energy to the lattice via the electron–phonon coupling and it starts to expand. These processes correspond to times up to several picoseconds.

### 3.2.1 Thermal melting

Lattice stability is mediated by electrons. The nonthermal melting results from liberation of the binding electrons into antibonding states followed by lattice disruption. Contrary to that, according to Lindemann criterion, thermal melting occurs when kinetic energy of atoms exceeds the binding forces [49, 136]. The crystal lattice does not gain energy directly from the laser pulse but through the electron–phonon coupling, where free electrons from the conduction band transfer their energy to ions via Coulombic interaction. Although collisions between electrons and ions may occur instantly after the excitation, typical time scale of this interaction is ∼0.5 ps [157, 174]. Equilibration of the electron and ion



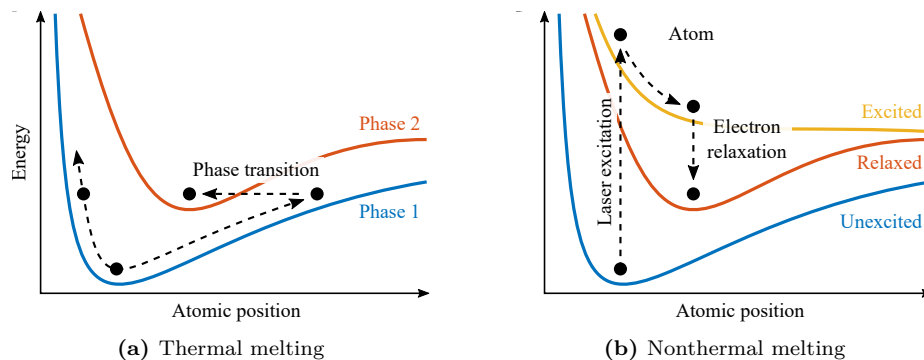**(a)** Thermal melting  **(b)** Nonthermal melting

**Figure 3.7:** Fundamental difference between thermal (a) and nonthermal (b) melting. Thermal melting is induced by phase transition of heated material within the same potential, whereas nonthermal melting is induced by a direct change of interatomic potential which may or may not further relax into different stable phase. Adapted from [173].

temperature then takes from sub-picosecond times up to several tens of picoseconds [44, 80, 174–178]. Ultrafast (∼100 fs) excitation of phonons can be observed in samples of small dimensions because of phonon softening [177]. In this process, a coherent atomic motion is driven by altered potential induced by excited electrons and not by the thermal excitation [152]. A fundamental difference between the thermal and nonthermal melting is described in Figure 3.7.

## 3.2.2 Desorption and ablation

Depending on the laser intensity, various processes on typical time scale of ∼10 ps like melting, spallation and phase explosion might result from intense heating of the crystal lattice. The latter two result in material ablation [179].

The first systematic study of laser desorption and ablation was published by R. F. Haglund in 1996 who described material response to intense UV light [180]. These two processes are supposed to originate in distortions of lattice followed by its instability and bond breaking. He defined laser desorption as "emission of ions, atoms and molecules without any substantial disturbance in the surrounding surface." Desorption is also considered to happen before absorbed energy dissipates into surroundings, it is not accompanied with corona formation and it results in removal of less than a half of a single atomic layer. Compared to that, laser ablation is "a large-scale disruption of surface and near-surface geometrical and electronic structure associated with corona formation of ejected material." It is driven by excitation, thermalization and lattice instability and results in removal of more than a half of the atomic monolayer per pulse. However, later in 2009 J. Chalupský *et al.* [181] showed that Haglund's criterion defined for UV regime must be modified for soft X-ray pulses. They found that desorption is about an order of magnitude more efficient in case of poly(methyl methacrylate) — PMMA exposed to more energetic photons. Approximately 5 nm of PMMA surface can be removed after single-shot irradiation. The ablation depth increases with deposited dose but this response does not have to be strictly linear as described in Chapter 6.3. It is also worth recalling that long-pulse ablation is much more efficient for shorter wavelengths because of the absence of critical surface in the plasma plume.

At the first sight, an opposite process to the ablation was observed after exposing samples of amorphous carbon to modest fluences of 60-nm radiation [144]. A few picoseconds after the irradiation the material expanded to ∼ 1.3× the initial volume as a result of partial graphitization and a hillock was observed instead of a crater. Amorphization of SiC followed by its expansion was observed also in our experiment described in Chapter 7.2 and [55].

## 3.2.3 Spallation

Very fast heating connected with formation of large stresses is typical especially for a few-nm near-surface layer of high-absorbing material [157]. The pressure is induced by ultrafast expansion generated by the heating which cannot be followed by a slow mechanical motion or surrounding material. This so-called stress confinement regime is responsible for the photomechanical spallation of a single or multiple surface layers [53, 179]. It has been shown that melting threshold is

about 5× lower than spallation threshold which is dependent not only on the fluence but also on the intensity of the laser pulse. Simulations show that spallation is not observed for long 50-ps pulses because of an absence of the stress confinement regime [179]. The phase explosion, observed as explosive phase transition from liquid to vapour, has fluence threshold about 2× higher than the spallation threshold.

Fast temperature increase is also accompanied by formation of a compressive wave followed by its tensile counterpart. Velocities of these waves are limited by the speed of sound (∼km/s) and typical pressures are ∼10 GPa [134]. Higher pressures are induced by highly absorbing radiation of low penetration depth because of high-temperature gradients. During the first few picoseconds, an interface between the solid and liquid material propagates into the material at a very high speed. Propagation slows down and stops after ∼100 ps and depth ∼10–100 nm. Molten material resolidificates at the time scale of hundreds of picoseconds up to a several nanoseconds [179]. Time evolution of depth of interface between solid and liquid phase for all melting, spallation, and phase explosion is shown in Figure 3.8.
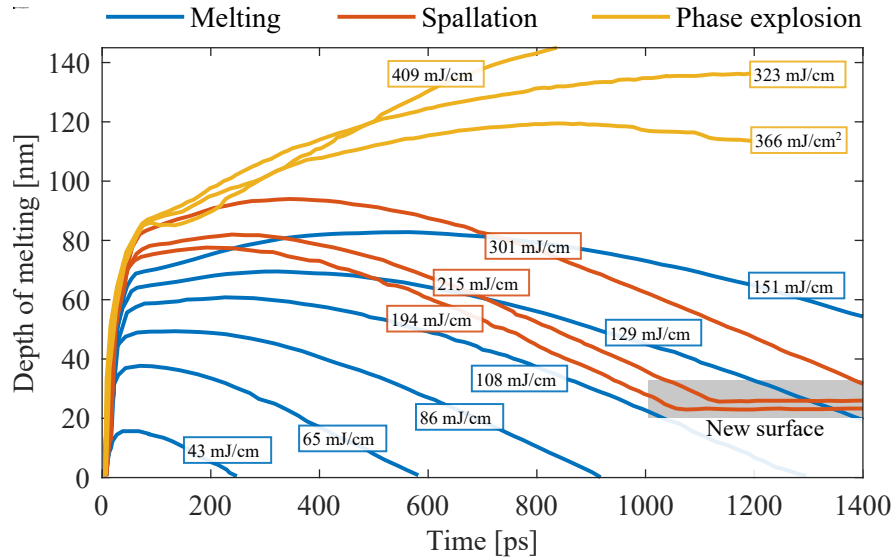


**Figure 3.8:** Time evolution of melting and resolidification of a nickel target irradiated with 1-ps laser pulses at different fluences. Data obtained by theoretical simulations, which combines molecular dynamics, electron–phonon coupling, and electron heat conduction, are taken from [179].

Except of the thermal melting and start of a corona formation connected with the hydrodynamic expansion, the picosecond time scale is, for example, typical also for skyrmion formation [182], ultrafast magnetic transitions [183], and heterogeneous gold transition which can last up to 1 ns [178].

## 3.3   Nanosecond

Nanosecond time scale can be considered as a time scale of corona effects and propagation of waves and cracks. As the heat conduction is much slower than fast mechanical response, evolution of these processes can be treated separately and mechanical motions considered as adiabatic.

### 3.3.1 Corona

Material ejected into space via ablative processes creates a plasma plume called corona which can last up to several tens of nanoseconds. Schematic description is shown in Figure 3.9. Laser radiation is reflected at the critical surface and heating of the material is thus limited. The main absorption mechanism in the corona is inverse bremsstrahlung on free electrons. Generated hot electrons of energies up to ~10 keV transfer energy to the target which simultaneously leads to accumulation of negative charge. Created field pushes and accelerates slow electrons from the sample back to the corona. A very strong fields up to GV/cm can be created in laser plasmas and might serve as acceleration media for generation of multi-GeV electron beams [184, 185]. Inasmuch as the corona formation takes at least a few picoseconds it is not relevant to pulses of duration shorter than one picosecond. More about the corona formation and dynamics can be found in [186].
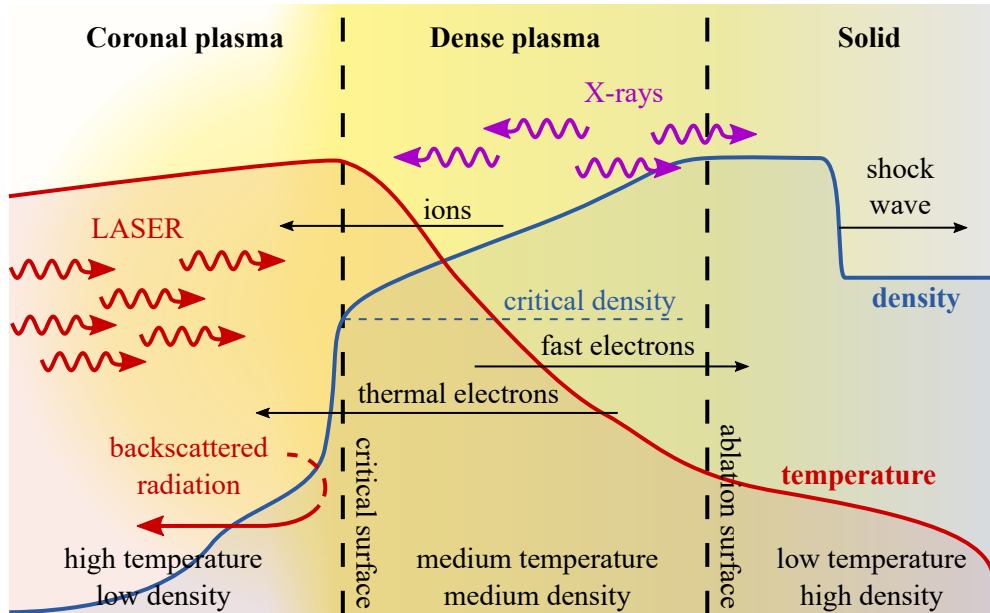


**Figure 3.9:** Schematic description of processes accompanying corona formation. Figure inspired by [63].

### 3.3.2 Shock waves

High pressures can be reached either by static experiments, where a sample is compressed between two anvils or pistons for several seconds, or by dynamic experiments, where matter undergoes an extreme squeezing which lasts only for a very short time. The dynamic compression can be reached by a shock wave excitation.

A shock wave is a strong pressure wave with velocity greater than the sound speed in a given medium [187]. Difference from a classical sound wave resides in a discontinuity or a sudden change of material properties (such as pressure, density or temperature) at the wavefront. It can be generated in medium exposed to a sudden impact of external forces. The most typical is generation by an accelerated foil [188] and by an intense laser pulse which creates a very hot plasma

— the corona. Momentum of the ablated material together with the thermal pressure acts on the target and drives the shock wave. Experiments typically employ focused nanosecond pulses of energy in range $\sim$ 1–100 J reaching intensities $>$TW/cm$^2$ [26]. Some advanced methods use two pulses where the first pulse pre-compresses the target material and the second one generates a shock wave compressing the material to a very high pressure ($\sim$ Mbar) but still at relatively low temperature ($\sim$ 1000 K) [33,151]. Another methods use irradiation by two [26] or multiple [22] beams from different angles to ensure more homogeneous compression. Homogeneity is an important prerequisite, for example, for ICF.

Speed of shock waves in metals is typically $\sim$10 km/s which was also confirmed by temporally-resolved experiments where compression of $\sim 10 - \mu$m-thick samples followed by lattice melting is observed within first few nanoseconds after the optical pulse arrival [26,33]. The material is compressed to density several times higher than the original one and heated to temperatures of a few electron-volts [26,28,29]. Hence shock waves can also be used to enter the WDM regime. Propagation of laser-induced shock waves as well as corona formation can be nicely observed by a shadowgraph method [189], see Figure 3.10.
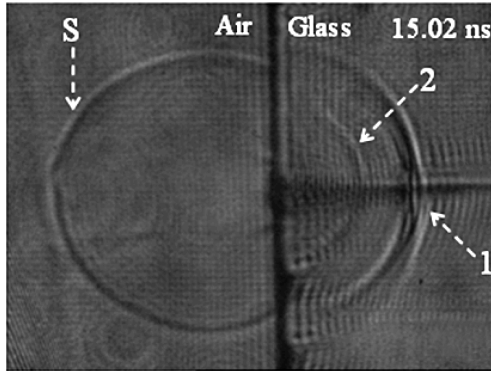


**Figure 3.10:** A shadowgraph imaging laser ablation of silica glass captured 15 ns after 50-fs pulse arrival (at 800 nm). A shock wave (S) propagating into air as well as first (1) and second (2) stress waves can be observed. Picture from [189].

When probing a shock-compressed material with a laser pulse, several criteria must be met: The pulse duration must be very short in order to capture a static state of the material, it must be able to penetrate through the laser-generated plasma and its wavelength must be comparable with structure dimensions so Bragg peaks might be observed in a diffraction. These constraints clearly point out to the XFEL pulses. The characterization methods then rely on angularly, spectrally and temporally resolved X-ray detection, i.e. diffraction measurements of Bragg reflections [33,151] and X-ray scattering [26,28,29].

It has been also shown that shock waves are responsible for liquid drop explosions[5] and consequent distortion of a liquid jet important for protein crystallography experiments and others [191]. Liquid jets are extremely important for delivering miniature samples (like viruses) into the beam and their dynamics spanning to hundreds of microseconds is studied for many years [192]. As the structure of these tiny samples is determined with use of CDI, plenty of diffractive patterns have to be recorded and high repetition rate of XFELs thus matters. Pioneering experiments at MHz rep. rate showed that flow of liquid jets is significantly distorted by propagating shock waves generated by the XFEL pulse [191].

---

[5]By capturing loads of pictures at different time delays, it is possible to record continuous evolution of the drop explosion. This breathtaking movie experience is strongly recommended and can be watched at [190].

Nevertheless, later experiments revealed that MHz crystallography employing liquid jets is feasible for jet speeds exceeding 50 m/s at which jets recover in time for the next pulse [193]. Femtosecond crystallography designed for MHz rep. rate is nowadays available at XFEL instruments [166].

Opposite to the shock waves are rarefaction waves which play a crucial role in material spallation [194]. Mathematical description of the waves and their propagation can be found in [63].

The nanosecond time scale is also characteristic for evolution of quasiparticles such as magnons or excitons. Dynamics of spin waves, propagating collective excitations in magnetic materials also known as magnons, resonating at a few GHz was observed by synchrotron radiation [195]. Lifetime of excitons, where an electron and a hole form a bound state via coulombic attraction, is typically $\approx 100$ ns [196]. Formation of excitons plays an important role in luminescence yield of Ce:YAG scintillator exposed to short-wavelength radiation [197]. Photoexcited charge carriers form excitons which later decay into several different channels. Main energy transfer from a decaying exciton to $Ce^{3+}$ ion, important for observable photoemission, can be however suppressed by mutual quenching of neighbouring excitons. This process emerges from dipole–dipole interaction and its probability significantly increases with density of excitons. Consequent saturation of the luminescence yield at high irradiation intensities is critical for usage of these scintillators in X-ray laser beam monitors as discussed in Chap. 6.

The nanosecond lifetime is also typical for energy levels within semiconductor band structure whose exponential decay results in emission of fluorescent light. Phosphorescence connected with charge trapping and detrapping ranges from milliseconds up to several hours [198].

## 3.4  Microseconds

Microsecond time scale is characteristic for heat conduction. Electron–phonon coupling is now finished and lattice vibrations transmit deposited heat away from the irradiated spot. As the thermal diffusivity is relatively slow ($\sim 100$ $\mu m^2/\mu s$ [199]) we may surely state that no energy dissipates via heat conduction during the sub-picosecond pulse. Moreover, most of the energy does not diffuse but is spent on the latent heat of fusion (enthalpy of fusion). Hence possible effects of heat conductivity on thermally-induced damage can be observed only for sufficiently long pulses, continuous exposure and femtosecond pulses delivered at high repetition rate.

Influence of heat accumulation on damage threshold at high repetition rate was examined by R. Sobierajski *et al.* [52]. Samples of bulk silicon were exposed to 13.5-nm 400-fs pulses delivered as single-shots and at 10 Hz and 1 MHz repetition rate. Measured damage thresholds and theoretical calculations revealed that surface irradiated at 1 MHz rep. rate can be damaged at fluences $10\times$ lower than fluences needed for the single-shot damage. One microsecond delay between individual pulses is thus not enough for a sufficient heat dissipation and there is still a significant portion of heat left by the previous pulse when the next pulse arrives. High repetition rate therefore leads to heat accumulation and consequent significant decrease of the damage threshold. It was also shown, that 100 ms delay between pulses delivered at 10 Hz rep. rate is sufficiently long for

relaxation of the irradiated material and no decrease of the damage threshold compared to that measured by single-shots was detected. Described observation is immensely important for optical elements of megahertz beamlines which can be unintentionally damaged even at low fluences entirely safe for low repetition rate.

Beside the others, microsecond is also a typical time scale for liquid injector dynamics [191, 193] or molecular nucleation [200].

## 3.5 Final state

During and after the irradiation the target material undergoes irreversible changes which can be examined post-process by a wide variety of different methods (see Chapter 5). A characteristic time when these changes can be inspected spans up to infinity but starts immediately after the material relaxation, i.e. milliseconds after the exposure. The irradiated surface may show signs of various damage mechanisms like ablation or desorption [180], already mentioned phase transition to amorphous or crystalline structure and others. Low fluences induce melting of a thin surface layer. Its resolidification usually results in surface roughening induced by tensile stress waves and cavity formation [53] or recrystallization into nano-droplets of sizes 30–50 nm [52]. High mechanical tension in the stress confinement regime is responsible for creation of crystal defects up to depth of $\sim$100 nm [52] and spallation of the material (typically $\sim$10 nm) which might be also considered as the leading effect of the single-shot ablation [53].

A very important feature of each damage process is the minimum average dose absorbed per atom at which the given structural change occurs. This is usually termed as damage threshold which is highly dependent on the photon wavelength, light intensity, material, incidence angle and others [201]. Regarding the imprinting method employed in focused beam characterization, the most important is the estimation of the ablation damage threshold fluence.

Study of damage thresholds and related mechanisms is very important for optical elements [52, 139, 201] as well as for ICF. Although damage to optics is usually unwanted, ablation might be employed in nanostructuring process of various samples [202, 203]. This method, compared to transient gratings common in the visible regime, imprints the interference pattern directly into the material where it stays for later use.

## 3.6 Summary

In the previous paragraphs we have described processes which follow after absorption of one up to $10^{12}$ photons with energy ranging from XUV region up to hard X-rays. The interaction can be generally divided into four main phases: 1) absorption of the laser pulse by electrons (femtoseconds), 2) electron–phonon coupling leading to equilibration of electron and ion temperatures (picoseconds), 3) energy propagation through the medium (nanoseconds to microseconds), 4) cooling of the material and formation of the final state ($>$ milliseconds). Each phase is accompanied by processes, which are summarized and compared with interaction of visible light in the following text.

In the first stage, the laser pulse interacts with the target material. High-energy photons create core holes by a direct photoionization of the innermost electrons. These holes are filled either by the Auger effect (small Z) or fluorescence (high Z). Emitted electrons, forming a highly non-equilibrium energy distribution, then promote secondary electrons into the conduction band by electron–ion impact ionization and, on the time scale of hundreds of femtoseconds, equilibrate into the Fermi–Dirac distribution. The crystal lattice at this stage remains dense and relatively cold and two-temperature model can be thus applied here. Intense ultrashort visible pulses interact in a quite similar way, however, with two significant differences. First, atoms irradiated by the visible pulses are being stripped of electrons starting from outer shells down to the core. Weakly-bound electrons can be directly photoionized, whereas deeper shells are usually being excited or ionized via collisional processes. Multiphoton ionization and optical field ionization may also play significant role at high intensities. Second, visible light cannot propagate beyond the critical surface typical for metals coronal plasma. Volumetric heating of metals is therefore possible only with the use of the short-wavelength radiation. Deposition of all optical-pulse energy only to the surface layer of metal increases thermal gradients which may consequently result in lower damage thresholds. Absorption of the pulse energy in coronal plasma is important only for optical pulses with nanosecond or longer duration.

Transfer of energy from electrons to the lattice via electron–phonon coupling occurs on the time scale of several picoseconds. The thermal energy gained by the atomic (ionic) lattice within several picoseconds is high enough to surpass the melting temperature, release the bonds and allow the material to melt thermally. With increasing pulse energy, melting can be potentially followed by spallation, phase explosion, ablation, etc. Nevertheless, the interatomic potential might be changed by a strong photoionization of bonding electrons leading to lattice destabilization within hundreds of femtoseconds. This ultrafast phase transition achievable by ultrashort pulses within a wide spectrum of wavelengths is appropriately called nonthermal melting.

Time scale from picoseconds up to microseconds is typical for corona formation, hydrodynamic expansion of created plasma, propagation of shock and rarefaction waves, heat conduction throughout the sample, and consequent material damage, respectively. Intense ionization, heating and ablation processes result in irreversible material changes like phase transitions, ablation or desorption, local changes of optical parameters, etc., observable with the use of microscopic techniques. It has been shown by I. Milov *et al.* [53, 134], that final differences after irradiation of certain materials by visible and XUV light might be quite small and primary processes like electron cascades thus play a negligible role in a final shape of the material damage.

Summary of main processes and their time scales is illustrated in Figure 3.11.
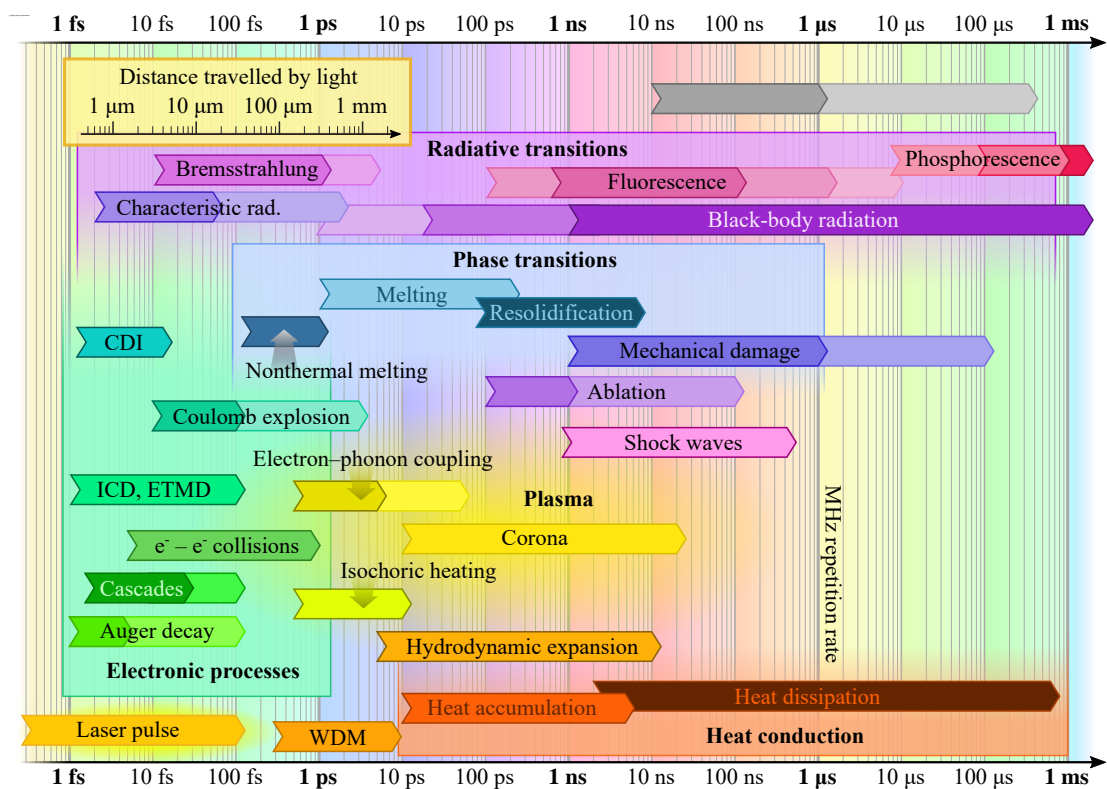
**Figure 3.11:** Time scale of light–matter interaction. All values should be considered as approximate due to a large complexity of the interaction.

# 4. Sources of short-wavelength radiation

This chapter provides description of sources employed in experiments described in the second part of this work. It starts with a brief introduction to synchrotron radiation and free-electron lasers (FELs). Extensive description of sources of the synchrotron radiation is beyond the scope of this work and can be found elsewhere [204,205]. In the next part, functionality of plasma-based short-wavelength lasers used for irradiation of graphene (Chap. 7.2) and CdTe (Chap. 7.3) is described. Comparison of parameters of other large and powerful laser facilities is also provided here. Finally, a short overview of X-ray optics is given in the end of this chapter.

Theoretically predicted synchrotron radiation was first observed by F. R. Elder in 1947 as "a small spot of brilliant white light" coming from a small synchrotron tangentially to orbiting electrons [206]. The synchrotron radiation is nowadays known as radiation emitted by a charged particle during its centripetal acceleration. It can be produced in man-made sources, like bending magnets, wigglers and undulators, but also in nature. The most famous natural source is Crab Nebula emitting pulses of radiation ranging from radio waves to gamma rays [207]. Other natural sources of XUV and X-ray radiation are, for example, radionuclides and solar corona.

Dipole accelerators focused on high-energy particle research emitted synchrotron radiation in a parasitic mode which actually limited further approach to higher photon energies. This so-called first generation of the synchrotron source was quite soon followed by the second one. The first facility dedicated solely to the X-ray generation using bending magnets, Synchrotron Radiation Source (SRS) at the Daresbury Laboratory (UK), started its operation in 1981 and was the representative of the second generation. Large divergence and very broad spectrum of light coming from bending magnets was significantly improved by implementation of wigglers and undulators, devices employing alternating magnetic fields to wiggle relativistic electrons. Utilization of these new devices laid the foundations of the third generation of synchrotron radiation sources.



**Figure 4.1:** Historical development of (peak) brilliance with years. Data are approximate.

Although synchrotrons and storage rings are great instruments for tomography, nanotomography, fast 2D imaging and others [208], some experiments involving, for example, CDI or WDM research are not possible. To conduct these advanced measurements, one needs an extreme number of photons of a very sim-
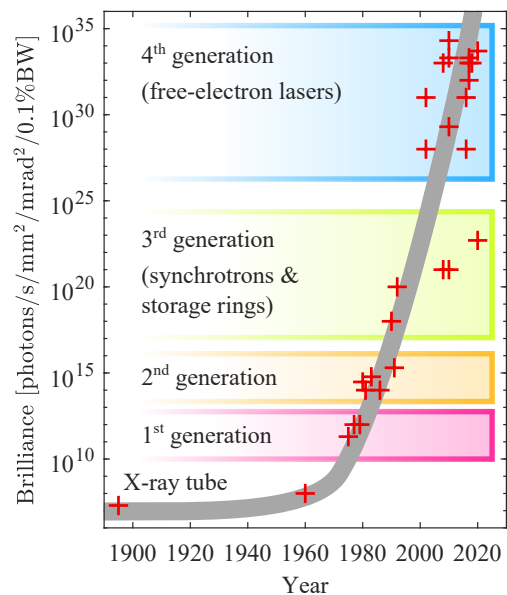
ilar energy focused on a tiny spot during a very short period of time. This can be ensured by high brilliance[(1)] of the source.

Even though brilliance of synchrotrons is very high, there is, as Figure 4.1 shows, also the fourth generation of synchrotron radiation sources whose brilliance reaches astronomical values. These are the free-electron lasers.

## 4.1 Free-electron lasers

The first idea of an FEL came in 1970's when J. Madey proposed a possible stimulated emission of bremsstrahlung during a passage of a relativistic electron bunch through an alternating magnetic field [209]. A. M. Kondratenko and E. L. Saldin then published a detailed study of the electron bunch self-modulation and generation of coherent radiation during its single passage through an undulator which has no resonator [210]. Although they proposed this idea mainly for a submillimeter spectral range, it became popular mostly for generation of photons at much higher energies. Just a few years later R. Bonifacio and C. Pellegrini published a paper where they calculated optimum parameters of the electron density, undulator length and others to produce a high peak-power radiation [211].

### 4.1.1 List of FELs

Although first proposals appeared so early, it took over 30 years to construct a laser capable of coherent short-wavelength radiation delivery. It was Free-electron laser in Hamburg (FLASH) in Germany which began its test operation in 2002 and started the first era of short-wavelength FELs [212]. Other lasers built in next few years were Linac Coherent Light Source (LCLS) in California-USA [3], SPring-8 Compact SASE Source (SCSS) in Japan [4] later replaced by Spring8 Angstrom Compact FEL (SACLA) [5] and FERMI@Elletra in Italy [6], the first representative of a seeded FEL operating in short-wavelength regime. These facilities of the first generation of FELs were designed to deliver femtosecond pulses at moderate repetition rates ($\sim$10 Hz) with energies up to few millijoules and photon wavelengths reaching those of hard X-rays. Parameters of novel FELs are designed to satisfy strong demands of complex experiments such as CDI or HEDP investigation. An emphasis is therefore put on high repetition rates, higher photon energies and greater number of photons in each pulse. These new facilities involve SWISS FEL in Switzerland [7], European X-ray free-electron laser (EuXFEL) [8], Pohang Accelerator Laboratory XFEL (PAL-XFEL) in South Korea [9] and Soft XFEL (SXFEL) in China [10]. Lasers from the first generation are continuously upgraded in order to provide even brighter, shorter and more energetic pulses at higher repetition rates. This is the case of LCLS-II [11] and FLASH II [12]. All mentioned facilities are pictured in the Figure 4.2. As can be seen, several more are proposed to be built across the world. Except of the short-wavelength FELs there is, of course, a large number of lasers operating at lower photon energies not pictured in the figure. List of these facilities can be found in [213].

---

[(1)]Brilliance is sometimes confused with brightness: brilliance is brightness per 0.1% bandwidth of the central wavelength.
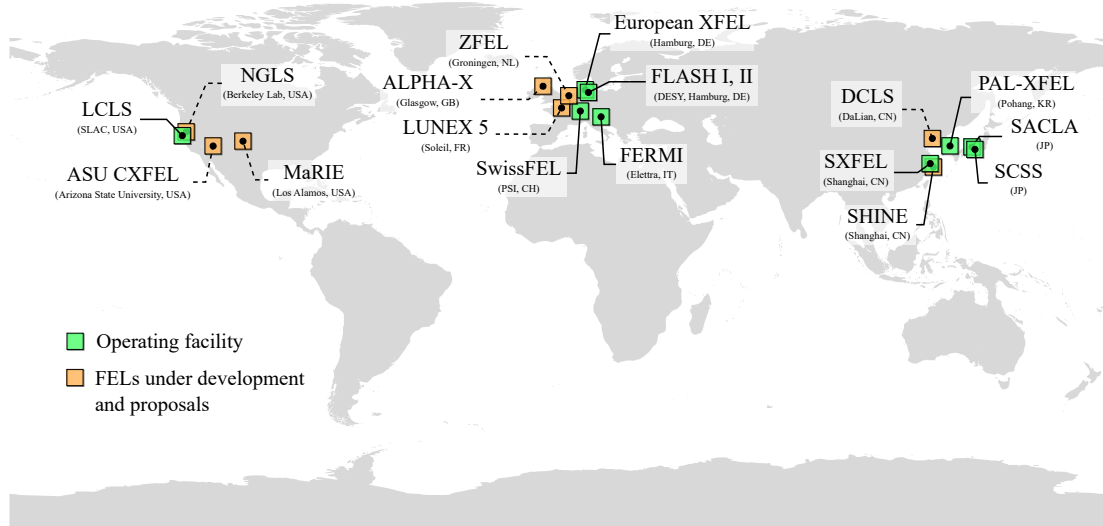
**Figure 4.2:** World map of FELs operating in the short-wavelength regime. There are only a few FELs producing short-wavelength radiation but many more being built and proposed.

## 4.1.2  Self-amplified spontaneous emission

Both synchrotrons and FELs use electrons and periodic magnetic fields to produce light. The main difference resides in the way how the light is produced: Electrons in the electron bunch passing through wigglers or undulators oscillate and emit radiation. Photons generated in the undulator however constructively interfere with each other which results in summing of electric field amplitudes instead of intensities as it happens in wigglers. Furthermore, thanks to high-quality of electron bunches an effect called microbunching takes place in well-tuned undulators used in FELs. During this process, generated photons interact with the electron bunch which is redistributed into micro-bunches emitting the coherent radiation. This process, which stands behind high-gain FELs delivering extremely bright pulses, is called self-amplified spontaneous emission (SASE). An exponential increase of laser beam intensity during one passage through an undulator is, contrary to synchrotrons, characteristic for SASE FELs. The SASE process puts strong requirements on electron bunches, such as high peak current and perfect monochromaticity, as well as on undulator's magnetic field periodicity and intensity. These requirements can be met because of the use of proper linear accelerators containing series of electron compressors and collimators and modern magnetic alloys. Radiation spectrum emitted by the electron bunch in the undulator is not broad, as in cases of bending magnets or wigglers, but consists of a narrow fundamental spectral line being followed by less intense harmonic orders. A closer look at the line shape (see Figure 4.3) reveals many peaks representing spectral modes emerging from each particular microbunch.

## 4.1.3  Self-seeding

One of the main problems of the SASE process is a stochastic origin of first photons emerging from the shot noise. Random phase and amplitude of initial field entering the amplification process causes shot-to-shot instabilities of output parameters such as pulse energy and spectral, spatial and temporal pulse shape.
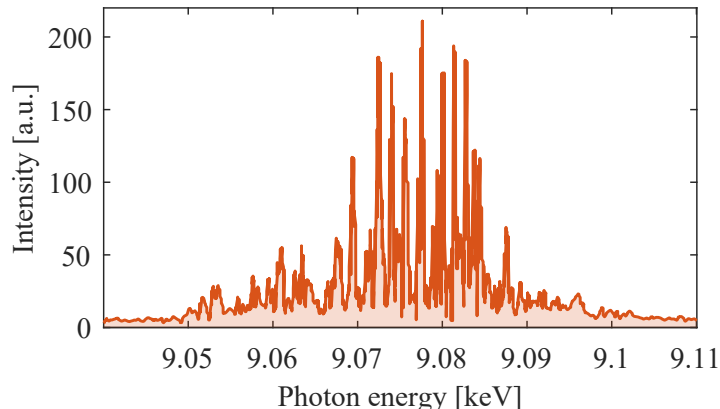
**Figure 4.3:** A single-shot FEL spectrum measured at SACLA shows its typical spiky profile. Data from [214].

For this reason, a self-seeding technique, first implemented at FERMI, was developed [215–217]. This method employs two (or more) undulators where the first one serves as an oscillator for generation of a weak photon pulse of well-defined parameters which is further amplified in the next undulator(s).

### 4.1.4 Burst mode

FELs usually deliver photon pulses in the so-called burst mode. It is mostly dictated by capabilities of injectors and linear accelerators. A typical scheme, used also during the experiment with MHz desorption at the FLASH facility (Chapter 6.3), is shown in Figure 4.4. In a standard mode, when a fast shutter selecting individual pulses is kept open, there are 10 trains per second each consisting of 400 ~100-fs pulses separated by 1 $\mu$s. The MHz repetition rate is thus available only for a very short time (400 $\mu$s). Together there are 4000 pulse per



**Figure 4.4:** Structure of the burst mode at FLASH.

second, i.e. an effective repetition rate is 4 kHz. A very similar situation is at the EuXFEL where individual 10–100-fs pulses are separated by 220 ns and each of 10 trains per second consists of 2700 pulses resulting in an effective rep. rate of 27 kHz.[2] An exception should be LCLS-II (a new superconductive version of LCLS) which promises a quasi-continuous wave operation (1 MHz rep. rate) due to use of new superconducting accelerator technology [11]. Using extreme rep. rates, one has to pay attention not only to possible overheating of optical elements but also to collection of data. High-resolution detectors can already produce up to 10 GB/s and sophisticated data storage plans must be thus involved.

---

[2]An interesting situation occurs when one calculates a ratio of time when EuXFEL delivers 10-fs pulses and is "switched on" to "dark" delay between the pulses. Despite astonishing 27-kHz rep. rate, the laser is "off" for 99.999999973% of the operating time. It corresponds to 8 milliseconds of light produced every year of permanent operation!

### 4.1.5 Pulse properties and diagnostics

Each experiment has slightly different requirements to specific properties of the photon pulse. Most of them can be met by using various instruments implemented in each beamline. Starting already at undulators, different arrangement of magnets leads to linear or circular polarization of FEL pulses [218]. A proper choice of polarization determines direction of photoelectrons and possibly also damage threshold. Another important instrument is a monochromator which selects only photons within a defined energy range. A typical bandwidth of the spiky FEL spectrum is 0.5% and monochromatization might be essential for a class of experiments requiring narrow-band spectra rather than quasimonochromatic radiation. Temporal profile of the pulse is obviously characterized with use of THz streaking [219, 220] or other methods [221, 222]. In optical lasers the pulse compression is usually achieved via chirped pulse compression technique. This situation is slightly more complicated at FELs as all-optical pulse compressors, employing diffraction gratings, are inefficient. However, the chirp can be introduced already to the electron bunch in order to get a chirp in the photon pulse [223]. The pulse length can be furthermore shortened by lowering the bunch charge. Nevertheless, from the perspective of ultrafast electronic processes and phase transitions, it seems that temporal shape of the pulse (Gaussian, box, noisy SASE) is not very important at all [45].

A direct impact of possible experiments at modern FEL facilities can be clearly observed in the field of HEDP. Their bright and extremely short XUV pulses provide a perfect tool for the isochoric heating and reaching the WDM/HDM conditions. Furthermore, integration of an autocorrelator (split-and-delay unit) into the beamline makes pump–probe experiments possible. The forthcoming energetic pulse usually serves as a pump isochorically heating the target and the second delayed pulse is used to probe the created dense plasma. Spectrally-resolved X-ray scattering, emission spectroscopy, Thomson scattering, Bragg reflections and other methods are used for a detailed diagnosis of plasma properties. Moreover, some beamlines also provide optical lasers synchronized with FEL pulses making it possible to perform two-colour pump–probe experiments. An advantage of visible pulses is that their high pulse energies can be used for creation of extreme pressures which are then probed by FEL pulses.

## 4.2 Other short-wavelength sources

### 4.2.1 PALS

Prague Asterix Laser System (PALS) is an iodine laser system situated in Prague, Czech Republic. This system was developed at the Max-Planck-Institute of Quantum Optics as Asterix IV and later it was transferred to the Czech Republic [224]. Nowadays, it is capable to deliver 400-ps pulses at 1315 nm and energy up to 1 kJ which can be focused to power density up to $3 \times 10^{16}$ W/cm$^2$. Recovery time between individual full energy pulses is approx. 20 minutes [225].

In 1994 B. Rus et al. showed that heating of a zinc target with powerful laser pulses ($10^{13}$ W/cm$^2$) can lead to production of neon-like zinc plasma with high population inversion. They focused on a particular transition J=0 to J=1
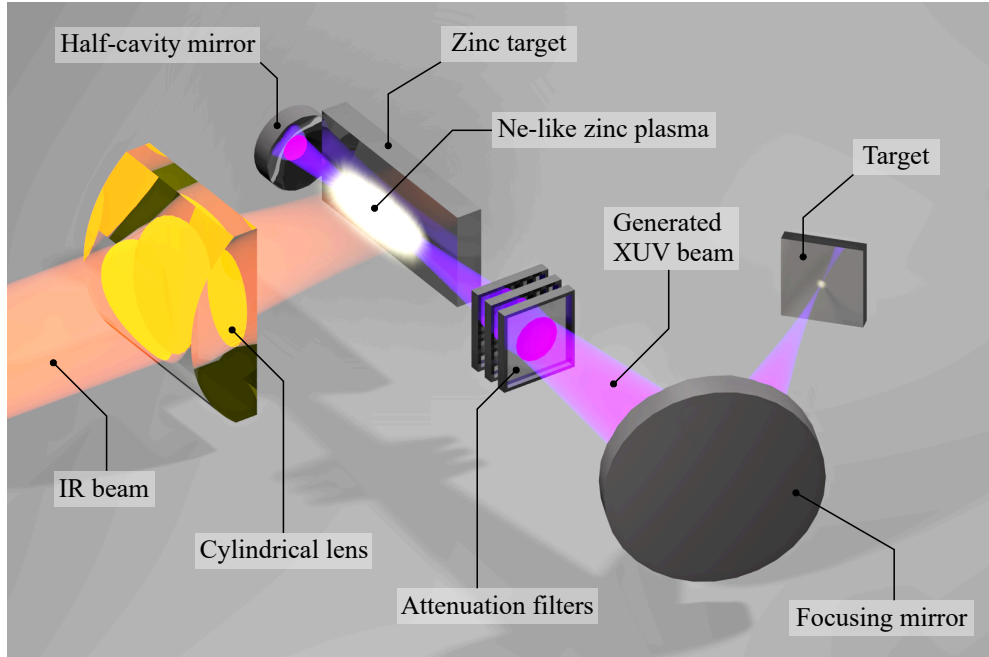
**Figure 4.5:** Illustration of an experimental arrangement focused on XUV pulse generation.

which exhibited a significant gain and achieved generation of intense laser pulses at 21.2 nm [226]. Several years later, this experiment was realized at the PALS facility with even better results as described below [227].

Figure 4.5 shows the way how the IR beam, provided by the PALS facility, is converted into the XUV pulse and focused onto the target. An infrared pre-pulse with energy of $\sim 1$ J and delayed main pulse with energy of 0.5 kJ are both focused by a tandem of cylindrical and spherical lenses (the spherical is not shown in the figure) on the zinc target placed in a vacuum chamber. Energy of the IR pulses is thus transferred into a 3-cm-long column of highly ionized zinc plasma. Electron–ion collisions lead to a removal of twenty outermost electrons from most of the zinc atoms. Collisional ionization of the ten remaining electrons is not probable because of the ionization bottleneck (see Chapter 2.4.2).[3] Created highly ionized plasma with high abundance of Ne-like zinc atoms further undergoes an atomic transition $(2p_{1/2}^5 3p_{1/2})_{J=0} \rightarrow (2p_{1/2}^5 3s_{1/2})_{J=1}$ and via the amplified spontaneous emission (ASE) it starts to lase at 21.2 nm. The described effect is schematically shown in Fig. 4.6a. Figure 4.6b shows that radiative deexcitation also occurs at different dipole-allowed transitions but the transition from $J = 0$ to $J = 1$ has the greatest amplification factor and yields the best signal. It is worth noting that transition $2p^5 3p \rightarrow 2p^6$ is forbidden which makes the state $2p^5 3p$ metastable with an increased lifetime compared to other states. This fact enables formation of inversion and ASE process. In order to increase the efficiency of the ASE process, a half-cavity mirror is used and some of the photons thus propagate through the plasma twice stimulating more radiative transitions. Generated $\sim 100$-ps XUV pulse of multi-millijoule energy can be attenuated using solid metallic foils and focused onto the target by an Al/Mo multilayer mirror (capped with a $B_4C$

---

[3]As the ionization energy of the 11$^{th}$ electron is 737 eV and of the 10$^{th}$ electron 1846 eV the plasma temperature is assumed to be around 1 keV [88]. This makes also a condition for a proper intensity in the focus which should be $3 \times 10^{13}$ W/cm$^2$.

coating) of reflectivity 70% and focal length 300 mm. Attenuation foils also shield scattered IR photons which might otherwise propagate through the beamline and disturb measurements on the target. The parasitic effect of the IR photons was employed in CdTe damage experiment to compare an impact of photons at different energies. See Section 7.3 and/or [54].
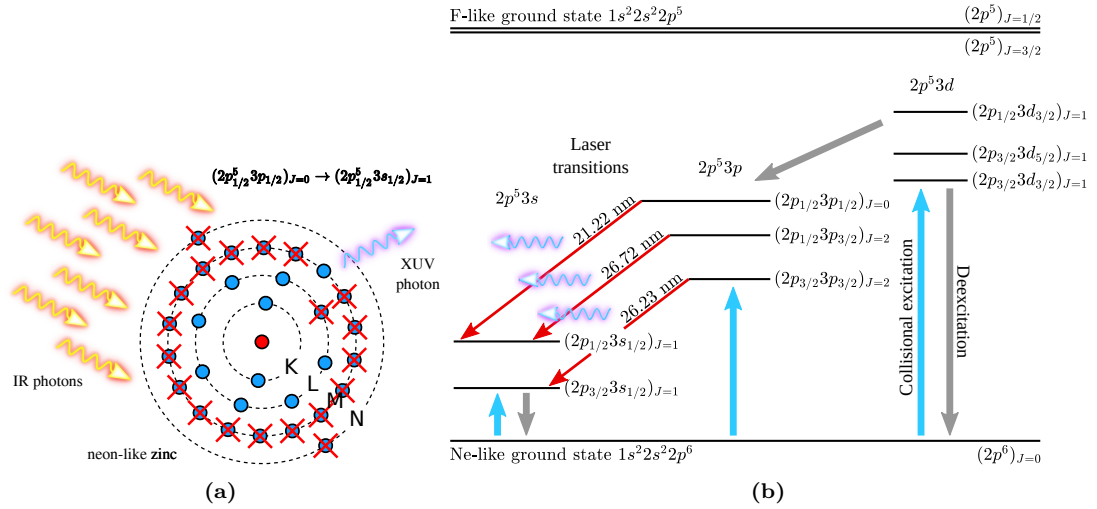


**Figure 4.6:** Description of IR light conversion to XUV pulse employing the neon-like zinc plasma. (a) Collisional ionization of the zinc atom by IR photons. Subsequent transition within the M-shell is accompanied by XUV photon emission. (b) Simplified diagram of essential energetic levels and transitions.

## 4.2.2 Capillary discharge laser

Compact sources of coherent XUV pulses are of interest to many researches as the FELs are quite expensive and do not fit to most laboratories. Although a recent development of compact electron accelerators promises miniaturization of FELs to table-top scales their future and utilization is still uncertain. Capillary discharge lasers (CDL) represent one of several possible compact alternatives to FELs.

CDL used in our experiments (Chapters 7.2 and 7.3) shown in Figure 4.7 is based on ASE of neon-like argon plasma produced by an intense current pulse. A high voltage source is used to charge ceramic capacitors which quickly discharge through a spark-gap pressurized with air shown in Figure 4.7a. Generated current pulse of $\approx 20$ kA propagates through a 21 cm long ceramic capillary with 3.2 mm inside diameter filled with argon at pressure of $\sim 1$ mbar. Strong magnetic field of the current pulse compresses the argon plasma into a hot and dense column with high axial uniformity. Electron impact excitation creates a population inversion in the neon-like plasma between $3p\,^1S_0$ and $3s\,^1P_1$ and lasing thus starts through the ASE process at 46.9 nm. The generated pulse has duration of $\approx 1.5$ ns and energy of $E_{\text{pulse}} \approx 10\ \mu\text{J}$ [228]. Interaction experiments are conducted in a high-vacuum chamber (Figure 4.7b) equipped with a motorized target holder and diagnostic devices.
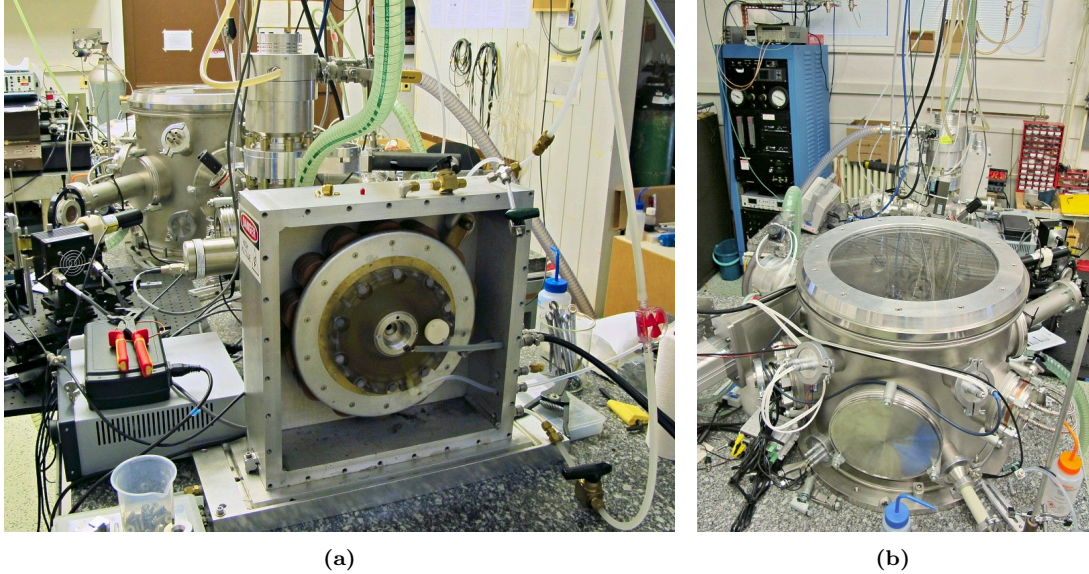
**Figure 4.7:** Capillary discharge laser at the Institute of Physics of the Czech Academy of Sciences. An uncovered main spark-gap, which is during the operation immersed into an insulating and cooling oil bath, is shown in (a). All components are enclosed in an aluminium construction shielding the electromagnetic pulse generated during the discharge process. The front view (b) shows the interaction chamber with the target holder and diagnostic devices.[4]

### 4.2.3 Laser on inner-shell atomic transitions

The two previous XUV sources employ a photonic or current pulse to create a population inversion in the produced plasma which lases at short-wavelengths as outer-shell electrons change their electronic states via stimulated emission. One can certainly think about a laser based on more energetic inner-shell atomic transitions. The first observation of that type was performed by Yoneda et al. who used a tunable soft XFEL for a direct photoionization of copper $K_\alpha$ electrons. Created plasma generated strong ASE at 1.5 Å [132]. This approach was not possible until the advent of FELs as it was extremely difficult to create sufficient population inversion between two electronic levels of such high energy difference and hence extremely short lifetimes ($\approx 1$ fs).

### 4.2.4 Laser facilities with extreme parameters

The most powerful pulses nowadays exceed 1 PW limit with use of chirped pulse amplification (CPA). The origin of these lasers can be traced back to Lawrence Livermore National Laboratory (LLNL). First petawatt pulses were generated in 1990's by Nova (LLNL) laser which was built to study possible approaches towards fast ignition fusion [229]. Its successor, National Ignition Facility (NIF-LLNL), aims to achieve the ignition directly with use of multi-directional irradiation of the hohlraum employing 192 pulsed laser beams of total power 0.5 PW and energy $\sim$2 MJ [230]. Similarly, Laser Mégajoule facility build in France was also designed for ICF experiments [231].

One of the greatest projects — Extreme Light Infrastructure (ELI), initiated

---

[4]Please, forgive the mess which suddenly and unexpectedly formed during our experimental work. It is attributed to imps who also hide 6-mm allen keys from us.

by G. Mourou, nowadays contains three facilities aiming at generation of 10 fs 10-PW laser pulses (ELI Beamlines), powerful attosecond pulses (ELI-ALPS) and highly intense optical and gamma radiation (ELI-NP) [232, 233]. The final part of the project will be Ultrahig Field Facility where 100 PW pulses of intensities $10^{25}$ W/cm$^2$ should approach the Schwinger limit and polarize vacuum into electron–positron pairs [234].

The first laser with multi-joule pulses with average power exceeding the 1 kW threshold (100 J, 10 ns pulses at 10 Hz) was developed by the DiPOLE team at the HiLASE facility in the Czech Republic [235].[5] The main problem of such lasers is overheating due to high fluences. This particular laser employs thin Yb:YAG discs in a multi-pass geometry and diamond plates for heat dissipation.

The shortest controlled laser pulse ever created was a 43-attosecond pulse composed of soft X-ray supercontinuum as a result of high-harmonic generation from femtosecond IR pulse [236].

Future plans aim to increase power of the lasers in order to reach attractive high-field effects, shorten pulses to observe ultrafast electronic transitions and also to miniaturize the large-scale facilities to fit them into conventional laboratories. One promising way suggests to replace radio-frequency electron accelerators by accelerators using optically-generated THz pulses which can provide ∼100-keV electrons within a few centimetres [237, 238]. Even larger acceleration field can be reached using laser-wakefield accelerators based on laser-plasma. Using this method, electrons can gain almost MeV energies per centimetre [239]. Such electrons can directly enter undulators and emit synchrotron radiation without the use of very long and complex electron accelerator [240]. Nevertheless, quality of electron bunches generated by compact accelerators must be significantly improved in order to generate X-ray pulses comparable to those delivered by current facilities. Shortening of FEL can be done also by reducing the undulator period but such facility would be still many tens of metres long [241]. It seems that lots of effort is still needed before these concepts will be transformed into fully working lab-scale instruments.

## 4.3   X-ray optics

Formation of brilliant ultrashort pulses containing an immense number of high-energy photons would not be certainly so glorious if there was no way of focusing these beams down to the interaction targets placed far away from undulators in experimental hutches. X-ray optics is a very important part of each beamline and the availability of a tiny focus is of great interest to high-resolution X-ray microscopy and also to HEDP research requiring extreme intensities. Considering the short-wavelength of the X-ray pulses, it is clear that it should be possible to focus them down to a few nanometre-wide spots as the diffraction limit drops. Nevertheless, it is the short wavelength which actually brings great difficulties in proper choice of material and fabrication of precise optics suitable for this light.

Optical properties of materials significantly vary with increasing photon energy and conventional approaches, typical for visible region, are often not ap-

---

[5]Although the peak power of this laser reaches those of nuclear power plants, its average power is still at the order of an ordinary electric kettle.

plicable in the short-wavelength regime. The main issue resides in the complex refractive index $n$ which can be described as $n = 1 - \delta + i\beta$, where $\delta \ll 1$ and $\beta > 0$. Since the real part of $n$ is close to 1, the normal incidence reflectivity as well as refractivity is very small. Non-negligible $\beta$ is responsible for strong absorption of short-wavelength radiation. Reflectivity of mirrors can be significantly improved when the incidence angle falls below the critical angle (measured from surface). The critical angle is usually quite small and mirrors are thus used in grazing incidence configuration. Another problem of mirrors is the roughness which must be much lower than the wavelength of used light. These two requirements make fabrication of such mirrors very difficult as they must be up to a meter long and totally flat. Use of interferometric measurements [242] shows that error of precisely polished ∼1 meter long mirrors is only a few nanometres [243,244].[6] These mirrors are used for beam distribution, in Kirkpatrick-Baez (K–B) focusing optics, etc.[7]

Reflectivity of mirrors designed to work under or close to normal incidence angle might be increased by coating the reflective surface with a multilayer structure. An off-axis parabola coated with a Mo/Si multilayer, a similar one was used in aluminium free-free opacity measurements (Chapter 7.1), had an initial reflectivity above 60% at 13.5 nm [15,245].

Use of refractive optics in XUV region is problematic due to high absorption of convenient materials. Situation in the hard X-ray regime is more favourable as the absorption coefficient decreases with increasing photon energy. Mostly used materials for fabrication of such optics are lightweight elements like flammable lithium or poisonous beryllium. The fact that real part of the refractive index is only slightly smaller than unity means that focusing lenses must be of concave shape and many of them must be used to achieve a significant effect. A set of 20 Be lenses together with a corrective phase plate reducing spherical aberration was used to reach a diffraction-limited focus of 8-keV FEL beam at LCLS [246].

Fresnel zone plates (FZPs) consist of alternating transparent and opaque zones. Light transmitted through the FZP diffracts on the opaque zones and constructively interferes in the focal plane. Clear disadvantage of FZPs is that large portion of light is absorbed by the opaque material. Another transparent material with different refraction index is therefore used to change the light phase by $\pi$ instead of filtering it out [247]. Thickness of such FZP where widths of outermost zones are only ∼10 nm must be several microns. Fabrication of FZPs for XUV, soft X-ray and hard X-ray radiation is very difficult obviously employing lithographic procedures like, for example, e-beam lithography. Instead, multilayer Laue lenses (MLLs) were developed. MLL is composed of a stack of 2D sheets of two alternating materials which can be tilted or wedged in order to meet Bragg condition, see Figure 4.8. Because one MLL provides focusing only in one, vertical or horizontal, direction, a pair of MLLs must be used to get a point focus [248,249]. An extensive development of this kind of X-ray optics resulted in

---

[6]Let us now assume there is a flat 200-km-long highway connecting two cities like Prague and Brno. If we had wanted a comparable flatness of the highway to the mirror (2 nm error per 90 cm), the largest bump would have been just 0.4 mm high!

[7]The necessity of utilization of distribution mirrors in grazing incidence configuration is also a partial answer to the question why FELs are so long. A modest requirement of separating two beamline stations only by a few metres gives a result that distribution mirror must be situated tens up to hundreds of metres upstream the beamline.

high-quality MLL being composed of thousands of layers with nanometre periods. Nowadays, an utilization of MLLs makes it possible to focus hard X-rays to focal spots smaller than 10 nm [250, 251].
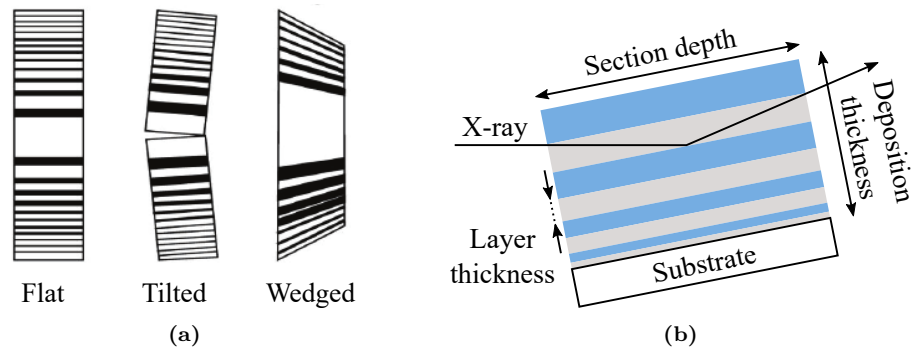


**Figure 4.8:** (a) Three different types of MLL. (b) Schematic of light diffraction. Adapted from [249].

Other optical elements fabricated by coating an etched substrate by a pile of alternating layers are diffraction gratings employed in chirped-pulse compressors, monochromators and spectrometers. Materials used for the coating are radiation-hard like, for example, $B_4C$ or ruthenium. An extremely high density of lines (over 20000 line pairs/mm) is required for use in the short-wavelength regime [223].

# 5. Methods

This chapter brings an overview of methods used for *ex situ* analysis. A summary of microscopic techniques providing a detailed information about surface topography is given in the first section. The second section describes an operation of several spectroscopic methods.

## 5.1 Microscopic methods

Information such as colour, topography or hardness of an object or its surface can be obtained by several different methods. Resolution of classical microscopes based on optical magnification is limited by a relatively long wavelength of visible light. Provided that we want to observe how much room is at the bottom,[1] we have to use light of shorter wavelengths. The object shape and its structure is then usually reconstructed from diffraction patterns as it was mentioned for the CDI technique in Chapter 4.1. Knowledge of quantum physics and wave–particle duality shows that except of photons we can employ also electrons and another particles for object visualization. Both direct imaging as well as diffraction imaging techniques can be adapted for fermions. Representatives of these methods can be transmission/scanning electron microscopy (TEM/SEM) and reflection high-energy electron diffraction, respectively. Height profiles of 3D structures can also be measured by visible light. This method called white light interferometry (WLI) is, as the name prompts, based on interference of reference beam and beam which is reflected from the surface. Another technique is based on a gentle touching of the surface with a tiny mechanical probe. It is based on interatomic forces and is hence called atomic force microscopy (AFM).

### 5.1.1 Nomarski microscopy

Nomarski microscopy was invented by G. Nomarski in order to optically increase contrast of the image. In the first part, a polarized light coming from a light source is split into ordinary and extraordinary rays by Nomarski prism (also known as Wollaston prism). These rays are then focused onto a transparent sample and merged together by another set of focusing lens and prism. Enhanced contrast is obtained from an interference in the detector because each ray has different phase shift after transmitting through (or reflecting from) the sample. Hence differential interference contrast (DIC) is another designation of this technique. Figure 5.1 shows an optical layout of Nomarski microscope built for transparent samples which uses two prisms. Slightly different arrangement used for opaque specimens consists of one prism but requires a one-way mirror.

---

[1] In 1959 R.P. Feynman entitled one of his lectures as "There's plenty of room at the bottom". In this talk he essentially predicted a possible advent of nanotechnology although the word 'nanotechnology' was not known at that time [252].
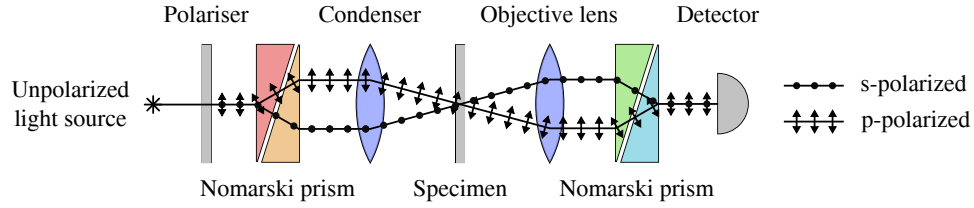
**Figure 5.1:** Schematic of Nomarski DIC microscope.

## 5.1.2 WLI

The white light interferometry (WLI) is a non-contact method used for measuring height profiles of 3D structures which may vary in a range from few nanometres to several centimetres. As the Figure 5.2 shows, WLI is based on a principle of the Michelson interferometer with full-spectrum white light at the input. The beam splitter separates light into a reference beam and beam which is reflected from the sample surface. Interference of these two beams is used to calculate height profile with a high precision. The principle is based on a very short coherence length of white light. The sample is placed on a motorized stage which is moved in a longitudinal direction during the measurement and although the whole sample



**Figure 5.2:** WLI based on Michelson interferometer. Interference of two beams reflected from the reference mirror and the sample surface serves for height profile reconstruction.

is illuminated, only light reflected from a narrow depth interval may interfere. This is possible because of a very small difference of its phase shift compared to the phase shift of the reference beam. In our measurements we employed a white light interferometer Zygo NewView 7200 with several different magnification objectives.

## 5.1.3 AFM

The atomic force microscopy (AFM) employs a mechanical probe (cantilever with a small tip) to touch the sample surface and reconstruct its 3D height profile by measuring the cantilever deflection. A correct interpretation of measured data can lead up to an atomic resolution of a given structure. The AFM usually operates in one of the three following modes: During the contact mode, the most intuitive one, the cantilever is constantly in contact with the sample surface. The tip is kept in a constant distance from the surface using a feedback loop which controls position of the z-scanner holding the cantilever. Position of the z-scanner therefore directly copies the height profile of the sample. It is therefore sufficient for measurements of the height profile or friction. Drawbacks of this method are scratches on the sample, tip wear and lack of more additional information about the surface. An advanced tapping mode is schematically shown in Figure 5.3. A driving signal forces the cantilever to oscillate at its resonant frequency very close to the surface and mechanical contact is present only for a very limited time. In-

teraction with the surface induces changes of oscillations which are recorded using a reflected laser beam and four-segment photodiode. The feedback mechanism uses this signal to control the z-position of the cantilever to maintain a constant distance from the surface. The tapping mode can be also used for phase imaging by monitoring the phase difference between the driving and output signal. This information in cooperation with another techniques can be used to measure not only the surface topography but also friction, adhesion, stiffness, elasticity, thermal and electrical conductivity and others. Calculation of stiffness and adhesion from a force-distance curve is shown also in the Figure 5.3. The third mode, very similar to the tapping mode, is called non-contact mode. The cantilever in this mode also oscillates above the surface but precise electronic keeps its lowest deflection still above the surface.

Our AFM measurements were done in the tapping mode using Dimension 3100 scanning probe microscope driven by a NanoScope IV controller (Veeco, USA).
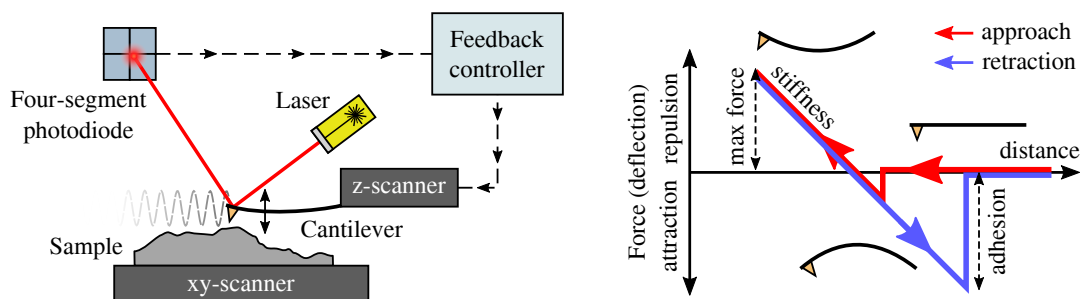
**Figure 5.3:** Schematic of the AFM in the tapping mode (left) and force-distance curve explaining interaction of the cantilever with a sample surface (right).

## 5.2 Spectroscopic methods

Except of getting information about physical appearance of investigated samples it is often desired to get more knowledge also about its electronic properties such as band structure, binding energies and lattice vibrations which cannot be obtained by standard microscopy. Techniques which can measure such properties often operate with energy of emitted particles which is measured by different kinds of spectrometers. Resulting spectra may provide great information of energetic levels of single atoms, vibrational and rotational states of molecules, state of plasma and many others. An overview of several spectroscopic methods is given in this section.

### 5.2.1 Raman spectroscopy

Light propagating through matter interacts with electronic states of atoms, molecules, crystal band structure and quasiparticles. Re-emission of an absorbed photon into different directions with different or equal energy is called inelastic or elastic scattering, respectively. Various mechanisms of the scattering are shown in Fig. 5.4. When irradiating a sample with intense monochromatic light we find out that most of the scattered light is at the same wavelength. This is called
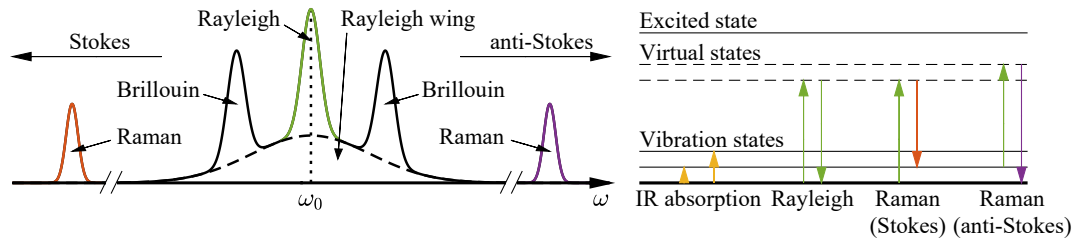
**Figure 5.4:** Schematic overview of different scattering mechanisms. A green colour denotes initial photon frequency at $\omega_0$. Redshift and blueshift in case of the Raman scattering is symbolized by red and purple colour, respectively.

elastic Rayleigh scattering which is a great diagnostic tool for characterization of gasses [253]. Other valuable data of the irradiated material structure can be obtained from inelastic scattering at wavelengths close but different from that of excitation light. Inelastic scattering is divided into Brillouin and Raman scattering according to the magnitude of the wavelength change. While Brillouin scattering is connected with phonons propagating in condensed matter, Raman scattering originates at vibrational and rotational states typical also for molecules. Discovery and the first observation of the Raman scattering is attributed to an Indian scientist C. V. Raman who was awarded Nobel prize in 1930, two years after his pioneering discovery [254]. The scattering is nowadays employed in the Raman spectroscopy which measures energy difference between photons from the excitation laser and the scattered light. This shift in the photon frequency, also called the Raman shift, provides information about rotational and vibrational spectra of molecules. It is therefore applicable to investigation of solid, liquid as well as gaseous samples.

The first part of classical non-resonant Raman scattering is an electron photoexcitation from a ground level to a virtual level. In the second step, the electron relaxes to a vibration state which is above the original ground state. During this relaxation a new photon of slightly lower energy is emitted. Described effect is called normal Stokes Raman scattering. If the initial state of electron is above the final state, the emitted photon is blueshifted and we call it anti-Stokes Raman scattering. In order to enhance weak Raman signal, resonant Raman scattering can be used. In this case, wavelength of the excitation laser is tuned either to the first (incoming resonance) or to the second (outgoing resonance) electronic transition. Resonance can be used for stimulated electronic transitions and construction of Raman laser [255].

Measured spectrum of the Raman shift consists of several peaks which correspond to vibrations of individual bonds, collective vibrations of groups of atoms like benzene-ring breathing mode or polymer chain stretching modes and phonon modes in crystals. Spectra can thus serve for identification of the material, purity and contamination measurements and others. Quite typical effect is also shift of certain peaks which may reflect strain in the material. This effect was crucial for identification of damage mechanisms in case of graphene (Sec. 7.2, [55]) and CdTe (Sec. 7.3, [54]).

Measurements of Raman spectra in this work employed a confocal Raman microscope WITec alpha300 RSA (WITec, Germany) with 532-nm laser excitation in the backscattering geometry with two objectives EC Epiplan (Zeiss, Germany)

of magnifications $20\times$ and $100\times$ and numerical apertures 0.4 and 0.9. This device provides raster-scanning of the sample surface with high spatial resolution ($< 1 \ \mu$m). All measurements were recorded at room temperature.

## 5.2.2 Photoluminescence

An ability of a material to spontaneously emit light which has no origin in heat is called luminescence. It is divided into several categories related to the excitation source: photoluminescence, electroluminescence, chemiluminescence, mechanoluminescence, etc. Here we used photoluminescence which employs laser radiation to excite electrons to higher energy levels. Photoluminescence can be further divided according to the lifetime of excited states into phosphorescence and fluorescence. The phosphorescence denotes light emission which lasts for a long time after the irradiation and fluorescence is the opposite — light emission with 'immeasurably' short[2] glowing when the excitation source stops [198].



**Figure 5.5:** Schematic of the photoluminescence including excitation, relaxation and recombination process.

This section describes the principle of photoluminescence which lies in the electronic band structure of semiconductors as sketched in Fig. 5.5. A photon from an excitation laser with energy greater than energy of the bandgap excites an electron from the valence to the conduction band. Created electron–hole pair relaxes towards the bandgap minimum and undergoes a radiative recombination. The energy conservation law ensures that energy of the emitted photon must be less than or equal to the energy of the excitation photon, i.e. the emitted photon is red-shifted, provided that multiphoton processes are not present. Please note the figure shows only a basic approach which does not involve interaction with phonons or possible transfer to a triplet state. The emitted light is analysed using a spectrometer and the resulting spectrum may provide valuable information about surface recombination effects like shallow and deep levels, impurities, excitons, and others. Despite high sensitivity of this method, estimation of absolute numbers such as defect concentration is difficult to obtain and one must settle for relative changes [256].

In order to suppress parasitic effects and measure a relative increase of dislocations in tellurium sublattice of CdTe, we used the low-temperature photoluminescence spectroscopy. The sample was placed in a helium flow cryostat (manufactured by CryoVac) operating at $\sim 10 - 20$ K. The photoluminescence was excited by a red laser line (638 nm, 1.94 eV) emitted by a semiconductor laser Radius (Coherent). The luminescence signal was recorded by Bruker IFS 66s FTIR spectrometer equipped with a $CaF_2$ beamsplitter and Ge photodiode. A colour glass filter in front of the Ge detector was used to eliminate the scattered red light coming from the laser. Further details of this experiment can be found
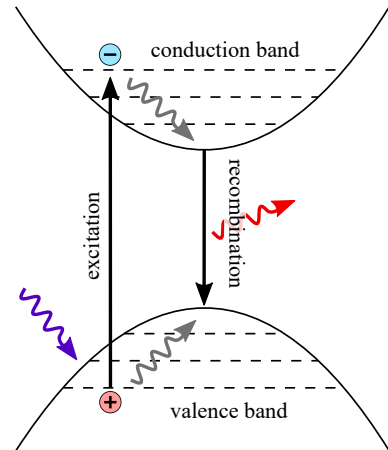
---

[2]Time scale of this archaic specification might be nowadays probably considered as 'less than $\sim$100 ns'.

in Chapter 7.3 and [54].

## 5.2.3 XPS

X-ray photo-electron spectroscopy (XPS), also
known as Electron spectroscopy for chemical anal-
ysis (ESCA), is a technique for characterization an
elemental composition of material's surface. Com-
pared to previous methods, it does not employ
photons emitted from or scattered by the investi-
gated medium but it employs photoelectrons emit-
ted from the surface due to the impact of high-
energy X-ray photons. The photoelectrons are
emitted from the near-surface layer ($\approx 1 - 10$ nm)
and their kinetic energy, which carries information
about the surface chemistry, is analysed using a
hemi-spherical electron energy analyser employing
a magnetic field and electron counter to calculate



**Figure 5.6:** Schematic drawing
of the XPS method.

the final spectrum. A sketch of the XPS instrument is shown in Fig. 5.6. The
measured spectrum consists of several peaks corresponding to binding energy of
the photoelectrons. Positions and intensities of the peaks thus allow us to iden-
tify not only the elemental composition but also chemical and electronic states
including orbitals of the photoelectrons and chemical environment of affected
atoms [257].

The XPS measurements are performed in an ultrahigh vacuum and this tech-
nique is therefore appropriate primarily for solid samples. In this work we used
XPS for characterization of epitaxial graphene on SiC substrate. Measurements
were done using Axis Supra (Kratos Analytical) spectrometer employing $K_\alpha$ ir-
radiation (1486 eV). We also used argon cluster sputtering (2.5 keV, $Ar_{500}^+$) to
clean the surface prior to XPS measurements. Nevertheless, results of the mea-
surements (see Sec. 7.2) showed that spatial resolution of this instrument is not
sufficient for characterization of imprints which are several tens of micron in diam-
eter. A better resolution could be provided by nano-ESCA (also a high-resolution
XPS) which is achievable with synchrotron radiation.

# 6. Beam characterization

With the advent of FELs delivering intense short-wavelength radiation several technical and scientific challenges have emerged. Although it is already almost two decades after the first FEL flash, beam diagnostics still belongs among the most difficult tasks. At the same time, a proper knowledge of the beam energy distribution, size, position of its focus and other beam properties is one of the main prerequisites for a correct interpretation of measured experimental data obtained with that beam. Considering very high intensities ($> 10^{17}$ W/cm$^2$) of focused XFEL pulses, it is clear that we can easily access a nonlinear regime where the response of the irradiate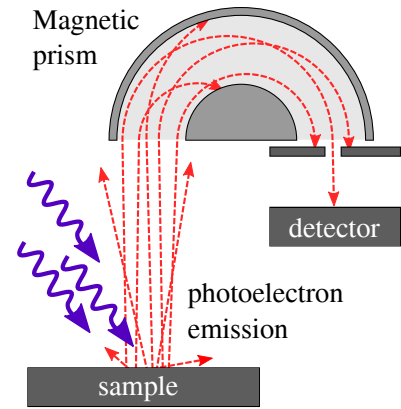d material is a function of intensity. Typical example might be the WDM regime. In an experiment performed by S. M. Vinko *et al.* [60], free-free opacity of warm dense aluminium was measured. The forthcoming energetic pulse heated Al foil to high temperatures exceeding 20 eV and the delayed probe beam measured transmission which is highly dependent on the temperature and so the intensity (see Chapter 7.1). It was shown that beam characterization in this and similar cases (see [91]) is extremely important for an accurate interpretation of measured data. Besides the experimental work, proper diagnostics of intense FEL pulses and its impact to surfaces of various materials is important also for beamline optical elements which can be damaged even at fluences below a single-shot ablation threshold due to overheating effects [52].

This chapter provides a short overview of current methods used for beam characterization. Stress is then put on methods of ablative and desorption imprints which were employed in experiments described in Chap. 7. A novel method used for recovery of a nonlinear response function from desorption imprints is described in Sec. 6.3.

## 6.1   Overview of current methods

The problem of the focused beam characterization resides in a very small (even sub-micron) focal spot size, immense beam intensity, necessity of measurements situated in a vacuum chamber, high energy of photons and others. Any sensing element placed into the focus must therefore possess a great resolution power and strong radiation hardness. Although there are pixel CCD chips operating also in the short-wavelength range, their usage directly in the focus is, because of the mentioned requirements, very limited.[1] Instead, different methods or their combinations are employed. With respect to the position where the beam is actually measured we can divide them into three classes: indirect, semi-direct and direct.

A typical representative of indirect methods is the Hartmann sensor [258,259]. This method consists of a pinhole array and X-ray CCD detector, both placed outside the focus. The wavefront of the a beam is calculated from positions of spots displayed on the detector. Comparison of several indirect wavefront sensing methods can be found in [260].

---

[1]Although CCD chips were several times unexpectedly used as targets for recording of ablation imprints during experimental work, this method is beyond ordinary scientific founding.

Semi-direct methods also employ a CCD chip placed into a safe distance out of the focus where the intensity is sufficiently low, but a well-defined mask is placed directly into the focus. An ordinary knife-edge scanning method [243] can be considered as one of the simplest. Nevertheless, this can be used only for beam size measurements and its utilization is problematic for non-Gaussian beams. In comparison to that, a scanning coherent diffraction microscopy, also known as ptychography, is capable of complex wavefield calculations from several diffraction patterns created by a fine mask which is scanned through the focused beam [261]. A similar method called Ronchi shearing interferometry uses a grating in the focus and a CCD in the far field to observe interference fringes between different diffraction orders emanating from the grating. It can reveal not only aberrations of the focused beam [262] but also its amplitude and phase [263]. An advantage of this method, as compared to ptychography, is that it does require neither a high-precision motorized stage for the movement of the mask nor high pointing stability of the beam. In order to calculate the focused beam profile, all of these methods require complex phase-retrieval algorithms which often have to deal with several theoretical difficulties such as usually unknown partial coherence. In order to get around this problem, direct methods which do not require X-ray CCD for recording scattered or diffracted light can be used.

It has been shown, that X-ray irradiation of lithium fluoride (LiF) crystals induces colour centres (point defects) which, under blue optical pumping, emit light via photoluminescence. The irradiated volume containing information about the beam shape can be thus characterized with a microscope. Although this method provides a sub-micrometer spatial resolution, accumulation of typically hundreds of shots is needed and linearity of the signal is not guaranteed [264, 265]. Other direct methods use luminescence from Ce:YAG crystal [197], calculates fluence distribution from gas ionization measurements [266] or uses ablative imprints created by the X-ray beam of intensity exceeding damage threshold of a given material [50, 51, 181, 267, 268].

It is clear that none of the mentioned methods is absolutely versatile and suitable for every experiment. In each particular case it has to be considered whether the beam pointing stability is good enough to measure an average profile from multiple pulses and whether the beam characterization must be done *in situ*, i.e. in the chamber, or *ex situ* post-process analysis is sufficient. The *in situ* characterization is great for on-line monitoring of the beam which facilitates alignment of focusing optics while keeping the ultrahigh vacuum in the chamber. An overview of beam characterization methods can be found in [268].

In the next section we focus on beam description from the perspective of imprinting method which was the main approach to beam characterization at experiments described in this work. Although beam imprinting typically requires recording of large sets of data and time-consuming *ex situ* characterization, it provides great and valuable results. An instrument which is capable of *in situ* beam monitoring was presented [269], but its implementation into the beamline was rather difficult. New version of such an instrument called AbloCAM is currently under development [270].

## 6.2 Imprinting methods

Method of ablation imprints employs the threshold character of the ablation process where the material is damaged only when the laser fluence exceeds the ablation threshold specific for a given material, pulse wavelength, duration, etc. The contour surrounding the imprint thus represents a closed iso-fluence curve created right at the threshold fluence. Imprint depth profile as well as its area encircled by the contour can be then used for beam characterization. The first one who employed ablative imprints in the focused laser beam characterization was J.M. Liu already in 1982. He measured areas of imprints in silicon induced by VIS and UV pulses and plotted them as a function of pulse energy logarithm [271] (see Figure 6.2a). In case of a perfect Gaussian beam the created curve is a straight line which determines both energy damage threshold (cross section with $x$-axis) and beam size area at $1/e$ of its maximum (slope of the curve).[2] Because of non-Gaussian profiles and also different nature of interaction in the short-wavelength regime, the method had to be entirely modified for characterization of FEL beams. The greatest benefit of this improvement can be certainly ascribed to work of J. Chalupský *et al.* [50, 51, 181, 267, 268, 272].

### 6.2.1 Materials

One of the best materials for imprinting is undoubtedly already mentioned polymer poly(methyl methacrylate) (PMMA) also known as acrylic glass or plexiglass. PMMA is widely used as a resist in lithography and its response to XUV, X-ray and electron beams was thus well studied. Relatively high ablation rate of PMMA dependent on deposited dose of short-wavelength radiation makes this material suitable for nanostructuring and creation of ablation imprints [273]. Smoothness of ablated surface and sharp edges of craters also indicate that main processes responsible for ablation are nonthermal [274, 275]. Damaged area is thus not affected by thermal effects and is restricted to the irradiated area which is an important prerequisite for the beam characterization. Use of PMMA at photon energies exceeding $> 300$ eV becomes problematic because of surface roughening incurred by increased absorption depth of the radiation. Inorganic scintillators (Ce:YAG, $PbWO_4$, ZnO) and high-Z materials (e.g. $PbWO_4$, $PbI_2$) deposited on low-Z materials (CVD diamond, silicon) have proven their worth in this high-energy regime [56, 84, 117, 131, 276]. The design of current beam characterization targets aims at maximization of ablation contour contrast and minimization of thermal effects. Hence highly absorbing radiation-sensitive thin layers are deposited on thermally conductive and weakly absorbing (radiation-resistant) substrates.

### 6.2.2 Theoretical description

The main aim of imprinting methods is to reconstruct the transverse beam fluence profile $F(x, y)$ from a set of imprints at a given $z$ location along the beam propagation axis. A direct reconstruction of $F(x, y)$ from a single ablative imprint is also possible but requires several assumptions: First of all, the shape of

---

[2]Although Gaussian beam profiles can be observed at FELs from time to time [272], it is rather a rare effect worth celebration which is definitely not a part of daily routine.

the beam must vary slowly along its propagation axis. This so-called slowly vary-ing envelope approximation (SVEA) is fulfilled as depth of the shallow imprint ($\sim$ 100 nm) is several orders smaller then a typical Rayleigh range of focused beam (100 $\mu$m – 1 mm). Second, the response of the material to the absorbed radiation must be sudden and well-localized. Using this assumption, it is possi-ble to neglect heat penetration which could result in removal of non-irradiated material. It also supports calculations with fluence instead of time-dependent intensity. This assumption is correct only for low-energy beams which do not in-duce strong thermal gradients leading to spallation of surrounding material and extensive melting. Compliance with described prerequisites allows to use Beer-Lambert law of radiation absorption and calculate fluence profile $F(x,y)$ directly from the imprint depth profile $d(x,y)$ measured by means of AFM or WLI [272]:

$$F(x,y) = F_0 f(x,y) = F_{\text{th}} \exp\left(\frac{d(x,y)}{l_{\text{at}}}\right), \qquad (6.1)$$

where $F_0$ is a peak fluence, $f(x,y)$ is a normalized fluence profile, $F_{\text{th}}$ is a thresh-old fluence and $l_{\text{at}}$ is an attenuation length characteristic for a given material and wavelength. The threshold fluence $F_{\text{th}}$ denotes fluence below which no ablative damage of the material is observed. Low-energy wings of the beam thus remain unexplored and dynamic range remains restricted to the peak-to-threshold flu-ence ratio $p = E_{\text{pulse}}/E_{\text{th}}$, where $E_{\text{pulse}}$ is the pulse energy and $E_{\text{th}}$ threshold energy, i.e. pulse energy which causes no damage. Moreover, this method re-quires time-consuming AFM measurements and it relies on a perfect material removal according to the Beer-Lambert law which does not apply at very high fluences where nonlinear and melting effects play role. Nevertheless, it is ex-tremely beneficial when a sufficiently large ensemble of data is not available and the fluence profile has to be reconstructed from a few or even a single imprint. This was the case of irradiation experiment at the PALS facility which delivers one pulse every 20 minutes and creation of large set of imprints was thus not possible. Figure 6.1a shows an imprint in PMMA measured by means of WLI and rendered with the WSxM software [277]. The corresponding fluence profile in Fig. 6.1b, reconstructed with the use of the Beer-Lambert law (Eq. 6.1), served for estimation of two different damage thresholds observed on graphene samples (Chapter 7.2).

In contrast to direct beam profile reconstruction, more advanced F-scan method offers a significantly extended dynamic range and avoids nonlinear issues occurring in the high-energy central part of the beam [267]. This method is based on measuring contour areas $S_i$, where $i = 1, \ldots N$, of $N$ single-shot imprints at monotonically increasing attenuation levels, i.e. decreasing pulse energies $E_{\text{pulse}}^i$. Inverse values of energies $E_{\text{pulse}}^i$ are then plotted as a function of the corresponding contours $S_i$. No damage ($S_j = 0$) is induced by $j$-th pulse with $E_{\text{pulse}}^j = E_{\text{th}}$. The threshold value is important for obtaining a normalized f-scan $f(S_i) = E_{\text{th}}/E_{\text{pulse}}^i$. An area below the curve is called effective area $A_{\text{eff}} = \int_0^\infty f(S)\mathrm{d}S$ which uniquely characterizes the beam spot size of non-Gaussian beams. Using the effective area we can also calculate peak fluence $F_0 = E_{\text{pulse}}/A_{\text{eff}}$ and F-scan $F(S) = F_0 f(S)$. These relations yield $\int_0^\infty F(S)\mathrm{d}S = E_{\text{pulse}}$ or $\mathrm{d}E_{\text{pulse}} = F(S)\mathrm{d}S$. Hence, the F-scan tells us how much does an interval $(S, S + \mathrm{d}S)$ contribute to the total energy of the pulse. More details about the f-scan method and a very detailed
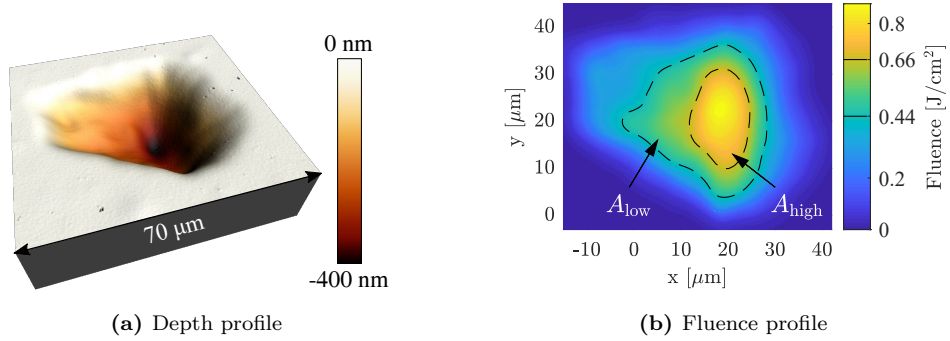
**(a)** Depth profile

**(b)** Fluence profile

**Figure 6.1:** Beam profile reconstruction from an ablative imprint in PMMA. (a) shows a 3D imprint profile measured by means of WLI and (b) shows a corresponding fluence profile reconstructed with the use of the Beer-Lambert law. The two iso-fluence contours represents damage thresholds observed after exposing graphene samples to the 21.2-nm radiation, discussed in Chapter 7.2.

and comprehensible description of valuable information which can be read from the f-scan and its inverse counterpart, so-called if-scan, can be found in [50]. An example of measured f-scan and Liu's plot is shown in Figure 6.2.

A novel method improving the limited dynamic range of PMMA imprints has been proposed by B. Rösner *et al.* [278]. Authors immersed PMMA samples with X-ray-induced imprints into organic solvents which effectively removed exposed material. The fluence threshold of imprints developed in this way was remarkably reduced and a significant enhancement of the dynamic range by up to three orders of magnitude was achieved.

In order to collect information also about the low-energy parts of the beam, method of desorption imprints has been developed. This method uses the fact that the desorption process does not exhibit any threshold behaviour and full beam can be thus revealed. As we have mentioned before, desorption of some materials (e.g. PMMA) in the short-wavelength regime is much more efficient than in VIS or UV [181]. However, despite the relatively high efficiency of the material removal, accumulation of multiple shots is usually needed for creation of an imprint suitable for AFM or WLI measurements. This places additional demands on beam pointing stability which otherwise results in a worthless blurry imprint. Development of a phase-recovery algorithm demonstrates the usefulness of this method [51]. Using this approach, it has been shown that several desorption imprints obtained at different *z*-positions (i.e. alongside the beam propagation axis) close to the focus may serve for numerical retrieval of spatial intensity distribution, beam phase and even transverse coherence.

Under certain circumstances described at the beginning of this section the desorbed imprint shape is nearly proportional to the transverse profile of the deposited dose. Linearity of desorbed PMMA material with deposited dose and legitimacy of usage of the desorbed imprint shape for the beam profile recovery was discussed several times in the cited works [51, 181, 273, 274]. In the next section we introduce a recently developed method published in [61] using which we can calculate a proper response function (i.e. depth as a function of absorbed dose) and hence also accurate fluence profile even in the nonlinear regime of material removal.
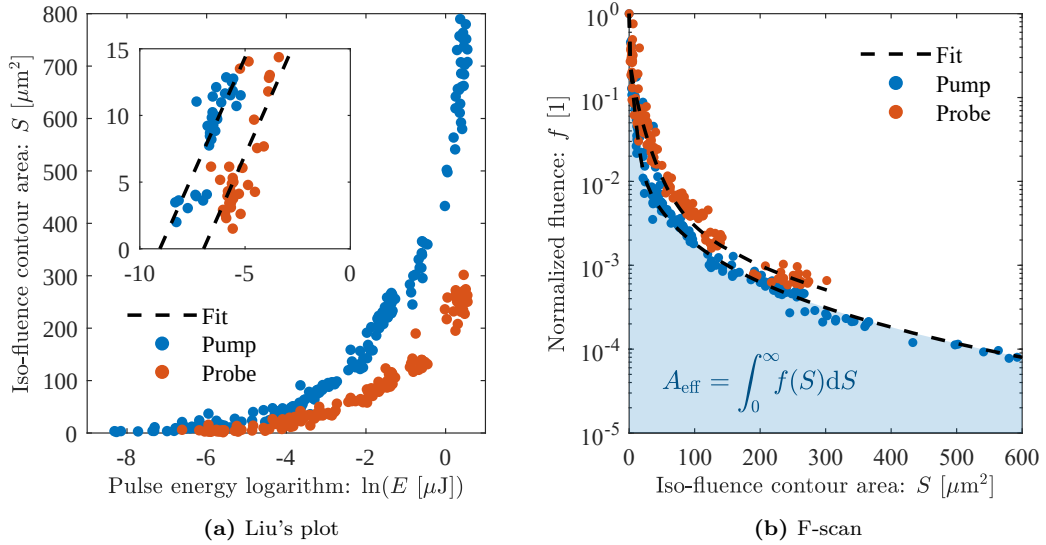
**(a)** Liu's plot

**(b)** F-scan

**Figure 6.2:** An example of Liu's plots (a) and corresponding normalized f-scans (b). Data sets were obtained during the pump–probe free-free opacity experiment (Chapter 7.1). As can be seen from (a), the threshold energy was lower for the pump than for probe. This effect results from a split ratio where more energy of the incoming pulse was directed into the pump than into the probe. The energy corresponds to the value relevant for the non-splitted pulse. Furthermore, splitting of the FEL pulse in the split-and-delay unit is done by cutting the beam into two beams of unequal sizes determining the energy split ratio. The more energetic pump beam was thus larger which resulted in a better focusing (lower effective area) than for the probe beam. Each of the f-scan curves in (b) was fitted by a sum of two stretched exponential functions.

## 6.3 Nonlinear response function recovery

The main problem with use of desorbed imprints for beam profile recovery resides in hardening of the PMMA with increasing accumulated dose, i.e. in nonlinear response function. The hardening process results from formation of C=C double bonds, also termed as cross-linking, networking together individual PMMA chains which are then more radiation-resistant [279–282]. An increase of the radiation hardness thus decreases the single-pulse etch rate, which consequently modifies the linear dependence between the imprint and dose (fluence) profiles, and a different approach to beam profile recovery must be used. In order to retrieve accumulated dose profile $\varepsilon(x,y)$ and hence the beam profile $f(x,y)$ from a desorption imprint $d(x,y)$, we need to know a calibration curve $\varepsilon(d)$, an inverse of the response function $d(\varepsilon)$, relating the depth profile and accumulated dose profile as $\varepsilon(x,y) = \varepsilon(d(x,y))$.

Basic approach takes into account the fact that deepest point of the crater $\max\{d(x,y)\}$ corresponds to the global maximum of the accumulated dose profile $\max\{\varepsilon(x,y)\}$. Maximum crater depths derived from WLI measurements and corresponding total accumulated energies can be thus directly used for the calibration curve reconstruction. By measuring a large set of imprints of increasing number of accumulated pulses, i.e. total accumulated energy, very large dynamic range can be covered. Finally, the beam profile and its effective area can be deduced from calibrated depth profiles.

### 6.3.1 Algorithm description

The method described above is technically legitimate but retrieval of the calibration curve $\varepsilon(d)$ omits a large portion of imprint profile data as it uses only the deepest point. For this reason, a novel **No**nlinear **Re**sponse **F**unction Recove**ry** (NoReFry) algorithm was developed to extract the calibration curve to a much higher accuracy. The algorithm requires $N$ ($N \geq 2$) desorption imprints created at different peak accumulated doses, i.e. different numbers of accumulated pulses or pulses of various energies. The algorithm solves equation $d(x, y) = d(\varepsilon_0 f(x, y))$ to retrieve both the (inverse) response function as well as the fluence profile $f(x, y)$. Description of the algorithm is provided in Appendix A.1, here we focus to the experimental results.

### 6.3.2 Experiment

Experimental data were obtained at the FLASH facility for three different operation modes, namely, single-pulse operation, 10-Hz low-repetition rate and 1-MHz high-repetition rate operation.[3] The beam (13.5 nm, $\sim$100 fs) was characterized 133 mm downstream from the focus, attained by a carbon-coated elliptical grazing incidence mirror [283] with a focal length of 200 cm. Maximum fluence of the non-attenuated pulse was 110 mJ/cm$^2$ which sufficiently exceeds measured ablation threshold of PMMA ( 25 mJ/cm$^2$). Recording of ablation imprints at this out-of-focus position was therefore feasible. Figure 6.3 shows Nomarski photographs of imprints obtained in the three operation modes.

Ablation imprints shown in Figs. 6.3 (a)–(c) were done at various attenuation levels where the beam was attenuated by the gas attenuator ($T = 80\%$) and
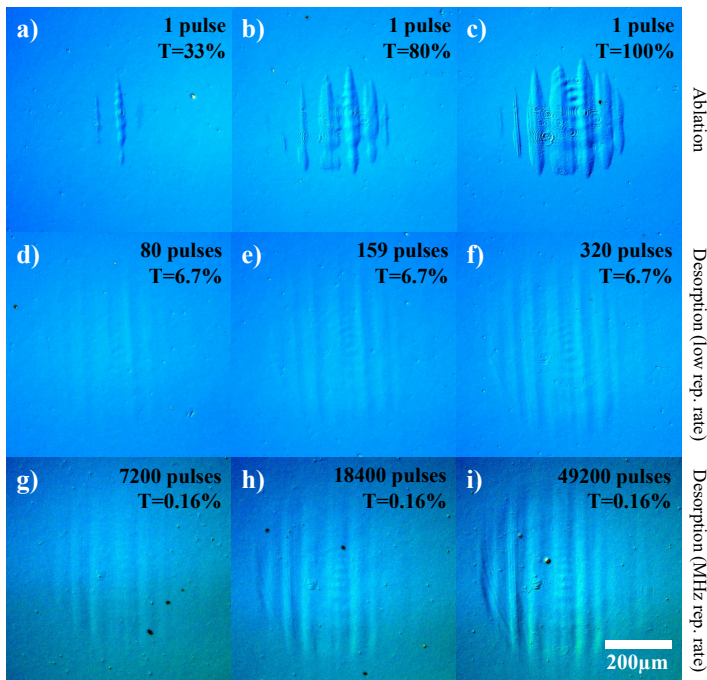


**Figure 6.3:** Nomarski images of ablation imprints at different attenuation levels (a)–(c) and desorption imprints at low (d)–(f) and high (g)–(i) repetition rates at one attenuation level but for different number of accumulated pulses. Figure from [61].

---

[3]The 1-MHz high-repetition rate was in correspondence with the beam structure as described earlier in Figure 4.4. The effective rep. rate was 4 kHz but each of 10 trains a second consisted of 400 pulses separated by 1 $\mu$s.

with both the gas attenuator ($T = 80\%$) and 203-nm zirconium filter ($T = 41\%$) resulting in $T = 33\%$. Beamline optics induced formation of fine structures such as rings and fringes. Their shapes and positions are thus constant throughout the shots. Vertical fringes originate at imperfections of the grazing incidence focusing mirror.

Desorption imprints at low repetition rate (10 Hz) shown in Figs. 6.3 (d)–(f) were done with the beam attenuated to $T = 6.7\%$ by two 296.1 nm zirconium foils which also effectively blocked higher harmonics being, to some extent, naturally present in the FEL beam. Instead of changing the beam attenuation, various numbers of shots were accumulated in each spot.

In order to compare the response of PMMA at low and high rep. rate, imprints shown in Figs. 6.3 (g)–(i) were done with an open shutter, i.e. at 1 MHz. In order to be sure that heat accumulation will not induce ablation, the beam was attenuated to $T = 0.16\%$ by a gas attenuator ($T = 2.64\%$) and two niobium foils with thicknesses of 197 nm and 384 nm ($T = 6.0\%$). Fine structures observable in desorption imprints (Figs. 6.3 (d)–(i)) ensure that the beam stability, important for the characterization with multishot imprints, was at a very good level.

Comparison of ablation and desorption imprints in Fig. 6.3 clearly shows the threshold nature of the ablation process. This induces that low-intensity wings remain hidden and cannot be observed neither with a full-power power beam.

### 6.3.3  Results

The NoReFry algorithm was applied to WLI data of the three datasets, i.e. ablation (34 imprints), 10-Hz desorption (5 imprints) and 1-MHz desorption (8 imprints). Figure 6.4 shows the corresponding response functions recovered by the NoReFry algorithm (small dots) as well as data obtained from maximum depths as described above (circles). As can be seen, the ablation data show a clear threshold behaviour. Resulting ablation threshold dose 1.28 kJ/cm$^3$ corresponds to ablation threshold of 24.6 mJ/cm$^2$. This is in a good agreement with in-focus measurements (30 mJ/cm$^2$ [267]). Similarity of desorption datasets obtained at different repetition rates means that effects connected with MHz rep. rate, such as local overheating, do not play a significant role at moderate intensities. Furthermore, we can state that material removal depends almost solely on the accumulated dose in a broad range of pulse intensities.

The calibration curves of desorption data in Fig. 6.4 were fitted by a model function (black dashed line) described in Appendix A.2, Eq. (A.4). Model response function for nonthermal single-pulse ablation imprints immediately follows from Eq. (6.1) as:

$$d(\varepsilon) = l_{\mathrm{at}} \ln\left(\frac{\varepsilon}{\varepsilon_{\mathrm{th}}}\right), \tag{6.2}$$

where the dose and threshold dose is related to the local fluence and threshold fluence as $\varepsilon = F/l_{\mathrm{at}}$ and $\varepsilon_{\mathrm{th}} = F_{\mathrm{th}}/l_{\mathrm{at}}$, respectively. Description of the data by analytical function is important for beam fluence profile $F(x,y)$ reconstruction and estimation of attenuation length $l_{\mathrm{at}}$.

Fluence scan curves retrieved by the NoReFry algorithm from the experimental data and contour areas of ablation imprints from Nomarski photographs are displayed in Figure 6.5. Areas below the curves stand for the effective areas of the
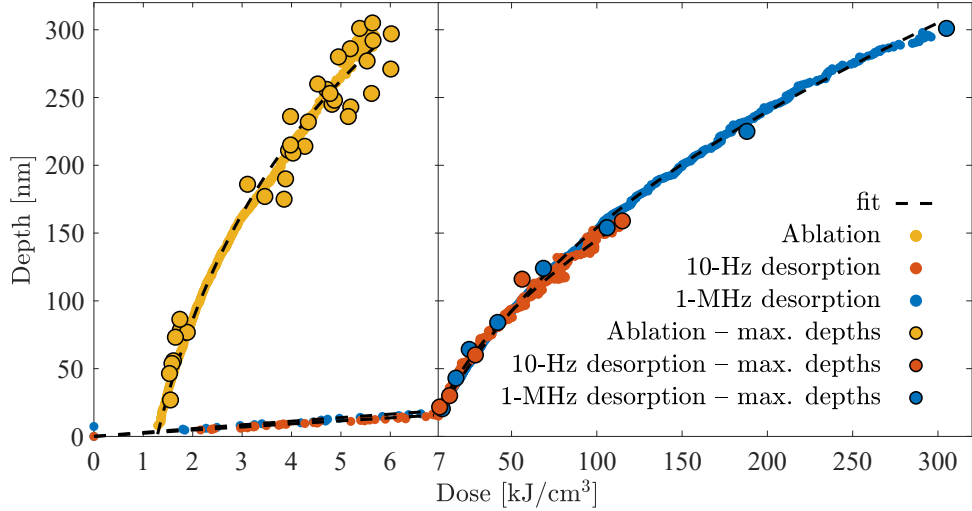
**Figure 6.4:** Response functions recovered by the NoReFry algorithm for PMMA ablation and 10-Hz and 1-MHz desorption. Large solid circles indicate maximum depths of imprints used in the recovery process and dashed black lines represent model function fits. Please notice a different scale of the $x$-axis which is stretched in an interval (0–7) kJ/cm$^2$ for better readability of the ablation data. Threshold behaviour of the ablation process is clearly visible in the stretched left part of the figure.

beam. These and their error bars were determined by a numerical integration of the fluence scan curves with the aid of the Monte Carlo method[4] and resulting values are shown in Table 6.1.

Finally, Figure 6.6 shows representative imprints, as measured by means of WLI, and normalized beam fluence profiles recovered with use of the response functions. Although the profiles in the first and the second row look very similar at the first glance, it can be seen that retrieved beam profiles are more spiky. Calculated areas from recovered beam profiles are shown in Table 6.1. These areas are in a great agreement with those calculated from recovered f-scans. This validates correctness of our method. Moreover, while the first two rows are in a good agreement, the last row indicates that the calibration to nonlinear phenomena is absolutely necessary in beam profile characterization and that the assumption of linear response can no longer be considered valid.

Effective areas shown in each row of the table are quite different despite very similar shapes of the fluence scan curves (Fig. 6.5). The smallest effective area was obtained from the ablative imprints. This clearly results from a small dynamic range of the ablation imprints which is limited by the threshold value and the finite laser power. Numerical integral below the curve thus represents only a fraction of the real effective area. Fitting by appropriate beam profile is necessary (as shown in Fig. 6.2b) for a proper evaluation which otherwise leads to underestimation of this value as reported, for example, in [259]. Relatively high effective area determined by the 1-MHz desorption is attributed to non-uniformities of niobium attenuation foils which blurred vertical speckle fringes (compare Figs. 6.6 (e) and (f)) and consequently increased the effective area. Distortion of the beam

---

[4]Averaged f-scans were randomly varied within a confidence band (see an inset in Fig. 6.5) normally distributed around their curves where the 1-sigma width was in every point determined by a standard deviation of the average. In total 20000 realizations were generated for each f-scan curve.
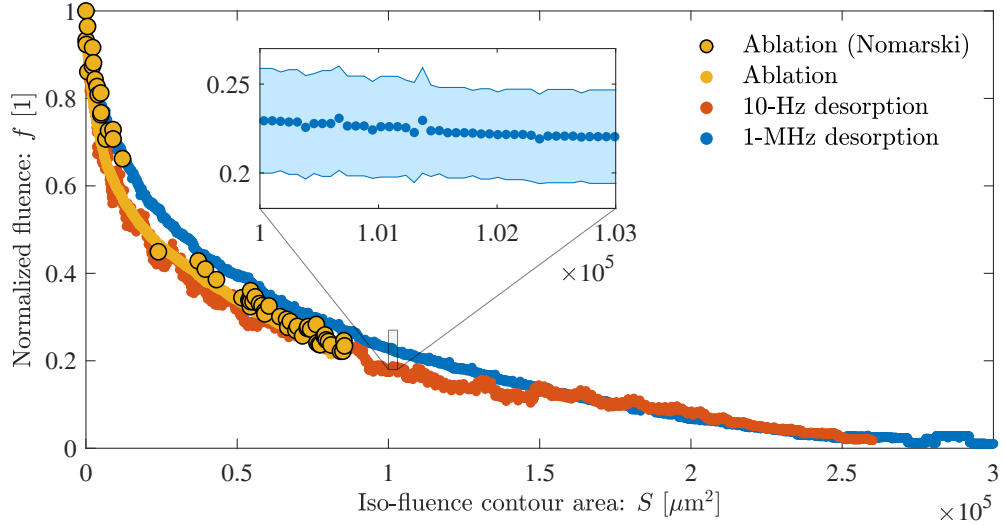
**Figure 6.5:** Fluence scan curves recovered by the NoReFry algorithm for PMMA ablation and 10-Hz and 1-MHz desorption. Orange solid circles depict the Nomarski measurement of ablation contour areas. The inset shows a detail of one of the confidence bands which were not plotted for a better readability.
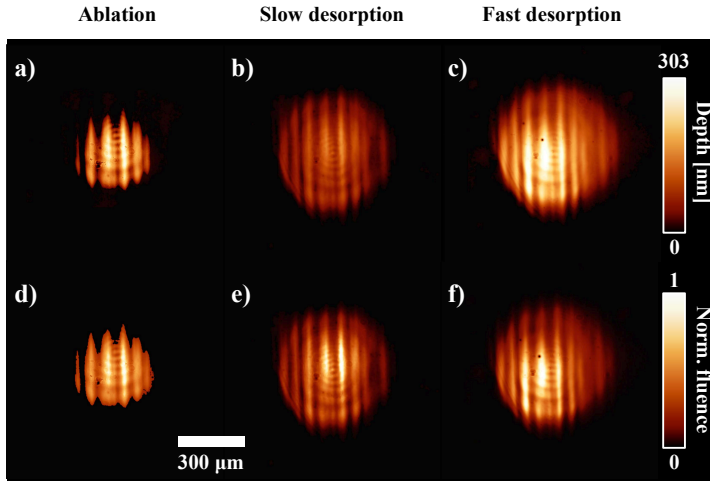


**Figure 6.6:** WLI depth profiles of a representative ablation imprint (a), 10-Hz desorption imprint (b) and 1-MHz desorption imprint (c). Corresponding beam profiles (d)–(f) were recovered using the fits of calibration curves retrieved by the NoReFry algorithm. All images are in the same scale. Colour scales indicate the maximum depth (from 0 nm to 303 nm) and normalized intensity (from 0 to 1).

by niobium and zirconium foils was also confirmed with the use of an X-ray CCD camera located in safe distance downstream the focus. Negligible distortion was observed in case when only aluminium foils were used.

## 6.3.4 Conclusions

Novel NoReFry algorithm was developed in order to reconstruct the nonlinear response function of material removal to total accumulated dose. It was applied to experimental data containing ablation imprints and desorption imprints obtained at low (10 Hz) and high (1 MHz) repetition rate. Great reproducibility of the reconstructed response functions measured under considerably different beam conditions promises that PMMA could be employed as an absolutely calibrated dosimeter.

It should be also noted that except of desorption imprints the NoReFry algorithm is applicable also in other situations where the response function monotonically but nonlinearly increases with the accumulated or single-pulse dose. This

|                      | Ablation    | 10-Hz des.  | 1-MHz des.  |
|----------------------|-------------|-------------|-------------|
| Recovered f-scan     | 33900±2600  | 52500±5300  | 62100±6200  |
| Recovered profiles   | 34700       | 49500       | 64600       |
| Without calibration  | 33400       | 75100       | 97100       |

applies, for example, to LiF crystals used as fluorescence-based detectors [264] or saturating Ce:YAG screen producing luminescence [197]. The algorithm can be also applied to a set of ablation imprints induced by single pulses at different energies.

## 6.4 Closure

In this chapter we have described various methods used for characterization of focused short-wavelength laser beams. A comparison of experimental data with theoretical models clarifies a great importance of detailed knowledge of the beam profile. A natural question is which fluence profile is the most ideal for experiments? Figure 6.7 compares three beams with obviously different profiles but identical effective areas.

Let us consider a simple transmission experiment where the intensity dependent transmission is measured just as a single number. Various parts of a typical Gaussian beam, as pictured in Fig. 6.7a, probe the examined target at absolutely different conditions. While the high-intensity beam centre enters a strong nonlinear regime, its low-intensity wings containing still quite a lot of overall energy remain in the linear part. By integration of the transmission into a single number, i.e. by measuring the transmitted pulse energy, we loose all information about the beam fluence profile and the resultant number is an average of both the linear as well as the nonlinear part of the interaction. Therefore, the top-hat beam, as pictured in Fig. 6.7c, would be absolutely ideal for experimental work and data analysis. Unfortunately, beam profiles delivered by FELs are definitely not flat



(a) Gaussian  (b) Non-Gaussian  (c) Top-hat
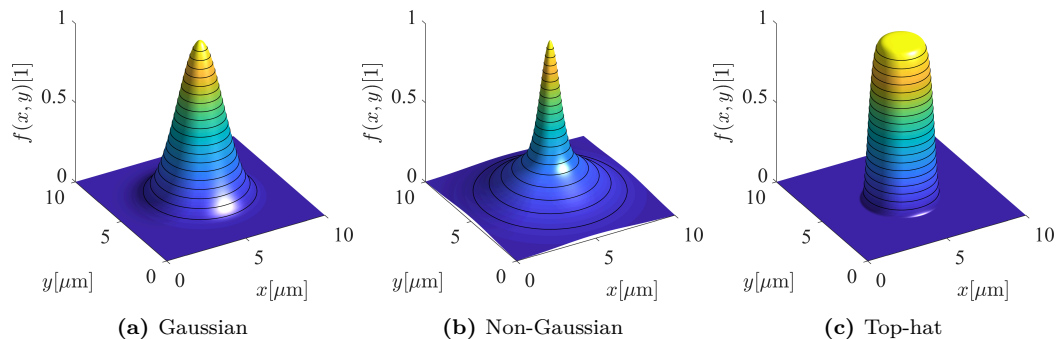
**Figure 6.7:** Various beam profiles of identical effective area. Instead of a typical Gaussian beam (a) a simple non-Gaussian (b), i.e. an incoherent sum of two Gaussians, is usually observed. An ideal top-hat beam (c) described as a super-Gaussian is mostly unavailable at FEL facilities.

and rather than top-hat their shape is usually more or less spiky non-Gaussian as shown in Fig. 6.7b. One possible way how to deal with the averaged transmission, which at the first glance irrecoverably smears all valuable information, is described in the following experiment focused on the aluminium free-free opacity measurements.

# 7. Experiments

This chapter is focused on analysis of experimental data obtained during several campaigns. The first section describes free-free opacity measurements conducted at the FLASH facility. This experiment contains irradiation of thin aluminium foils by intense ultrashort 40-eV pulses. An advanced method is used for reconstruction of the absorption coefficient dependent on electron temperature $\kappa(T_e)$. Pump–probe data further provides temporally-resolved measurements confirming that electronic response occurs on time scale shorter than $\approx 100$ fs pulse duration. The second experiment describes detachment of epitaxial graphene from SiC substrate by XUV laser radiation provided by the PALS facility. Crucial data from created imprints were obtained by micro-Raman spectroscopy and local modifications in the graphene layer are observed via changes in Raman spectra corresponding to given vibration modes. Reduction of a substrate influence on the graphene layer is important for charge carrier mobility and possible application in micro-electronics. The third experiment monitors thermal diffusion of tellurium inclusions through cadmium telluride lattice. Analysis of imprints created mainly at PALS and CDL is done with use of micro-Raman spectroscopy and photoluminescence. These three experiments realized at three different materials nicely cover time scale ranging from femtosecond electronic processes up to microseconds typical for heat conduction.

## 7.1 Free-free opacity

Importance of studying aluminium free-free opacity (FFO), i.e. absorption of photons with energy between the plasma frequency and the L-edge, has been discussed in previous chapters. It is one of the main heating mechanisms in laser-driven plasmas which are important for further research. As the inverse bremsstrahlung is a 3-body process based on collisions of free-electrons with other particles, we may expect strong variations of the opacity with increasing electron temperature tightly related to the collisional rates. Conditions in strongly coupled plasma moreover invalidate a classical description of collisions based on the Coulomb logarithm as defined in Eq. (2.5) and experimental data is hence very interesting for theoreticians and development of new and more precise models. For this purpose, an experiment focused on time-resolved measurements of XUV transmission through thin aluminium foils was designed. The results are presented here and also in [60].

### 7.1.1 Current state of knowledge

Aluminium is chosen as a prototypical low-Z metal suitable for theoretical modelling with relatively free valence electrons and with extensive research history focused to FFO over the past two decades [78, 91, 107, 115, 130, 284–293]. Besides that, aluminium foils are routinely used as attenuation filters and their transmission over a wide range of photon energies is thus indeed desirable. Nevertheless, despite the best efforts performed by theoreticians and experimentalists, values of the absorption coefficient in cold aluminium ($\kappa_{\text{cold}}$) are still not consis-
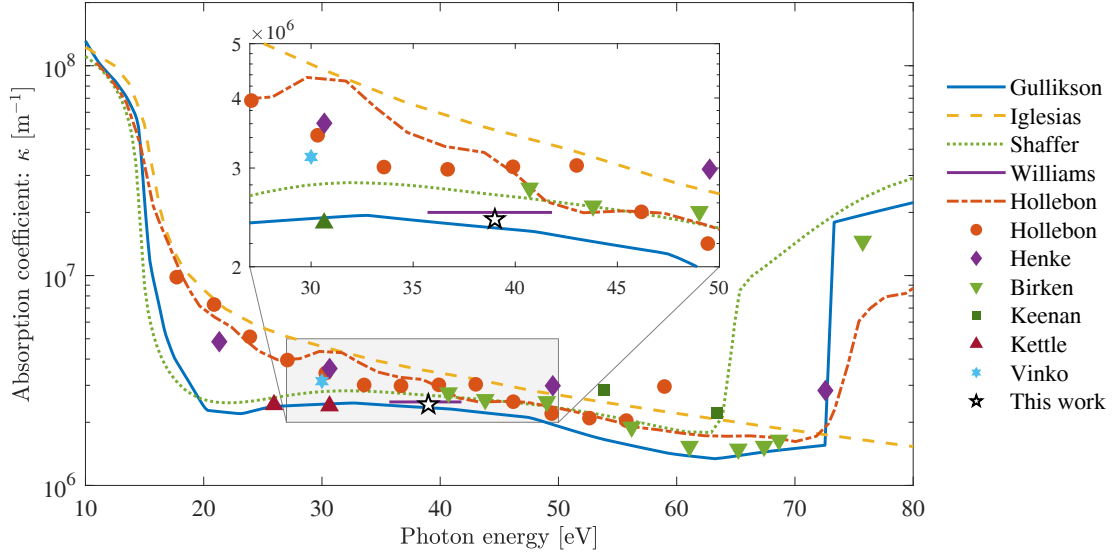
**Figure 7.1:** Theoretical calculations and experimental measurements of the absorption co-efficient of cold aluminium across the region between the plasma frequency and the L-edge. Data are from E.M. Gullikson *et al.* [284], C.A. Iglesias *et al.* [287], N.R. Shaffer *et al.* [291], G.O. Williams *et al.* [293], P. Hollebon *et al.* [78], B.L. Henke *et al.* [107], H.G. Birken *et al.* [294], R. Keenan *et al.* [285], B. Kettle *et al.* [289] and S.M. Vinko *et al.* [286]. Errorbars are excluded for clarity. The rectangle indicates limits of the inset.

tent as shown in Figure 7.1. Latest measurements of $\kappa_{\text{cold}}$ supported by density functional theory (DFT) calculations published by P. Hollebon *et al.* [78] agree with [107, 294] but disagree with [284, 289]. On the contrary, the value obtained from experiment described below agrees with the last two works.

Even more striking discrepancies appear in the evolution of the absorption coefficient with increasing electron temperature, $\kappa = \kappa(T_e)$. The opacity is first expected to increase as the temperature reaches the Fermi energy [78, 286, 287, 291] and then to fall because the collisional rate is, according to the inverse bremsstrahlung theory, proportional to $T_e^{-2/3}$ [295]. The first measurements were done by B. Rus *et al.* [296] who measured time-resolved transmission of 200-ps single pulses. Nevertheless, no change of the transmission with increasing incident intensity and induced temperature reaching up to 20 eV was observed there neither in a later experiment where B. Kettle *et al.* [289] reached electron temperatures of $\approx 1$ eV. A measurable decrease of the transmission followed by its steep increase with fluence observed by A. Di Cicco *et al.* [130] was attributed to combination of electron heating and some kind of saturable absorption without specified mechanism [292]. Significant decrease of the transmission, but still much lower than predicted by theoretical works, related to heating of ions about 1 ps after the pulse arrival was measured by G.O. Williams *et al.* [293]. The same time delay before the change in the material response was reported also by F. Bisio *et al.* [290] where time-resolved reflectivity of the Al heated by XUV pulse was measured. This delay in change is, according to [133], caused by a long-living low-density population of high-energy electrons. The fact that results of the mentioned experiments show apparently distinct behaviour underlines the real difficulty of these measurements.

In this chapter we describe time-resolved experiment based on transmission measurements. We use a novel approach to retrieve $\kappa(T_e)$ using forward mod-

elling which confirms that opacity calculation directly from transmission values is systematically incorrect and it significantly underestimates real values of the absorption coefficient.

## 7.1.2 Experiment

The experiment was conducted on the FLASH facility which delivered ultrashort 100–150 fs pulses important for isochoric heating at 32 nm (39 eV) and energy around 60 $\mu$J. Schematic diagram of the experiment is shown in Figure 7.2. The XUV pulse was split into two parallel beams (pump and probe) in the autocorrelator unit. Detailed description of this device, explaining also the possibility of setting negative time delays, is given in [297]. The two pulses can be time-delayed with respect to each other up to several picoseconds. Focusing of the two parallel beams was done by a multilayer-coated off-axis parabolic mirror (OAP) with reflectivity of 31% at the given wavelength. Thin aluminium target foils of two different thicknesses (200 nm and 300 nm) were placed into the focus and heated by an advanced pump pulse creating dense aluminium plasma being subsequently probed by a delayed probe pulse. After every shot, damaged sample had to be moved to a fresh spot. The focal spot and the beam overlap was monitored by an online *in situ* microscope which had a hole drilled in the centre of its objective to allow the XUV beam to pass through. Energy of non-splitted pulses was measured upstream by a gas monitor detector (GMD) and correlated with the transmitted signal detected by an X-ray CCD camera.
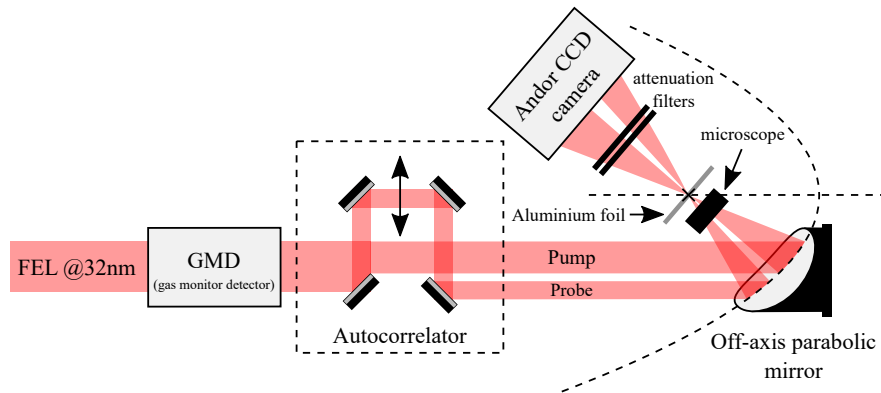


**Figure 7.2:** Schematic of experimental setup: The XUV beam passes through the GMD which measures the total pulse energy. Then it is spatially split and temporally delayed in the autocorrelator. The two parallel beams are focused with the OAP onto the aluminium target. The transmitted signal is measured by the CCD camera. Mesh-supported attenuation filters can be optionally placed in front of the CCD to prevent saturation of pixels.

Calibration of the CCD signal was done in the absence of target foils. Dynamic range of the CCD was sufficient to detect pulses at all energies with one single-set of attenuation foils. Alignment of the OAP and micro-focus characterization was done with use of ablative imprints in PMMA. A great attention was paid to a precise overlap of the pump and the probe beam which was extremely important for valid transmission measurements. An image from Nomarski microscope showing imprints of the beam along its propagation axis (*z*-scan) is presented in Fig. 7.3a. Sizes of the focal spots in terms of the effective area were

**(a)** Z-scan
          **(b)** CCD signal
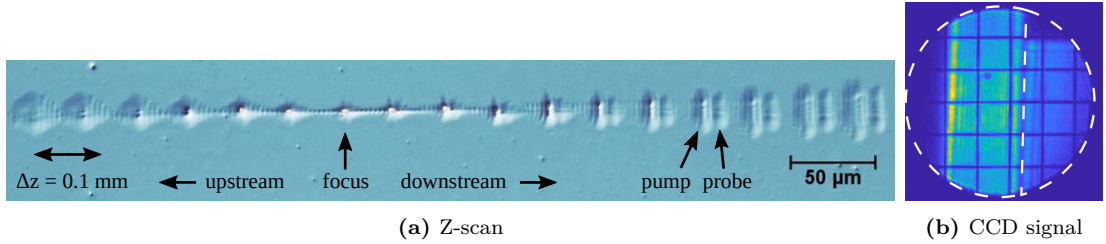
**Figure 7.3:** (a) An image from Nomarski microscope depicting PMMA ablative imprints of XUV FEL pulses taken during a scan along the beam propagation axis. Spatially separated pump (left) and probe (right) beams can be easily distinguished on the right-hand-side of the scan and in (b) which shows detected signal on CCD.

evaluated as $(4.0 \pm 0.5)$ $\mu m^2$ and $(5.4 \pm 0.7)$ $\mu m^2$ for the pump and the probe beam, respectively.

While the relative transmission of the target can be easily calculated from the calibrated CCD signal, the transmission of the beamline including all cropping apertures and mirror reflectivities placed between the GMD and the target must be known for calculation of absolute pulse energy on target. The beamline transmission of $(4.6 \pm 0.2)\%$ and $(1.8 \pm 0.2)\%$ for the pump and probe beam was estimated employing the Fresnel propagation as described in Appendix A.3.

Measured CCD signal as shown in Fig. 7.3b was corrected by a scattering factor which was between 5–25%. Scattering observed as a significant increase of a background signal was induced by intensity-dependent real part of the refractive index $n(I(x, y))$. Heated sample then behaves like a concave lens which diffracts light out of the detected area and the transmission hence appears lower.

An exposure of used aluminium foils to atmospheric oxygen caused a contamination of their surfaces with a few-nanometre thick passivated $Al_2O_3$ layer (see Fig. 7.4) with an absorption coefficient by an order of magnitude higher than that of aluminium [298]. This contamination induces a substantial complication for opacity measurements and absorption of the oxide layers must be subtracted in order to get the pure aluminium opacity. A linear fit of an equation for transmission which follows from the Beer-Lambert law $\ln(T) = -\kappa d - \alpha$, where $\kappa$ is the absorption coefficient of aluminium, $d$ thickness of the foil and $\alpha$ the absorption of the oxide layers, resulted in $Al_2O_3$ thicknesses $(5.7 \pm 0.3)$ nm on each side, which is in agreement with previous experiments [296, 299]. In total, 350 shots at two different thicknesses (200 nm and 300 nm) served as an input for the fitting procedure. The absorption coefficient of the $Al_2O_3$ was taken from the CXRO database [107]. We assumed that the oxide layer thickness did not vary across the targets and was identical for all samples.
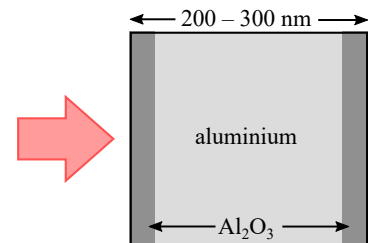


**Figure 7.4:** Schematic of the Al foil covered with $Al_2O_3$ layers.

### 7.1.3 Results

**Single-shot transmission**

The simplest experiment contains measurements of a single-shot transmission as a function of the pulse energy. Measured data are shown in Figure 7.5. The tiny dots, representing each of the 5000 used pulses, were merged into several groups marked with large circles for clarity. The error bars stand for standard deviations. Despite a very short duration of the pulse, it is evident that the front of the high-intensity pulse transfers enough energy to conduction band electrons so the tail already probes a heated material of increased opacity.

Calculation of real values of the absorption coefficient directly from measured target transmission is not completely pointless, nevertheless, because of averaging of the absorbed energy in both transverse and longitudinal direction, the calculated values could be misleading. A slightly better is the calculation of a cold absorption coefficient $\kappa_{\text{cold}}$ from measurements done on foils of different thicknesses, in our case 200 nm and 300 nm. The contribution of the 100-nm difference in thickness ($d_{100}$) can be attributed solely to the pure aluminium since the oxide layers are assumed to be identical for both samples. Moreover, the additional 100-nm layer can be considered cold since nonlinear phenomena occur in the front part of the sample. The cold transmission of this 100-nm Al layer can be obtained by dividing the 200-nm ($T_{200}$) and 300-nm ($T_{300}$) foil transmissions: $\ln\left(\frac{T_{200}}{T_{300}}\right) = \kappa_{\text{cold}} d_{100}$. The values of $\kappa_{\text{cold}}$ shown in the inset of Fig. 7.5 were calculated for the groups of equal pulse energy. Comparison with a DFT-calculated value is also provided in the inset. Because the heating of the rear 100 nm by energetic pulses cannot be entirely excluded, we calculated averaged value only from shots where $E_{\text{TRG}} < 1.5$ $\mu$J which gave $\kappa_{\text{cold}} = (2.43 \pm 0.15) \times 10^6$ m$^{-1}$ regardless the oxide layer thickness and incident pulse energy. This number agrees very well with E.M. Gullikson measurements ($2.35 \times 10^6$ m$^{-1}$) [284] but is smaller then the value obtained from the DFT calculations ($2.8 \times 10^6$ m$^{-1}$) [78].



**Figure 7.5:** Target transmission measured with a calibrated CCD. A systematic decrease for both thicknesses is observed. Tiny dots represent all over 5000 single-shots which are grouped into several larger points. Inset shows the calculated cold opacity $\kappa_{\text{cold}}$.

**Retrieval of the functional form of the absorption coefficient**
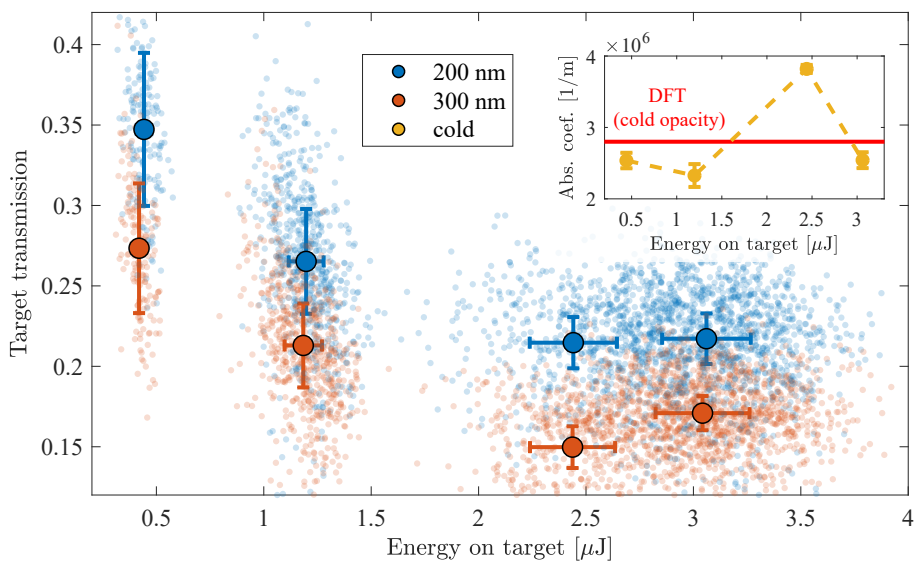
Problem with actual measurements of the absorption coefficient as a function of the electron temperature $\kappa(T_e)$, i.e. absorbed energy density, resides in difficulty of achieving homogeneously heated plasma which could be probed by truly low-energy probe. Despite relatively long absorption length of the XUV radiation, the front side of the foil is heated more than its back side [288]. This fact allows us to retrieve "cold opacity" but makes measurements of the $\kappa(T_e)$ harder. Moreover, the beam profile shown in Fig. 6.2b, is far from the top-hat beam ideal for uniform heating. Both longitudinal decrease of the energy density and the spiky beam profile contribute to generation of steep and non-homogeneous temperature gradients which cause that only an averaged value of the absorption coefficient can be measured.

Transverse temperature profile is related to the beam shape which can be measured by ablative imprints. In the cold state absorption in the longitudinal direction follows the Beer-Lambert law and spatial distribution of the absorbed energy can be thus easily modelled. Figure 7.6 shows energy density calculated by this simplified model where absorption coefficient was constant ($\kappa = 2.4 \text{ m}^{-1}$) with temperature. The spatial $xy$-profile of the beam was derived from the measured f-scan of the pump and incident energy was 1 $\mu$J. Several isosurfaces represent volumes inside which a given fraction of the pulse energy was absorbed. Energy density measured in the experiment is typically calculated as averaged value inside the effective volume $V_{\text{eff}} = A_{\text{eff}}d$. Ratio of absorbed energy inside this volume, represented by a wired cylinder in the figure 7.6, is, in this particular case, less than 50% of the overall energy loss and mean energy density is over two times less than the maximal value.
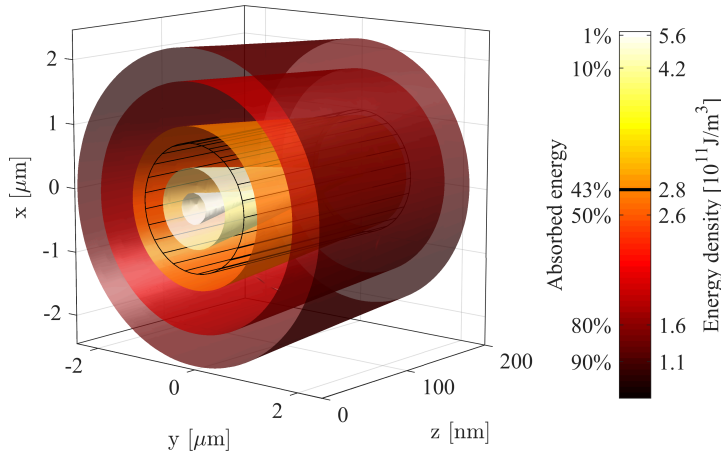


**Figure 7.6:** Spatial distribution of absorbed energy of a non-Gaussian beam in the cold Al foil. Each isosurface indicates boundary of a volume inside which a given fraction of the 1-$\mu$J-pulse energy is absorbed. A wired cylinder represents the effective volume defined as $V_{\text{eff}} = A_{\text{eff}}d$.

Described forward model, where simulated data can be compared to experimental measurements, can be used for calculation of the absorption coefficient as a function of the free-electron temperature $T_e$. If we involve also the change of the electron density $n_e$, the $\kappa(\cdot)$ could be retrieved as a complex function $\kappa(T_e, n_e)$. This would be important for temperatures above $\approx 10$ eV when ionization of $2p$ and $2s$ states occurs and the electron density becomes a function of the temperature $n_e(T_e)$. The relationship between the absorbed energy density and the electron temperature follows from a conventional quantum-mechanical model which is described in Appendix A.4.

Each of experimentally measured single-shot transmissions contains encoded information about range of different plasma conditions. Retrieval of the functional form of $\kappa(\bullet)$ from one single data-point is thus not possible. Nevertheless, a large set of pulses at different energies and their transmissions provides enough constraints on the shape of $\kappa(T_e, n_e)$. The flowchart of the recovery algorithm is schematically drawn in Figure 7.7. Pulse propagation and calculation of its transmission is described by the forward model: Time-sampled pulse of given energy and measured fluence profile is propagated through the foil which is discretized into many small bins. Absorbed energy in each of the bin is calculated and absorption coefficient is changed according to suggested shape of $\kappa(T_e, n_e)$. Modelled transmissions of all single-pulses[1] are then compared with experimentally measured values and new shape of $\kappa(T_e, n_e)$ is suggested until these two sets of data match up to a desired precision. It is worth noting that temperature- and density-dependent form of the absorption coefficient can be retrieved without actual measurements of the plasma temperature.



**Figure 7.7:** Schematic diagram of $\kappa(T_e, n_e)$ retrieval algorithm using the forward model and experimentally measured energies on target with corresponding transmissions. Adapted from [60].

The optimization algorithm for finding the best form of the $\kappa(T_e, n_e)$ involves sampling the absorption function at every 2 eV up to 50 eV. Around 8000 iterations were done to ensure convergence. As can be seen from Fig. 7.5, uncertainties of target transmissions at given energies are quite large and impact of these variances on the final form of the $\kappa$ was thus tested. This was done with use of Bayesian inference described in detail in [60].

Reconstructed shape of the absorption coefficient as a function of the electron temperature is compared in Figure 7.8 with faulty values obtained from averaging of plasma properties over the effective volume $V_{\mathrm{eff}}$. First of all, temperatures calculated directly from the absorbed energy overestimate real values as quite a lot of energy is absorbed outside the $V_{\mathrm{eff}}$ as shown in Fig. 7.6. Second, volume-averaged opacity is much smaller as it involves cold regions at the end of the sample as well as regions irradiated by lower fluences. This fact also partially explains why authors in previous works observed none [289, 296] or only a slight increase [130, 292, 293] of the opacity with the plasma temperature. Figure also shows theoretical predictions calculated by P. Hollebon *et al.* [78]. Disagreement between experiment and the DFT is not explained yet.

**Time-resolved opacity**

Knowledge of the absorption behaviour as a function of absorbed energy now enables a correct interpretation of the pump–probe measurements as shown in Figure 7.9. The 0.5–1.5 $\mu$J probe pulse was delayed with respect to the 2–4 $\mu$J

---

[1]To speed up the algorithm, a curve of the target transmission dependent on the $E_{\mathrm{TRG}}$ obtained from data shown in Fig. 7.5 was used in [60].
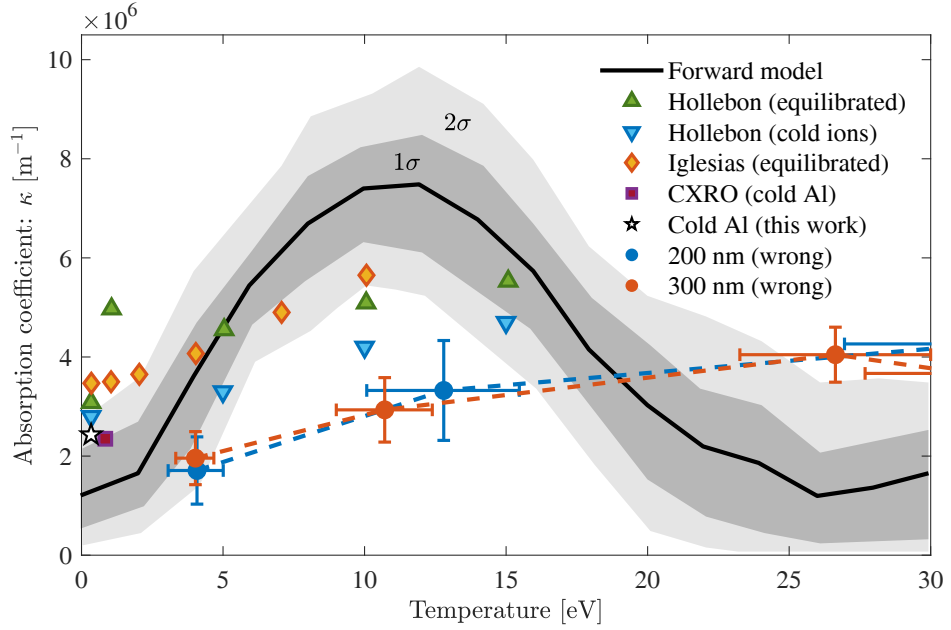
**Figure 7.8:** Temperature dependence of the absorption coefficient retrieved from the forward model. Also plotted is the cold opacity value calculated from the target transmission (Fig. 7.5), DFT predictions calculated by P. Hollebon *et al.* [78] for heated electrons (cold ions) and equilibrated system, results from inverse bremsstrahlung model presented by C. A. Iglesias [287], cold opacity from the CXRO database [107], and opacity calculated directly from absorbed energy in the 200-nm and 300-nm foils. The last two data sets are systematically wrong due to volume-averaging. This explains unexpectedly low changes of absorption reported by other authors. Adapted from [60].

pump pulse in time interval ranging from -1 ps up to 5 ps. Negative time delay means that probe (blue) came prior to the pump (red). Observation of further plasma evolution at later times is not possible with the experimental setup. As discussed before (Fig. 7.5), the self-induced increase of the opacity is present also for the low-energy $\approx$1-$\mu$J probe which, when coming first, therefore partially acts as a pump and pre-heats the sample.

A steep decrease of the probe transmission is observed around $t = 0$ when also pump arrives. It is therefore clear that heating of the system, which affects the transmission, occurs within the pulse duration, i.e. on the 10–100 fs time scale. This is also clarified with a sigmoid fit of the data within $\pm 1$ ps. As the probe transmission does not increase for longer delays, it is clear that system remains heated for several picoseconds. A similar behaviour but in a reverse direction is observed for the pump data acquired at the same time. The pump transmission decreases upon the arrival of the probe. This decrease is not so significant as in the case of probe beam because the system is already heated to significant temperatures by the pump and the probe adds only a minor amount of additional energy.

Large points in Figure 7.9 stand for transmissions calculated using the forward model applied to the presented data. Diamonds indicate single pulses and squares transmissions of the sample already heated by the preceding pump or probe. Great agreement is observed for all cases which clarifies consistency of our results.
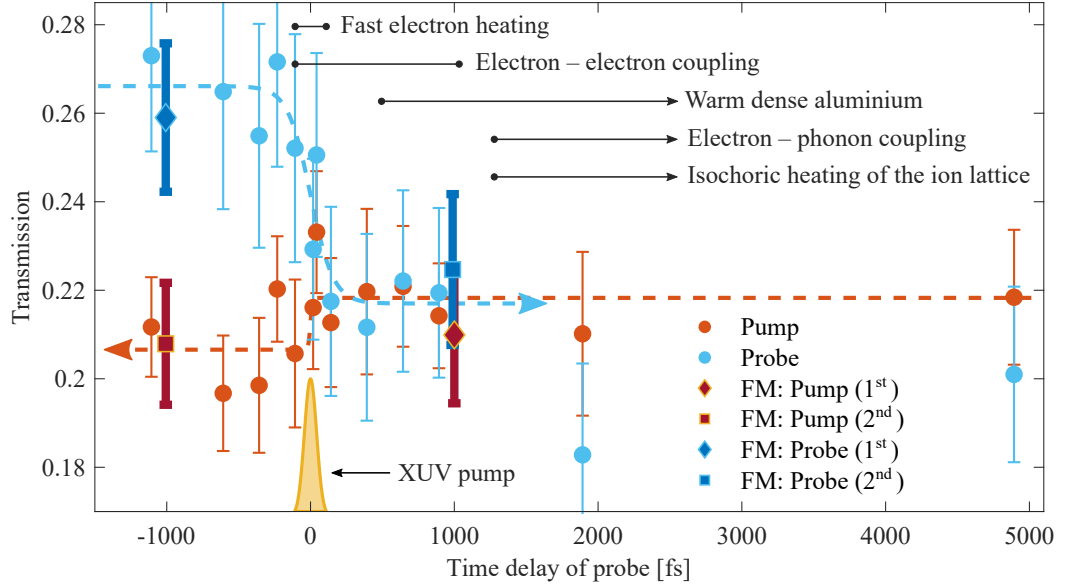
**Figure 7.9:** Time-resolved transmission through 200-nm Al foil. Experimental data fitted by a sigmoid function (dashed lines) are compared with values obtained from the forward model (FM). Data are partially taken from [60].

## 7.1.4 Conclusions

Retrieved functional form of the absorption coefficient $\kappa(T_e, n_e)$ (Fig. 7.8) shows that simple calculation of the coefficient only from space- and time-integrated relative transmission does not provide reliable results. This novel approach employing the forward model explains unexpectedly low changes of the opacity and transmission reported in previous works.

Observed increase of the absorption coefficient with temperature comes from two different kinds of processes: The first group results from increasing electron temperature which affects the collisional rate. These processes are faster than the pulse duration and occur on 10–100 fs time scale. In our experimental data, they are observed as self-induced increase of the opacity (Fig. 7.5) and as a steep drop of the probe transmission after the arrival of the pump (Fig. 7.9). The second group results from heating of ions followed by melting of the crystalline structure. This is observed as further decrease of the probe transmission for delays beyond 1 ps (Fig. 7.9). More experimental data would be nevertheless needed for conclusive evidence of this further decrease.

We have also estimated cold absorption coefficient as $\kappa_{\text{cold}} = (2.43 \pm 0.15) \times 10^6$ m$^{-1}$ which fits into the wide band of current measurements (Fig. 7.1) and agrees with $\kappa(T_e = 0)$ in Fig. 7.8 within the confidence band.

For an improvement of our results we suggest an utilization of thinner Al foils with more than two thicknesses so the estimation of absorption in the oxide layers would be more precise. Oxidation could be also suppressed by adding a thin gold coating of defined thickness onto the Al foils during the manufacturing process. Furthermore, larger CCD would be useful for detection of possible scattered signal and more precise estimation of transmission values.

## 7.2 Graphene

Recent experiments with interesting results studying interaction of short-wavelength radiation with various carbon allotropes [33, 45, 47, 135, 144, 148–151] and outstanding properties of graphene lead us to conduct further experiment. It was focused on irradiation of epitaxial graphene and *ex situ* analysis of induced damage and structure modifications. Results presented in this chapter were also published in [55].

### 7.2.1 Introduction

Graphene, a carbon allotrope, is a two-dimensional (2D) planar sheet of $sp^2$ bonded carbon atoms organized into a benzene-ring structure. It might be considered as a basic building element for all other graphitic materials such as fullerenes, nanotubes and graphite. Due to its exceptional parameters such as high thermal conductivity [300], excellent carrier mobility [301, 302] and possible scalability [303, 304] it is a promising candidate for a new generation of electronic devices, photodetectors, transistors, touch screens and others.

**Brief history**

Although the term 'graphene' was first mentioned in 1986 by Boehm *et al.*, who defined it as a name for "a single carbon layer of the graphitic structure" [305], a boom in systematic study of the graphene begun in 2004 when K. S. Novoselov and A. K. Geim *et al.* published paper where they examined graphene's astonishing electronic properties [306, 307]. They were the first authors who demonstrated the existence of free-standing 2D atomic crystals which were with respect to the curved shapes of fullerenes and nanotubes considered as unstable [301]. This structure attracted great public interest due to the presence of the electric field effect, high carrier concentration $n =$



**Figure 7.10:** Graphene is a basic building unit for other graphitic materials (adapted from [302]).

$10^{13}$ cm$^{-2}$ and very high mobility of $\mu \geq 10.000$ cm$^2$/Vs which was almost independent of absolute temperature; see [302] and references cited therein. Moreover, a year later they also found out that electron transport in graphene is governed by Dirac's relativistic equation which inspired many scientist to experimentally test quantum electrodynamics on this two-dimensional system [301]. Work of Novoselov and Geim was awarded the Nobel Prize in 2010 *"for groundbreaking experiments regarding the two-dimensional material graphene"* [308].

**Graphene vs graphite**

In this chapter we study an impact of XUV radiation on epitaxial graphene grown on a silicon carbide substrate (SiC). First of all, we take a closer look at the structure of multi-layer graphene and how does it differ from graphite. The latter material comprises of many graphene layers where atoms in each layer are

bonded covalently. Hexagonal honeycomb structure prompts that only three of the four bonding electrons mediate the covalent bond. The fourth electron is free to move in the plane making the structure electrically conductive. Layers are linked together by a weak Van der Waals (VdW) force provided by a $\pi$-orbital delocalized in the perpendicular direction to the sheet. Individual layers might be stacked in different order or even twisted one to each other [309]. Although the true graphene is by definition a single-layer material (appropriately called single-layer graphene – SLG) the term 'multi-layer graphene' (MLG) is widely used for material in which individual graphene layers have the same orientation but they are shifted in the lateral direction. One can therefore certainly think about an approach where a few atomic layers of a bulk graphite are torn off by an adhesive tape and graphene is produced in this way. However absurdly and unscientifically it may sound, this was indeed the method used by the Nobelists to amaze the world. Graphene obtained in this way is called exfoliated graphene.

## 7.2.2   Theory of epitaxial graphene on SiC

The thermal decomposition of silicon carbide (SiC) is a great technique for fabrication of epitaxial graphene (EG) which exhibits excellent electrical properties useful especially for field-effect transistors [310–312]. Samples described in this chapter were grown on a silicon face of 4H-SiC(0001) in a graphite crucible which was placed in vacuum ($10^{-5}$ mbar) and heated to $\approx 1600°C$ for 5 minutes. More details on the epitaxial growth and its dependence on a residual gas composition are described by J. Kunc et al. [313].

The first layer of EG grown on a silicon face of SiC exhibits an interesting phenomenon of strong coupling to the substrate. This layer called buffer or zero-layer graphene is semiconducting and, although it looks like graphene, its electronic structure is quite different. About 26% of delocalized $\pi$-electrons (upper limit) tend to bind with topmost silicon atoms and create strong sp$^3$ bonds [314, 315]. Another carbon layer grown on top of the buffer is now bonded with the usual VdW bonds and although two carbon layers were grown on top of the SiC the structure behaves like SLG. Nevertheless, the strong coupling to the substrate significantly reduces the carrier mobility.

This effect partially originates in scattering of charge carriers on substrate phonons and partially in crystal imperfections [316, 317]. In order to eliminate the influence of substrate phonons and increase the carrier mobility back to high level, it is essential to suppress the strong coupling between the substrate and the buffer. Reduction of sp$^3$ bonds and production of the so-called quasi-free-standing graphene can be done by two different methods: The first approach employs intercalation of hydrogen [315, 318] or oxygen [319] atoms which migrate under the buffer layer, break bonds between Si (substrate) and C (buffer) and attach to Si atoms. The other technique utilizes different thermal expansion coefficients of the graphene layer and SiC substrate [320]. If the structure undergoes a rapid-cooling process, the graphene layer partially detaches from the substrate. It is worth mentioning that detached buffer behaves like a usual graphene layer and the structure consisting of buffer and one additional graphene layer is thus transformed into two-layer graphene, also called bilayer graphene (BLG). This happens without delivery of any additional material. Described process is schematically drawn in

Figure 7.11. Multilayer epitaxial graphene (MEG) has the neighbouring layers stacked rotationally shifted. The rotational stacking makes layers electronically decoupled and they behave like individual graphene layers [312].
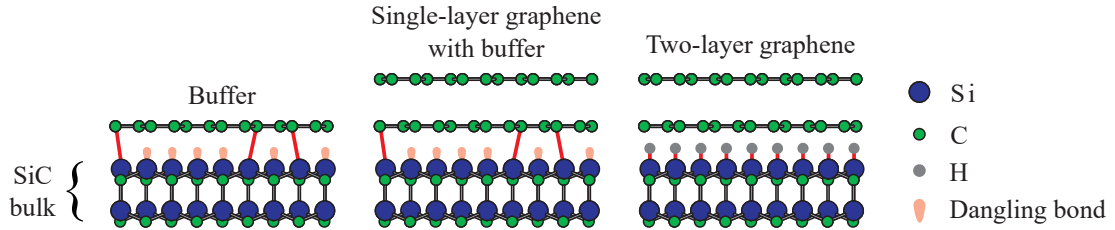


**Figure 7.11:** Structure of the epitaxial graphene grown on SiC. The first case (left) shows the buffer strongly coupled to the substrate. Second example (middle) shows a structure which behaves like a SLG although two graphene layers were actually deposited on the substrate. The third case (right) shows BLG obtained from SLG with buffer via hydrogen intercalation. Adapted form [315].

### Calculations

An impact of the 21.2 nm XUV radiation on multilayer graphene on SiC was examined using a hybrid code XTANT (X-ray-induced thermal and nonthermal transitions) [79]. The simulation assumed 4H-SiC polytype which corresponds to the substrate used in our experiment. Three threshold-limited processes occurring with increasing energy were observed: detachment of the buffer from the SiC ($0.68$ eV/atom, i.e. $0.08$ J/cm$^2$), damage of SiC ($1.3$ eV/atom, $0.16$ J/cm$^2$), and damage of graphene ($6$ eV/atom, $0.72$ J/cm$^2$). Energy required for detachment of the graphene layer including buffer was calculated as a cohesive energy of the buffer to the substrate. This energy might differ according to a particular configuration of the graphene layer on the SiC. Formation of defects on edges of SiC or graphene might be also observed at lower doses.

### Intrinsic strain

Except of the strong coupling of the buffer to the substrate, there is another effect related to the epitaxial growth which originates in a mismatch of SiC and graphene lattice constants. The lattice constant of SiC is $a_{\text{SiC},0} \approx 3.073$ Å [321] whereas the graphene lattice constant is $a_{\text{G},0} \approx 2.462$ Å [322]. This discrepancy naturally results in an intrinsic strain present in the EG grown on SiC. Although $a_{\text{SiC},0} > a_{\text{G},0}$ the strain is not tensile but compressive. The reason for this is that it is not a single graphene cell, which is tremendously stretched to fit onto the SiC lattice, but a graphene supercell consisting of 169 unit cells which is slightly compressed. A nice illustrative drawing can be found in [323]. Theoretical value of the strain $\epsilon$ can be calculated as $\epsilon_{\text{theory}} = (13a_{\text{G},0} - 6\sqrt{3}a_{\text{SiC},0})/(13a_{\text{G},0}) = 0.22\%$ [324]. To determine the real value, we employed Raman spectroscopy and the following formula [325]:

$$\epsilon = \frac{\omega_{2D} - \omega_{2D,0}}{2\omega_{2D,0}\gamma_{2D}}, \tag{7.1}$$

where $\omega_{2D}$ is the position of the 2D peak as measured on the investigated sample, $\omega_{2D,0} = 2677$ cm$^{-1}$ is the 2D peak position of completely relaxed graphene and

$\gamma_{2D} = 2.8$ is Grüneisen parameter for the 2D peak. Commonly observed blueshift of the 2D peak is induced by the compressive (or tensile) stress applied to the graphene layer [324, 326, 327]. Phonon frequencies and related peak positions, might be to a minor extent ($\sim 1$ cm$^{-1}$) also influenced by the carrier (or doping) concentration [328–330]. Raman spectrum and description of given peaks is provided in the following section.

### Raman spectrum

Raman spectroscopy is a versatile tool for studies of graphene electronic structure, its strain, number of layers as well as sizes of individual graphene flakes [331]. Here we focus on D, G and 2D peaks located at $\approx$ 1350, 1583 and 2680 cm$^{-1}$, respectively. Representative Raman spectrum is shown as a solid black line in Figure 7.12. Low-energy D peak represents breathing modes of six-atom rings and requires a defect for activation. More intense G peak is assigned to stretching of sp$^2$ bonds in individual atomic planes [332]. Origin of the 2D peak (also G' peak), the second order of the D peak, which does not require defects for activation, can be described by a double-resonance process: In the first stage, an electron–hole pair is produced by an incoming photon from the excitation. The electron inelastically scatters from two phonons of opposite directions and emits a new photon during recombination with the hole. If there are lattice defects, one of the scattering processes might be elastic and emitted photon gives rise to the D peak and not to the 2D one [333, 334].

As might be seen in Figure 7.12, the 2D peak is blue-shifted from 2680 cm$^{-1}$ to $\approx$ 2750 cm$^{-1}$ because of the compressive strain. According to the equation (7.1), the measured strain of the graphene layer is 0.46% which is two times higher than the theoretical value ($\epsilon_{\text{theory}} = 0.22\%$). This disagreement originates in different thermal expansion coefficients of graphene and SiC. The $\epsilon_{\text{theory}}$ is calculated for structures at room temperature. In our case, the graphene was grown at temperatures $\approx$ 1600°C at which the SiC substrate was significantly



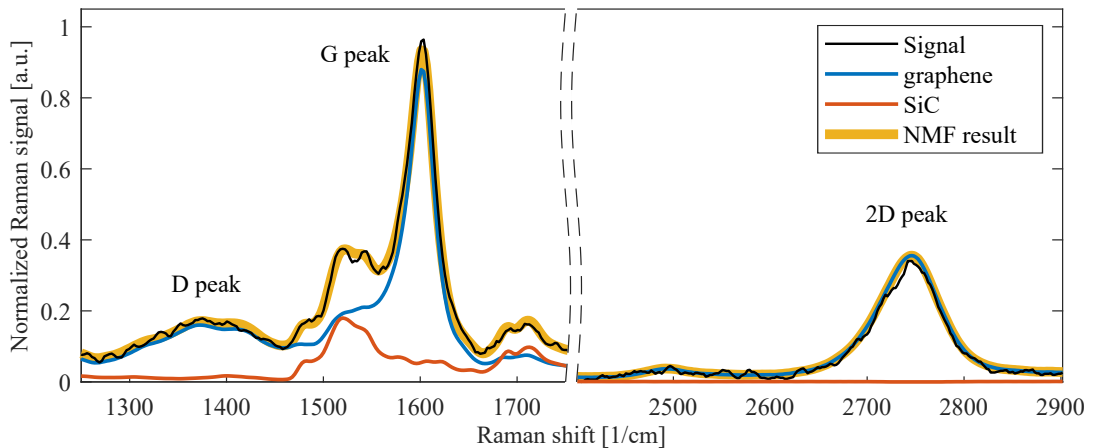**Figure 7.12:** Graphene Raman spectrum with identified main peaks. The measured signal (black) is decomposed using non-negative matrix factorization (NMF) into two base spectra: one belongs to the bare SiC substrate (red) and the second to the pure graphene (blue). The sum of the two decomposed spectra (orange) confirms the quality of the NMF decomposition as it precisely coincides with the measured signal.

stretched. Upon cooling, graphene lattice parameters stay almost constant (up to 0.02%) but the SiC lattice shrank by 0.6% [335, 336]. This induced a significant increase of the compressive strain in the graphene layer.

Raman signal collected from structures containing thin multilayers carries information not only about the topmost layer but also about layers beneath it. This is caused by non-zero penetration depth of the excitation laser. In this particular case, graphene signal was mixed with a parasitic signal from the SiC substrate. Basic method utilizing subtraction of a pure SiC signal may lead to non-physical regions with negative signal. Therefore, an advanced method called non-negative matrix factorization (NMF) is used here [304]. Although this method is applicable to many different problems, J. Kunc *et al.* [337] showed it can be easily applied to this particular case. NMF solves a linear algebra problem: It calculates a desired number of basis spectra (vectors) for a given large set of experimentally measured spectra. Each of the measured spectra can be, up to a certain accuracy, described as a linear combination of the basis vectors. The NMF procedure finds the basis vectors to minimize sum of all deviations. Here, experimental data set contained 100 spectra measured on bare SiC and 765 spectra measured at different locations of non-irradiated sample. Inclusion of 100 bare SiC spectra ensured that one of the basis spectrum should converge to the spectrum representing bare SiC. The second base spectrum must then represent a signal related exclusively to the graphene layer. Figure 7.12 shows results of the NMF decomposition. The two basis spectra (red and blue) are multiplied by coefficients corresponding to the black spectrum which is a representative of the 765 spectra. The yellow spectrum, which is a sum of the two basis spectra, perfectly matches with the black one and thus clarifies the correctness of the NMF procedure.

Raman spectroscopy also provides a guess about the number of graphene layers. This can be estimated using an empiric rule by calculating the ratio of the 2D and G peak intensities ($I_{2D}/I_G$). Lower ratio indicates more graphene layers [338, 339]. Because of ambiguity of the peak intensity, here we used two different approaches: In the first case, the intensities were calculated as integrated signal in regions (1535–1650) cm$^{-1}$ and (2550–2850) cm$^{-1}$ for the G and 2D peak, respectively. In the second case, the intensities were calculated as area below fitted Gaussian curve. Ratios obtained by these two methods are ≈1.1 and differ only by 10%. This corresponds to approximately 2–3 graphene layers on the SiC.

### X-ray photoelectron spectroscopy

Number of layers can be estimated also from XPS measurements as shown in Figure 7.13. Two XPS spectra measured on the pristine area (yellow) and graphene exposed to XUV radiation (blue) are shown in Fig. 7.13a. This figure also contains designation of two main peaks. The first peak at energy ≈ 284.7 eV represents C bonds within the graphene layer. Two components known as S1 and S2 may partially contribute to its intensity. The S1 component at 284.8 eV emerges from approximately one third of buffer carbons which are strongly bonded (sp$^3$) to substrate silicon atoms. Remaining two thirds of unbonded buffer carbons contribute to S2 at 285.6 eV [323]. SiC bulk substrate gives rise to the second peak at ≈ 283.7 eV [319, 323]. Ratios of intensities of the two peaks are compared in Fig. 7.13b. K. V. Emtsev et al. [323] showed that this ratio is dependent on num-

ber of graphene layers. Comparison of ratios calculated from peak amplitudes gives 1.4 and 0.8 layers for the pristine and irradiated graphene, respectively. Nevertheless, the XPS signal is a mixture of signals collected from the central part of the imprint and from the pristine area. This follows from insufficient spatial resolution of the used device and results obtained from micro-Raman spectroscopy are therefore definitely more reliable.
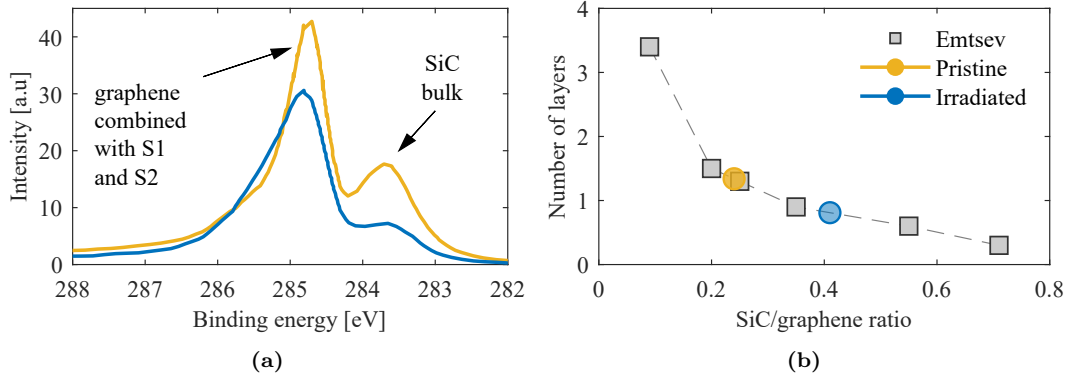


**Figure 7.13:** XPS measurements: (a) shows XPS spectra with indication of graphene and SiC peak. (b) shows calculated ratio of the two peaks compared with data published by K. V. Emtsev et al. [323]. These were used for estimation of the number of layers. Colours are consistent in both figures.

### 7.2.3 Results

Motivation of the irradiation experiment was to observe possible graphitization typical for carbon allotropes and/or detachment of the graphene layer from the SiC substrate accompanied by a potential increase of the carrier mobility. According to the XTANT simulation, the detachment of the buffer is feasible as energy needed for this process is lower than damage threshold of the SiC as well as of the graphene layer.

Samples of EG and bare SiC substrate were irradiated by $(100 \pm 20)$ $\mu$J XUV pulses at wavelength of 21.2 nm delivered by the PALS facility (see Chapter 4.2.1). Created ablative imprints are shown in Figure 7.14. As can be seen, pulses of high peak fluences $F_0$ (Figs. 7.14a–7.14c) induced irreversible ablative damage which spans through the graphene layer deep into the bulk SiC (maximum depth is $\approx 350$ nm). These imprints could be possibly used for beam characterization, but for the study of XUV — graphene interaction they are not very valuable. Our attention was thus paid to the imprint obtained with the pulse attenuated by 1600-nm aluminium filter to 10% [107] and irradiation thus induced only mild surface modifications keeping the graphene layer still in place. The imprint obtained at full power shown in Fig. 7.14a was used for XPS measurements as its area was large enough to observe otherwise undetectable changes in the XPS spectra.

In order to identify fluence thresholds of induced changes we characterized the beam with the method of ablation imprints in PMMA. Due to low repetition rate of the PALS facility and small set of imprints was created. The fluence profile, shown earlier in Fig. 6.1b, was calculated from a single-shot

**(a)** $F_0 = 8.2$ J/cm² **(b)** $F_0 = 4.6$ J/cm² **(c)** $F_0 = 2.6$ J/cm² **(d)** $F_0 = 0.9$ J/cm²
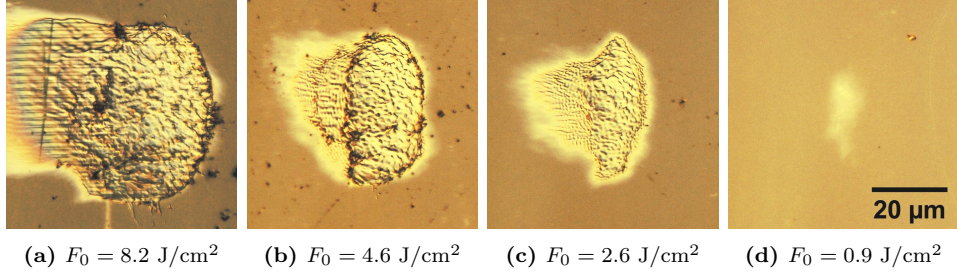
**Figure 7.14:** Nomarski photographs of imprints induced by XUV pulses delivered by the PALS facility. (a) was created by non-attenuated pulse, whereas pulses (b–d) were attenuated by aluminium foils of thicknesses 400, 800 and 1600 nm, respectively. All images are to scale. Horizontal lines visible on the left side of (a) were created by a 532-nm excitation laser during micro-Raman measurements.

($F_0 = (0.9 \pm 0.2)$ J/cm²) ablation imprint (Fig. 6.1a) using the Eq. 6.1. Two iso-fluence contours at 0.44 and 0.66 J/cm², as shown in the fluence profile, define two areas of low and high fluence $A_{\text{low}}$ and $A_{\text{high}}$ used in the following text. Measured effective area of the beam is $A_{\text{eff}} = (840 \pm 90)$ $\mu$m².

Structural and morphological changes of the area around the imprint shown in Figure 7.14d were analysed by means of WLI, AFM (in tapping mode), micro-Raman spectroscopy and XPS. Results from the WLI and AFM measurements are shown in Figure 7.15. Comparison with a reference imprint on the pure SiC substrate without the graphene layer (Fig. 7.15a) is also shown in the figure. There are two different interaction regimes marked by dashed lines standing for threshold fluences obtained from the Fig. 6.1b. High fluences exceeding $\approx 1.7$ J/cm² induce serious damage to the SiC substrate and create a deep ablation imprint. Moderate fluences in range 1.1–1.7 J/cm² result in formation of 4-nm-high hillock also shown in the cross-section profile (Fig. 7.15b) which was taken along the black dashed line. Surface expansion upon exposure of material to XUV radiation is a known effect typical, for example, for amorphous carbon [144]. It was observed also on $SrTiO_3$ after exposure to swift heavy ions [340]. L. L. Snead *et al.* [341] studied SiC amorphization in detail and found out that material density decreases by 11% when it transforms from crystalline to amorphous phase. Measured hillock height of 4 nm indicates that amorphization of the SiC should reach up to 30 nm which approximately agrees with attenuation length (15 nm [107]) of 21.2-nm radiation in SiC.

Approximate damage threshold of a given effect can be obtained by mapping the fluence profile (Fig. 6.1b) onto the WLI and AFM data. The iso-fluence contour is selected such that its shape and area fits the corresponding threshold contour most precisely. This mapping procedure results in estimation of threshold fluences as follows: SiC ablation at $(1.7\pm0.7)$ J/cm² and hillock formation (amorphization threshold) at $(1.1 \pm 0.5)$ J/cm² and $(0.66 \pm 0.25)$ J/cm² for bare SiC (Fig. 7.15a) and SiC with graphene (Fig. 7.15c), respectively. Errors were obtained from the largest inscribed and the smallest circumscribed contours to the given area combined with uncertainty of the pulse energy. The latter error is relatively large as XUV pulse generation is a highly stochastic effect and pulse energy may thus significantly vary from shot to shot. Fluences needed for the hillock creation obtained from the bare SiC and graphene (1.1 and 0.66 J/cm²) match within the estimated error. AFM analysis in Figs. 7.15e and 7.15f reveals
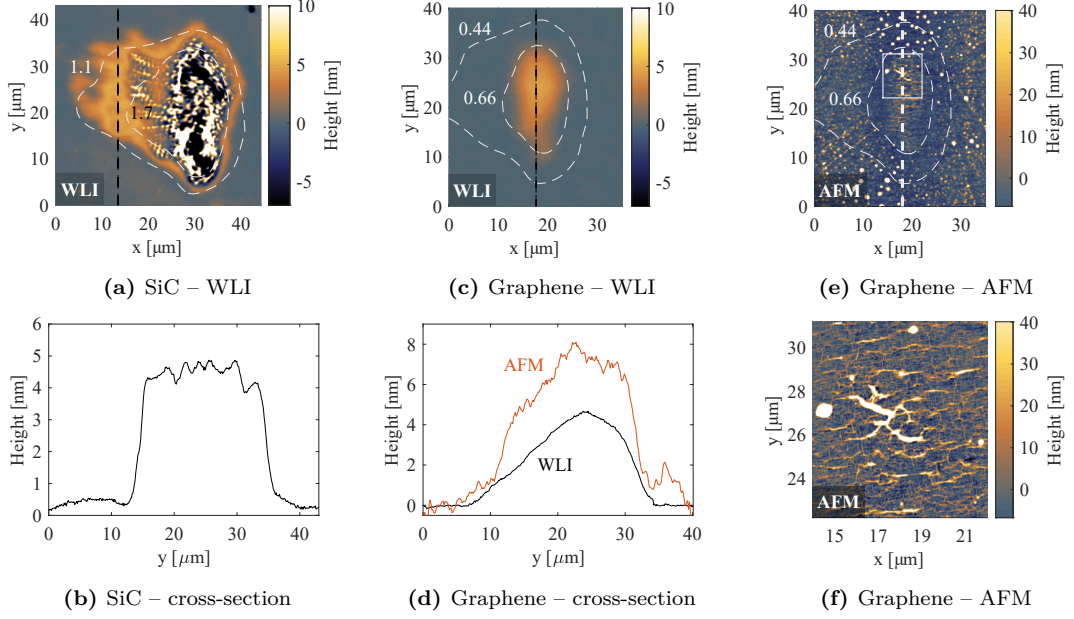
**Figure 7.15:** Comparison of topographical changes observed by WLI and AFM on bare SiC and SiC with graphene. Ablation imprint in the centre and SiC amorphization in outer area is observed after irradiation of the reference SiC substrate (a). Amorphization followed by material expansion is also observed after irradiation of SiC with graphene (c). Cross section profiles are compared in (b) and (d). AFM analysis in (e) with a detail focused on the central part (f) shows disruption of the graphene layer.

that expansion of the SiC substrate partially damaged structure of the graphene layer lying on top of it. Formation of defects in the central part of the imprint $A_{high}$ is further verified with the micro-Raman spectroscopy.

Further characterization of the irradiated area was done using the micro-Raman spectroscopy in a 2D mapping mode. This method consists of acquisition of 35×40 spectra at different positions with 1 $\mu$m step and analysis of peak properties in each of them. It provides a great tool for observation of spatially-resolved changes as shown in Figure 7.16. The first figure (Fig. 7.16a) shows 2D peak position. Map of mechanical strain is, according to Eq. (7.1), identical to the map of the 2D peak except for the absolute scale which is indicated in the colour bar.

The figure shows a strong red-shift of the 2D peak down to $\approx 2700$ cm$^{-1}$ in $A_{high}$. This corresponds to decrease of the strain down to 0.15%. Lower but still relatively high decrease is also observed in the outer area around the hillock $A_{low}$. This effect is very interesting as the shape of the affected area nicely correlates with the iso-fluence contour and no change in the height profile (Fig. 7.15c) nor in optical response (Fig. 7.14d) is observed. All the measured spectra (1400) were separated into three groups (pristine, $A_{low}$ and $A_{high}$) as indicated in Fig. 7.16b.

Overlaying the map of the 2D peak position (Fig. 7.16a) and the fluence profile (Fig. 6.1b) was used for calculation of the correlation figure as shown in Fig. 7.16d. As can be clearly seen, higher fluence of the XUV pulse induces greater red-shift of the 2D peak and hence also relaxation of the strain. The two horizontal dashed lines indicate iso-fluence contours encircling $A_{low}$ (at 0.44 J/cm$^2$) and $A_{high}$ (at 0.66 J/cm$^2$). Histogram plotted in the background of the figure indicates counts

**(a)** Mechanical strain / Position of 2D peak    **(b)** Definition of 3 areas    **(c)** Intensity of D peak



**(d)** Correlation of 2D peak position and fluence    **(e)** Distribution of 2D peak FWHM
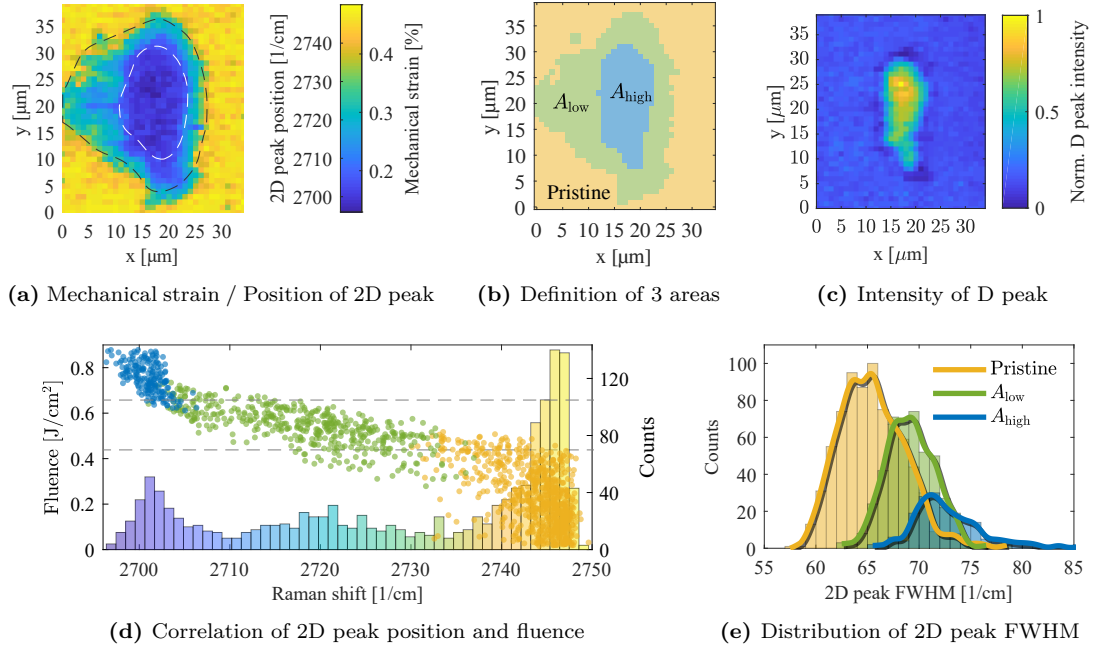
**Figure 7.16:** Micro-Raman analysis of the irradiated area. (a) shows a map of the mechanical strain (2D peak position) which can be divided into three groups as indicated in (b). (d) shows a correlation of the 2D peak position with fluence and (e) distribution of the 2D peak FWHM. Finally, (c) shows an increase of the D peak intensity in $A_{high}$.

of the 2D peak positions. Three different groups distinguishable in the histogram support division of the investigated region into the three areas.

Figure 7.16e shows analysis of the 2D peak FWHM. It clearly indicates the 2D peak is narrowest in the pristine area and widens in direction towards to centre of the imprint. This is probably caused by nanometre-scale strain variations which are beyond the resolution of our micro-Raman measurements. Raman excitation laser focused to a $\sim 1\ \mu$m spot might irradiate area where both completely relaxed as well as highly strained graphene are present. Each of them contributes to formation of the 2D peak at different positions which are then mixed into one large and broad 2D peak [342]. Moreover, it was shown that a long exposure of graphene to visible laser radiation may induce disassembly of large graphene grains into many nanocrystals [334]. This effect may contribute to further broadening of the peak. Graphene in the area $A_{high}$ is thus probably damaged and almost completely relieved of the intrinsic strain. Damage of the graphene is also supported by a strong increase of the D peak intensity as shown in Fig. 7.16c. Formation of defects accompanied by a strong increase of the D peak is a well-known effect which might occur also at fluences below the damage threshold [343–347]. This process originates in XUV-induced oxidation which might be enhanced by photo-induced electrons from the valence band breaking the $sp^2$ bonds [348]. Intensity of the D peak in area $A_{low}$ remains identical to that in the pristine area and formation of defects is therefore connected mainly with the hillock formation. Broadening of the 2D peak in $A_{low}$ originates in a mixture of sub-pixel parts which contain both relaxed and strained graphene. The intensity of the D peak was calculated as an integral of the signal within an interval (1260–1450) cm$^{-1}$.

Figure 7.17 compares three pure graphene spectra corresponding to the three
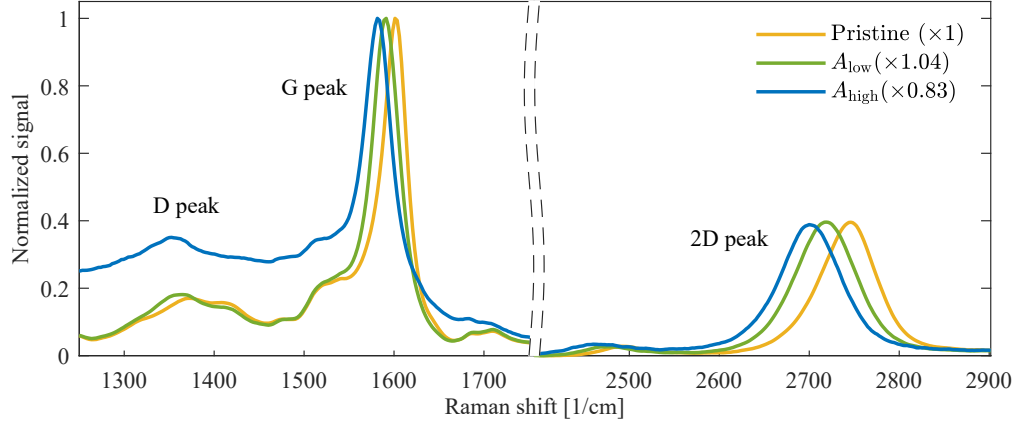
**Figure 7.17:** Pure graphene spectra obtained by the NMF method representing the three areas. Spectra are normalized to the G peak intensity.

areas. These spectra were obtained using the NMF procedure where each set of input data consisted of all spectra from the particular area and arbitrary 100 pure SiC spectra. An increase of the D peak in $A_{\text{high}}$ (blue) as well as red-shift of the 2D peak and G peak is clearly visible in the figure. A similar increase of the signal around the D peak was observed as a result of amorphous carbon formation on the graphene surface [349].

## 7.2.4 Discussion

Figure 7.18a shows the ratio of the 2D peak and G peak intensities ($I_{2D}$ and $I_G$) which corresponds to the number of layers. As can be also seen in Fig. 7.18b, comparing histograms of the calculated ratio in the three areas, the ratio decreases towards the centre of the imprint and the number of layers thus increases. This observation is in agreement with the theoretical assumption that strong sp$^3$ bonds between the SiC substrate and the buffer can be disturbed upon the XUV irradiation and the graphene layer including the buffer thus decouples from the substrate.



**(a)** Map of 2D/G peak ratio.



**(b)** Histogram of 2D/G peak ratio.
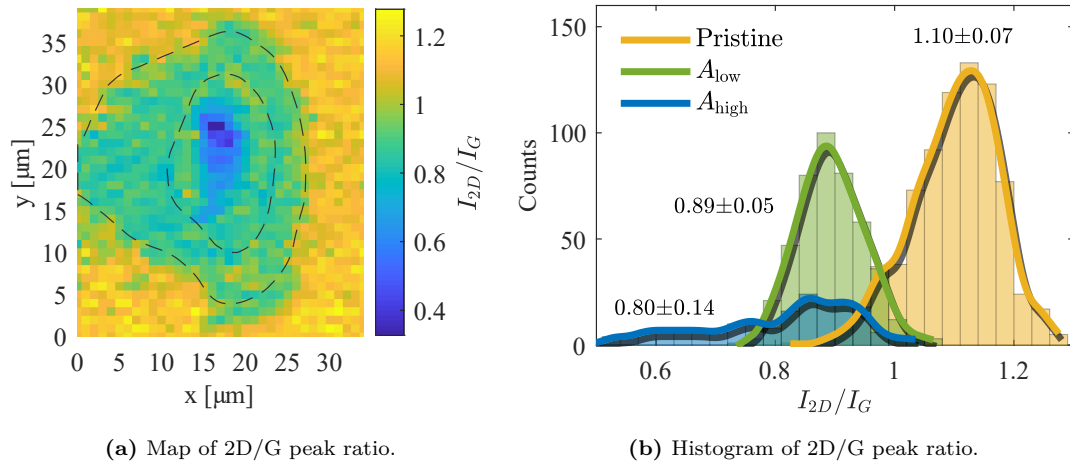
**Figure 7.18:** (a) Map of the 2D peak and G peak intensity ratio. (b) Comparison of three histograms calculated from (a) for the three particular areas. The ratio evidently decreases towards the centre of the imprint.

84

**High fluence**

The central part of the imprint, where fluence exceeded 0.66 J/cm$^2$, shows the smallest values of the $I_{2D}/I_G$ ratio, nevertheless, as the comparison of irradiated SiC with graphene has shown, the SiC substrate is amorphized in this area and the graphene layer damaged. Created defects are visible with AFM (Fig. 7.15f) and micro-Raman spectroscopy (Fig. 7.16c). The observed decrease of the ratio within $A_{\text{high}}$ is thus not attributed to further increase of the number of graphene layers (which is not possible as the buffer is just one atomic layer) but to calculation inaccuracy. It can be seen in Fig. 7.17 that precise estimation of $I_G$ without an influence of the strong background is very difficult and the calculated ratio in $A_{\text{high}}$ is just approximate.

**Intermediate fluence**

The most interesting is the intermediate regime within the area $A_{\text{low}}$ where the fluence was in a short interval 0.44–0.66 J/cm$^2$. It was too low to damage SiC but still high enough to disrupt strong covalent bonds between the buffer and silicon atoms of the SiC substrate. Detached buffer now has a very small coupling to the substrate and behaves as a common graphene layer with a corresponding lattice constant and relaxed strain as observed in Figure 7.16a. The relaxed graphene in $A_{\text{low}}$ does not attach back to the SiC substrate because of a mismatch of the lattice constants which mechanically prevents recovery of the strong sp$^3$ bonds.

Great correlation between the shape of the iso-fluence contour at 0.44 J/cm$^2$ and the outer contour of $A_{\text{low}}$ suggests that relaxation of the mechanical strain is not induced by a sheet-stretching effect resulting from the hillock formation. In spite of two different shots captured on two different materials (PMMA and graphene) and examined by two different methods (WLI and micro-Raman spectroscopy), there is an excellent agreement between the iso-fluence contours and areas of different mechanical strain (Fig. 7.16a). The most plausible explanation of observed effects is thus the radiation-induced threshold-limited process — detachment of the buffer from the SiC substrate.

**Low fluence**

Irradiation at fluences below 0.44 J/cm$^2$ did not induce any changes detectable by any of our techniques. This happens in spite of very weak ($\sim$10 meV/atom [350]) van der Waals (VdW) bonds binding individual graphene layers together. It means, that even at fluences as low as $\sim$ 1 mJ/cm$^2$ deposited energy density is sufficient to break these bonds. Because no changes are observed, breaking of the VdW bonds is assumed as a reversible process in which bonds renew after the irradiation. Breaking of the VdW bonds in carbon allotropes by short-wavelength radiation is already observed effect. While work of M. Toufarova *et al.* [144] describes Coulomb explosion of fullerenes, H. Jeschke *et al.* [351] irradiated graphite at relatively modest intensities and observed ablation of the material without destruction of individual graphene planes. Nevertheless, this effect occurs at energy density of 2.4 eV/atom and cannot be thus observed on graphene grown on SiC as this energy is above the SiC damage threshold.

**Damage thresholds**

Threshold character of the graphene detachment and SiC amorphization is confirmed by the possibility to divide measured 2D peak positions into the three separate groups (Fig. 7.16d) and by presence of steep edges of the hillocks (Figs. 7.15b and 7.15d). The values of fluence thresholds were calculated by mapping the fluence profile onto the map of the 2D peak position (Fig. 7.16a). These were estimated as $(0.44 \pm 0.18)$ J/cm$^2$ and $(0.66 \pm 0.25)$ J/cm$^2$ for the graphene layer detachment and the SiC amorphization, respectively. Relatively large errors originate in the uncertainty of pulse energy. More stable source and/or acquisition of many imprints is required for more precise results.

A comparison of measured fluence thresholds with theoretically calculated values is provided in Table 7.1. It can be seen, that XTANT calculations predict much lower thresholds than observed in the experiment. Nevertheless, the simulation does not consider any heat and particle transfer (e.g. escaping photoelectrons) within the sample and is thus convenient for femtosecond pulses where deposition of the pulse energy can be considered as immediate. Fluence thresholds measured by sub-nanosecond pulses are thus at higher levels, at which particle and heat transfer may play a role. Theoretically predicted values represent the lower estimate. The table also shows SiC damage threshold measured by S. P. Hau-Riege *et al.* [352] who irradiated SiC with $\approx 100$ fs FEL pulses and estimated damage threshold to 0.3 J/cm$^2$ at 21.7 nm. The value measured in our experiment is about two times higher mainly because of the use of long sub-nanosecond pulses. If the SiC damage threshold was dependent on intensity, the discrepancy would be much higher. Therefore, damage mechanism depends mainly on absorbed dose and only partially on intensity. Calculated damage threshold of the free-standing graphene layer was not observed here as the SiC substrate amorphizes and damages the graphene structure at much lower fluences. Finally, we note here that absorption in the graphene layer was neglected in calculations of the SiC amorphization and detachment thresholds as its transmission is very high ($>98\%$ [107]).

**Table 7.1:** Table of estimated damage thresholds of the three different processes at the wavelength of 21.2 nm. All fluence values are in J/cm$^2$.

|  | Theory | Hau-Riege [352] | Experiment |
|---|---|---|---|
| Buffer/SiC | 0.08 | — | $0.44 \pm 0.18$ |
| SiC damage | 0.16 | 0.3 | $0.66 \pm 0.25$ |
| Graphene damage | 0.72 | — | — |

What is perhaps surprising in this work, is that only two imprints (one in PMMA, second in SiC with graphene) were sufficient to describe several different processes and calculate two damage thresholds. Although our data has poor statistical evidence, reproducibility was ensured by two repetitions of the sequence shown in the Fig. 7.14 with very similar results.

## 7.2.5 Conclusions

In this chapter we have described an experimental work focused on XUV laser-induced detachment of epitaxial graphene from the SiC substrate. Three different regimes have been observed upon irradiation with 21.2-nm sub-nanosecond pulses: Irradiation at fluences above 0.7 J/cm$^2$ induce amorphization of the SiC which expands and forms a 4-nm high hillock. The graphene layer on the top of the hillock has many defects and almost completely released intrinsic strain. Presence of the SiC ablation at high fluences disabled observation of direct graphene damage and/or potential graphitization which should occur at even higher fluences. Partial decrease of the intrinsic strain has been observed in regions irradiated in an intermediate fluence interval 0.4–0.7 J/cm$^2$. This is the consequence of breaking strong sp$^3$ bonds between the SiC substrate and the first graphene layer called buffer. The proof has been provided by monitoring the number of layers which increased by one towards the center of the imprint. Lattice mismatch between the stretched graphene and unharmed substrate mechanically prevents the graphene from attaching back to the substrate. Although VdW bonds between individual graphene layers are very weak, neither structural nor optical change has been detected for fluences $< 0.4$ J/cm$^2$. Disruption of the VdW bonds is therefore considered as a reversible process where bonds are restored shortly after the irradiation. Because XUV-induced detachment of the graphene layer is observed at quite low fluences, we believe that this method might be also performed with common laboratory lasers. Described process of XUV-induced graphene detachment is schematically shown in Figure 7.19. We expect the interaction occurs on 100-fs up to few nanosecond time scale as both thermal and nonthermal effects are present.

A significant increase of charge carrier mobility in detached graphene is expected [318]. This is a subject for further studies. Production of the quasi-free-standing graphene with high mobility has a great potential in micro-electronics and micro-patterning.
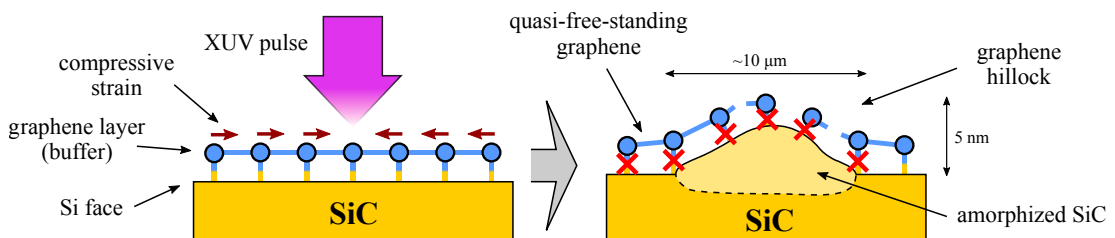


**Figure 7.19:** Schematic description of interaction between XUV pulse and epitaxial graphene on SiC.

## 7.3 CdTe

The last experiment in this thesis describes surface changes induced by XUV laser radiation in cadmium telluride (CdTe). These results were published in [54].

### 7.3.1 Introduction

CdTe is a semiconducting crystalline compound material known mainly because of its use in photovoltaics [353]. It is often doped with zinc to form $Cd_{1-x}Zn_xTe$ (x=0.1–0.2) which is an important II–VI semiconductor with wide applications in room temperature X-ray and gamma-ray detectors [354], electro-optical modulators and multiple optical applications [355]. Production of high-quality Cd(Zn)Te is very difficult and grown crystals usually have large concentrations of point defects, dislocations, twins, reveal cracks as well as volume defects (i.e. tellurium inclusions and precipitates) [354]. Presence of defects may significantly decrease performance of the final device and defect elimination is thus indeed welcome. However, manipulation with CdTe and its mechanical treatment is complicated due to its very low hardness [356, 357] and there is a high risk of damaging the sample. Among the large variety of mentioned defects, tellurium (Te) inclusions attract a great attention as they are detrimental to charge collection in hard X-ray and gamma-ray detectors [358, 359].

Impact of laser radiation on compounds of the CdTe family has been studied mainly from the perspective of possible improvements of the material characteristics. Among the studies closely related to our work we should mention A. Zappettini *et al.* [358] who used IR light (1064 nm = 1.17 eV) to stimulate migration and annealing from Te inclusions. He utilized a difference between bandgaps of the CdTe matrix (≈1.45 eV) and Te (0.33 eV). The IR radiation can thus freely propagate through the CdTe but is strongly absorbed in Te. Heated Te inclusions then diffuse away from the irradiated area. An improvement of CdZnTe:In parameters upon irradiation by IR light was also reported by A. Mychko *et al.* [360]. Formation of gradient temperature field around Te inclusions induced precipitation of uncontrollable impurities around them followed by an increase of solubility of indium atoms in the crystal lattice. Interaction of laser radiation at photon energies exceeding the CdTe bandgap was investigated in [361, 362]. L. C. Teague *et al.* [362] studied surface damage induced by Raman excitation lasers and tried to estimate the threshold fluence to minimize the damage. A. Medvid *et al.* [361] irradiated the surface of CdZnTe crystals with 532-nm laser radiation and studied formation of nanocones.

In this chapter we report on the first study focused on irradiation in the XUV regime. An impact of two types of laser pulses at wavelengths of 21.2 and 46.9 nm on semi-insulating CdTe:In hard X-ray and gamma ray radiation detector is described in detail. It is also compared with effects of irradiation with above-bandgap continuous laser at 532 nm and pulsed below-bandgap 1315-nm.

### 7.3.2 Experiment

Samples used in this experiment were cut from a CdTe single crystal grown by vertical gradient freeze method. The material was intentionally doped with indium at concentration of $5{\times}10^{15}$ cm$^{-3}$. Dimensions of the samples were 6×6×6 mm$^3$

and their resistivity was $10^9$ $\Omega\text{cm}^{-1}$. Surfaces of the samples were mechanically polished using an abrasive made of 1 $\mu$m alumina ($\text{Al}_2\text{O}_3$) grains and then etched for 2 minutes in a 3% Br–methanol solution.

Samples were exposed to intense XUV laser pulses delivered by the PALS facility (Chapter 4.2.1) and the CDL (Chapter 4.2.2). In the first case, both impact of a pure XUV pulse (21.2 nm) as well as a dual action of XUV and IR photons (1315 nm) was studied. It was attained by presence/absence of a 400 nm thick aluminium foil which shielded scattered IR photons and attenuated XUV pulse to $\approx$56% [107]. In the latter case, 100 XUV pulses at 46.9 nm were accumulated to one spot due to low intensity of the CDL. In order to further compare an impact of photons at different wavelengths, one sample was also exposed to continuous 532-nm Ar laser with power of 40 mW.

Irradiated samples were characterized by optical microscopy, AFM, micro-Raman spectroscopy and photoluminescence.

### 7.3.3 Results and Discussion

Figure 7.20 shows three examined imprints induced by dual action of a single-shot PALS X-ray and IR pulse (PXI), sole PALS X-ray pulse (PX) and accumulation of 100 CDL pulses. The imprints were measured with AFM and analysed with use of WSxM 4.0 software [277] for rendering of final images. As can be seen, irradiation led to ablation of material in all three cases. However, as shown in the previous chapter, some other surface modifications might be induced by low-energy wings around the actual ablative imprints.

PXI imprint in Fig. 7.20a represents dual action of the XUV pulse accompanied by scattered IR radiation. The main central spot surrounded by molten material was induced by the XUV pulse and shallow crater visible on the left side originates solely from the IR photons. Aluminium filter used for the PX



**(a)** PXI imprint      **(b)** PX imprint      **(c)** CDL imprint
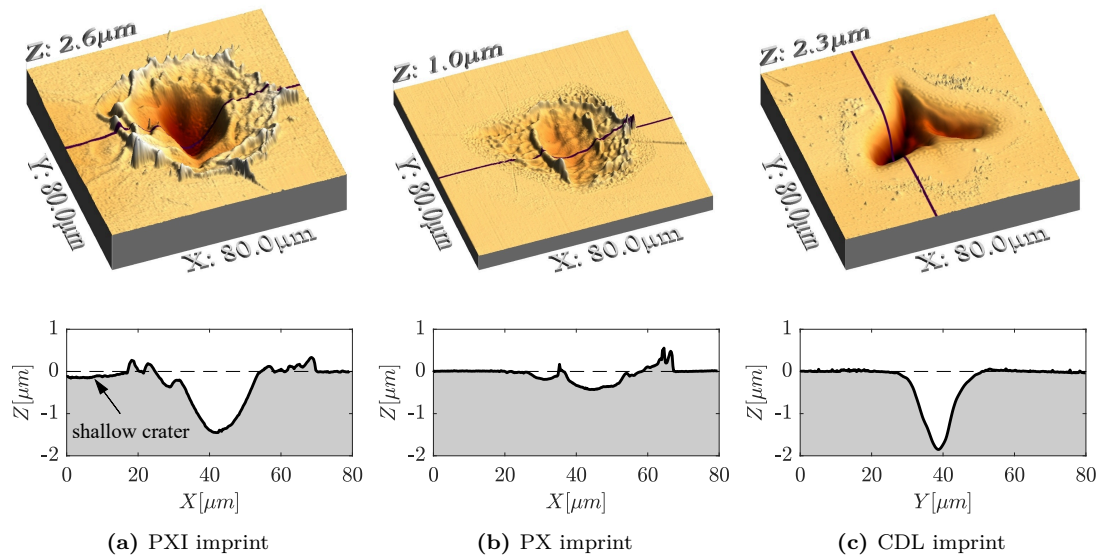
**Figure 7.20:** Ablation imprints measured with use of AFM and corresponding cross sections. The first two imprints were acquired at the PALS facility. (a) was induced by dual action of XUV and IR photons (PXI) and (b) by a single XUV pulse (PX). (c) was induced by accumulation of 100 XUV pulses delivered by the capillary discharge laser (CDL). All images are to scale.

imprint (Fig. 7.20b) shielded the IR radiation and attenuated the XUV pulse so the ablated crater is not so deep. Accumulation of 100 shots of CDL (Fig. 7.20c) induced a relatively smooth profile with a characteristic triangular shape. Surface of increased roughness can be seen in a close vicinity around the imprint. It originates from diffused Te inclusions as discussed later.

In order to characterize changes in the lattice structure we performed micro-Raman measurements with EC Epiplan 20×/0.4 objective (Chapter 5.2.1). Because of a very low damage threshold of CdTe at the excitation wavelength (532-nm) of the Ar laser, a very low (< 5 mW) power had to be applied. This prolonged the exposure time which was 20 s for each spectrum. In order to obtain better signal, five spectra were accumulated and averaged in case of linescans.

Figure 7.21 shows Raman spectra measured in different locations. A typical Raman signal from as-grown CdTe is shown as a solid black line. The main peaks indicated in the spectrum were identified according to [363]. The peak E(Te) at $\approx$127.5 cm$^{-1}$ corresponds to vibrations of elemental Te. It is blueshifted from its initial position 121 cm$^{-1}$ due to a compressive stress applied by the CdTe matrix to Te inclusions [364] and is in a good agreement with observations of micro-Raman imaging of Te precipitates [363]. The Te droplets were formed during the crystal growth and their origin resides in morphological instability of a solid-liquid interface which can be only partially controlled by the growth velocity and furnace temperature [365]. Internal pressure of the crystal exerted on inclusions is balanced by distortion of the CdTe lattice. Laser-induced heating or another means of lattice disruption may result in release of the applied stress consequently observed as a red-shift of the E(Te) peak back to its original position. A combination of signal from elemental Te vibrations and transversal optical
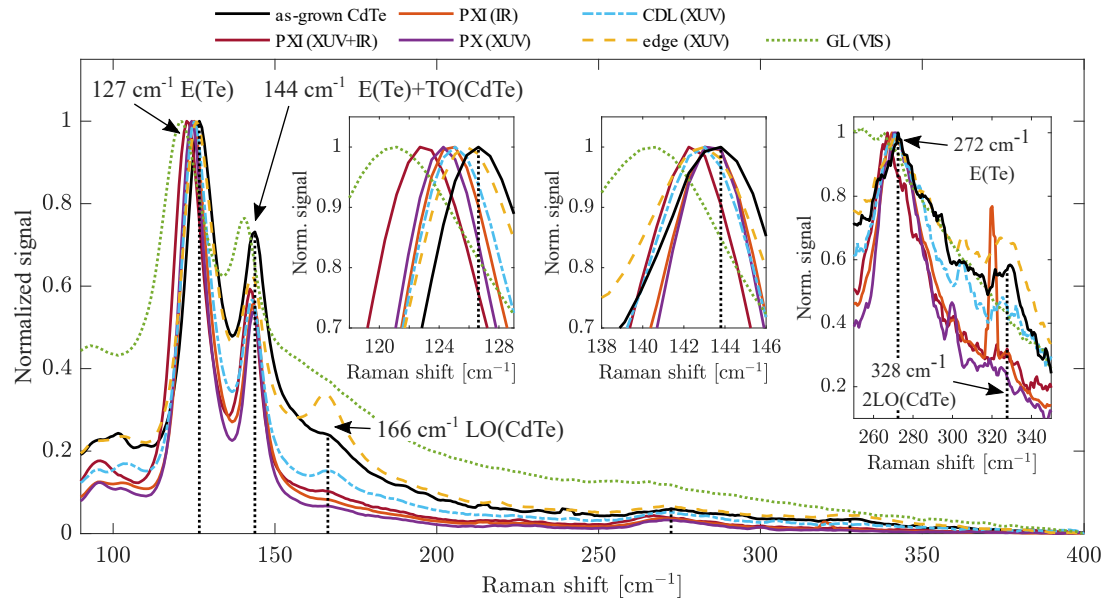


**Figure 7.21:** Comparison of Raman spectra collected from various locations on the sample. Signal from as-grown CdTe is represented by a solid black line. Insets show details of peaks corresponding to E(Te), E(Te)+TO(CdTe) and higher modes. For clarity, separate normalization of all spectra was done for each inset. The edge spectrum (dashed yellow line) is taken from the edge of the CDL imprint and its shape is very similar to other spectra observed at edges of other imprints.

phonons (TO) of CdTe gives rise to TO(CdTe)+E(Te) peak located at 144 cm$^{-1}$. Its interpretation is partially ambiguous because of mixture of the two signals. Nevertheless, due to its relation to the E(Te) it should partially reflect behaviour of the peak at 127.5 cm$^{-1}$. A weak signal from longitudinal optical phonons (LO) of CdTe is observed at 166 cm$^{-1}$. Higher modes of E(Te) vibrations and 2LO(CdTe) at 272 cm$^{-1}$ and 328 cm$^{-1}$ are also present.

### PXI imprint

A summary of the micro-Raman mapping of the PXI imprint is given in Figure 7.22. An image of the imprint from an optical microscope is displayed in Fig. 7.22a. Arrows in the figure point to the central part induced by a dual action of the XUV+IR and to the tail created solely by the scattered IR photons. Figure 7.22b shows intensity of the E(Te) mode at $\approx$127 cm$^{-1}$. The intensity apparently increases everywhere in the irradiated area and slightly also around the central (XUV+IR) part. Great correlation between the peak intensity and its position can be observed by comparing Figs. 7.22b and Fig. 7.22c. Relaxed stress around the Te inclusions, observed as a redshift of the E(Te) mode, is accompanied by increasing intensity of this mode. The redshift is also very well distinguishable in Fig. 7.22e showing a linescan across the imprint: Energy of the E(Te) vibrations is shifted down to 123.5 cm$^{-1}$ in the central part of the imprint. A smaller shift to 125 cm$^{-1}$ is detected in area irradiated by the IR light. Position of the E(Te)+TO(CdTe) mode which correlates with the E(Te) mode is also shown in the linescan. It is expected that this shift originates from modifications in the E(Te) part while TO(CdTe) mode remains unaffected. Intensity map of the E(Te)+TO(CdTe) mode is almost identical to that of the E(Te). A slight increase of the LO(CdTe) vibrations at 166 cm$^{-1}$ just around the imprint



**(a)** PXI imprint      **(b)** Intensity of E(Te)      **(c)** Raman shift of E(Te)

**(d)** Intensity of LO(CdTe)      **(e)** Linescan across the PXI imprint

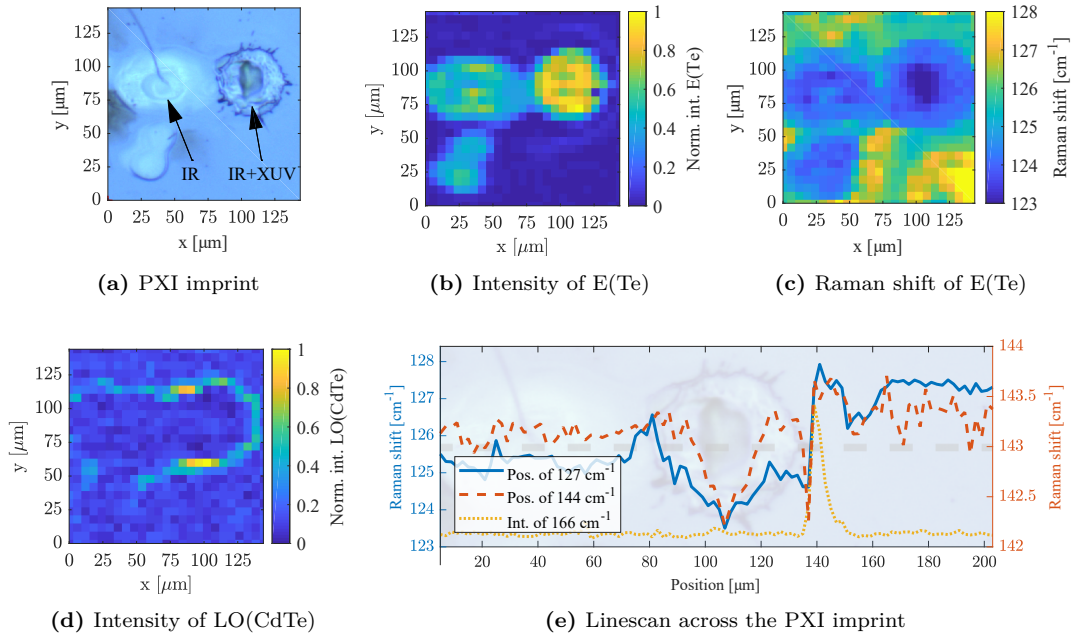**Figure 7.22:** Analysis of the PXI imprint: (a) image from the optical microscope, (b) and (c) intensity and Raman shift of the E(Te) mode at $\sim$127 cm$^{-1}$, (d) intensity of the LO(CdTe) mode at 166 cm$^{-1}$, (e) linescan of positions of the E(Te) (127 cm$^{-1}$) and E(Te)+TO(CdTe) (144 cm$^{-1}$) modes and relative intensity of the LO(CdTe) mode at 166 cm$^{-1}$.

edges can be observed in Fig. 7.22d. Intensity of its second order 2LO(CdTe) at 328 cm$^{-1}$ grows accordingly.

## PX imprint

Figure 7.23 shows data of the PX imprint. Image from the optical microscope of the imprint is in Figure 7.23a. A very similar behaviour of the E(Te) mode at $\approx$127 cm$^{-1}$ as in PXI imprint can be observed in Fig. 7.23b (intensity) and Fig. 7.23c (position) as the intensity increases and position decreases in the irradiated area. A halo of moderately increased E(Te) intensity surrounding the central part is much better pronounced in this case. The linescan in Fig. 7.23e reveals that redshift of the E(Te) is about 3.2 cm$^{-1}$. A smaller value compared to the PXI imprint might be caused either by a possible dual action of XUV + IR light or weaker intensity (56%) of the XUV pulse. By comparing intensity of the E(Te) to intensity of LO(CdTe) mode at 166 cm$^{-1}$, Fig. 7.23d, we can conclude there are two complementary processes occurring around the imprint (intensity of E(Te) drops where LO(CdTe) rises). This means, that decreasing concentration of the Te inclusions gives increase to quality of the CdTe lattice. It is assumed that XUV pulse heats the Te inclusions which then thermo-diffuse towards the surface and evaporate. Annealed CdTe lattice without the inclusions is then observed as strong increase of the LO(CdTe) mode. Outer ring of increased E(Te) intensity at distance $\approx$ 30$\mu$m from the ablation imprint in Fig. 7.23b, also detected as a small red-shift of the E(Te) in Fig. 7.23e, indicates that the Te inclusions probably diffused towards the surface and remained bound there.



**(a)** PX imprint     **(b)** Intensity of E(Te)     **(c)** Raman shift of E(Te)

**(d)** Intensity of LO(CdTe)     **(e)** Linescan across PX imprint

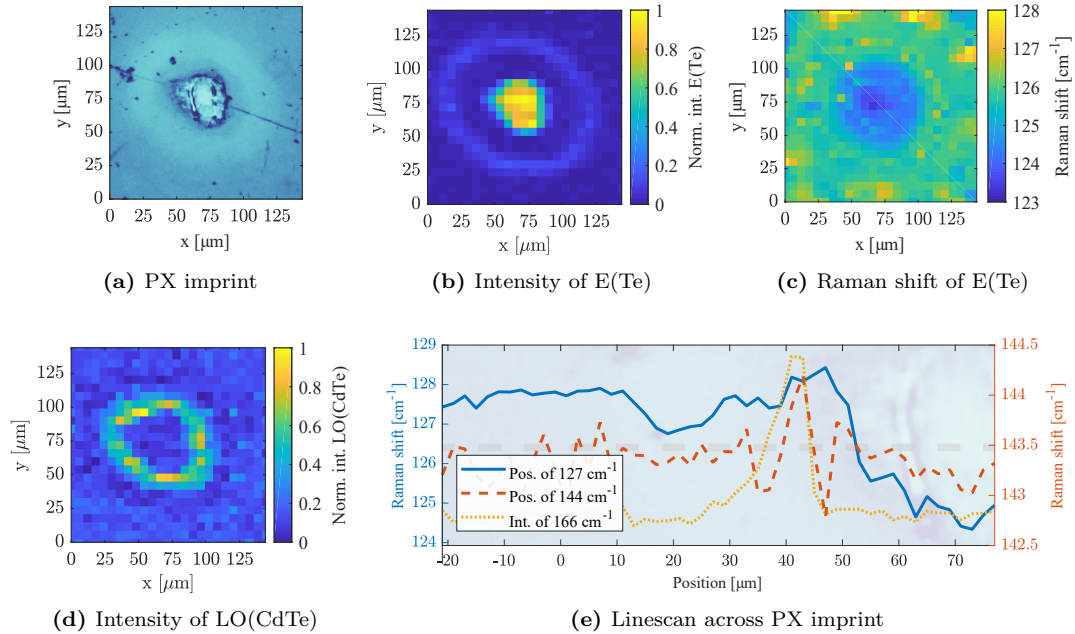**Figure 7.23:** Analysis of the PX imprint: (a) image from the optical microscope, (b) and (c) intensity and Raman shift of the E(Te) mode at $\approx$127 cm$^{-1}$, (d) intensity of the LO(CdTe) mode at 166 cm$^{-1}$, (e) linescan of positions of the E(Te) (127 cm$^{-1}$) and E(Te)+TO(CdTe) (144 cm$^{-1}$) modes and relative intensity of the LO(CdTe) mode at 166 cm$^{-1}$.

## CDL imprint

Figure 7.24 shows results obtained from the multishot CDL imprint whose image from the optical microscope is in Fig. 7.24a. Its triangular shape is surrounded by a similar halo as observed around the PX imprint. Intensity and position corresponding to the E(Te) and LO(CdTe) modes behaves in a very similar way as in previous cases. Shift of the E(Te) mode is relatively small, $\approx$2.5 cm$^{-1}$. This corresponds to rather small energy of the CDL pulses and small amount of modified material. While single pulses delivered by PALS created craters 1.5 $\mu$m (PXI) and 100 nm (PX) deep, each CDL pulse removed less than 20 nm of material. Moreover, penetration depth of the Raman excitation laser is $\sim$100 nm [109] and signal from the modified surface layer is therefore mixed with as-grown CdTe. A slight improvement could be possibly reached using the NMF procedure as described in the previous chapter. An increased surface roughness surrounding the imprint can be observed in the topographic AFM map shown in Fig. 7.24d. It is attributed to thermo-diffused Te inclusions which resolidified on the surface and formed $\approx$100-nm high hillocks.



**(a)** CDL imprint     **(b)** Intensity of E(Te)     **(c)** Raman shift of E(Te)

**(d)** Topographic map     **(e)** Intensity of LO(CdTe)
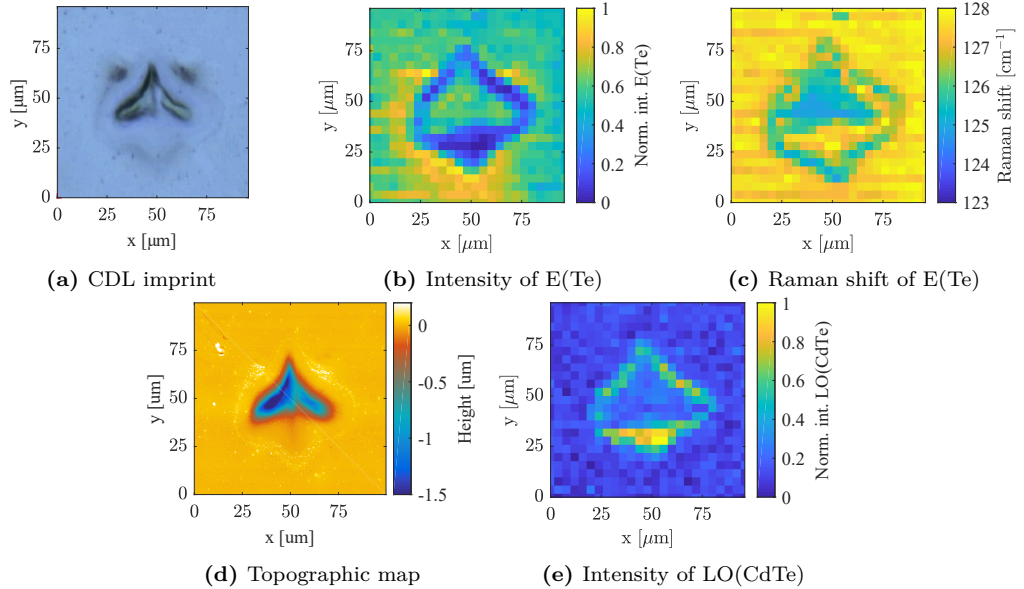
**Figure 7.24:** Analysis of the CDL imprint: (a) image from the optical microscope, (b) and (c) intensity and position of the E(Te) mode at $\sim$127 cm$^{-1}$, (d) topographic map from AFM, (e) Raman shift of LO(CdTe) mode at 166 cm$^{-1}$.

## GL imprint

Continuous laser radiation at 532 nm was used to verify that red-shift of the E(Te) mode at 127 cm$^{-1}$ corresponds to the thermal energy transferred from the laser radiation to the lattice. High-power mode (40 mW) of this radiation induced melting of the CdTe [362] and irradiated spots were characterized by micro-Raman imaging. Results are indicated as GL imprint. As shown in the Raman spectra (Fig. 7.21), the mode in this case shifted down to 121 cm$^{-1}$ and compressive stress exerted by the CdTe lattice was therefore completely released. No measurable signal from LO(CdTe) at 166 cm$^{-1}$ was detected because of a strong background caused by amorphized (burned) material.

**Summary of the micro-Raman analysis**

Comparison of all Raman spectra is given in Fig. 7.21. Positions of the fundamental E(Te) mode for all investigated imprints are compared in Table 7.2. The results clearly show that any kind of irradiation induces red-shifts of both peaks at 127 cm$^{-1}$ and 144 cm$^{-1}$. The largest shift is observed after exposing the material to the green laser. Increased background signal presented in the spectrum indicates burned material. Figure also shows that LO(CdTe) vibrations at 166 cm$^{-1}$ are almost completely suppressed everywhere except of edges of imprints. Signal from the E(Te) vibrations at 272 cm$^{-1}$ is significant mainly for centres of PXI and PX imprints where also intensity of the E(Te) mode at 127 cm$^{-1}$ substantially increased.

**Table 7.2:** Sorted positions of the Raman peak E(Te) and its relative shift to its position in as-grown CdTe.

| Area | Position of E(Te) [cm$^{-1}$] | Position change relative to background [cm$^{-1}$] |
|---|---|---|
| As-grown CdTe | 127.5 | — |
| CDL (XUV) | 125.0 | 2.5 |
| PXI (IR) | 124.9 | 2.6 |
| PX (XUV) | 124.3 | 3.2 |
| PXI (XUV+IR) | 122.8 | 4.7 |
| GL (VIS) | 121.0 | 6.5 |

## 7.3.4 Photoluminescence

Photoluminescence (PL) measurements were done in order to analyze changes of the Y-band which reflects dislocations in the CdTe lattice. A typical PL spectrum of as-grown CdTe is shown in Fig. 7.25a. The signal in range 1.35–1.48 eV shows A-centre (at 1.45 eV) followed by its LO phonon replicas [366]. So-called Y-band surrounding a Y-line at 1.474 eV originates from dislocations in the Te sublattice of CdTe [367]. Signal in spectral range 1.48–1.6 eV comes from shallow acceptors and bound excitons and their phonon replicas. Strong signal at 1.584 eV known as a C-line is attributed to recombination of excitons bound to various defects including In atoms [368]. Dropping sensitivity of the germanium detector used in the PL study causes loss of the signal beyond $\approx$1.6 eV.

PL spectra focused on changes in the Y-band obtained from PXI and PX imprints are compared in Fig. 7.25b. As can be seen, the increase of the Y-band signal is present at areas irradiated solely by the IR radiation and by the IR radiation mixed with XUV. Exposure to a single XUV pulse does not induce any significant changes. Dislocations are therefore probably induced by the IR radiation and not by the short-wavelength photons. These measurements well correspond to absorption mechanisms in the material: Because of very high energy of the 21.2-nm photons, XUV radiation is absorbed in both the CdTe matrix and the Te inclusions. It results in effective melting and ablation. The IR light is, on the contrary, absorbed only in the narrow bandgap of the Te inclusions (0.33 eV). Higher kinetic energy of Te increases the stress which is transferred to the CdTe matrix leading to formation of dislocations. XUV-induced melting of the material
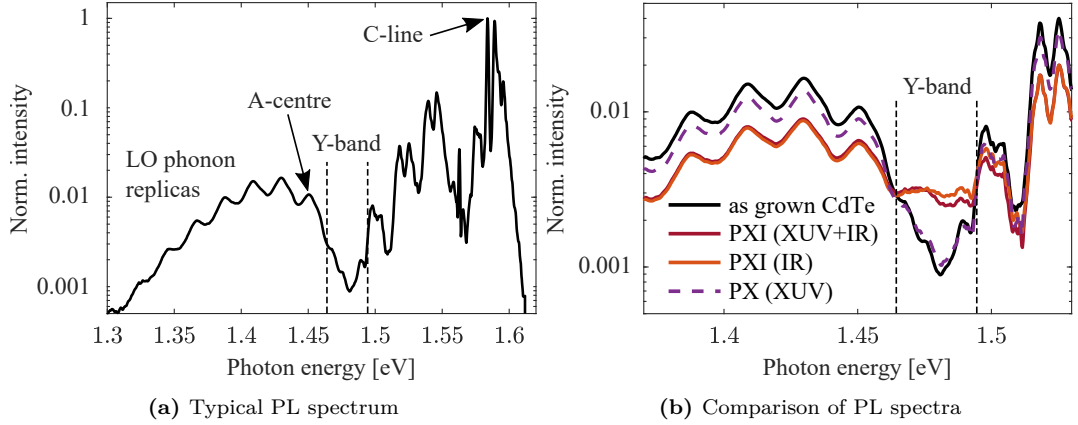
(a) Typical PL spectrum      (b) Comparison of PL spectra

**Figure 7.25:** (a) Photoluminescence spectrum of pristine CdTe. (b) Comparison of PL spectra from the PXI and PX imprints.

as well as described absorption of the IR radiation lead to distortion of the CdTe lattice accompanied by release of the compressive stress around the Te inclusions.

### 7.3.5 Conclusions

CdTe lattice contains a significant amount of Te inclusions which suppress its longitudinal vibrations, LO(CdTe), observed in the Raman spectra at 166 cm$^{-1}$. Strain in the inclusions induced by surrounding CdTe matrix is observed in Raman spectra as a blueshift of the E(Te) mode from 121 cm$^{-1}$ to 127 cm$^{-1}$. Based on the experimental results obtained from ablation imprints and other surface modifications induced by XUV radiation, we suggest division of the interaction into three different regimes: molten and resolidified central part, area close to the central part with annealed CdTe without Te inclusions and outer area with diffused Te inclusions bound on the surface.

High fluence induced melting and ablation of the material which resulted in creation of the imprints. Central parts of the imprints contain resolidified material without crystalline structure and compressive stress around the Te inclusions is thus partially or completely released. This is observed as redshift of E(Te) vibrations towards initial position. Short absorption length of the incident XUV radiation, typically less than 50 nm [107], induced very steep temperature gradients which lead to thermal diffusion of the Te inclusions towards the surface (also [369]). This is observed as increased intensity of the E(Te) mode.

Not only Te inclusions in the central parts of ablation imprints but also inclusions surrounding the imprints gained a significant portion of thermal energy. This came either from low-intensity wings of the beam or from heat which spread from the centre. High thermal gradients lead to diffusion of inclusions towards the surface and, in case of sufficiently high energy, possible evaporation. Absence of the inclusions in annular areas closely surrounding the ablation imprints is observed as a decrease of the signal from E(Te) and strong increase of LO(CdTe) mode at 166 cm$^{-1}$. Due to the absence of this signal in as-grown material as well as in all other areas, we assume that suppression of the LO(CdTe) vibrations is caused by presence of Te inclusions.

Inclusions in parts where temperature was below the evaporation threshold, i.e. in outer areas of the imprints, only diffused towards the surface where part of

them resolidified. This led to a mild increase of the surface roughness of typical height ∼100 nm, which can be well recognized on AFM topographic maps, and to a slight increase of the E(Te) signal.

Due to the ambiguity of the 144 cm$^{-1}$ peak we cannot say much about the TO(CdTe) vibrations but, considering similar behaviour of the 127 cm$^{-1}$ and 144 cm$^{-1}$ peaks, we suppose that 144 cm$^{-1}$ peak changes only due to variations in the E(Te) mode and TO(CdTe) mode remains unaffected.

Finally, according to the photoluminescence measurements on the PXI and PX imprints, we conclude that IR light is effectively absorbed only in the narrow bandgap of Te inclusions. This process is connected with creation of dislocations in the CdTe lattice observed as increase of the PL signal of the Y-line.

Although A. Zappettini *et al.* [358] observed microscopic diffusion ($\sim 100~\mu$m) of Te inclusions on time scales of several hours, we guess this process takes place as long as temperature gradients exists in the material, i.e. from $\sim 10$ ps up to $\sim 1$ ms when material resolidifies and cools down.

# 8. Conclusions

The primary aim of this work is to extend current state of knowledge in the field of short-wavelength laser-matter interactions. This includes an extensive and detailed review of processes occurring after the arrival of first photons, consequent heating of the material, cooling down and resolidification and also a description of induced irreversible changes. The summary of participating processes is given with a great emphasis on time scales at which the phenomena occur. We believe this review might serve as a study material for students and scientists interested in this field.

Author's publications fully cover described time scale beginning from the first femtoseconds up to formation of final state. Pump–probe transmission and spectroscopic measurements were used to describe ultrafast electronic processes belonging to first ∼100 fs [56, 58, 60]. Employing damage experiments it was possible to characterize lattice heating and consequent bond-breaking and ablation occurring within the first nanosecond [53, 55, 57, 59, 61] as well as role of heat accumulation and diffusion at microsecond–millisecond time scale [52, 54].

All these experiments were conducted at state-of-the-art facilities including large free-electron lasers, complex iodine laser system as well as tabletop capillary discharge laser. These facilities are able to deliver powerful laser pulses with exceptional parameters in the short-wavelength regime.

Characterization of beam profiles was done with use of ablation and desorption imprinting method which was, as a part of this work, extended to characterization of pulses delivered at MHz repetition rate. It has been shown that knowledge of spatial intensity distribution is immensely important for estimation of thresholds fluences of various processes as well as for correct interpretation of measured data. In addition to that, imprinting methods confirmed their usefulness in finding best focal position, alignment of beamline elements and others. We have also developed a novel and versatile method useful for an accurate determination of the fluence profile from ablation and desorption imprints in situations where material response function increases monotonically but nonlinearly with accumulated dose.

Experimental work on thin aluminium foils transmission measurement was focused on determination of absorption induced by inverse bremsstrahlung. Decreasing transmission with increasing single-pulse energy revealed that rise of electronic temperature is responsible for stronger absorption, a phenomenon occurring on time scales shorter than 100-fs pulse duration. The transmission data was used for retrieval of a functional form of the absorption coefficient dependent on electron temperature. Comparison of this function with misleading volume-averaged values explained discrepancies between experimental measurements and theoretical predictions published in earlier works. A possible further increase of the opacity induced by thermal effects on the picosecond time scale is suggested by time-resolved measurements.

A combination of thermal and nonthermal effects is also responsible for XUV-induced detachment of epitaxial multilayer graphene layer from the SiC substrate. An exposure to high fluences induces amorphization of the SiC which expands and forms a hillock instead of a crater. Pulse attenuated to modest energy can however break strong bonds between the SiC and the first carbon layer called

buffer. Detached graphene layer is stretched while releasing its intrinsic strain which mechanically preserves it from attaching back to the substrate. Strong coupling between the graphene and the SiC is detrimental for charge carrier mobility in the graphene layer and a suppression of the substrate influence is thus desirable.

Pure thermal character of laser-matter interaction was observed in CdTe where tellurium inclusions diffused from the area surrounding the irradiated spot towards the surface and partially evaporated while leaving the annealed CdTe lattice behind. An activation of a phonon mode corresponding to longitudinal vibrations of the CdTe lattice in the annealed area suggests that these vibrations are intrinsically suppressed owing to the presence of tellurium inclusions. Purifying CdTe crystals from the Te inclusions is important for radiation detectors as they are harmful for charge collection.

Future work should be focused primarily on detailed analysis of the charge carrier mobility changes in the detached graphene layer. By employing lasers of higher repetition rates it should be possible to irradiate pre-contacted samples and create highly conductive channels with a great potential to be used in microelectronics.

# Bibliography

[1] T. H. Maiman. "Stimulated optical radiation in ruby." *Nature*, 187(4736):493–494, August 1960. URL http://dx.doi.org/10.1038/187493a0.

[2] D. Strickland and G. Mourou. "Compression of amplified chirped optical pulses." *Optics Communications*, 56(3):219–221, December 1985. URL http://dx.doi.org/10.1016/0030-4018(85)90120-8.

[3] P. Emma, R. Akre, J. Arthur, *et al.* "First lasing and operation of an ångstrom-wavelength free-electron laser." *Nature Photonics*, 4(9):641–647, August 2010. URL http://dx.doi.org/10.1038/nphoton.2010.176.

[4] T. Shintake, H. Tanaka, T. Hara, *et al.* "A compact free-electron laser for generating coherent radiation in the extreme ultraviolet region." *Nature Photonics*, 2(9):555–559, July 2008. URL http://dx.doi.org/10.1038/nphoton.2008.134.

[5] D. Pile. "First light from SACLA." *Nature Photonics*, 5(8):456–457, July 2011. URL http://dx.doi.org/10.1038/nphoton.2011.178.

[6] E. Allaria, C. Callegari, D. Cocco, *et al.* "The FERMI@elettra free-electron-laser source for coherent x-ray physics: photon properties, beam transport system and applications." *New Journal of Physics*, 12(7):075002, July 2010. URL http://dx.doi.org/10.1088/1367-2630/12/7/075002.

[7] C. Milne, T. Schietinger, M. Aiba, *et al.* "SwissFEL: The swiss x-ray free electron laser." *Applied Sciences*, 7(7):720, July 2017. URL http://dx.doi.org/10.3390/app7070720.

[8] M. Altarelli. "The european x-ray free-electron laser facility in hamburg." *Nuclear Instruments and Methods in Physics Research Section B: Beam Interactions with Materials and Atoms*, 269(24):2845–2849, December 2011. URL http://dx.doi.org/10.1016/j.nimb.2011.04.034.

[9] S. H. Park, M. Kim, C.-K. Min, *et al.* "PAL-XFEL soft x-ray scientific instruments and x-ray optics: First commissioning results." *Review of Scientific Instruments*, 89(5):055105, May 2018. URL http://dx.doi.org/10.1063/1.5023557.

[10] Z. Zhao, D. Wang, Q. Gu, *et al.* "SXFEL: A soft x-ray free electron laser in china." *Synchrotron Radiation News*, 30(6):29–33, November 2017. URL http://dx.doi.org/10.1080/08940886.2017.1386997.

[11] R. W. Schoenlein, S. Boutet, M. P. Minitti, and A. M. Dunne. "The linac coherent light source: Recent developments and future plans." *Applied Sciences*, 7(8):850, aug 2017. URL http://dx.doi.org/10.3390/app7080850.

[12] B. Faatz, E. Plönjes, S. Ackermann, *et al.* "Simultaneous operation of two soft x-ray free-electron lasers driven by one linear accelerator." *New Journal of Physics*, 18(6):062002, June 2016. URL http://dx.doi.org/10.1088/1367-2630/18/6/062002.

[13] R. W. Lee, H. A. Baldis, R. C. Cauble, *et al.* "Plasma-based studies with intense x-ray and particle beam sources." *Laser and Particle Beams*, 20(3):527–536, July 2002. URL http://dx.doi.org/10.1017/s0263034602202293.

[14] R. W. Lee, S. J. Moon, H.-K. Chung, *et al.* "Finite temperature dense matter studies on next-generation light sources." *Journal of the Optical Society of America B*, 20(4):770, April 2003. URL http://dx.doi.org/10.1364/josab.20.000770.

[15] A. J. Nelson, S. Toleikis, H. Chapman, *et al.* "Soft x-ray free electron laser microfocus for exploring matter under extreme conditions." *Optics Express*, 17(20):18271, September 2009. URL http://dx.doi.org/10.1364/oe.17.018271.

[16] H. Yoneda, Y. Inubushi, M. Yabashi, *et al.* "Saturable absorption of intense hard x-rays in iron." *Nature Communications*, 5(1), October 2014. URL http://dx.doi.org/10.1038/ncomms6080.

[17] R. Lee and D. O. Gericke. "High energy density physics - journal - elsevier." https://www.journals.elsevier.com/high-energy-density-physics, 2014. (Accessed on 10/15/2019).

[18] B. F. Rozsnyai. "Solar opacities." *Journal of Quantitative Spectroscopy and Radiative Transfer*, 71(2-6):655–663, October 2001. URL http://dx.doi.org/10.1016/s0022-4073(01)00106-6.

[19] T. Guillot. "Interiors of giant planets inside and outside the solar system." *Science*, 286(5437):72–77, 1999. URL http://dx.doi.org/10.1126/science.286.5437.72.

[20] N. Nettelmann, B. Holst, A. Kietzmann, *et al.* "Ab initio equation of state data for hydrogen, helium, and water and the internal structure of jupiter." *The Astrophysical Journal*, 683(2):1217–1228, aug 2008. URL http://dx.doi.org/10.1086/589806.

[21] G. Fontaine, P. Brassard, and P. Bergeron. "The potential of white dwarf cosmochronology." *Publications of the Astronomical Society of the Pacific*, 113(782):409–435, April 2001. URL http://dx.doi.org/10.1086/319535.

[22] J. D. Lindl, P. Amendt, R. L. Berger, *et al.* "The physics basis for ignition using indirect-drive targets on the national ignition facility." *Physics of Plasmas*, 11(2):339–491, 2004. URL http://dx.doi.org/10.1063/1.1578638.

[23] S. X. Hu, L. A. Collins, V. N. Goncharov, *et al.* "First-principles opacity table of warm dense deuterium for inertial-confinement-fusion applications." *Physical Review E*, 90(3), 2014. URL http://dx.doi.org/10.1103/PhysRevE.90.033111.

[24] A. Friedman, J. J. Barnard, R. J. Briggs, *et al.* "Toward a physics design for NDCX-II, an ion accelerator for warm dense matter and HIF target physics studies." *Nuclear instruments and methods in physics research section A: Accelerators, spectrometers, detectors and associated equipment*, 606(1-2):6–10, July 2009. URL http://dx.doi.org/10.1016/j.nima.2009.03.189.

[25] N. Price. "Gérard mourou: Nobel lecture in physics, 2018.", 2018. URL https://www.youtube.com/watch?v=W5Fz_BsWCjU.

[26] L. B. Fletcher, H. J. Lee, T. Döppner, *et al.* "Ultrabright x-ray laser scattering for dynamic warm dense matter physics." *Nature Photonics*, 9(4):274–279, 2015. URL http://dx.doi.org/10.1038/nphoton.2015.41.

[27] H. J. Lee, P. Neumayer, J. Castor, *et al.* "X-ray thomson-scattering measurements of density and temperature in shock-compressed beryllium." *Physical Review Letters*, 102(11), March 2009. URL http://dx.doi.org/10.1103/physrevlett.102.115001.

[28] A. L. Kritcher, P. Neumayer, J. Castor, *et al.* "Ultrafast x-ray thomson scattering of shock-compressed matter." *Science*, 322(5898):69–71, October 2008. URL http://dx.doi.org/10.1126/science.1161466.

[29] T. Ma, L. Fletcher, A. Pak, *et al.* "Observations of strong ion-ion correlations in dense plasmas." *Physics of Plasmas*, 21(5):056302, May 2014. URL http://dx.doi.org/10.1063/1.4872161.

[30] D. H. Kalantar, J. F. Belak, G. W. Collins, *et al.* "Direct observation of the $\alpha$-$\epsilon$transition in shock-compressed iron via nanosecond x-ray diffraction." *Physical Review Letters*, 95(7), August 2005. URL http://dx.doi.org/10.1103/physrevlett.95.075502.

[31] M. Bykov, S. Chariton, H. Fei, *et al.* "High-pressure synthesis of ultraincompressible hard rhenium nitride pernitride re2(n2)(n)2 stable at ambient conditions." *Nature Communications*, 10(1), July 2019. URL http://dx.doi.org/10.1038/s41467-019-10995-3.

[32] M. Ross. "The ice layer in uranus and neptune–diamonds in the sky?" *Nature Physics*, 292:435–436, 07 1981. URL https://www.nature.com/articles/292435a0.

[33] D. Kraus, J. Vorberger, A. Pak, *et al.* "Formation of diamonds in laser-compressed hydrocarbons at planetary interior conditions." *Nature Astronomy*, 1(9):606–611, August 2017. URL http://dx.doi.org/10.1038/s41550-017-0219-9.

[34] P. Dalladay-Simpson, R. T. Howie, and E. Gregoryanz. "Evidence for a new phase of dense hydrogen above 325 gigapascals." *Nature*, 529(7584):63–67, January 2016. URL http://dx.doi.org/10.1038/nature16164.

[35] E. Wigner and H. B. Huntington. "On the possibility of a metallic modification of hydrogen." *The Journal of Chemical Physics*, 3(12):764–770, December 1935. URL http://dx.doi.org/10.1063/1.1749590.

[36] N. Dubrovinskaia, L. Dubrovinsky, N. A. Solopova, *et al.* "Terapascal static pressure generation with ultrahigh yield strength nanodiamond." *Science Advances*, 2(7):e1600341, July 2016. URL http://dx.doi.org/10.1126/sciadv.1600341.

[37] A. P. Drozdov, P. P. Kong, V. S. Minkov, *et al.* "Superconductivity at 250 k in lanthanum hydride under high pressures." *Nature*, 569(7757):528–531, May 2019. URL http://dx.doi.org/10.1038/s41586-019-1201-8.

[38] P. Vagovič, T. Sato, L. Mikeš, *et al.* "Megahertz x-ray microscopy at x-ray free-electron laser and synchrotron sources." *Optica*, 6(9):1106, August 2019. URL http://dx.doi.org/10.1364/optica.6.001106.

[39] H. N. Chapman, A. Barty, M. J. Bogan, *et al.* "Femtosecond diffractive imaging with a soft-x-ray free-electron laser." *Nature Physics*, 2(12):839–843, November 2006. URL http://dx.doi.org/10.1038/nphys461.

[40] H. N. Chapman, P. Fromme, A. Barty, *et al.* "Femtosecond x-ray protein nanocrystallography." *Nature*, 470(7332):73–77, February 2011. URL http://dx.doi.org/10.1038/nature09750.

[41] M. M. Seibert, T. Ekeberg, F. R. N. C. Maia, *et al.* "Single mimivirus particles intercepted and imaged with an x-ray laser." *Nature*, 470(7332):78–81, February 2011. URL http://dx.doi.org/10.1038/nature09748.

[42] J. Miao, T. Ishikawa, I. K. Robinson, and M. M. Murnane. "Beyond crystallography: Diffractive imaging using coherent x-ray light sources." *Science*, 348(6234):530–535, April 2015. URL http://dx.doi.org/10.1126/science.aaa1394.

[43] M. Makita, I. Vartiainen, I. Mohacsi, *et al.* "Femtosecond phase-transition in hard x-ray excited bismuth." *Scientific Reports*, 9(1), January 2019. URL http://dx.doi.org/10.1038/s41598-018-36216-3.

[44] N. Medvedev, Z. Li, and B. Ziaja. "Thermal and nonthermal melting of silicon under femtosecond x-ray irradiation." *Physical Review B*, 91(5), February 2015. URL http://dx.doi.org/10.1103/physrevb.91.054113.

[45] N. Medvedev, V. Tkachenko, and B. Ziaja. "Modeling of nonthermal solid-to-solid phase transition in diamond irradiated with femtosecond x-ray FEL pulse." *Contributions to Plasma Physics*, 55(1):12–34, January 2015. URL http://dx.doi.org/10.1002/ctpp.201400026.

[46] A. Rousse, C. Rischel, S. Fourmaux, *et al.* "Non-thermal melting in semiconductors measured at femtosecond resolution." *Nature*, 410(6824):65–68, March 2001. URL http://dx.doi.org/10.1038/35065045.

[47] F. Tavella, H. Höppner, V. Tkachenko, *et al.* "Soft x-ray induced femtosecond solid-to-solid phase transition." *High Energy Density Physics*, 24:22–27, 2017. URL http://dx.doi.org/10.1016/j.hedp.2017.06.001.

[48] N. Medvedev, M. Kopecky, J. Chalupsky, and L. Juha. "Femtosecond x-ray diffraction can discern nonthermal from thermal melting." *Physical Review B*, 99(10), March 2019. URL http://dx.doi.org/10.1103/physrevb.99.100303.

[49] S. R. Phillpot, S. Yip, and D. Wolf. "How co crystals melt?" *Computers in Physics*, 3(6):20, 1989. URL http://dx.doi.org/10.1063/1.4822877.

[50] J. Chalupský, T. Burian, V. Hájková, *et al.* "Fluence scan: an unexplored property of a laser beam." *Optics Express*, 21(22):26363, October 2013. URL http://dx.doi.org/10.1364/oe.21.026363.

[51] J. Chalupský, P. Boháček, T. Burian, *et al.* "Imprinting a focused x-ray laser beam to measure its full spatial characteristics." *Physical Review Applied*, 4(1), July 2015. URL http://dx.doi.org/10.1103/physrevapplied.4.014004.

[52] R. Sobierajski, I. Jacyna, P. Dłużewski, *et al.* "Role of heat accumulation in the multi-shot damage of silicon irradiated with femtosecond xuv pulses at a 1 mhz repetition rate." *Optics Express*, 24(14), 2016. URL http://dx.doi.org/10.1364/OE.24.015468.

[53] I. Milov, I. A. Makhotkin, R. Sobierajski, *et al.* "Mechanism of single-shot damage of ru thin films irradiated by femtosecond extreme uv free-electron laser." *Optics Express*, 26(15), 2018. URL http://dx.doi.org/10.1364/OE.26.019665.

[54] V. Vozda, T. Burian, J. Chalupský, *et al.* "Micro-raman mapping of surface changes induced by xuv laser radiation in cadmium telluride." *Journal of Alloys and Compounds*, 763:662–669, 2018. URL http://dx.doi.org/10.1016/j.jallcom.2018.05.332.

[55] V. Vozda, N. Medvedev, J. Chalupský, *et al.* "Detachment of epitaxial graphene from SiC substrate by XUV laser radiation." *Carbon*, 161:36–43, May 2020. URL http://dx.doi.org/10.1016/j.carbon.2020.01.028.

[56] T. R. Preston, S. M. Vinko, O. Ciricosta, *et al.* "Measurements of the k-shell opacity of a solid-density magnesium plasma heated by an x-ray free-electron laser." *Physical Review Letters*, 119(8), 2017. URL http://dx.doi.org/10.1103/PhysRevLett.119.085001.

[57] I. A. Makhotkin, R. Sobierajski, J. Chalupský, *et al.* "Experimental study of euv mirror radiation damage resistance under long-term free-electron laser exposures below the single-shot damage threshold." *Journal of Synchrotron Radiation*, 25(1):77–84, 2018. URL http://dx.doi.org/10.1107/S1600577517017362.

[58] Q. Y. van den Berg, E. V. Fernandez-Tello, T. Burian, *et al.* "Clocking femtosecond collisional dynamics via resonant x-ray spectroscopy." *Physical Review Letters*, 120(5), 2018. URL http://dx.doi.org/10.1103/PhysRevLett.120.055002.

[59] I. A. Makhotkin, I. Milov, J. Chalupský, *et al.* "Damage accumulation in thin ruthenium films induced by repetitive exposure to femtosecond xuv pulses below the single-shot ablation threshold." *Journal of the Optical Society of America B*, 35(11), 2018. URL http://dx.doi.org/10.1364/JOSAB.35.002799.

[60] S. M. Vinko, V. Vozda, J. Andreasson, *et al.* "Time-resolved xuv opacity measurements of warm dense aluminum." *Phys. Rev. Lett.*, 124:225002, Jun 2020. URL http://dx.doi.org/10.1103/PhysRevLett.124.225002.

[61] V. Vozda, T. Burian, V. Hájková, *et al.* "Characterization of megahertz x-ray laser beams by multishot desorption imprints in pmma." *Optics Express*, submitted.

[62] S. P. Hau-Riege. *High-intensity X-rays–interaction with matter*. Wiley-VCH, Weinheim, 2011. ISBN 978-3-527-40947-1.

[63] S. Eliezer. *The interaction of high-power lasers with plasmas*, volume 45. IOP Publishing, January 2003. ISBN 9780750307475. URL http://dx.doi.org/10.1088/0741-3335/45/2/701.

[64] R. P. Drake. *High-energy-density physics: fundamentals, inertial fusion, and experimental astrophysics (shock wave and high pressure phenomena)*. Springer, 2006. URL https://www.amazon.com/High-Energy-Density-Physics-Fundamentals-Experimental-Astrophysics-ebook/dp/B00FQ0QIU0?SubscriptionId=AKIAIOBINVZYXZQZ2U3A&tag=chimbori05-20&linkCode=xm2&camp=2025&creative=165953&creativeASIN=B00FQ0QIU0.

[65] D. Salzmann. *Atomic physics in hot plasmas (international series of monographs on physics)*. Oxford University Press, 1998. ISBN 0195109309. URL https://www.amazon.com/Atomic-Physics-Plasmas-International-Monographs/dp/0195109309?SubscriptionId=AKIAIOBINVZYXZQZ2U3A&tag=chimbori05-20&linkCode=xm2&camp=2025&creative=165953&creativeASIN=0195109309.

[66] R. Fitzpatrick. *Plasma physics: An introduction*. CRC Press, 2014. ISBN 1466594268. URL http://farside.ph.utexas.edu/.

[67] M. Bonitz, C. Henning, and D. Block. "Complex plasmas: a laboratory for strong correlations." *Reports on Progress in Physics*, 73(6):066501, may 2010. URL http://dx.doi.org/10.1088/0034-4885/73/6/066501.

[68] V. E. Fortov. "Extreme states of matter on earth and in space." *Physics-Uspekhi*, 52(6):615–647, June 2009. URL http://dx.doi.org/10.3367/ufne.0179.200906h.0653.

[69] T. Dornheim, S. Groth, and M. Bonitz. "The uniform electron gas at warm dense matter conditions." *Physics Reports*, 744:1–86, May 2018. URL http://dx.doi.org/10.1016/j.physrep.2018.04.001.

[70] J. Christensen-Dalsgaard, W. Dappen, S. V. Ajukov, *et al.* "The current state of solar modeling." *Science*, 272(5266):1286–1292, May 1996. URL http://dx.doi.org/10.1126/science.272.5266.1286.

[71] S. X. Hu, L. A. Collins, T. R. Boehly, *et al.* "A review on ab initio studies of static, transport, and optical properties of polystyrene under extreme conditions for inertial confinement fusion applications." *Physics of Plasmas*, 25(5), 2018. URL http://dx.doi.org/10.1063/1.5017970.

[72] P. Mulser and D. Bauer. *High Power Laser-Matter Interaction.* Springer Berlin Heidelberg, 2010. URL http://dx.doi.org/10.1007/978-3-540-46065-7.

[73] P. Mulser, G. Alber, and M. Murakami. "Revision of the coulomb logarithm in the ideal plasma." *Physics of Plasmas*, 21(4):042103, April 2014. URL http://dx.doi.org/10.1063/1.4870501.

[74] T. Bornath, M. Schlanges, F. Morales, and R. Prenzel. "Dynamical screening effects on rate coefficients for dense plasmas." *Journal of Quantitative Spectroscopy and Radiative Transfer*, 58(4-6):501–508, October 1997. URL http://dx.doi.org/10.1016/s0022-4073(97)00056-3.

[75] S. Pfalzner and P. Gibbon. "Direct calculation of inverse-bremsstrahlung absorption in strongly coupled, nonlinearly driven laser plasmas." *Physical Review E*, 57(4):4698–4705, April 1998. URL http://dx.doi.org/10.1103/physreve.57.4698.

[76] S. M. Vinko, O. Ciricosta, T. R. Preston, *et al.* "Investigation of femtosecond collisional ionization rates in a solid-density aluminium plasma." *Nature Communications*, 6(1), March 2015. URL http://dx.doi.org/10.1038/ncomms7397.

[77] G. J. Tallents. "Free electron degeneracy effects on collisional excitation, ionization, de-excitation and three-body recombination." *High Energy Density Physics*, 20:9–16, September 2016. URL http://dx.doi.org/10.1016/j.hedp.2016.06.001.

[78] P. Hollebon, O. Ciricosta, M. P. Desjarlais, *et al.* "Ab initio simulations and measurements of the free-free opacity in aluminum." *Physical Review E*, 100(4), October 2019. URL http://dx.doi.org/10.1103/physreve.100.043207.

[79] N. Medvedev, V. Tkachenko, V. Lipp, Z. Li, and B. Ziaja. "Various damage mechanisms in carbon and silicon materials under femtosecond x-ray irradiation." *4open*, 1, 2018. URL http://dx.doi.org/10.1051/fopen/2018003.

[80] A. Rämer, O. Osmani, and B. Rethfeld. "Laser damage in silicon: Energy absorption, relaxation, and transport." *Journal of Applied Physics*, 116(5):053508, August 2014. URL http://dx.doi.org/10.1063/1.4891633.

[81] G. Ecker and W. Kröll. "Lowering of the ionization energy for a plasma in thermodynamic equilibrium." *Physics of Fluids*, 6(1):62, 1963. URL http://dx.doi.org/10.1063/1.1724509.

[82] J. C. Stewart and J. P. Kedar D. "Lowering of ionization potentials in plasmas." *The Astrophysical Journal*, 144:1203, June 1966. URL http://dx.doi.org/10.1086/148714.

[83] G. B. Zimmerman and R. M. More. "Pressure ionization in laser-fusion target simulation." *Journal of Quantitative Spectroscopy and Radiative Transfer*, 23(5):517–522, May 1980. URL http://dx.doi.org/10.1016/0022-4073(80)90055-2.

[84] O. Ciricosta, S. M. Vinko, H.-K. Chung, *et al.* "Direct measurements of the ionization potential depression in a dense plasma." *Physical Review Letters*, 109(6), 2012. URL http://dx.doi.org/10.1103/PhysRevLett.109.065002.

[85] O. Ciricosta, S. M. Vinko, B. Barbrel, *et al.* "Measurements of continuum lowering in solid-density plasmas created from elements and compounds." *Nature Communications*, 7(1), May 2016. URL http://dx.doi.org/10.1038/ncomms11713.

[86] D. Kraus, B. Bachmann, B. Barbrel, *et al.* "Characterizing the ionization potential depression in dense carbon plasmas with high-precision spectrally resolved x-ray scattering." *Plasma Physics and Controlled Fusion*, 61(1):014015, November 2018. URL http://dx.doi.org/10.1088/1361-6587/aadd6c.

[87] L. B. Fletcher, A. L. Kritcher, A. Pak, *et al.* "Observations of continuum depression in warm dense matter with x-ray thomson scattering." *Physical Review Letters*, 112(14), April 2014. URL http://dx.doi.org/10.1103/physrevlett.112.145004.

[88] D. Attwood. *Soft x-rays and extreme ultraviolet radiation.* Cambridge University Press, August 1999. URL http://dx.doi.org/10.1017/cbo9781139164429.

[89] Y. Ping, A. A. Correa, T. Ogitsu, *et al.* "Warm dense matter created by isochoric laser heating." *High Energy Density Physics*, 6(2):246–257, June 2010. URL http://dx.doi.org/10.1016/j.hedp.2009.12.009.

[90] S. M. Vinko. "X-ray free-electron laser studies of dense plasmas." *Journal of Plasma Physics*, 81(5), July 2015. URL http://dx.doi.org/10.1017/s0022377815000902.

[91] S. M. Vinko, O. Ciricosta, B. I. Cho, *et al.* "Creation and diagnosis of a solid-density plasma with an x-ray free-electron laser." *Nature*, 482(7383):59–62, January 2012. URL http://dx.doi.org/10.1038/nature10746.

[92] R. Ernstorfer, M. Harb, C. T. Hebeisen, *et al.* "The formation of warm dense matter." *Science*, 323(5917):1033–1037, 2009-02-20. URL http://dx.doi.org/10.1126/science.1162697.

[93] S. P. Hau-Riege, A. Graf, T. Döppner, *et al.* "Ultrafast transitions from solid to liquid and plasma states of graphite induced by x-ray free-electron laser pulses." *Physical Review Letters*, 108(21), May 2012. URL http://dx.doi.org/10.1103/physrevlett.108.217402.

[94] S. H. Glenzer and R. Redmer. "X-ray thomson scattering in high energy density plasmas." *Reviews of Modern Physics*, 81(4):1625–1663, December 2009. URL http://dx.doi.org/10.1103/revmodphys.81.1625.

[95] P. Sperling, E. Gamboa, H. Lee, *et al.* "Free-electron x-ray laser measurements of collisional-damped plasmons in isochorically heated warm dense matter." *Physical Review Letters*, 115(11), September 2015. URL http://dx.doi.org/10.1103/physrevlett.115.115001.

[96] E. E. McBride, T. G. White, A. Descamps, *et al.* "Setup for meV-resolution inelastic x-ray scattering measurements and x-ray diffraction at the matter in extreme conditions endstation at the linac coherent light source." *Review of Scientific Instruments*, 89(10):10F104, October 2018. URL http://dx.doi.org/10.1063/1.5039329.

[97] B. Witte, L. Fletcher, E. Galtier, *et al.* "Warm dense matter demonstrating non-drude conductivity from observations of nonlinear plasmon damping." *Physical Review Letters*, 118(22), May 2017. URL http://dx.doi.org/10.1103/physrevlett.118.225001.

[98] S. K. Sundaram and E. Mazur. "Inducing and probing non-thermal transitions in semiconductors using femtosecond laser pulses." *Nature Materials*, 1(4):217–224, December 2002. URL http://dx.doi.org/10.1038/nmat767.

[99] N. Medvedev, Z. Fang, C. Xia, and Z. Li. "Thermal and nonthermal melting of III-v compound semiconductors." *Physical Review B*, 99(14), April 2019. URL http://dx.doi.org/10.1103/physrevb.99.144101.

[100] J. N. Hodgson. *Optical absorption and dispersion in solids*. Springer US, 1971. URL http://dx.doi.org/10.1007/978-1-4613-3321-0.

[101] C. Kittel. *Introduction to solid state physics*. Wiley, Hoboken, NJ, 2005. ISBN 978-0-471-41526-8.

[102] C. Hamaguchi. *Basic semiconductor physics*. Springer International Publishing Imprint Springer, Cham, 2017. ISBN 978-3-319-66860-4.

[103] A. Föhlisch, P. Feulner, F. Hennies, *et al.* "Direct observation of electron dynamics in the attosecond domain." *Nature*, 436(7049):373–376, July 2005. URL http://dx.doi.org/10.1038/nature03833.

[104] M. Sabbar, H. Timmers, Y.-J. Chen, *et al.* "State-resolved attosecond reversible and irreversible dynamics in strong optical fields." *Nature Physics*, 13(5):472–478, February 2017. URL http://dx.doi.org/10.1038/nphys4027.

[105] C. Peltz, C. Varin, T. Brabec, and T. Fennel. "Fully microscopic analysis of laser-driven finite plasmas using the example of clusters." *New Journal of Physics*, 14(6):065011, June 2012. URL http://dx.doi.org/10.1088/1367-2630/14/6/065011.

[106] F. Krausz and M. Ivanov. "Attosecond physics." *Reviews of Modern Physics*, 81(1):163–234, February 2009. URL http://dx.doi.org/10.1103/revmodphys.81.163.

[107] B. L. Henke, E. M. Gullikson, and J. C. Davis. "X-ray interactions." *Atomic Data and Nuclear Data Tables*, 54(2):181–342, 1993. URL http://dx.doi.org/10.1006/adnd.1993.1013.

[108] A. Einstein. "Über einen die erzeugung und verwandlung des lichtes betreffenden heuristischen gesichtspunkt." *Annalen der Physik*, 322(6):132–148, 1905. URL http://dx.doi.org/10.1002/andp.19053220607.

[109] R. Ahrenkiel. *Theory and methods of photovoltaic material characterization*. World Scientific, New Jersey, 2019. ISBN 978-981-3277-09-0.

[110] A. Das. *Introduction to nuclear and particle physics*. World Scientific, River Edge, N.J, 2003. ISBN 981-238-744-7.

[111] N. Rohringer and R. Santra. "X-ray nonlinear optical processes using a self-amplified spontaneous emission free-electron laser." *Physical Review A*, 76(3), September 2007. URL http://dx.doi.org/10.1103/physreva.76.033416.

[112] G. Doumy, C. Roedig, S.-K. Son, *et al.* "Nonlinear atomic response to intense ultrashort x-rays." *Physical Review Letters*, 106(8), February 2011. URL http://dx.doi.org/10.1103/physrevlett.106.083002.

[113] B. Rudek, S.-K. Son, L. Foucar, *et al.* "Ultra-efficient ionization of heavy atoms by intense x-ray free-electron laser pulses." *Nature Photonics*, 6(12):858–865, November 2012. URL http://dx.doi.org/10.1038/nphoton.2012.261.

[114] J. Yeh and I. Lindau. "Atomic subshell photoionization cross sections and asymmetry parameters: $1 \leq Z \leq 103$." *Atomic Data and Nuclear Data Tables*, 32(1):1–155, January 1985. URL http://dx.doi.org/10.1016/0092-640x(85)90016-6.

[115] U. Zastrau, C. Fortmann, R. R. Fäustlin, *et al.* "Bremsstrahlung and line spectroscopy of warm dense aluminum plasma heated by xuv free-electron-laser radiation." *Physical Review E*, 78(6), December 2008. URL http://dx.doi.org/10.1103/physreve.78.066406.

[116] B. Nagler, U. Zastrau, R. R. Fäustlin, *et al.* "Turning solid aluminium transparent by intense soft x-ray photoionization." *Nature Physics*, 5(9):693–696, 09 2009. URL http://dx.doi.org/10.1038/nphys1341.

[117] O. Ciricosta, S. M. Vinko, H.-K. Chung, *et al.* "Detailed model for hot-dense aluminum plasmas generated by an x-ray free electron laser." *Physics of Plasmas*, 23(2):022707, February 2016. URL http://dx.doi.org/10.1063/1.4942540.

[118] A. Müller, A. Borovik, T. Buhr, *et al.* "Observation of four-electron auger processes." *Journal of Physics: Conference Series*, 635(1):012033, September 2015. URL http://dx.doi.org/10.1088/1742-6596/635/1/012033.

[119] O. Keski-Rahkonen and M. O. Krause. "Total and partial atomic-level widths." *Atomic Data and Nuclear Data Tables*, 14(2):139–146, August 1974. URL http://dx.doi.org/10.1016/s0092-640x(74)80020-3.

[120] S. T. Perkins, D. E. Cullen, M. H. Chen, *et al.* "Tables and graphs of atomic subshell and relaxation data derived from the LLNL evaluated atomic data library (EADL), z = 1–100." Technical report, October 1991. URL http://dx.doi.org/10.2172/10121422.

[121] M. Uda, K. Maeda, A. Koyama, and Y. Sasa. "Chemical effects of f kvv auger spectra induced by photon impact." *Physical Review A*, 29(3):1258–1260, March 1984. URL http://dx.doi.org/10.1103/physreva.29.1258.

[122] S.-K. Son, L. Young, and R. Santra. "Impact of hollow-atom formation on coherent x-ray scattering at high intensity." *Physical Review A*, 83(3), March 2011. URL http://dx.doi.org/10.1103/physreva.83.033402.

[123] A. S. Schlachter, M. M. Sant'Anna, A. M. Covington, *et al.* "Lifetime of a k-shell vacancy in atomic carbon created by 1s→2p photoexcitation of c$^+$." *Journal of Physics B: Atomic, Molecular and Optical Physics*, 37(5):L103–L109, February 2004. URL http://dx.doi.org/10.1088/0953-4075/37/5/103.

[124] V. Stumpf, K. Gokhberg, and L. S. Cederbaum. "The role of metal ions in x-ray-induced photochemistry." *Nature Chemistry*, 8(3):237–241, January 2016. URL http://dx.doi.org/10.1038/nchem.2429.

[125] L. S. Cederbaum, J. Zobeley, and F. Tarantelli. "Giant intermolecular decay and fragmentation of clusters." *Physical Review Letters*, 79(24):4778–4781, December 1997. URL http://dx.doi.org/10.1103/physrevlett.79.4778.

[126] V. Averbukh, P. Demekhin, P. Kolorenč, *et al.* "Interatomic electronic decay processes in singly and multiply ionized clusters." *Journal of Electron Spectroscopy and Related Phenomena*, 183(1-3):36–47, January 2011. URL http://dx.doi.org/10.1016/j.elspec.2010.03.003.

[127] U. Hergenhahn. "Interatomic and intermolecular coulombic decay: The early years." *Journal of Electron Spectroscopy and Related Phenomena*, 184(3-6):78–90, April 2011. URL http://dx.doi.org/10.1016/j.elspec.2010.12.020.

[128] V. Stumpf, P. Kolorenč, K. Gokhberg, and L. S. Cederbaum. "Efficient pathway to neutralization of multiply charged ions produced in auger processes." *Physical Review Letters*, 110(25), June 2013. URL http://dx.doi.org/10.1103/physrevlett.110.258302.

[129] A. Rudenko, L. Inhester, K. Hanasaki, *et al.* "Femtosecond response of polyatomic molecules to ultra-intense hard x-rays." *Nature*, 546(7656):129–132, May 2017. URL http://dx.doi.org/10.1038/nature22373.

[130] A. D. Cicco, K. Hatada, E. Giangrisostomi, *et al.* "Interplay of electron heating and saturable absorption in ultrafast extreme ultraviolet transmission of condensed matter." *Physical Review B*, 90(22), December 2014. URL http://dx.doi.org/10.1103/physrevb.90.220303.

[131] D. S. Rackstraw, O. Ciricosta, S. M. Vinko, *et al.* "Saturable absorption of an x-ray free-electron-laser heated solid-density aluminum plasma." *Physical Review Letters*, 114(1), January 2015. URL http://dx.doi.org/10.1103/physrevlett.114.015003.

[132] H. Yoneda, Y. Inubushi, K. Nagamine, *et al.* "Atomic inner-shell laser at 1.5-ångström wavelength pumped by an x-ray free-electron laser." *Nature*, 524(7566):446–449, August 2015. URL http://dx.doi.org/10.1038/nature14894.

[133] N. Medvedev, U. Zastrau, E. Förster, D. O. Gericke, and B. Rethfeld. "Short-time electron dynamics in aluminum excited by femtosecond extreme ultraviolet radiation." *Physical Review Letters*, 107(16), October 2011. URL http://dx.doi.org/10.1103/physrevlett.107.165003.

[134] I. Milov, V. Lipp, D. Ilnitsky, *et al.* "Similarity in ruthenium damage induced by photons with different energies: From visible light to hard x-rays." *Applied Surface Science*, 501:143973, January 2020. URL http://dx.doi.org/10.1016/j.apsusc.2019.143973.

[135] N. Medvedev, H. O. Jeschke, and B. Ziaja. "Nonthermal graphitization of diamond induced by a femtosecond x-ray laser pulse." *Physical Review B*, 88(22):224304, 2013. URL http://dx.doi.org/10.1103/PhysRevB.88.224304.

[136] N. Medvedev, A. Volkov, and B. Ziaja. "Electronic and atomic kinetics in solids irradiated with free-electron lasers or swift-heavy ions." *Nuclear Instruments and Methods in Physics Research Section B: Beam Interactions with Materials and Atoms*, 365:437–446, 2015. URL http://dx.doi.org/10.1016/j.nimb.2015.08.063.

[137] N. A. Medvedev, R. A. Rymzhanov, and A. E. Volkov. "Time-resolved electron kinetics in swift heavy ion irradiated solids." *Journal of Physics D: Applied Physics*, 48(35):355303, August 2015. URL http://dx.doi.org/10.1088/0022-3727/48/35/355303.

[138] V. Lipp, N. Medvedev, and B. Ziaja. "Classical monte-carlo simulations of x-ray induced electron cascades in various materials." In L. Juha, S. Bajt, and R. Soufli, editors, "Damage to VUV, EUV, and X-ray Optics VI," SPIE, May 2017. URL http://dx.doi.org/10.1117/12.2267939.

[139] S. D. Farahani, J. Chalupsky, T. Burian, *et al.* "Damage threshold of amorphous carbon mirror for 177ev FEL radiation." *Nuclear Instruments and Methods in Physics Research Section A: Accelerators, Spectrometers, Detectors and Associated Equipment*, 635(1):S39–S42, April 2011. URL http://dx.doi.org/10.1016/j.nima.2010.10.133.

[140] D. You, H. Fukuzawa, Y. Sakakibara, *et al.* "Charge transfer to ground-state ions produces free electrons." *Nature Communications*, 8(1), January 2017. URL http://dx.doi.org/10.1038/ncomms14277.

[141] B. F. Murphy, T. Osipov, Z. Jurek, *et al.* "Femtosecond x-ray-induced explosion of c60 at extreme intensity." *Nature Communications*, 5(1), June 2014. URL http://dx.doi.org/10.1038/ncomms5281.

[142] M. Hoener, C. Bostedt, H. Thomas, *et al.* "Charge recombination in soft x-ray laser produced nanoplasmas." *Journal of Physics B: Atomic, Molecular and Optical Physics*, 41(18):181001, September 2008. URL http://dx.doi.org/10.1088/0953-4075/41/18/181001.

[143] N. Berrah, L. Fang, T. Osipov, *et al.* "Emerging photon technologies for probing ultrafast molecular dynamics." *Faraday Discuss.*, 171:471–485, April 2014. URL http://dx.doi.org/10.1039/c4fd00015c.

[144] M. Toufarová, V. Hájková, J. Chalupský, *et al.* "Contrasting behavior of covalent and molecular carbon allotropes exposed to extreme ultraviolet and soft x-ray free-electron laser radiation." *Physical Review B*, 96(21):214101, 2017. URL http://dx.doi.org/10.1103/PhysRevB.96.214101.

[145] B. Ziaja, H. Wabnitz, F. Wang, E. Weckert, and T. Möller. "Energetics, ionization, and expansion dynamics of atomic clusters irradiated with short intense vacuum-ultraviolet pulses." *Physical Review Letters*, 102(20), May 2009. URL http://dx.doi.org/10.1103/physrevlett.102.205002.

[146] T. Gorkhover, S. Schorb, R. Coffee, *et al.* "Femtosecond and nanometre visualization of structural dynamics in superheated nanoparticles." *Nature Photonics*, 10(2):93–97, January 2016. URL http://dx.doi.org/10.1038/nphoton.2015.264.

[147] D. Rupp, L. Flückiger, M. Adolph, *et al.* "Recombination-enhanced surface expansion of clusters in intense soft x-ray laser pulses." *Physical Review Letters*, 117(15), October 2016. URL http://dx.doi.org/10.1103/physrevlett.117.153401.

[148] H. O. Jeschke, M. E. Garcia, and K. H. Bennemann. "Microscopic analysis of the laser-induced femtosecond graphitization of diamond." *Physical Review B*, 60(6):R3701–R3704, August 1999. URL http://dx.doi.org/10.1103/physrevb.60.r3701.

[149] J. Gaudin, N. Medvedev, J. Chalupský, *et al.* "Photon energy dependence of graphitization threshold for diamond irradiated with an intense xuv fel pulse." *Physical Review B*, 88(6):060101, 2013. URL http://dx.doi.org/10.1103/PhysRevB.88.060101.

[150] N. Medvedev and B. Ziaja. "Multistep transition of diamond to warm dense matter state revealed by femtosecond x-ray diffraction." *Scientific Reports*, 8(1), March 2018. URL http://dx.doi.org/10.1038/s41598-018-23632-8.

[151] D. Kraus, A. Ravasio, M. Gauthier, *et al.* "Nanosecond formation of diamond and lonsdaleite by shock compression of graphite." *Nature Communications*, 7(1), March 2016. URL http://dx.doi.org/10.1038/ncomms10970.

[152] D. M. Fritz, D. A. Reis, B. Adams, *et al.* "Ultrafast bond softening in bismuth: mapping a solid's interatomic potential with x-rays." *Science*, 315(5812):633–636, February 2007. URL http://dx.doi.org/10.1126/science.1135009.

[153] A. M. Lindenberg. "Atomic-scale visualization of inertial dynamics." *Science*, 308(5720):392–395, April 2005. URL http://dx.doi.org/10.1126/science.1107996.

[154] I. Inoue, Y. Inubushi, T. Sato, *et al.* "Observation of femtosecond x-ray interactions with matter using an x-ray–x-ray pump–probe scheme." *Proceedings of the National Academy of Sciences*, 113(6):1492–1497, January 2016. URL http://dx.doi.org/10.1073/pnas.1516426113.

[155] K. Nagaya, K. Motomura, E. Kukk, *et al.* "Ultrafast dynamics of a nucleobase analogue illuminated by a short intense x-ray free electron laser pulse." *Physical Review X*, 6(2), June 2016. URL http://dx.doi.org/10.1103/physrevx.6.021035.

[156] K. R. Beyerlein, H. O. Jönsson, R. Alonso-Mori, *et al.* "Ultrafast nonthermal heating of water initiated by an x-ray free-electron laser." *Proceedings of the National Academy of Sciences*, 115(22):5652–5657, May 2018. URL http://dx.doi.org/10.1073/pnas.1711220115.

[157] T. Q. Qiu and C. L. Tien. "Heat transfer mechanisms during short-pulse laser heating of metals." *Journal of Heat Transfer*, 115(4):835–841, November 1993. URL http://dx.doi.org/10.1115/1.2911377.

[158] R. Neutze, R. Wouts, D. van der Spoel, E. Weckert, and J. Hajdu. "Potential for biomolecular imaging with femtosecond x-ray pulses." *Nature*, 406(6797):752–757, August 2000. URL http://dx.doi.org/10.1038/35021099.

[159] J. D. Watson and F. H. C. Crick. "Molecular structure of nucleic acids: A structure for deoxyribose nucleic acid." *Nature*, 171(4356):737–738, April 1953. URL http://dx.doi.org/10.1038/171737a0.

[160] M. F. Perutz, M. G. Rossmann, A. F. Cullis, *et al.* "Structure of hæmoglobin." *Nature*, 185(4711):416–422, February 1960. URL http://dx.doi.org/10.1038/185416a0.

[161] P. F. Lindley. "The use of synchrotron radiation in protein crystallography." *Radiation Physics and Chemistry*, 45(3):367–383, March 1995. URL http://dx.doi.org/10.1016/0969-806x(93)e0005-p.

[162] H. M. Berman. "The protein data bank." *Nucleic Acids Research*, 28(1):235–242, January 2000. URL http://dx.doi.org/10.1093/nar/28.1.235.

[163] R. Henderson. "The potential and limitations of neutrons, electrons and x-rays for atomic resolution microscopy of unstained biological molecules." *Quarterly Reviews of Biophysics*, 28(2):171–193, May 1995. URL http://dx.doi.org/10.1017/s003358350000305x.

[164] K. J. Gaffney and H. N. Chapman. "Imaging atomic structure and dynamics with ultrafast x-ray scattering." *Science*, 316(5830):1444–1448, June 2007. URL http://dx.doi.org/10.1126/science.1135923.

[165] C. Song, H. Jiang, A. Mancuso, *et al.* "Quantitative imaging of single, unstained viruses with coherent x-rays." *Physical Review Letters*, 101(15), October 2008. URL http://dx.doi.org/10.1103/physrevlett.101.158101.

[166] A. P. Mancuso, A. Aquila, L. Batchelor, *et al.* "The single particles, clusters and biomolecules and serial femtosecond crystallography instrument of the european XFEL: initial installation." *Journal of Synchrotron Radiation*, 26(3):660–676, April 2019. URL http://dx.doi.org/10.1107/s1600577519003308.

[167] C. Aponte-Santamaría, J. S. Hub, and B. L. de Groot. "Dynamics and energetics of solute permeation through the plasmodium falciparum aquaglyceroporin." *Physical Chemistry Chemical Physics*, 12(35):10246, 2010. URL http://dx.doi.org/10.1039/c004384m.

[168] C. Gutt, L.-M. Stadler, A. Duri, *et al.* "Measuring temporal speckle correlations at ultrafast x-ray sources." *Optics Express*, 17(1):55, December 2008. URL http://dx.doi.org/10.1364/oe.17.000055.

[169] F. Perakis, G. Camisasca, T. J. Lane, *et al.* "Coherent x-rays reveal the influence of cage effects on ultrafast water dynamics." *Nature Communications*, 9(1), May 2018. URL http://dx.doi.org/10.1038/s41467-018-04330-5.

[170] A. Classen, K. Ayyer, H. N. Chapman, R. Röhlsberger, and J. von Zanthier. "Incoherent diffractive imaging via intensity correlations of hard x-rays." *Physical Review Letters*, 119(5), July 2017. URL http://dx.doi.org/10.1103/physrevlett.119.053401.

[171] M. Holler, M. Odstrcil, M. Guizar-Sicairos, *et al.* "Three-dimensional imaging of integrated circuits with macro- to nanoscale zoom." *Nature Electronics*, 2(10):464–470, October 2019. URL http://dx.doi.org/10.1038/s41928-019-0309-z.

[172] F. García-Moreno, P. H. Kamm, T. R. Neu, *et al.* "Using x-ray tomoscopy to explore the dynamics of foaming metal." *Nature Communications*, 10(1), August 2019. URL http://dx.doi.org/10.1038/s41467-019-11521-1.

[173] N. Medvedev. "Modeling warm dense matter formation within tight binding approximation." In L. Juha, S. Bajt, and S. Guizard, editors, "Optics Damage and Materials Processing by EUV/X-ray Radiation VII," SPIE, April 2019. URL http://dx.doi.org/10.1117/12.2520805.

[174] U. Zastrau, P. Sperling, M. Harmand, *et al.* "Resolving ultrafast heating of dense cryogenic hydrogen." *Physical Review Letters*, 112(10), March 2014. URL http://dx.doi.org/10.1103/physrevlett.112.105002.

[175] B. Rethfeld, A. Kaiser, M. Vicanek, and G. Simon. "Ultrafast dynamics of nonequilibrium electrons in metals under femtosecond laser irradiation." *Physical Review B*, 65(21), May 2002. URL http://dx.doi.org/10.1103/physrevb.65.214303.

[176] A. Ng. "Outstanding questions in electron-ion energy relaxation, lattice stability, and dielectric function of warm dense matter." *International Journal of Quantum Chemistry*, 112(1):150–160, September 2011. URL http://dx.doi.org/10.1002/qua.23197.

[177] K. Sokolowski-Tinten, R. K. Li, A. H. Reid, *et al.* "Thickness-dependent electron–lattice equilibration in laser-excited thin bismuth films." *New Journal of Physics*, 17(11):113047, November 2015. URL http://dx.doi.org/10.1088/1367-2630/17/11/113047.

[178] M. Z. Mo, Z. Chen, R. K. Li, *et al.* "Heterogeneous to homogeneous melting transition visualized with ultrafast electron diffraction." *Science*, 360(6396):1451–1455, June 2018. URL http://dx.doi.org/10.1126/science.aar2058.

[179] L. V. Zhigilei, Z. Lin, and D. S. Ivanov. "Atomistic modeling of short pulse laser ablation of metals: connections between melting, spallation, and phase explosion." *The Journal of Physical Chemistry C*, 113(27):11892–11906, June 2009. URL http://dx.doi.org/10.1021/jp902294m.

[180] R. F. Haglund. "Microscopic and mesoscopic aspects of laser-induced desorption and ablation." *Applied Surface Science*, 96-98:1–13, April 1996. URL http://dx.doi.org/10.1016/0169-4332(95)00371-1.

[181] J. Chalupský, L. Juha, V. Hájková, *et al.* "Non-thermal desorption/ablation of molecular solids induced by ultra-short soft x-ray pulses." *Optics Express*, 17(1):208–, 2009. URL http://dx.doi.org/10.1364/OE.17.000208.

[182] F. Büttner, I. Lemesh, M. Schneider, *et al.* "Field-free deterministic ultrafast creation of magnetic skyrmions by spin–orbit torques." *Nature Nanotechnology*, 12(11):1040–1044, October 2017. URL http://dx.doi.org/10.1038/nnano.2017.178.

[183] S. O. Mariager, F. Pressacco, G. Ingold, *et al.* "Structural and magnetic dynamics of a laser induced phase transition in FeRh." *Physical Review Letters*, 108(8), February 2012. URL http://dx.doi.org/10.1103/physrevlett.108.087201.

[184] T. Tajima and J. M. Dawson. "Laser electron accelerator." *Physical Review Letters*, 43(4):267–270, July 1979. URL http://dx.doi.org/10.1103/physrevlett.43.267.

[185] P. A. Walker, P. D. Alesini, A. S. Alexandrova, *et al.* "Horizon 2020 EuPRAXIA design study." *Journal of Physics: Conference Series*, 874:012029, July 2017. URL http://dx.doi.org/10.1088/1742-6596/874/1/012029.

[186] D. Giulietti and L. A. Gizzi. "X-ray emission from laser-produced plasmas." *La Rivista del Nuovo Cimento*, 21(10):1–93, October 1998. URL http://dx.doi.org/10.1007/bf02874624.

[187] Zel'dovich. *Physics of shock waves and high-temperature hydrodynamic phenomena.* Dover Publications, Mineola, N.Y, 2002. ISBN 978-0486420028.

[188] R. Cauble, D. W. Phillion, R. W. Lee, and T. J. Hoover. "X-ray driven flyer foil experiments near 1.0 gbar." *Journal of Quantitative Spectroscopy and Radiative Transfer*, 51(1-2):433–437, January 1994. URL http://dx.doi.org/10.1016/0022-4073(94)90107-4.

[189] H. Hu, X. Wang, and H. Zhai. "High-fluence femtosecond laser ablation of silica glass: effects of laser-induced pressure." *Journal of Physics D: Applied Physics*, 44(13):135202, March 2011. URL http://dx.doi.org/10.1088/0022-3727/44/13/135202.

[190] "Caught on camera: First movies of droplets getting blown up by x-ray laser.", 2016 (accessed March 15, 2020). URL https://www6.slac.stanford.edu/news/2016-05-23-caught-camera-first-movies-droplets-getting-blown-x-ray-laser.aspx.

[191] C. A. Stan, D. Milathianaki, H. Laksmono, *et al.* "Liquid explosions induced by x-ray laser pulses." *Nature Physics*, 12(10):966–971, May 2016. URL http://dx.doi.org/10.1038/nphys3779.

[192] Y. Wang, X. Liu, K.-S. Im, *et al.* "Ultrafast x-ray study of dense-liquid-jet flow dynamics using structure-tracking velocimetry." *Nature Physics*, 4(4):305–309, January 2008. URL http://dx.doi.org/10.1038/nphys840.

[193] M. O. Wiedorn, D. Oberthür, R. Bean, *et al.* "Megahertz serial crystallography." *Nature Communications*, 9(1), October 2018. URL http://dx.doi.org/10.1038/s41467-018-06156-7.

[194] E. Moshe, S. Eliezer, Z. Henis, *et al.* "Experimental measurements of the strength of metals approaching the theoretical limit predicted by the equation of state." *Applied Physics Letters*, 76(12):1555–1557, March 2000. URL http://dx.doi.org/10.1063/1.126094.

[195] L. Bocklage, C. Swoboda, K. Schlage, *et al.* "Spin precession mapping at ferromagnetic resonance via nuclear resonant scattering of synchrotron radiation." *Physical Review Letters*, 114(14), April 2015. URL http://dx.doi.org/10.1103/physrevlett.114.147601.

[196] M. Kirm, A. Andrejczuk, J. Krzywinski, and R. Sobierajski. "Influence of excitation density on luminescence decay in y3al5o12:ce and BaF2 crystals excited by free electron laser radiation in VUV." *Physica Status Solidi (C)*, 2(1):649–652, January 2005. URL http://dx.doi.org/10.1002/pssc.200460255.

[197] J. Krzywinski, A. Andrejczuk, R. M. Bionta, *et al.* "Saturation of a ce:y_3al_5o_12 scintillator response to ultra-short pulses of extreme ultraviolet soft x-ray and x-ray laser radiation." *Optical Materials Express*, 7(3):665, February 2017. URL http://dx.doi.org/10.1364/ome.7.000665.

[198] I. Pelant and J. Valenta. *Luminescence spectroscopy of semiconductors.* Oxford University Press, 2016. ISBN 0198757549. URL https://www.oxfordscholarship.com/view/10.1093/acprof:oso/9780199588336.001.0001/acprof-9780199588336.

[199] W. J. Parker, R. J. Jenkins, C. P. Butler, and G. L. Abbott. "Flash method of determining thermal diffusivity, heat capacity, and thermal conductivity." *Journal of Applied Physics*, 32(9):1679–1684, September 1961. URL http://dx.doi.org/10.1063/1.1728417.

[200] D. Bai, G. Chen, X. Zhang, and W. Wang. "Microsecond molecular dynamics simulations of the kinetic pathways of gas hydrate formation from solid surfaces." *Langmuir*, 27(10):5961–5967, May 2011. URL http://dx.doi.org/10.1021/la105088b.

[201] J. Chalupský, V. Hájková, V. Altapova, *et al.* "Damage of amorphous carbon induced by soft x-ray femtosecond pulses above and below the critical angle." *Applied Physics Letters*, 95(3):031111, July 2009. URL http://dx.doi.org/10.1063/1.3184785.

[202] A. Frolov, K. Kolacek, J. Schmidt, J. Straus, and A. Choukourov. "Nanostructuring of PMMA, GaAs, SiC and si samples by focused XUV laser beam." In L. Juha, S. Bajt, and S. Guizard, editors, "Optics damage and materials processing by EUV/X-ray radiation VII," SPIE, April 2019. URL http://dx.doi.org/10.1117/12.2521444.

[203] C. Svetina, R. Mankowsky, G. Knopp, *et al.* "Towards x-ray transient grating spectroscopy." *Optics Letters*, 44(3):574, January 2019. URL http://dx.doi.org/10.1364/ol.44.000574.

[204] P. Willmott. *An Introduction to Synchrotron Radiation*. Wiley, June 2011. URL http://dx.doi.org/10.1002/9781119970958.

[205] W. A. Barletta, J. Bisognano, J. N. Corlett, *et al.* "Free electron lasers: Present status and future challenges." *Nuclear Instruments and Methods in Physics Research Section A: Accelerators, Spectrometers, Detectors and Associated Equipment*, 618(1-3):69–96, June 2010. URL http://dx.doi.org/10.1016/j.nima.2010.02.274.

[206] F. R. Elder, A. M. Gurewitsch, R. V. Langmuir, and H. C. Pollock. "Radiation from electrons in a synchrotron." *Physical Review*, 71(11):829–830, June 1947. URL http://dx.doi.org/10.1103/physrev.71.829.5.

[207] T. C. Weekes, M. F. Cawley, D. J. Fegan, *et al.* "Observation of TeV gamma rays from the crab nebula using the atmospheric cerenkov imaging technique." *The Astrophysical Journal*, 342:379, July 1989. URL http://dx.doi.org/10.1086/167599.

[208] T. Beuvier, I. Probert, L. Beaufort, *et al.* "X-ray nanotomography of coccolithophores reveals that coccolith mass and segment number correlate with grid size." *Nature Communications*, 10(1), February 2019. URL http://dx.doi.org/10.1038/s41467-019-08635-x.

[209] J. M. J. Madey. "Stimulated emission of bremsstrahlung in a periodic magnetic field." *Journal of Applied Physics*, 42(5):1906–1913, April 1971. URL http://dx.doi.org/10.1063/1.1660466.

[210] A. M. Kondratenko and E. L. Saldin. "Generation of coherent radiation by a relativistic electron beam in an ondulator." *Particle Accelerators*, 10:207–216, 1980.

[211] R. Bonifacio, C. Pellegrini, and L. Narducci. "Collective instabilities and high-gain regime in a free electron laser." *Optics Communications*, 50(6):373–378, July 1984. URL http://dx.doi.org/10.1016/0030-4018(84)90105-6.

[212] V. Ayvazyan, N. Baboi, I. Bohnet, *et al.* "Generation of GW radiation pulses from a VUV free-electron laser operating in the femtosecond regime." *Physical Review Letters*, 88(10), February 2002. URL http://dx.doi.org/10.1103/physrevlett.88.104802.

[213] P. J. Neyman, J. Blau, K. R. Cohn, *et al.* "Free Electron Lasers in 2017." In "Proc. of International Free Electron Laser Conference (FEL'17), Santa Fe, NM, USA, August 20-25, 2017," Number 38 in International free electron laser conference, pages 204–209. JACoW, Geneva, Switzerland, Feb. 2018. ISBN 978-3-95450-179-3. URL http://dx.doi.org/https://doi.org/10.18429/JACoW-FEL2017-MOP066. Https://doi.org/10.18429/JACoW-FEL2017-MOP066.

[214] Y. Inubushi, I. Inoue, J. Kim, *et al.* "Measurement of the x-ray spectrum of a free electron laser with a wide-range high-resolution single-shot spectrometer." *Applied Sciences*, 7(6):584, June 2017. URL http://dx.doi.org/10.3390/app7060584.

[215] A. A. Zholents. "Method of an enhanced self-amplified spontaneous emission for x-ray free electron lasers." *Physical Review Special Topics - Accelerators and Beams*, 8(4), April 2005. URL http://dx.doi.org/10.1103/physrevstab.8.040701.

[216] E. Allaria, R. Appio, L. Badano, *et al.* "Highly coherent and stable pulses from the FERMI seeded free-electron laser in the extreme ultraviolet." *Nature Photonics*, 6(10):699–704, September 2012. URL http://dx.doi.org/10.1038/nphoton.2012.233.

[217] E. Allaria, D. Castronovo, P. Cinquegrana, *et al.* "Two-stage seeded soft-x-ray free-electron laser." *Nature Photonics*, 7(11):913–918, October 2013. URL http://dx.doi.org/10.1038/nphoton.2013.277.

[218] A. A. Lutman, J. P. MacArthur, M. Ilchen, *et al.* "Polarization control in an x-ray free-electron laser." *Nature Photonics*, 10(7):468–472, May 2016. URL http://dx.doi.org/10.1038/nphoton.2016.79.

[219] U. Frühling, M. Wieland, M. Gensch, *et al.* "Single-shot terahertz-field-driven x-ray streak camera." *Nature Photonics*, 3(9):523–528, August 2009. URL http://dx.doi.org/10.1038/nphoton.2009.160.

[220] R. Ivanov, J. Liu, G. Brenner, M. Brachmanski, and S. Düsterer. "FLASH free-electron laser single-shot temporal diagnostic: terahertz-field-driven streaking." *Journal of Synchrotron Radiation*, 25(1):26–31, January 2018. URL http://dx.doi.org/10.1107/s160057751701253x.

[221] R. Riedel, A. Al-Shemmary, M. Gensch, *et al.* "Single-shot pulse duration monitor for extreme ultraviolet and x-ray free-electron lasers." *Nature Communications*, 4(1), April 2013. URL http://dx.doi.org/10.1038/ncomms2754.

[222] R. Ivanov, I. Bermudez, G. Brenner, J. Liu, and S. Dusterer. "Single shot temporal characterization of SASE XUV FEL pulses." In "2019 Conference on Lasers and Electro-Optics Europe & European Quantum Electronics Conference (CLEO/Europe-EQEC)," IEEE, June 2019. URL http://dx.doi.org/10.1109/cleoe-eqec.2019.8871504.

[223] S. Bajt, H. N. Chapman, A. Aquila, and E. Gullikson. "High-efficiency x-ray gratings with asymmetric-cut multilayers." *Journal of the Optical Society of America A*, 29(3):216, February 2012. URL http://dx.doi.org/10.1364/josaa.29.000216.

[224] H. Baumhacker, G. Brederlow, E. Fill, *et al.* "Layout and performance of the asterix IV iodine laser at MPQ, garching." *Applied Physics B Laser and Optics*, 61(4):325–332, October 1995. URL http://dx.doi.org/10.1007/bf01081531.

[225] K. Jungwirth, A. Cejnarova, L. Juha, *et al.* "The prague asterix laser system." *Physics of Plasmas*, 8(5):2495–2501, May 2001. URL http://dx.doi.org/10.1063/1.1350569.

[226] B. Rus, A. Carillon, B. Gauthé, *et al.* "Observation of intense soft-x-ray lasing at the j = 0 to j = 1 transition in neonlike zinc." *Journal of the Optical Society of America B*, 11(4):564, April 1994. URL http://dx.doi.org/10.1364/josab.11.000564.

[227] B. Rus, T. Mocek, A. R. Präg, *et al.* "Multimillijoule, highly coherent x-ray laser at 21 nm operating in deep saturation through double-pass amplification." *Physical Review A*, 66(6):–, 2002. URL http://dx.doi.org/10.1103/PhysRevA.66.063806.

[228] S. Heinbuch, M. Grisham, D. Martz, and J. J. Rocca. "Demonstration of a desk-top size high repetition rate soft x-ray laser." *Optics Express*, 13(11):4050–, 2005. URL http://dx.doi.org/10.1364/OPEX.13.004050.

[229] M. Perry. "The amazing power of the petawatt." *Science & Technology Review*, pages 4–12, March 2000. URL https://str.llnl.gov.

[230] M. J. Edwards, P. K. Patel, J. D. Lindl, *et al.* "Progress towards ignition on the national ignition facility." *Physics of Plasmas*, 20(7):070501, July 2013. URL http://dx.doi.org/10.1063/1.4816115.

[231] N. Fleurot, C. Cavailler, and J. Bourgade. "The laser mégajoule (LMJ) project dedicated to inertial confinement fusion: Development and construction status." *Fusion Engineering and Design*, 74(1-4):147–154, November 2005. URL http://dx.doi.org/10.1016/j.fusengdes.2005.06.251.

[232] S. Gales, K. A. Tanaka, D. L. Balabanski, *et al.* "The extreme light infrastructure–nuclear physics (ELI-NP) facility: new horizons in physics with 10 PW ultra-intense lasers and 20 MeV brilliant gamma beams." *Reports on Progress in Physics*, 81(9):094301, August 2018. URL http://dx.doi.org/10.1088/1361-6633/aacfe8.

[233] "Extreme light infrastructure - nuclear physics (eli-np)." https://www.eli-np.ro/. (Accessed on 03/20/2020).

[234] "Extreme light." *Nature Materials*, 15(1):1–1, December 2015. URL http://dx.doi.org/10.1038/nmat4533.

[235] P. Mason, M. Divoký, K. Ertel, *et al.* "Kilowatt average power 100 j-level diode pumped solid state laser." *Optica*, 4(4):438, April 2017. URL http://dx.doi.org/10.1364/optica.4.000438.

[236] T. Gaumnitz, A. Jain, Y. Pertot, *et al.* "Streaking of 43-attosecond soft-x-ray pulses generated by a passively CEP-stable mid-infrared driver." *Optics Express*, 25(22):27506, October 2017. URL http://dx.doi.org/10.1364/oe.25.027506.

[237] E. A. Nanni, W. R. Huang, K.-H. Hong, *et al.* "Terahertz-driven linear electron acceleration." *Nature Communications*, 6(1), October 2015. URL http://dx.doi.org/10.1038/ncomms9486.

[238] D. Zhang, A. Fallahi, M. Hemmer, *et al.* "Segmented terahertz electron accelerator and manipulator (STEAM)." *Nature Photonics*, 12(6):336–342, April 2018. URL http://dx.doi.org/10.1038/s41566-018-0138-z.

[239] W. P. Leemans, B. Nagler, A. J. Gonsalves, *et al.* "GeV electron beams from a centimetre-scale accelerator." *Nature Physics*, 2(10):696–699, September 2006. URL http://dx.doi.org/10.1038/nphys418.

[240] H.-P. Schlenvoigt, K. Haupt, A. Debus, *et al.* "A compact synchrotron radiation source driven by a laser-plasma wakefield accelerator." *Nature Physics*, 4(2):130–133, December 2008. URL http://dx.doi.org/10.1038/nphys811.

[241] T. Ishikawa, H. Aoyagi, T. Asaka, *et al.* "A compact x-ray free-electron laser emitting in the sub-ångström region." *Nature Photonics*, 6(8):540–544, June 2012. URL http://dx.doi.org/10.1038/nphoton.2012.141.

[242] M. Vannoni and I. F. Martìn. "Absolute interferometric characterization of an x-ray mirror surface profile." *Metrologia*, 53(1):1–6, December 2015. URL http://dx.doi.org/10.1088/0026-1394/53/1/1.

[243] H. Yumoto, H. Mimura, T. Koyama, *et al.* "Focusing of x-ray free-electron laser pulses with reflective optics." *Nature Photonics*, 7(1):43–47, December 2012. URL http://dx.doi.org/10.1038/nphoton.2012.306.

[244] I. Freijo-Martín, R. Bean, M. Vannoni, and H. Sinn. "Metrology of micron focusing KB mirrors for SPB/SFX instrument and preliminary commissioning results at european XFEL." In D. Spiga and H. Mimura, editors, "Adaptive X-Ray Optics V," SPIE, September 2018. URL http://dx.doi.org/10.1117/12.2322979.

[245] S. Bajt, H. N. Chapman, A. J. Nelson, *et al.* "Sub-micron focusing of soft x-ray free electron laser beam." In L. Juha, S. Bajt, and R. Sobierajski, editors, "Damage to VUV, EUV, and X-Ray Optics II," SPIE, May 2009. URL http://dx.doi.org/10.1117/12.822498.

[246] F. Seiboth, A. Schropp, M. Scholz, *et al.* "Perfect x-ray focusing via fitting corrective glasses to aberrated optics." *Nature Communications*, 8(1), March 2017. URL http://dx.doi.org/10.1038/ncomms14623.

[247] R. M. Bionta, K. M. Skulina, and J. Weinberg. "Hard x-ray sputtered-sliced phase zone plates." *Applied Physics Letters*, 64(8):945–947, February 1994. URL http://dx.doi.org/10.1063/1.110968.

[248] H. Yan, R. Conley, N. Bouet, and Y. S. Chu. "Hard x-ray nanofocusing by multilayer laue lenses." *Journal of Physics D: Applied Physics*, 47(26):263001, June 2014. URL http://dx.doi.org/10.1088/0022-3727/47/26/263001.

[249] R. Conley, N. Bouet, Y. S. Chu, *et al.* "Multilayer laue lens: A brief history and current status." *Synchrotron Radiation News*, 29(4):16–20, July 2016. URL http://dx.doi.org/10.1080/08940886.2016.1198669.

[250] A. J. Morgan, M. Prasciolu, A. Andrejczuk, *et al.* "High numerical aperture multilayer laue lenses." *Scientific Reports*, 5(1), June 2015. URL http://dx.doi.org/10.1038/srep09892.

[251] S. Bajt, M. Prasciolu, H. Fleckenstein, *et al.* "X-ray focusing with efficient high-NA multilayer laue lenses." *Light: Science & Applications*, 7(3):17162–17162, November 2018. URL http://dx.doi.org/10.1038/lsa.2017.162.

[252] R. P. Feynman. "There's plenty of room at the bottom [data storage]." *Journal of Microelectromechanical Systems*, 1(1):60–66, March 1992. URL http://dx.doi.org/10.1109/84.128057.

[253] R. B. Miles, W. R. Lempert, and J. N. Forkey. "Laser rayleigh scattering." *Measurement Science and Technology*, 12(5):R33–R51, April 2001. URL http://dx.doi.org/10.1088/0957-0233/12/5/201.

[254] R. Singh. "C. v. raman and the discovery of the raman effect." *Physics in Perspective*, 4(4):399–420, Dec 2002. URL http://dx.doi.org/10.1007/s000160200002.

[255] G. Eckhardt, R. W. Hellwarth, F. J. McClung, *et al.* "Stimulated raman scattering from organic liquids." *Physical Review Letters*, 9(11):455–457, December 1962. URL http://dx.doi.org/10.1103/physrevlett.9.455.

[256] V. M. Gerrish. "Hapter 13 - characterization and quantification of detector performance." In T. Schlesinger and R. B. James, editors, "Semiconductors and Semimetals," volume 43 of *Semiconductors and Semimetals*, pages 493 – 530. Elsevier, 1995. URL http://dx.doi.org/https://doi.org/10.1016/S0080-8784(08)62752-0.

[257] J. F. Moulder and J. Chastain. *Handbook of x-ray photoelectron spectroscopy: A reference book of standard spectra for identification and interpretation of XPS data.* Physical Electronics Division, Perkin-Elmer Corporation, 1992. ISBN 9780962702624. URL https://books.google.cz/books?id=A_XGQgAACAAJ.

[258] S. L. Pape, P. Zeitoun, M. Idir, *et al.* "Electromagnetic-field distribution measurements in the soft x-ray range: Full characterization of a soft x-ray laser beam." *Physical Review Letters*, 88(18), April 2002. URL http://dx.doi.org/10.1103/physrevlett.88.183901.

[259] B. Flöter, P. Juranić, S. Kapitzki, *et al.* "EUV hartmann sensor for wavefront measurements at the free-electron LASer in hamburg." *New Journal of Physics*, 12(8):083015, August 2010. URL http://dx.doi.org/10.1088/1367-2630/12/8/083015.

[260] M. Seaberg, R. Cojocaru, S. Berujon, *et al.* "Wavefront sensing at x-ray free-electron lasers." *Journal of Synchrotron Radiation*, 26(4):1115–1126, June 2019. URL http://dx.doi.org/10.1107/s1600577519005721.

[261] A. Schropp, R. Hoppe, V. Meier, *et al.* "Full spatial characterization of a nanofocused x-ray free-electron laser beam by ptychographic imaging." *Scientific Reports*, 3(1), April 2013. URL http://dx.doi.org/10.1038/srep01633.

[262] D. Nilsson, F. Uhlén, A. Holmberg, *et al.* "Ronchi test for characterization of nanofocusing optics at a hard x-ray free-electron laser." *Optics Letters*, 37(24):5046, December 2012. URL http://dx.doi.org/10.1364/ol.37.005046.

[263] B. Nagler, A. Aquila, S. Boutet, *et al.* "Focal spot and wavefront sensing of an x-ray free electron laser using ronchi shearing interferometry." *Scientific Reports*, 7(1), October 2017. URL http://dx.doi.org/10.1038/s41598-017-13710-8.

[264] T. A. Pikuz, A. Y. Faenov, Y. Fukuda, *et al.* "Soft x-ray free-electron laser imaging by LiF crystal and film detectors over a wide range of fluences." *Applied Optics*, 52(3):509, January 2013. URL http://dx.doi.org/10.1364/ao.52.000509.

[265] F. Bonfigli, N. Hartley, Y. Inubushi, *et al.* "Photoluminescence properties and characterization of LiF-based imaging detector irradiated by 10 keV XFEL beam." In L. Juha, S. Bajt, and S. Guizard, editors, "Optics Damage and Materials Processing by EUV/X-ray Radiation VII," SPIE, April 2019. URL http://dx.doi.org/10.1117/12.2520907.

[266] K. Toyota, Z. Jurek, S.-K. Son, *et al.* "xcalib: a focal spot calibrator for intense x-ray free-electron laser pulses based on the charge state distributions of light atoms." *Journal of Synchrotron Radiation*, 26(4):1017–1030, May 2019. URL http://dx.doi.org/10.1107/s1600577519003564.

[267] J. Chalupský, J. Krzywinski, L. Juha, *et al.* "Spot size characterization of focused non-gaussian x-ray laser beams." *Optics Express*, 18(26):27836–27845, 2010. URL http://dx.doi.org/10.1364/OE.18.027836.

[268] J. Chalupský, P. Boháček, V. Hájková, *et al.* "Comparing different approaches to characterization of focused x-ray laser beams." *Nuclear Instruments and Methods in Physics Research Section A: Accelerators, Spectrometers, Detectors and Associated Equipment*, 631(1):130–133, March 2011. URL http://dx.doi.org/10.1016/j.nima.2010.12.040.

[269] N. Gerasimova, S. Dziarzhytski, H. Weigelt, *et al.* "In situ focus characterization by ablation technique to enable optics alignment at an XUV FEL source." *Review of Scientific Instruments*, 84(6):065104, June 2013. URL http://dx.doi.org/10.1063/1.4807896.

[270] K. Juráňová, T. Burian, V. Hájková, *et al.* "AbloCAM: a versatile optomechanical, semi-automated tool for an in situ characterization and optimization of focused XUV/x-ray laser beam (conference presentation)." In L. Juha, S. Bajt, and S. Guizard, editors, "Optics Damage and Materials Processing by EUV/X-ray Radiation VII," SPIE, May 2019. URL http://dx.doi.org/10.1117/12.2524883.

[271] J. M. Liu. "Simple technique for measurements of pulsed gaussian-beam spot sizes." *Optics Letters*, 7(5):196, May 1982. URL http://dx.doi.org/10.1364/ol.7.000196.

[272] J. Chalupský, L. Juha, J. Kuba, *et al.* "Characteristics of focused soft x-ray free-electron laser beam determined by ablation of organic molecular solids." *Optics Express*, 15(10):6036, 2007. URL http://dx.doi.org/10.1364/oe.15.006036.

[273] L. Juha, M. Bittner, D. Chvostova, *et al.* "Ablation of organic polymers by 46.9-nm-laser radiation." *Applied Physics Letters*, 86(3):034109, January 2005. URL http://dx.doi.org/10.1063/1.1854741.

[274] L. Juha. "Short-wavelength ablation of molecular solids: pulse duration and wavelength effects." *Journal of Micro/Nanolithography, MEMS, and MOEMS*, 4(3):033007, July 2005. URL http://dx.doi.org/10.1117/1.2037467.

[275] T. Mocek, B. Rus, M. Stupka, *et al.* "Focusing a multimillijoule soft x-ray laser at 21nm." *Applied Physics Letters*, 89(5):051501, July 2006. URL http://dx.doi.org/10.1063/1.2260822.

[276] T. Burian, V. Hájková, J. Chalupský, *et al.* "Soft x-ray free-electron laser induced damage to inorganic scintillators." *Optical Materials Express*, 5(2):254, January 2015. URL http://dx.doi.org/10.1364/ome.5.000254.

[277] I. Horcas, R. Fernández, J. M. Gómez-Rodríguez, *et al.* "WSxM." *Review of Scientific Instruments*, 78(1):013705–, 2007. URL http://dx.doi.org/10.1063/1.2432410.

[278] B. Rösner, F. Döring, P. R. Ribič, *et al.* "High resolution beam profiling of x-ray free electron laser radiation by polymer imprint development." *Optics Express*, 25(24):30686, November 2017. URL http://dx.doi.org/10.1364/oe.25.030686.

[279] E. M. Lehockey, I. Reid, and I. Hill. "The radiation chemistry of poly(methyl methacrylate) polymer resists." *Journal of Vacuum Science & Technology A: Vacuum, Surfaces, and Films*, 6(4):2221–2225, July 1988. URL http://dx.doi.org/10.1116/1.575014.

[280] T. Coffey, S. G. Urquhart, and H. Ade. "Characterization of the effects of soft x-ray irradiation on polymers." *Journal of Electron Spectroscopy and Related Phenomena*, 122(1):65–78, January 2002. URL http://dx.doi.org/10.1016/s0368-2048(01)00342-5.

[281] C. Peth, F. Barkusky, and K. Mann. "Near-edge x-ray absorption fine structure measurements using a laboratory-scale XUV source." *Journal of Physics D: Applied Physics*, 41(10):105202, April 2008. URL http://dx.doi.org/10.1088/0022-3727/41/10/105202.

[282] T. Burian, M. Toufarová, J. Chalupský, *et al.* "Efficient erosion of an organic polymer irradiated by multiple shots of the x-ray free-electron laser at a fluence below the single-shot ablation threshold: comparing the experiment with two models." *Physical Review Applied*, submitted.

[283] M. A. Bowler, B. Faatz, F. Siewert, and K. I. Tiedtke. "Investigating the effect of mirror imperfections in photon transport systems for fels." *Proc. 31st Int. Free Electron Laser Conf. (FEL'09)*, pages 534–537, August 2009. URL http://accelconf.web.cern.ch/AccelConf/FEL2009/papers/wepc16.pdf.

[284] E. M. Gullikson, P. Denham, S. Mrowka, and J. H. Underwood. "Absolute photoabsorption measurements of mg, al, and si in the soft-x-ray region below theL2, 3edges." *Physical Review B*, 49(23):16283–16288, June 1994. URL http://dx.doi.org/10.1103/physrevb.49.16283.

[285] R. Keenan, C. L. S. Lewis, J. S. Wark, and E. Wolfrum. "Measurements of the XUV transmission of aluminium with a soft x-ray laser." *Journal of Physics B: Atomic, Molecular and Optical Physics*, 35(20):L447–L451, September 2002. URL http://dx.doi.org/10.1088/0953-4075/35/20/102.

[286] S. M. Vinko, G. Gregori, M. P. Desjarlais, *et al.* "Free-free opacity in warm dense aluminum." *High Energy Density Physics*, 5(3):124–131, September 2009. URL http://dx.doi.org/10.1016/j.hedp.2009.04.004.

[287] C. A. Iglesias. "XUV absorption by solid-density aluminum." *High Energy Density Physics*, 6(3):311–317, September 2010. URL http://dx.doi.org/10.1016/j.hedp.2010.01.004.

[288] D. Rackstraw, S. Vinko, O. Ciricosta, *et al.* "Opacity effects in a solid-density aluminium plasma created by photo-excitation with an x-ray laser." *High Energy Density Physics*, 11:59–69, June 2014. URL http://dx.doi.org/10.1016/j.hedp.2014.02.003.

[289] B. Kettle, T. Dzelzainis, S. White, *et al.* "Experimental measurements of the collisional absorption of XUV radiation in warm dense aluminium." *Physical Review E*, 94(2), August 2016. URL http://dx.doi.org/10.1103/physreve.94.023203.

[290] F. Bisio, E. Principi, M. Magnozzi, *et al.* "Long-lived nonthermal electron distribution in aluminum excited by femtosecond extreme ultraviolet radiation." *Physical Review B*, 96(8), August 2017. URL http://dx.doi.org/10.1103/physrevb.96.081119.

[291] N. R. Shaffer, N. G. Ferris, J. Colgan, D. P. Kilcrease, and C. E. Starrett. "Free-free opacity in dense plasmas with an average atom model." *High Energy Density Physics*, 23:31–37, June 2017. URL http://dx.doi.org/10.1016/j.hedp.2017.02.008.

[292] K. Hatada and A. D. Cicco. "Modeling non-equilibrium dynamics and saturable absorption induced by free electron laser radiation." *Applied Sciences*, 7(8):814, August 2017. URL http://dx.doi.org/10.3390/app7080814.

[293] G. O. Williams, S. Künzel, S. Daboussi, *et al.* "Tracking the ultrafast XUV optical properties of x-ray free-electron-laser heated matter with high-order harmonics." *Physical Review A*, 97(2), February 2018. URL http://dx.doi.org/10.1103/physreva.97.023414.

[294] H.-G. Birken, W. Jark, C. Kunz, and R. Wolf. "Angular dependent photoelectric yield and optical constants of al between 40 and 600 eV." *Nuclear Instruments and Methods in Physics Research Section A: Accelerators, Spectrometers, Detectors and Associated Equipment*, 253(1):166–170, December 1986. URL http://dx.doi.org/10.1016/0168-9002(86)91141-1.

[295] C. D. Decker, W. B. Mori, J. M. Dawson, and T. Katsouleas. "Nonlinear collisional absorption in laser-driven plasmas." *Physics of Plasmas*, 1(12):4043–4049, December 1994. URL http://dx.doi.org/10.1063/1.870874.

[296] B. Rus, T. Mocek, M. Kozlová, *et al.* "High energy density matter generation using a focused soft-x-ray laser for volumetric heating of thin foils." *High Energy Density Physics*, 7(1):11–16, March 2011. URL http://dx.doi.org/10.1016/j.hedp.2010.05.001.

[297] M. Wöstmann, R. Mitzner, T. Noll, *et al.* "The XUV split-and-delay unit at beamline BL2 at FLASH." *Journal of Physics B: Atomic, Molecular and Optical Physics*, 46(16):164005, August 2013. URL http://dx.doi.org/10.1088/0953-4075/46/16/164005.

[298] K. Kolacek, A. Frolov, J. Schmidt, *et al.* "Aging of al thin film extreme ultraviolet filters." In L. Juha, S. Bajt, and S. Guizard, editors, "Optics Damage and Materials Processing by EUV/X-ray Radiation VII," SPIE, April 2019. URL http://dx.doi.org/10.1117/12.2521988.

[299] T. W. J. Dzelzainis, J. Chalupsky, M. Fajardo, *et al.* "Plasma emission spectroscopy of solids irradiated by intense XUV pulses from a free electron laser." *High Energy Density Physics*, 6(1):109–112, January 2010. URL http://dx.doi.org/10.1016/j.hedp.2009.05.017.

[300] A. A. Balandin, S. Ghosh, W. Bao, *et al.* "Superior thermal conductivity of single-layer graphene." *Nano Letters*, 8(3):902–907, 2008. URL http://dx.doi.org/10.1021/nl0731872.

[301] K. S. Novoselov, D. Jiang, F. Schedin, *et al.* "Two-dimensional atomic crystals." *Proceedings of the National Academy of Sciences*, 102(30):10451–10453, 2005. URL http://dx.doi.org/10.1073/pnas.0502848102.

[302] A. K. Geim and K. S. Novoselov. "The rise of graphene." *Nature Materials*, 6(3):183–191, 2007. URL http://dx.doi.org/10.1038/nmat1849.

[303] A. Reina, X. Jia, J. Ho, *et al.* "Large area, few-layer graphene films on arbitrary substrates by chemical vapor deposition." *Nano Letters*, 9(1):30–35, 2009. URL http://dx.doi.org/10.1021/nl801827v.

[304] J. Kim and H. Park. "Toward faster nonnegative matrix factorization." *2008 Eighth IEEE International Conference on Data Mining*, pages 353–362, 2008. URL http://dx.doi.org/10.1109/ICDM.2008.149.

[305] H. Boehm, R. Setton, and E. Stumpp. "Nomenclature and terminology of graphite intercalation compounds. report by a subgroup of the international committee for characterization and terminology of carbon and graphite on suggestions for rules for the nomenclature and terminology of graphite intercalation compounds." *Synthetic Metals*, 11(6):363–371, October 1985. URL http://dx.doi.org/10.1016/0379-6779(85)90068-2.

[306] K. S. Novoselov, A. K. Geim, S. V. Morozov, *et al.* "Electric field effect in atomically thin carbon films." *Science*, 306(5696):666–669, 2004. URL http://dx.doi.org/10.1126/science.1102896.

[307] A. K. Geim. "Graphene prehistory." *Physica Scripta*, T146:014003, January 2012. URL http://dx.doi.org/10.1088/0031-8949/2012/t146/014003.

[308] "The nobel prize in physics 2010." https://www.nobelprize.org/prizes/physics/2010/summary/. (Accessed on 10/15/2019).

[309] D. D. L. Chung. "Review graphite." *Journal of Materials Science*, 37(8):1475–1489, 2002. URL http://dx.doi.org/10.1023/a:1014915307738.

[310] K. V. Emtsev, A. Bostwick, K. Horn, *et al.* "Towards wafer-size graphene layers by atmospheric pressure graphitization of silicon carbide." *Nature Materials*, 8(3):203–207, 2009. URL http://dx.doi.org/10.1038/nmat2382.

[311] Y.-M. Lin, C. Dimitrakopoulos, K. A. Jenkins, *et al.* "100-GHz transistors from wafer-scale epitaxial graphene." *Science*, 327(5966):662–662, 2010. URL http://dx.doi.org/10.1126/science.1184289.

[312] M. Sprinkle, M. Ruan, Y. Hu, *et al.* "Scalable templated growth of graphene nanoribbons on sic." *Nature Nanotechnology*, 5(10):727–731, 2010. URL http://dx.doi.org/10.1038/nnano.2010.192.

[313] J. Kunc, M. Rejhon, E. Belas, *et al.* "Effect of residual gas composition on epitaxial growth of graphene on sic." *Physical Review Applied*, 8(4):044011, 2017. URL http://dx.doi.org/10.1103/PhysRevApplied.8.044011.

[314] M. Conrad, J. Rault, Y. Utsumi, *et al.* "Structure and evolution of semiconducting buffer graphene grown on SiC(0001)." *Physical Review B*, 96(19), November 2017. URL http://dx.doi.org/10.1103/physrevb.96.195304.

[315] C. Riedl, C. Coletti, T. Iwasaki, A. A. Zakharov, and U. Starke. "Quasi-free-standing epitaxial graphene on sic obtained by hydrogen intercalation." *Physical Review Letters*, 103(24):246804, 2009. URL http://dx.doi.org/10.1103/PhysRevLett.103.246804.

[316] J. Jobst, D. Waldmann, F. Speck, *et al.* "Quantum oscillations and quantum hall effect in epitaxial graphene." *Physical Review B*, 81(19):195434, 2010. URL http://dx.doi.org/10.1103/PhysRevB.81.195434.

[317] S. Weingart, C. Bock, U. Kunze, *et al.* "Influence of the growth conditions of epitaxial graphene on the film topography and the electron transport properties." *Physica E: Low-dimensional Systems and Nanostructures*, 42(4):687–690, 2010. URL http://dx.doi.org/10.1016/j.physe.2009.11.006.

[318] F. Speck, J. Jobst, F. Fromm, *et al.* "The quasi-free-standing nature of graphene on h-saturated sic(0001)." *Applied Physics Letters*, 99(12):122106, 2011. URL http://dx.doi.org/10.1063/1.3643034.

[319] M. H. Oliveira, T. Schumann, F. Fromm, *et al.* "Formation of high-quality quasi-free-standing bilayer graphene on sic(0001) by oxygen intercalation upon annealing in air." *Carbon*, 52:83–89, 2013. URL http://dx.doi.org/10.1016/j.carbon.2012.09.008.

[320] J. Bao, W. Norimatsu, H. Iwata, *et al.* "Synthesis of freestanding graphene on sic by a rapid-cooling technique." *Physical Review Letters*, 117(20):205501, 2016. URL http://dx.doi.org/10.1103/PhysRevLett.117.205501.

[321] L. S. Ramsdell. "The crystal structure of alpha-sic, type iv." *American Mineralogist*, 1944(29):431–442, 1944.

[322] M. Pozzo, D. Alfè, P. Lacovig, *et al.* "Thermal expansion of supported and freestanding graphene." *Physical Review Letters*, 106(13):135501, 2011. URL http://dx.doi.org/10.1103/PhysRevLett.106.135501.

[323] K. V. Emtsev, F. Speck, T. Seyller, L. Ley, and J. D. Riley. "Interaction, growth, and ordering of epitaxial graphene on sic0001 surfaces." *Physical Review B*, 77(15):155303, 2008. URL http://dx.doi.org/10.1103/PhysRevB.77.155303.

[324] Z. H. Ni, W. Chen, X. F. Fan, *et al.* "Raman spectroscopy of epitaxial graphene on a sic substrate." *Physical Review B*, 77(11):115416, 2008. URL http://dx.doi.org/10.1103/PhysRevB.77.115416.

[325] D. A. Schmidt, T. Ohta, and T. E. Beechem. "Strain and charge carrier coupling in epitaxial graphene." *Physical Review B*, 84(23):235422, 2011. URL http://dx.doi.org/10.1103/PhysRevB.84.235422.

[326] T. M. G. Mohiuddin, A. Lombardo, R. R. Nair, *et al.* "Uniaxial strain in graphene by raman spectroscopy: G peak splitting, grüneisen parameters, and sample orientation." *Physical Review B*, 79(20):205433, 2009. URL http://dx.doi.org/10.1103/PhysRevB.79.205433.

[327] M. Huang, H. Yan, T. F. Heinz, and J. Hone. "Probing strain-induced electronic structure change in graphene by raman spectroscopy." *Nano Letters*, 10(10):4074–4079, 2010. URL http://dx.doi.org/10.1021/nl102123c.

[328] S. Pisana, M. Lazzeri, C. Casiraghi, *et al.* "Breakdown of the adiabatic born–oppenheimer approximation in graphene." *Nature Materials*, 6(3):198–201, February 2007. URL http://dx.doi.org/10.1038/nmat1846.

[329] J. Yan, Y. Zhang, P. Kim, and A. Pinczuk. "Electric field effect tuning of electron-phonon coupling in graphene." *Phys. Rev. Lett.*, 98:166802, Apr 2007. URL http://dx.doi.org/10.1103/PhysRevLett.98.166802.

[330] R. Yang, Q. S. Huang, X. L. Chen, G. Y. Zhang, and H.-J. Gao. "Substrate doping effects on raman spectrum of epitaxial graphene on SiC." *Journal of Applied Physics*, 107(3):034305, February 2010. URL http://dx.doi.org/10.1063/1.3283922.

[331] D. Graf, F. Molitor, K. Ensslin, *et al.* "Spatially resolved raman spectroscopy of single- and few-layer graphene." *Nano Letters*, 7(2):238–242, 2007. URL http://dx.doi.org/10.1021/nl061702a.

[332] F. Tuinstra and J. L. Koenig. "Raman spectrum of graphite." *The Journal of Chemical Physics*, 53(3):1126–1130, August 1970. URL http://dx.doi.org/10.1063/1.1674108.

[333] C. Thomsen and S. Reich. "Double resonant raman scattering in graphite." *Physical Review Letters*, 85(24):5214–5217, December 2000. URL http://dx.doi.org/10.1103/physrevlett.85.5214.

[334] B. Krauss, T. Lohmann, D.-H. Chae, *et al.* "Laser-induced disassembly of a graphene single crystal into a nanocrystalline network." *Physical Review B*, 79(16):165428, April 2009. URL http://dx.doi.org/10.1103/physrevb.79.165428.

[335] K. V. Zakharchenko, M. I. Katsnelson, and A. Fasolino. "Finite temperature lattice properties of graphene beyond the quasiharmonic approximation." *Phys. Rev. Lett.*, 102:046808, Jan 2009. URL http://dx.doi.org/10.1103/PhysRevLett.102.046808.

[336] "Silicon carbide (SiC), lattice parameters, thermal expansion." In "Group IV Elements, IV-IV and III-V Compounds. Part b - Electronic, Transport, Optical and Other Properties," pages 1–11. Springer-Verlag. URL http://dx.doi.org/10.1007/10832182_600.

[337] J. Kunc, Y. Hu, J. Palmer, C. Berger, and W. A. de Heer. "A method to extract pure raman spectrum of epitaxial graphene on sic." *Applied Physics Letters*, 103(20):201911, 2013. URL http://dx.doi.org/10.1063/1.4830374.

[338] A. C. Ferrari, J. C. Meyer, V. Scardaci, *et al.* "Raman spectrum of graphene and graphene layers." *Physical Review Letters*, 97(18):187401, 2006. URL http://dx.doi.org/10.1103/PhysRevLett.97.187401.

[339] J.-S. Hwang, Y.-H. Lin, J.-Y. Hwang, *et al.* "Imaging layer number and stacking order through formulating raman fingerprints obtained from hexagonal single crystals of few layer graphene." *Nanotechnology*, 24(1):015702, December 2012. URL http://dx.doi.org/10.1088/0957-4484/24/1/015702.

[340] S. Akcoltekin, H. Bukowska, T. Peters, *et al.* "Unzipping and folding of graphene by swift heavy ions." *Applied Physics Letters*, 98(10):103103, 2011. URL http://dx.doi.org/10.1063/1.3559619.

[341] L. L. Snead, S. J. Zinkle, J. C. Hay, and M. C. Osborne. "Amorphization of sic under ion and neutron irradiation." *Nuclear Instruments and Methods in Physics Research Section B: Beam Interactions with Materials and Atoms*, 141(1-4):123–132, 1998. URL http://dx.doi.org/10.1016/S0168-583X(98)00085-8.

[342] C. Neumann, S. Reichardt, P. Venezuela, *et al.* "Raman spectroscopy as probe of nanometre-scale strain variations in graphene." *Nature Communications*, 6(1), 2015. URL http://dx.doi.org/10.1038/ncomms9429.

[343] S. Y. Zhou, C. O. Girit, A. Scholl, *et al.* "Instability of two-dimensional graphene." *Physical Review B*, 80(12):121409, 2009. URL http://dx.doi.org/10.1103/PhysRevB.80.121409.

[344] J. Hicks, R. Arora, E. Kenyon, *et al.* "X-ray radiation effects in multilayer epitaxial graphene." *Applied Physics Letters*, 99(23):232102, 2011. URL http://dx.doi.org/10.1063/1.3665953.

[345] A. Gao, P. J. Rizo, E. Zoethout, *et al.* "Extreme ultraviolet induced defects on few-layer graphene." *Journal of Applied Physics*, 114(4):044313, 2013. URL http://dx.doi.org/10.1063/1.4817082.

[346] A. Roberts, D. Cormode, C. Reynolds, *et al.* "Response of graphene to femtosecond high-intensity laser irradiation." *Applied Physics Letters*, 99(5):051912, August 2011. URL http://dx.doi.org/10.1063/1.3623760.

[347] Y. Stubrov, A. Nikolenko, V. Strelchuk, S. Nedilko, and V. Chornii. "Structural modification of single-layer graphene under laser irradiation featured by micro-raman spectroscopy." *Nanoscale Research Letters*, 12(1):297, 2017. URL http://dx.doi.org/10.1186/s11671-017-2089-6.

[348] A. Gao, C. J. Lee, and F. Bijkerk. "Graphene defect formation by extreme ultraviolet generated photoelectrons." *Journal of Applied Physics*, 116(5):054312, 2014. URL http://dx.doi.org/10.1063/1.4892485.

[349] J. Hong, M. K. Park, E. J. Lee, *et al.* "Origin of new broad raman d and g peaks in annealed graphene." *Scientific Reports*, 3(1), 2013. URL http://dx.doi.org/10.1038/srep02700.

[350] J.-C. Charlier, X. Gonze, and J.-P. Michenaud. "Graphite interplanar bonding: Electronic delocalization and van der waals interaction." *Europhysics Letters (EPL)*, 28(6):403–408, November 1994. URL http://dx.doi.org/10.1209/0295-5075/28/6/005.

[351] H. O. Jeschke, M. E. Garcia, and K. H. Bennemann. "Theory for the ultrafast ablation of graphite films." *Physical Review Letters*, 87(1):015003, June 2001. URL http://dx.doi.org/10.1103/physrevlett.87.015003.

[352] S. P. Hau-Riege, R. A. London, R. M. Bionta, *et al.* "Wavelength dependence of the damage threshold of inorganic materials under extreme-ultraviolet free-electron-laser irradiation." *Applied Physics Letters*, 95(11):111104, 2009. URL http://dx.doi.org/10.1063/1.3216845.

[353] J. M. Burst, J. N. Duenow, D. S. Albin, *et al.* "CdTe solar cells with open-circuit voltage breaking the 1 V barrier." *Nature Energy*, 1(3):16015–, 2016-2-29. URL http://dx.doi.org/10.1038/nenergy.2016.15.

[354] T. E. Schlesinger, J. E. Toney, H. Yoon, *et al.* "Cadmium zinc telluride and its use as a nuclear radiation detector material." *Materials Science and Engineering: R: Reports*, 32(4-5):103–189, 2001. URL http://dx.doi.org/10.1016/S0927-796X(01)00027-4.

[355] R. O. Bell. "Review of optical applications of CdTe." *Revue de Physique Appliquée*, 12(2):391–399, 1977. URL http://dx.doi.org/10.1051/rphysap:01977001202039100.

[356] R. Triboulet, A. Lasbley, B. Toulouse, and R. Granger. "Growth and characterization of bulk HgZnTe crystals." *Journal of Crystal Growth*, 79(1-3):695–700, 1986. URL http://dx.doi.org/10.1016/0022-0248(86)90539-7.

[357] R. J. Goble and S. D. Scott. "The relationship between mineral hardness and compressibility (or bulk modulus)." *The Canadian Mineralogist*, 23(2):273–285, 1985.

[358] A. Zappettini, N. Zambelli, G. Benassi, D. Calestani, and M. Pavesi. "Live-monitoring of Te inclusions laser-induced thermo-diffusion and annealing in CdZnTe crystals." *Applied Physics Letters*, 104(25):252105–, 2014. URL http://dx.doi.org/10.1063/1.4885116.

[359] E. Belas, M. Bugár, R. Grill, *et al.* "Reduction of inclusions in (CdZn)Te and CdTe." *Journal of Electronic Materials*, 37(9):1212–1218, 2008. URL http://dx.doi.org/10.1007/s11664-008-0479-3.

[360] A. Mychko, A. Medvid, and E. Dauksta. "Laser-induced increase of resistivity and improvement of optical properties of cdznte crystal." *Journal of Crystal Growth*, 415:47–50, 2015. URL http://dx.doi.org/10.1016/j.jcrysgro.2014.12.028.

[361] A. Medvid', A. Mychko, V. Gnatyuk, S. Levytskyi, and Y. Naseka. "Mechanism of nano-cone formation on $Cd_{0.9}Zn_{0.1}Te$ crystal by laser radiation." *Optical Materials*, 32(8):836–839, 2010. URL http://dx.doi.org/10.1016/j.optmat.2010.03.006.

[362] L. C. Teague, S. A. Hawkins, M. C. Duff, *et al.* "AFM characterization of raman laser-induced damage on CdZnTe crystal surfaces." *Journal of Electronic Materials*, 38(8):1522–1527, 2009. URL http://dx.doi.org/10.1007/s11664-009-0763-x.

[363] G. A. Kulkarni, V. G. Sathe, K. S. R. K. Rao, D. V. S. Muthu, and R. K. Sharma. "Micro-raman imaging of Te precipitates in CdZnTe (Zn 4%) crystals." *Journal of Applied Physics*, 105(6):063512–, 2009. URL http://dx.doi.org/10.1063/1.3086274.

[364] F. Cerdeira, C. J. Buchenauer, F. H. Pollak, and M. Cardona. "Stress-induced shifts of first-order raman frequencies of diamond- and zinc-blende-type semiconductors." *Physical Review B*, 5(2):580–593, 1972. URL http://dx.doi.org/10.1103/PhysRevB.5.580.

[365] P. Rudolph. "Fundamental studies on bridgman growth of cdte." *Progress in Crystal Growth and Characterization of Materials*, 29(1-4):275–381, 1994. URL http://dx.doi.org/10.1016/0960-8974(94)90009-4.

[366] W. Stadler, D. M. Hofmann, H. C. Alt, *et al.* "Optical investigations of defects in $Cd_{1-x}Zn_xTe$." *Physical Review B*, 51(16):10619–10630, 1995. URL http://dx.doi.org/10.1103/PhysRevB.51.10619.

[367] S. Hildebrandt, H. Uniewski, J. Schreiber, and H. S. Leipner. "Localization of Y luminescence at glide dislocations in cadmium telluride." *Journal de Physique III*, 7(7):1505–1514, 1997. URL http://dx.doi.org/10.1051/jp3:1997203.

[368] S. Seto, K. Suzuki, V. A. Jr, and K. Inabe. "Compensating related defects in in-doped bulk CdTe." *Journal of Crystal Growth*, 214-215:974–978, 2000. URL http://dx.doi.org/10.1016/S0022-0248(00)00220-7.

[369] K. Kim, J. Suh, A. Bolotnikov, *et al.* "Temperature-gradient annealing of CdZnTe under Te overpressure." *Journal of Crystal Growth*, 354(1):62–66, 2012. URL http://dx.doi.org/10.1016/j.jcrysgro.2012.03.058.

[370] N. W. Ashcroft and N. D. Mermin. *Solid state physics*. Science: Physics. Saunders College, 1976. ISBN 9780030493461. URL https://books.google.cz/books?id=FRZRAAAAMAAJ.

# List of Abbreviations

| | |
|---|---|
| ASE | Amplified Spontaneous Emission |
| BLG | BiLayer Graphene |
| CDI | Coherent Diffractive Imaging |
| CDL | Capillary Discharge Laser |
| CVD | Chemical Vapour Deposition |
| DFT | Density Function Theory |
| DIC | Differential interference contrast |
| EG | Epitaxial Graphene |
| ESCA | Electron Spectroscopy for Chemical Analysis |
| ETMD | Electron Transfer Mediated Decay |
| EuXFEL | European X-ray Free-Electron Laser |
| FEL | Free-Electron Laser |
| FFO | Free-Free Opacity |
| FLASH | Free-Electron LASer in Hamburg |
| FZP | Fresnel Zone Plate |
| GMD | Gas Monitor Detector |
| HDM | Hot Dense Matter |
| HEDP | High Energy Density Physics |
| ICD | Interatomic/Intermolecular Coulombic Decay |
| ICF | Inertial Confinement Fusion |
| IPD | Ionization Potential Depression |
| LCLS | Linac Coherent Light Source |
| LTE | Local Thermodynamic Equilibrium |
| MLG | Multi Layer Graphene |
| MLL | Multilayer Laue Lens |
| NoReFry | Nonlinear Response Function recovery |
| OAP | Off-Axis Parabola mirror |
| PALS | Prague Asterix Laser System |
| PL | PhotoLuminescence |
| PMMA | Poly(methyl methacrylate) |
| SACLA | Spring8 Angstrom Compact Free Electron Laser |
| SASE | Self-Amplified Spontaneous Emission |
| SLG | Single Layer Graphene |
| SXR | Soft X-Ray |
| TDE | ThermoDynamic Equilibrium |
| VdW | van der Waals (bond) |
| WDM | Warm Dense Matter |
| XFEL | X-ray Free-Electron Laser |
| XPS | X-ray Photo-electron Spectroscopy |
| XTANT | X-ray-induced Thermal And Nonthermal Transitions |
| XUV | eXtreme UltraViolet |

# List of publications

1. R. Antoš, V. Vozda, and M. Veis. "Plane wave expansion method used to engineer photonic crystal sensors with high efficiency." *Optics Express*, 22(3), 2014. URL http://dx.doi.org/10.1364/OE.22.002562

2. R. Sobierajski, I. Jacyna, P. Dłużewski, *et al.* "Role of heat accumulation in the multi-shot damage of silicon irradiated with femtosecond XUV pulses at a 1 MHz repetition rate." *Optics Express*, 24(14), 2016. URL http://dx.doi.org/10.1364/OE.24.015468

3. T. R. Preston, S. M. Vinko, O. Ciricosta, *et al.* "Measurements of the k-shell opacity of a solid-density magnesium plasma heated by an X-ray free-electron laser." *Physical Review Letters*, 119(8), 2017. URL http://dx.doi.org/10.1103/PhysRevLett.119.085001

4. I. A. Makhotkin, R. Sobierajski, J. Chalupský, *et al.* "Experimental study of EUV mirror radiation damage resistance under long-term free-electron laser exposures below the single-shot damage threshold." *Journal of Synchrotron Radiation*, 25(1):77–84, 2018. URL http://dx.doi.org/10.1107/S1600577517017362

5. Q. Y. van den Berg, E. V. Fernandez-Tello, T. Burian, *et al.* "Clocking femtosecond collisional dynamics via resonant x-ray spectroscopy." *Physical Review Letters*, 120(5), 2018. URL http://dx.doi.org/10.1103/PhysRevLett.120.055002

6. I. Milov, I. A. Makhotkin, R. Sobierajski, *et al.* "Mechanism of single-shot damage of Ru thin films irradiated by femtosecond extreme UV free-electron laser." *Optics Express*, 26(15), 2018. URL http://dx.doi.org/10.1364/OE.26.019665

7. V. Vozda, T. Burian, J. Chalupský, *et al.* "Micro-Raman mapping of surface changes induced by XUV laser radiation in cadmium telluride." *Journal of Alloys and Compounds*, 763:662–669, 2018. URL http://dx.doi.org/10.1016/j.jallcom.2018.05.332

8. I. A. Makhotkin, I. Milov, J. Chalupský, *et al.* "Damage accumulation in thin ruthenium films induced by repetitive exposure to femtosecond XUV pulses below the single-shot ablation threshold." *Journal of the Optical Society of America B*, 35(11), 2018. URL http://dx.doi.org/10.1364/JOSAB.35.002799

9. V. Vozda, N. Medvedev, J. Chalupský, *et al.* "Detachment of epitaxial graphene from SiC substrate by XUV laser radiation." *Carbon*, 161:36–43, May 2020. URL http://dx.doi.org/10.1016/j.carbon.2020.01.028

10. S. M. Vinko, V. Vozda, J. Andreasson, *et al.* "Time-resolved XUV opacity measurements of warm dense aluminum." *Physical Review Letters*, 124:225002, Jun 2020. URL http://dx.doi.org/10.1103/PhysRevLett.124.225002

11. V. Vozda, T. Burian, V. Hájková, *et al.* "Characterization of megahertz X-ray laser beams by multishot desorption imprints in PMMA." *Optics Express*, submitted

# A. Appendices

## A.1 NoReFry algorithm

The Nonlinear response function recovery (NoReFry) algorithm, used primary for determination of correct fluence profile from desorption imprints, is based on two assumptions: First, the response function (depth) $d(\varepsilon)$ is a monotonically increasing function of accumulated dose $\varepsilon$ which implies that a single value of depth is uniquely attributed to a single value of the dose, irrespective of the single-pulse intensity. Second, beam iso-fluence (or iso-dose) contour geometrically coincides with imprint iso-depth contour of the same area. An iso-depth contour of area $S$ is thus uniquely assigned to a normalized fluence $f(S)$. A complex 2D problem can be therefore reduced into one dimension: $d(S) = d(\varepsilon_0 f(S))$.

An input of the algorithm must be represented by at least two depth profiles of imprints such as shown in Figure A.1a. Two-dimensional data of the $n$-th imprint is denoted as $d_n(x, y)$. It can be numerically reshaped into a monotonically decreasing function $d_n(S; \varepsilon_n)$ called depth scan (d-scan) as shown in Fig. A.1b. Here $S$ stands for area of the given iso-depth contour and $\varepsilon_n$ for the peak dose accumulated in the given imprint. Coloured points in the figure stand for iso-depth contours as indicated in Fig. A.1a.
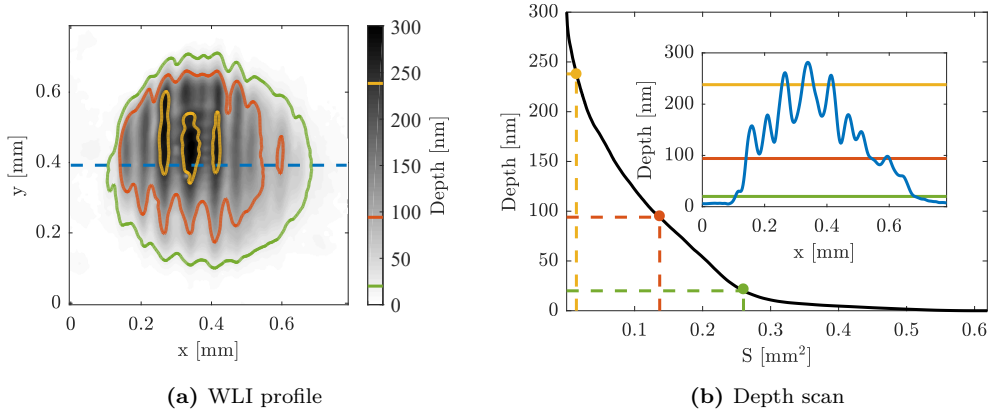


(a) WLI profile  (b) Depth scan

**Figure A.1:** (a) WLI data of desorption imprint. (b) Corresponding depth scan. The inset in (b) shows inverse cross-section profile as indicated in (a) by blue dashed line.

The principle of the algorithm with two depth scans $d_1(S; \varepsilon_1)$ and $d_2(S; \varepsilon_2)$ is described in Figure A.2. Total accumulated doses of the two imprints are $\varepsilon_1$ and $\varepsilon_2$ and maximum depths $d_1^{\max} = d_1(0; \varepsilon_1) = d_1$ and $d_2^{\max} = d_2(0; \varepsilon_2) = d_2$ which can be directly involved in the calibration curve as points $R_1(d_1, \varepsilon_1)$ and $R_2(d_2, \varepsilon_2)$. Next, according to the definition of the normalized fluence scan, we know that $f(0) = 1$ and point $F_1(0, 1)$ can be thus added for free. Further points in the calibration curve $R_i$ and the fluence scan $F_i$, where $i \geq 2$ are calculated step by step using the following procedure: The 1$^{\text{st}}$ assumption as stated above defines point $P_3$ from $P_2$. Iso-fluence contour at $P_3$ has the same depth $d_2$ and hence the same accumulated dose $\varepsilon_2$ but different iso-depth contour $S_2$. Applying the 2$^{\text{nd}}$ rule at the point $P_3$ we can find $F_2(S_2, \varepsilon_2/\varepsilon_1)$ as the doses are related through an equation $\varepsilon_1 f(S_2) = \varepsilon_2$. Using the same assumption again we can find
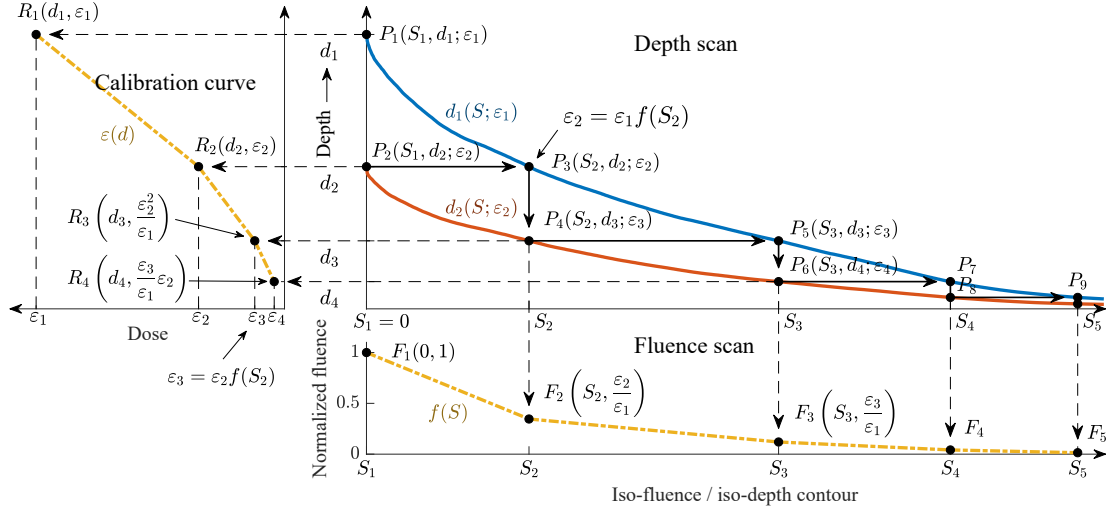
**Figure A.2:** Description of the NoReFry algorithm. Depth profiles of two imprints were transformed into d-scans (red and blue lines) using which we can reconstruct corresponding fluence scan as well as the calibration curve. Adapted from [61].

$P_4(S_2, d_3; \varepsilon_3)$, where $\varepsilon_3 = \varepsilon_2 f(S_2) = \varepsilon_2^2/\varepsilon_1$. It has the same iso-depth contour area $S_2$ but different depth $d_3$. This defines the point $R_3(d_3, \varepsilon_3)$ and closes the first iteration loop. Calculation of points $P_5$, $F_3$, $P_6$, etc. follows in the same way. A general formula for the $j$-th value calculated from the two d-scans is $\varepsilon_j = \varepsilon(d_j) = \varepsilon_2^{j-1}/\varepsilon_1^{j-2}$ and $f_k = f(S_k) = \varepsilon_k/\varepsilon_1 = (\varepsilon_2/\varepsilon_1)^{k-1}$. An improvement in precision of the calibration and f-scan curve recovery as well as higher density of derived points can be ensured by a larger set of input d-scans.

Description of the algorithm including its implementation into a matrix formalism for an arbitrary number of d-scan curves can be also found in [61].

## A.2 Response function model

Change of PMMA desorbed depth after the arrival of $(i+1)$-th X-ray laser pulse can be locally described by the following difference equation [282]:

$$d_{i+1} - d_i = l_{\text{at}}\kappa_0^D \varepsilon_{i+1}\left\{1 - \Delta\left(1 + \frac{\exp\left(-\gamma \sum\limits_{n=0}^{i} \varepsilon_n \exp\left(-\frac{d_i - d_{n-1}}{l_{\text{at}}}\right)\right) - 1}{\gamma \sum\limits_{n=0}^{i} \varepsilon_n \exp\left(-\frac{d_i - d_{n-1}}{l_{\text{at}}}\right)}\right)\right\}, \text{ (A.1)}$$

where $\varepsilon_0 = 0$ and $d_{-1} = d_0 = 0$. Parameter $\kappa_0^D$ stands for the initial desorption efficiency, $\Delta$ for its maximum relative decrease ranging from 0 to 1 and $\gamma$ for the hardening rate. Memory of the material which remembers absorption of all pulses up to the $i$-th one is provided by the summation in the exponential. Arrival of the next $(i+1)$ pulse which locally contributes to overall deposited dose by $\varepsilon_{i+1}$ increases depth $d_i$ to $d_{i+1}$. Under the assumption that the dose increments $\varepsilon_i$ are equal and very small, this equation can be rewritten into the following

integro-differential form:

$$d'(\varepsilon) \;=\; l_{\mathrm{at}}\kappa_0^D \left\{ 1 - \Delta \left( 1 + \frac{\exp\left(-\gamma \int_0^{\varepsilon} \exp\left(-\frac{d(\varepsilon)-d(u)}{l_{\mathrm{at}}}\right)\mathrm{d}u\right) - 1}{\gamma \int_0^{\varepsilon} \exp\left(-\frac{d(\varepsilon)-d(u)}{l_{\mathrm{at}}}\right)\mathrm{d}u} \right) \right\}, \qquad (A.2)$$

This equation can be simplified and analytically solved if we assume that $l_{\mathrm{at}} \gg d$. Assumption of very large attenuation depth is analogous to neglecting any longitudinal shift of the absorption surface with the deposited dose. The exponentials in integrals are reduced to unity yielding:

$$d'(\varepsilon) = l_{\mathrm{at}}\kappa_0^D \left\{ 1 - \Delta \left( 1 + \frac{e^{-\gamma\varepsilon} - 1}{\gamma\varepsilon} \right) \right\}. \qquad (A.3)$$

This finally gives an analytic solution in terms of the exponential integral $E_1(\bullet)$:

$$d(\varepsilon) = l_{\mathrm{at}}\tilde{\kappa}_0^D \left\{ \varepsilon + \frac{\tilde{\Delta}}{\tilde{\gamma}} \left[ E_1(\tilde{\gamma}\varepsilon) + \ln(\tilde{\gamma}\varepsilon) - \tilde{\gamma}\varepsilon + \Gamma \right] \right\}, \qquad (A.4)$$

where $\Gamma = 0.5772156649$ is the Euler-Mascheroni constant. Parameters with tildes, i.e. $\tilde{\kappa}_0^D$, $\tilde{\Delta}$ and $\tilde{\gamma}$, may to some extent deviate from the initial parameters defined in Eq. (A.1). Nevertheless, this approximate model interpolates the response function with a very good precision. This was verified by generation of a test dataset using Eq. (A.1) which was then fitted by the approximate solution as written in Eq. (A.4). Relatively small deviation of 5% for $\tilde{\kappa}_0^D$ and $\tilde{\Delta}$ and 20% for $\tilde{\gamma}$ assuming the attenuation length $l_{\mathrm{at}} = 193$ nm in PMMA at 13.5 nm confirms legitimacy of used approximations. Recovery of the fluence profile $F(x,y)$ is done by applying the inverse of the Eq. A.4 to the crater profile $d(x,y)$.

## A.3   Fresnel propagation model

**Beamline transmission**

Beamline transmission $T_{\mathrm{BML}}$ is important for knowledge of the absolute pulse energy impacting the target. It was calculated using following equation

$$T_{\mathrm{BML}} = R_{\mathrm{MIRRORS}} \times T_{\mathrm{AC}} \times R_{\mathrm{OAP}} \times T_{\mathrm{APERTURES}}, \qquad (A.5)$$

where $R_{\mathrm{MIRRORS}} = 81\%$ is reflectivity of three aC-coated static beam distributing mirrors in the beamline being equal for both pump and probe, $R_{\mathrm{OAP}} = 31.3\%$ is reflectivity of the OAP at 32 nm, $T_{\mathrm{AC}}$ is transmission of the autocorrelator which equals 74% for the pump and 60% for the probe [297] and $T_{\mathrm{APERTURES}}$ represents beam cropping by several apertures (AC mirrors, microscope with a hole drilled in the optics and a wire grid supporting attenuation filters) inserted in the beam path. $T_{\mathrm{APERTURES}}$ was calculated using the Fresnel propagation and optimization. During the experiment its value varied with a particular arrangement of the beamline. After alignment of supporting grids of attenuation filters this value increased to $(22 \pm 1)\%$ and $(11 \pm 1)\%$ for the pump and the probe. Errors stand for standard deviations obtained from averaging beamline transmissions

calculated for individual shots. These errors are present due to a jitter of the beam which also to some extent affects pump-to-probe intensity ratio. Total beamline transmission thus equals $(4.1 \pm 0.2)\%$ and $(1.6 \pm 0.2)\%$ for the pump and the probe, respectively.

In order to calculate energy on the target $E_{\text{TRG}}$, transmission of the supporting wire grids $T_{\text{GRID}}$ placed between the target and the CCD has to be omitted:

$$E_{\text{TRG}} = E_{\text{GMD}} \times \frac{T_{\text{BML}}}{T_{\text{GRID}}}, \tag{A.6}$$

where $E_{\text{GMD}}$ is the pulse energy measured by the gas monitor detector. Ratio $T_{\text{BML}}/T_{\text{GRID}}$ is $(4.6 \pm 0.2)\%$ and $(1.8 \pm 0.2)\%$ for the pump and the probe.

**Fresnel propagation model**

The Fresnel propagation was performed in the Fourier space where a Gaussian-shaped intensity profile was assumed as an input beam entering the autocorrelator. The size of the beam and its position with respect to autocorrelator's mirrors play a significant role in the total transmission of both the pump and probe beam. Nevertheless, the input beam parameters were initially unknown. Hence a multi-parameter optimization procedure was applied to vary the beam (position and size) and beamline (positions of mirror edges, radius and position of microscope's aperture, dimension and position of the wire grid) parameters and to minimize the $\chi^2$-difference (sum of squared deviations) between the Fresnel-propagated beam and real X-ray CCD image. A special attention was paid to periodicity of diffraction fringes emanating from inserted edges. A real signal from CCD is shown in Figure A.3a and modelled beam intensity using the Fresnel propagation in Fig. A.3b. Great agreement of both profiles can be seen.
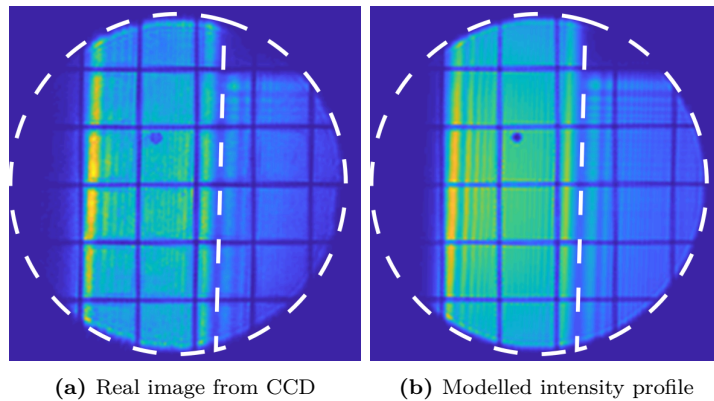


**(a)** Real image from CCD      **(b)** Modelled intensity profile

**Figure A.3:** (a) Typical image of the beam detected by the CCD camera, where the pump (left) and the probe (right) are indicated. Main interference fringes have typical shape of knife-edge effect induced by slicing mirror in the autocorrelator. Circular aperture of the transmission microscope cropped the beam, hence its round shape. Rectangular wire grid supporting the attenuation filters is also visible. (b) Intensity profile obtained from the Fresnel propagation used for calculation of the beamline transmission.

Apertures, mirror edges and wires can be easily implemented as binary masks of variable parameters. Insertion of a short-focal-length off-axis parabolic mirror, on the other hand, represents a difficult numerical task requiring either a sophisticated propagation routine or extremely dense phase sampling complying

with the Nyquist-Shannon sampling theorem. In order to overcome this issue we used the fact that the projection on the CCD represents a magnified image of an object field located (approx. 412 mm) upstream the OAP and cropped by the microscope's aperture located (100 mm) downstream. This approach makes it possible to exclude the OAP from the simulation and model only the object field in relative dimensions to find the best match with the CCD image. Since the divergence of the beam is small ($\sim$100 $\mu$rad), we assumed a Gaussian input beam with flat wavefront which excludes the initial wavefront curvature from the set of optimized parameters. The calculated errors are relatively small, however, systematic error induced by assumed Gaussian beam profile (typical profile is non-Gaussian) without any phase (i.e. ideally collimated beam) cannot be entirely excluded. It follows from the transmission values that the fraction of energy transmitted to the pump beam is approx. 86% which is in a perfect agreement with ablation imprint measurement resulting in 85%.

## A.4 Electron temperature

In this section we briefly describe relation between electron temperature and absorbed laser energy. Full and rigorous derivation can be found, for example, in [101].

Electron temperature $T_e$ of an ideal gas in TDE is connected to average electron energy via equipartition theorem. This theorem states, that each degree of freedom contributes to the system energy by one half of $k_B T_e$, where $k_B$ is the Boltzmann constant. The energy density of such ideal system with electron density $n_e$ and three degrees of motion is therefore calculated as:

$$E_{\text{dens}} = \frac{3}{2} n_e k_B T_e. \tag{A.7}$$

Nevertheless, this relation does not include the correct density of states very important for quantum-mechanical systems such as a Fermi gas which obeys the Pauli exclusion principle. The mean energy density of electrons in metal $\langle E_{\text{dens}} \rangle$ can be expressed in integral form:

$$\langle E_{\text{dens}}(T) \rangle = \int_0^\infty \mathcal{D}(E) f_{\text{FD}}(E, T, \mu(T)) E \, \mathrm{d}E \tag{A.8}$$

where $\mathcal{D}(E)$ is the density of states at system energy $E$ and $f_{\text{FD}}$ Fermi-Dirac distribution. The density of states for 3D system of minimum potential energy $E_0$ equals to:[1]

$$\mathcal{D}(E) = \frac{1}{2\pi^2} \left( \frac{2m_e}{\hbar^2} \right)^{3/2} \sqrt{E - E_0}, \tag{A.9}$$

where $m_e$ is the electron mass and $\hbar$ is the reduced Planck's constant. The Fermi-Dirac distribution is usually written as:

$$f_{\text{FD}}(E, T, \mu) = \frac{1}{e^{\frac{E-\mu}{k_B T}} + 1}, \tag{A.10}$$

---

[1]More precise form of density of states calculated by ABINIT code was used in the forward model described in [60].

where $\mu(T)$ is the chemical potential dependent on temperature. It cannot be expressed explicitly but can be found as a solution for known electron density $n_e$ of a given material:

$$n_e = \int_0^\infty \mathcal{D}(E) f_{\text{FD}}(E, T, \mu(T)) \mathrm{d}E. \tag{A.11}$$

This equation can be solved either numerically or using Sommerfeld expansion [370, p. 760].

To summarize, electron temperature $T_e$ of a system with experimentally measured absorbed energy density $E_{\text{abs}}$ is found by numerical minimization of term $|E_{\text{abs}} - \langle E_{\text{dens}}(T_e) \rangle - \langle E_{\text{dens}}(T = 0) \rangle|$, where $\langle E_{\text{dens}}(T_e) \rangle$ is given by Eq. (A.8). The $\langle E_{\text{dens}}(T = 0) \rangle$ is energy density at zero temperature which must be subtracted in order to compare with experimentally measured absorbed energy $E_{\text{abs}}$ and not the total energy of the system.
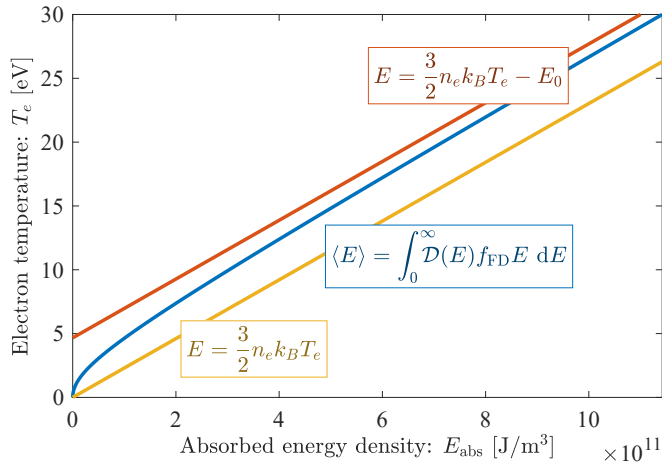


**Figure A.4:** Comparison of temperature as a function of the absorbed energy density calculated from Eq. (A.7) and (A.8). The greatest difference is at zero temperature, where almost no energy is needed to heat electrons. The blue curve asymptotically approaches the red one.